Manganese-based Positive-Contrast MRI for Non-invasive Monitoring of Biomaterials and Cells in Tissue Engineering

By

Daniel Andrzej Szulc

A thesis submitted in conformity with the requirements for the degree of Doctor of Philosophy

Institute of Biomedical Engineering, University of Toronto

Manganese-based Positive-Contrast MRI for Non-invasive Monitoring of Biomaterials and Cells in Tissue Engineering

Daniel Andrzej Szulc

Doctor of Philosophy

Institute of Biomedical Engineering

University of Toronto

2020

Abstract

Cells and scaffolds are the pillars of tissue engineering and regenerative medicine. They have the potential to regenerate any tissue or organ; however, a major unmet challenge limiting their clinical translation is the absence of non-invasive technologies for spatial and temporal tracking of implant fate in deep tissue and with high spatial resolution. Contrast-enhanced magnetic resonance imaging (CE-MRI) is highly suited for this task; however, current methods suffer from contrast agent toxicity or fail to provide longitudinal monitoring with high sensitivity and specificity. To address this need, this thesis aims to further develop positive-contrast MRI with manganese (Mn), an essential micronutrient, for *in vivo* imaging and tracking of cells and scaffolds. To image scaffolds and track their fate, biomaterials were labelled with manganese porphyrin (MnP) contrast agents, which exhibit anomalously high T_1 relaxivity and form stable Mn-chelates. Atypical conjugation approaches were explored to achieve facile, biocompatible and efficient labelling of a variety of decellularized extracellular matrix and collagen-based scaffolds including injectable hydrogels, tissue grafts and whole organ constructs. This thesis demonstrates the first report to track these materials *in vivo* with CE-MRI and the potential for quantitative tracking of degradation over time. For non-invasive cellular MRI, both direct and indirect labelling techniques with Mn-based agents were designed to guide cell injection in real-time and probe cell fate longitudinally. Firstly, the

utility of a commercially scalable MnP agent for safe and highly efficient labelling of human embryonic stem cells was demonstrated *ex vivo.* MR imaging of the labelled cells permitted detection of early cell fate and injection success *in vivo*. Secondly, to track cells longitudinally with high sensitivity and specificity, a reporter gene platform, bright-ferritin, was designed to produce endogenous T_1-cellular contrast by the formation of manganese-ferritin nanoparticles intracellularly. The bright-ferritin system exhibited superior relaxivity and contrast generation *in vitro* and *in vivo* over conventional T_2 iron-ferritin systems and T_1 manganese-transporter systems. This bright-ferritin platform has the potential for on-demand, longitudinal, and sensitive, quantitative cell-tracking *in vivo*. Overall, this body of work demonstrates the utility of Mn-based bright-MRI for the assessment of scaffold and cell implantations.

Acknowledgments

First and foremost, I would like to thank my supervisor, Professor Hai-Ling Margaret Cheng, for her extraordinary support and committed mentorship. Her dedicated work ethic and deep passion for scientific exploration profoundly shaped my development as a researcher. Not only did she contribute innumerably to this body of work with her scientific insights and expertise, but she was also always there to provide constant encouragement and advice. Regardless of the challenge, whether in life or research, she motivated and inspired me to push on and forwards. The work I accomplished would not have been possible without her support and guidance. I will always appreciate what she has taught me, and I am so thankful to have had such a kind and dedicated Ph.D. advisor.

I would also like to thank my committee members Prof. Herman Yeger and Prof. Ping Lee, for their support at all levels of my research projects. Their guidance and advice were invaluable during my doctoral work, and I am grateful for their contributions. I would also like to express my sincere thanks to Prof. Marc-André Fortin and Prof. Nilesh Ghugre for kindly providing their time and expertise as my external and internal examiners.

I would like to recognize Medicine by Design (MbD) for providing project funding and promoting collaborative teams that supported much of this work. Many thanks to Prof. Michael Laflamme and Rocco Romagnuolo for their scientific insights and advice in regenerative medicine and genetic cell editing. I also would like to extend my sincere gratitude to Prof. Hai-Ying Mary Cheng and Xavier Lee, who further guided the genetic cell work and provided the necessary materials and expertise to create stable cell lines with various genetic profiles. Their continued support of time, materials and academic oversight over the years facilitated many discoveries and the development of new avenues of research. I am also grateful to Prof. Thomas Waddell, Dr. Golnaz Karoubi, Mohammadali Ahmadipour and Dr. Fabio Aoki for their contribution of materials and tissues for scaffold tracking as well their academic insights and advice.

I would also like to recognize the Institute of Biomedical Engineering and the Ted Rogers Centre for Heart Research at the University of Toronto. Both are truly unique departments that foster and promote innovative and multi-disciplinary collaboration across academia and industry.

Many thanks to my colleagues and co-authors in the Cheng Lab. Thank you, Andrei Venter, Rohan Alvares, Tameshwar Ganesh, Sadi Loai and Inga Haedicke. It was a pleasure working with everyone and becoming close friends over the years. I appreciate all your hard work, expertise and advice dearly.

Finally, a large and warm thank you goes out to all my friends and family. My loving parents, Adam and Beata, and my brothers, Oliver and Konrad, have always been supportive of every step I have taken in life, and I cannot thank them enough for everything they do for me. I would also like to thank my caring uncle and aunt, Aldona and Piotr, and my amazing cousins, Karolina and Michalina, who have been inspiring role models and caring family members. Lastly, I must thank my dearest love, Jessica Blakeley, for her unwavering support and encouragement in all my endeavors. I feel incredibly lucky to have you all in my life.

Table of Contents

List of Figures

List of Tables

List of Abbreviations

ACN	Acetonitrile
ADC	Apparent diffusion coefficient
AES	Atomic emission spectroscopy
Apo-PNH_2	5-(4-aminophenyl)-10,15,20-(tri-4-sulfonatophenyl)porphyrin
CA	Contrast agent
Cas9	CRISPR associated protein 9
CE	Contrast enhancement
CEST	Chemical exchange saturation transfer
CHAPS	3-[(3-Cholamidopropyl)dimethylammonio]-1-propanesulfonate hydrate
CRISPR	Clustered regularly interspaced short palindromic repeats
CSF	cerebral spinal fluid
CT	Computed tomography
D	Diffusion coefficient
DA	Dopamine
DAPI	4′,6-Diamidino-2-phenylindole
dECM	Decellularized extracellular matrix
DIPEA	N,N-Diisopropylethylamine
DMEM	Dulbecco's modified eagle medium
DMF	Dimethylformamide
DMSO	Dimethyl sulfoxide
DMT-1	Divalent metal transport protein type-1
DTPA	Diethylenetriamine pentaacetate
ECM	Extracellular matrix
EDTA	Ethylenediaminetetraacetic acid
ESC	Embryonic stem cells
ESEM	Environmental scanning eletron microscopy
ESI	Electron spray ionization
ETL	Echo train length
FAAS	Flame atomic absorption spectroscopy
FBS	Fetal bovine serum
FDA	Food & drug administration
FFE	Fast field echo
FOV	Field of view
FTH	Ferritin heavy chain
FTL	Ferritin light chain
GBCA	Gadolinium based contrast agent
GFP	Green fluorescent protein
HA	Human influenza hemagglutinin

HEK293	Human embryonic kidney 293 cells
HEPES	(4-(2-Hydroxyethyl)-1-piperazineethanesulfonic acid
HPLC	High-performance liquid chromatography
HSV1	Herpes simplex virus type-1
HUVEC	Human umbilical vein endothelial cells
ICP	Inductively coupled plasma
iPSC	Induced pluripotent stem cells
LD_{50}	Lethal dose for 50% of test animals
LRP	Lysine rich protein
MnP	Manganese porphyrin
$MnPNH_2$	Manganese 5-(4-aminophenyl)-10,15,20-(tri-4-sulfonatophenyl)porphyrin
MnTPPS	Manganese (III) meso-tetra(4-sulfonatophenyl)porphyrin
MRI	Magnetic resonance imaging
MS	Mass spectrometry
MSC	Mesenchymal stem cell
MTR	Magnetization transfer ratio
MWCO	Molecular weight cut-off
NIR	Near-infrared
NMR	Nuclear magnetization resonance
NOD-SCID	Nonobese diabetic/severe combined immunodeficiency
NSA	Number of signal averages
NSF	Nephrogenic systemic fibrosis
P2A	2A self-cleaving peptide
PBS	Phosphate buffered saline
PCR	Polymerase chain reaction
PDA	Polydopamine
PEI	Polyethyleneimine
PET	Positron emission tomography
PFA	paraformaldehyde
PFC	Perfluorocarbons
PVDF	Polyvinylidene fluoride
R_1	Longitudinal relaxation rate
R_2	Transverse relaxation rate
RES	Reticuloendothelial system
RIPA	Radioimmunoprecipitation
RT	Room temperature
SC	Stem cells
SDC	sodium deoxycholate
SDS-PAGE	Sodium dodecyl sulphate-polyacrylamide gel electrophoresis
SE	Spin echo

SEM	Scanning electron microscopy
SNR	Signal-to-noise ration
SPECT	Single-photon emission computed tomography
SPIOs	Superparamagnetic iron oxide particles
T_1	Spin-lattice or longitudinal relaxation time
T_2	Spin-spin or transverse relaxation time
TE	Echo time
TEM	Transmission electron microscopy
TI	Inversion time
TK	Tyrosine kinase
TR	Repetition time
TSE	Turbo spin echo
TUNEL	Terminal deoxynucleotidyl transferase dUTP nick end labelling
TXR	Texas Red
US	Ultrasound
USPIO	Ultrasmall superparamagnetic iron oxide
UV	Ultraviolet
WT	Wild type

Chapter 1 : Introduction

1.1 Regenerative Medicine and Tissue Engineering

Tissue engineering is an emerging field that has rapidly expanded in the past decade with the development of interdisciplinary approaches utilizing physical and life science principles to regenerate injured and diseased organs. The field initially stemmed from work in the development of biomaterials, materials which interact with biological systems, to mimic natural tissues. These biomaterials could be used to study healthy or diseased tissues and potentially replace or restore whole organs; the ultimate goal within the broader field of regenerative medicine. To develop regenerative cures, the field quickly evolved to incorporate aspects of biological, medical and life science research. With the collective effort of scientists, clinicians and engineers, a multitude of medicinal materials, treatments and systems have been developed to regenerate almost every tissue and organ of the body. Despite the complex nature of these treatments, cells and materials remain the cornerstone of tissue engineering and regenerative medicine.[1] Materials provide the physical support necessary for generating 3D tissue structure, and cells provide the biological support needed to regenerate and re-integrate damaged tissue. At the end of 2019, there were over 262 tissue engineering therapies utilizing scaffolds and/or cells in clinical trials with 47 in phase III[2]. These trials span treatments in all areas of the body, from musculoskeletal and cardiovascular therapies to gastroenterology and hematology.

1.1.1 Cell Therapy

Cell therapies are treatments that use cells as the primary tool to cure or relieve the severity of an injury or disease. Cells can be used in two ways: 1) as a transplant where cells extracted from the patient or a donor are injected at the desired site or 2) as a target for a biologically active compound, where the intended effect is to stimulate resident cells to regenerate tissue. Within the context of transplantation, there are three main objectives: 1) regeneration of damaged tissue, 2) replacement of lost biological function such as secreting physiologically active molecules and 3) redirection of aberrant processes[3] (Figure **1.1B-D**). The use of cells in transplantation regenerative therapies has

been shown to improve the outcomes of a variety of injury/disease models from cardiac failure to skin regeneration.[4,5] This vast utility has largely been due to the isolation and identification of human stem cells, which hold great therapeutic potential for regenerative medicine because of their unlimited potential to differentiate into all primary cell layers (endoderm, ectoderm and mesoderm). Before this, partially or terminally differentiated cells isolated from adult tissues were primarily employed.[6] Now many cell types with varying degrees of stemness are being explored (Figure **1.1A**). This includes the aforementioned pluripotent stem cells (SC) such as human embryonic or induced pluripotent SCs, as well as 'adult' or multipotent SCs such as mesenchymal SCs which have a limited capacity for differentiation but demonstrate greater efficacy and fewer complications of tumorigenicity and teratoma formation in preclinical and clinical studies[1,7,8]. With regards to clinical application, the most common cell therapy available clinically utilizes multipotent hematopoietic stem cells for bone marrow transplants[1,7,8]. Many more promising therapies are being developed for clinical use such as direct injection of pancreatic beta cells to alleviate insulin deficiency in Type 1 diabetics, while others aim to restore heart function after a myocardial infarction by injection of multipotent mesenchymal stem cells (MSCs) or terminally differentiated cardiomyocytes[9,10]. Despite preclinical promise, most therapies have failed during clinical trials due to the lack of functional improvement in patient health, such as in cardiac regeneration, where a simple injection of cardiomyocytes has not been able to achieve sufficient electrical and mechanical integration with existing heart tissue to improve overall heart function.[11–14]

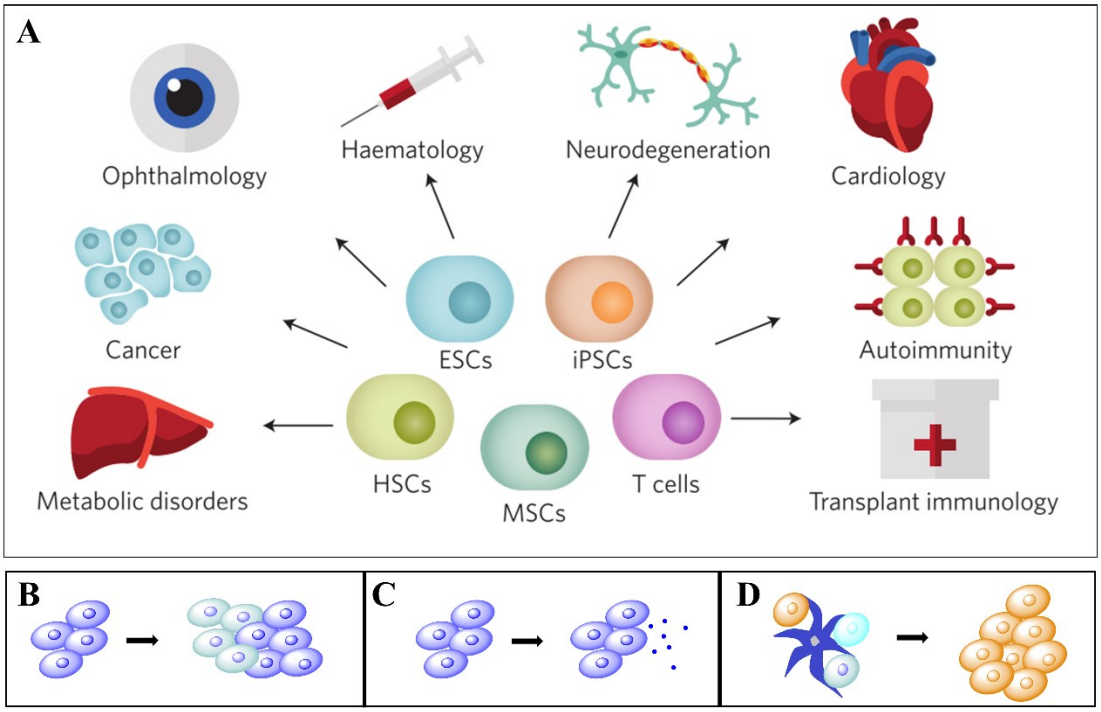

Figure 1.1: Cell therapy and regenerative medicine A) A variety of cell types, including somatic cells (T cells), adult stem cells (HSCs, MSCs) and pluripotent stem cell (ESCs, iPSCs) derivatives, have been studied and utilized to address a wide range of pathologies. Transplanted therapeutic cells can fulfill three main roles **B)** regenerate tissue, i.e. stem cell transplantation; **C)** replace lost tissue function, i.e. pancreatic islet transfer in insulin-dependent diabetes; **D)** redirect physiological processes, i.e. immune cell injection to target tumours and elicit host immune responses. Adapted with permission from Kooreman, N.G., Ransohoff, J. D., & Wu, J.C. *Nat. Mat.,* 2014, 13, 106-109. Copyright (2014) Springer Nature.

1.1.2 Biomaterials in Tissue Engineering

Within tissue engineering, biomaterials are also extensively utilized for regenerative medicine applications due to their ability to support and facilitate tissue repair. Many materials can induce a cellular response within a patient by recruiting host cells and tissue in-growth, and thus can be utilized without the addition of cells; however, many applications combine them for synergistic purposes.[1] The functional ability to support and promote 3D tissue formation has resulted in the colloquial term of "scaffold" to represent biomaterials utilized in regenerative medicine. Currently, scaffolds are made from a variety of materials, both natural (i.e. collagen) and synthetic (i.e. polyethylene glycol) to produce implants with optimal mechanical, structural, biocompatible and degradative properties that mimic tissues in the human body.[15] Scaffolds composed of natural

materials have traditionally played a vital role in this field; however, synthetic materials have received attention in recent years. While synthetic materials are less prevalent in regenerative medicine applications due to their foreign nature, they have, however, been extensively investigated and clinically used for biomedical devices due to their inertness, facile sterilization and scale-up potential. Synthetic materials can range from organic polymer grafts and hydrogels to ceramics and metals[16,17]. Organic polymer networks and gels composed of polyethylene glycol[18], poly(lactic-co-glycolic acid)[19], or polycaprolactone[20] have been the most widely explored synthetic materials for scaffold applications due to their biodegradability and biocompatibility coupled with low cost, controllable synthesis, and tunable properties and characteristics.

Despite significant strides made with synthetic polymers, natural-based materials continue to play a major role in regenerative medicine due to their innate biological activity. Natural materials provide an environment recognized by cells and promote excellent cell attachment, growth and biological signalling processes. However, these materials can cause immunogenic responses and pathogenic transmission if not correctly processed. Due to their ideal properties, several natural materials are clinically approved for use as scaffolds in tissue engineering applications. This includes collagen[21–23], hyaluronic acid[23,24], chondroitin sulfate[21,23,25] and chitosan[26] based materials. To date, collagen and extracellular matrix (ECM) based scaffolds have demonstrated the most significant clinical utility.[27] This is due to the highly conserved nature of ECM proteins, particularly collagen, which are found throughout the entire human body and in all connective tissues. This abundance and importance in the body has highlighted collagen as a prime target for use in tissue engineering and regenerative medicine. Its molecular and physical structure promotes cell attachment, migration, and proliferation. Additionally, its ability to form fibers under various conditions (heat, pH, ionic strength), the variety of cross-linking agents and the availability of different collagen types (I, II, III, V and XI) make collagen scaffolds highly versatile and tunable.[28] Research in this field has erupted over the past decade with collagen being used widely in both research settings and medical applications.[27,29–33] One specific area of research is cardiac regeneration due to the limited regenerative capacity of native heart tissue.[34] Promising research in this field has shown heart tissue regeneration with collagen hydrogels[35,36], in minimally invasive injection models as well as *ex vivo* whole heart replacements with decellularized ECM organ constructs.[37,38]

Regardless of the material chosen, whether synthetic or natural, all scaffolds must be optimized for a variety of properties to ensure they support cell and tissue growth. Firstly, scaffolds must have an ideal porosity and density with a high surface area to volume ratio, to permit cell infiltration and adequate perfusion and diffusion of nutrients.[15,39] The scaffold surface must also be properly functionalized to promote cell attachment and growth. Additionally, scaffold materials must exhibit mechanical strength to structurally support tissue-ingrowth but also maintain elastic flexibility to move with the body. Lastly, while support is needed upon initial implantation and the early stages of regeneration, scaffolds must eventually biodegrade at a rate ideally matched to that of new tissue formation. Due to these complex systems, accurate and regular feedback regarding the changes to a scaffold, and in-growing tissue is necessary to optimize engineering strategies and achieve structural and functional tissue restoration.

1.1.3 Current Therapeutic Challenges

As mentioned in the above sections, many different scaffold and cell therapies have shown success preclinically and have moved on to clinical testing[2]. However, despite this large entry into clinical testing, only a few scaffold and cell-based therapies have been approved and are on the market today.[2] Most regenerative therapies fail during clinical trials due to complications or simply not meeting the milestones required for clinical utility.[14,40] There are major issues with scaffold and cellular therapies that occur from the moment of injection to years later that have yet to be properly studied and optimized.

Regardless if the therapy is scaffold or cell-based, to better understand the reason behind the failure of a clinical trial, it is imperative to know the fate of the transplant, both temporally and spatially. Firstly, the implant must be placed in the appropriate location at the site of injury or disease. However, misplacement of materials occurs frequently due to inaccurate injection, even with ultrasound guidance.[41,42] This is further exacerbated when cells and scaffolds migrate offsite due to internal tissue motions such as a beating heart or physical migration of the cells themselves. Determining the exact location of the material early on and late in the therapy is essential for correlating to functional therapy success. Individual assessment is imperative in this context to achieve meaningful results. For example, discovering the misinjection of an implant would allow for a better understanding of the reason and rate of therapy failure. While scaffold and cell

therapies are plagued with misinjection and internal shifting, cellular therapies pose additional challenges to the viability of the transplant. A large fraction of cells, between 30-50%, die within 24 hours of transplantation. [3] This could be the result of many factors, including mechanical stress in the syringe during injection, movement of the tissue, and drastic change of environments. Furthermore, the extent to which these cells are retained in the target region and their mechanism of action remains unclear.[4,5]

Once injected, the materials begin to interact with the host tissue. These interactions deviate significantly from observations during in vitro experimentation and can result in unsatisfactory therapy outcomes. In regenerative medicine, the site of injury or disease is often ischemic, which restricts the delivery of nutrients needed for the survival and proliferation of the injected cells. Cardiac regeneration trials after myocardial infarction have shown greater than 90% cell death within one-week of injection. [3] This harsh environment and interindividual variability between patients also affect the stability and degradation rate of biomaterials. Accelerated loss of a scaffold early on in a therapy will significantly hinder the regeneration of new tissue and also alter the 3D structure and mechanical properties of the scaffold, such as the contraction of a cardiac patch.[39,43–45] On the other hand, slow degradation of a scaffold will prevent tissue ingrowth and proper integration over time. While degradation is not a factor with cell therapies, a parallel is the rate of cell growth. As discussed, earlier cell death is the primary factor that impacts therapy success; however, accelerated growth can also be problematic. A unique obstacle to cell therapies is the potential for uncontrolled growth and differentiation, which leads to tumorgenicity and teratoma formation, particularly with the use of stem cells. This has become a principal barrier to full regulatory approval of stem cell-based therapies and will require monitoring *in vivo* to be addressed. [46]

These variables and conditions become further complicated when there is a lack of standardization in the methods of administration. Injection volumes, frequency, location and cell number have all varied with recent clinical trials, making it difficult to draw conclusions and rationale regarding outcomes between treatments. [41] Injection location is particularly important but lacks consensus in the field. [47,48] Cardiac regeneration therapies have utilized various types of injections, including intravenous, intracoronary and intramyocardially, which is further complicated with a range injection depths within the tissue, and the number of injections to

sufficiently cover the injured or diseased areas. [47,48] Due the intricacies of these trials, the differential impact of methodologies has been difficult to ascertain and is largely measured at late time points with traditional functional assessments of tissue restoration, which are often too late to understand the early effects of injection methods on cells and materials. Characterizing how cells and materials change in a patient from viability and degradation to position and migration, will provide greater insight into clinical trials and permit comparison among patient cohorts and methodologies.

1.2 Medical Imaging for Tissue Engineering

Despite the distinct nature of these scaffolds and cells, the issues faced by their respective therapies have a shared commonality: lack of in vivo spatial and temporal identification.[45,49,50] Great advances have occurred in the development of scaffold and cell-based therapies but the methods to assess these treatments have lagged. Advances in medical imaging are required to understand the vast changes and unexpected outcomes that occur with scaffold and cell-based therapies as they transition from the laboratory bench to the body of a patient. Optical techniques utilizing fluorescence imaging have largely been employed for this reason in a laboratory setting; however, no fluoresce technique has entered the clinic due its shallow penetration.[51,52] To advance this field we must look to the utilization of traditional medical imaging modalities that have been extensively tested and routinely used on human patients. An overview of the most common modalities and their properties are summarized in Table **1.1**. Ideally, a methodology that is non-invasive, deep-tissue penetrating and visualizable in real-time would provide the greatest insight regarding scaffold and cellular changes during a therapy. The following sections will address each modality and their current methods and limitations for tracking scaffolds and cells.

Modality	MRI	PET	SPECT	X-ray/CT	US
Applications	Anatomy, Pathology Function Molecular	Metabolism, Function, molecular	Metabolism, Molecular	Anatomy, pathology, vascular, delivery, biopsy	Anatomy, pathology, vascular delivery. biopsy
Labels/Probes	Gd and Mn-Chelates, Iron oxide particles, perfluorocarbons	^{18}Fluorine molecules (ie. ^{18}FDG, ^{18}FHBG, ^{18}FDOPA)	Radioisotopes: Tc-99m, In-111	Iodine, barium	Microbubbles, microcapsules, liposomes
Signal Measured	Alterations in magnetic fields	Gamma-rays from the annihilation of positrons emitted by radioisotopes	Gamma-rays from radioisotopes	X-rays	Sound waves
Sensitivity (M)	10^{-9}-10^{-8}	10^{-15}	10^{-14}	10^{-6}	10^{-8}
Resolution	50 um	1-2 mm	1-2 mm	50 um	50 um
Strengths	Non-ionizing radiation, superior soft- tissue contrast, real-time guidance	Highly sensitive	Multiplex Imaging	Fast, cross-sectional images, real-time guidance	Real-time guidance, quick, harmless, cheap
Weaknesses	Limited multi-label tracking, cost, danger to patients with metallic implants	Ionizing radiation, can detect only one radionuclide, no anatomical information	Ionizing radiation, low resolution and no anatomical information	Ionizing radiation, poor resolution of soft tissues	Poor image contrast, works poorly in organs containing air

Table 1-1: Summary of clinical imaging modalities.[53,54]

1.3 Biomaterial Tracking

Biomaterial tracking is the use of imaging tools with or without tracers to track the fate of a scaffold post transplantation.[50] Imaging a scaffold in a patient provides insights regarding the movement and degradation of the material as well as new tissue formation. Traditional assessment of materials and engineering constructs are highly invasive, such as histological and biochemical analysis, which require sacrificial harvest of tissue for assessment. Consequently, this is not a feasible option for clinical applications and can result in ethical and statistical concerns in research settings where large animal cohorts are required for significant medical insights. Furthermore, it renders a researcher blind to real-time changes during a therapy. Due to the complex nature and variability between animals, it is ideal to track each scaffold independently in each patient; this would limit interindividual bias by permitting longitudinal tracking and trend analysis. This would provide more conclusive evidence regarding the success of a treatment in disease and injury models. It would also provide informed and fluid design of start and end-points for pre-clinical

trials. With the development and testing of a large variety of scaffolds and factors, the need for non-invasive longitudinal assessment of scaffolds is being heavily developed.

1.3.1 Optical Imaging

Most of the early work in biomaterial tracking focused on adapting traditional fluorescence and near-infrared (NIR) imaging techniques from adjacent molecular imaging fields. In these cases, fluorescent and/or near-infrared molecular probes were incorporated or conjugated to scaffold materials for longitudinal tracking in vivo.[55–57] This initially proved quite successful for tracking scaffolds quantitively, due to the strong linear correlation between fluorescent signal and probe concentration.[58] This provided a means for tissue engineers to measure properties such as degradation and erosion in vivo. Despite this success, fluorescence imaging suffers from many limitations as an *in vivo* imaging modality. The primary obstacle is its limited penetration in tissue and intractable photobleaching.[59] Advancements in multi-photon imaging and NIR have enhanced the penetration capability of optical techniques for *in vivo* subcutaneous models. However, optical and fluorescence microscopy remains incapable of imaging deep tissues and organs, which is necessary for scaffold engineering and regenerative medicine in a clinical setting.

1.3.2 Computed Tomography and Positron Emission Tomography

Standard X-ray and micro-computed tomography (CT) have been used to address the penetration problem experienced with optical modalities, and can provide information regarding scaffolds in dense tissues such as bone engineering.[60] CT takes advantage of the attenuation of the electromagnetic energy of x-rays to visualize the difference in physical densities of varying tissues and thus can also visualize a change in scaffold density during host-tissue infiltration. X-rays taken about a single axis of rotation produce 3D images which elucidate structural and positional changes of transplanted materials. Scaffolds can be further labeled with radiopaque contrast agents (CAs) to produce better visualization of scaffold features such as porosity, shape and size.[60] Often, however, when utilizing CT, scaffolds are labelled with radioisotopes which produce distinct signal that can be detected, imaged and quantified against natural tissue[54]. Certain radiotracers, decay and produce small particles called positrons, such as fluorine-18 , which are imaged with

positron emission tomography (PET)[53]. The emitted positrons annihilate with nearby electrons and generate gamma rays. These photons are detected by the PET scanner, and a 3D image is reconstructed to visualize their location. Other radioisotopes can emit gamma rays directly, such as indium-111, and are imaged with single-photon emission computed tomography (SPECT). When radioactive tracers are conjugated to scaffolds, PET and SPECT imaging permits *in vivo* detection and visualization.[53] These radioactive tracers are highly sensitive with a detection limit on the order of 10^{-15}, multiple orders of magnitude greater than CT (10^{-6}) agents [54]; however, they have short half-lives, ranging from a couple of hours to a few days, which limits their use for longitudinal studies. Their cytotoxicity and patient safety concerns further limit their long-term clinical utility.[60] For these reasons, significant focus has been directed towards non-radiative imaging modalities such as ultrasound and magnetic resonance imaging (MRI), where serial imaging over a prolonged timeframe is achievable and safe for monitoring regenerative therapies.

1.3.3 Ultrasound Imaging

Ultrasound imaging can visualize changes in tissue density, like CT, but does so by measuring the difference in attenuation of mechanical ultrasound waves through tissue.[54] Two-dimensional images are produced by the reflections and echoes of the sound waves on soft tissue.[54] In comparison to CT, ultrasound exhibits superior soft-tissue contrast without the use of ionizing radiation and is substantially lower in cost and portable.[53] For these reasons, ultrasound is routinely used in clinical settings as a preliminary screening diagnostic; however, it has been adapted for more specific applications in regenerative medicine such as imaging the structure, function and blood flow through scaffolds.[61–63] A major advancement in ultrasound has been the use of high frequencies that provide greater SNR for visualization of minute differences in anatomical features and changes in scaffold composition and structure.[61–63] The ease and safety of ultrasound imaging makes it an attractive option as a diagnostic technique for the clinic; however, its poor overall contrast and resolution and limited depth penetration with high-frequency ultrasound waves have prevented its wide adoption for *in vivo* imaging of scaffolds in tissue engineering.

1.3.4 Magnetic Resonance Imaging

In addition to ultrasound, magnetic resonance imaging (MRI) is also a non-radiative diagnostic modality but provides superior soft-tissue contrast and unlimited imaging depth in the body. MRI takes advantage of differences in water environments throughout the body to produce 2D images of tissues, which is further discussed in section 1.3.4.1. MRI can resolve submillimeter physiological features in three dimensions and can provide information regarding morphological, functional and molecular changes in tissue. Since a scaffold is simply the precursor of a tissue, logic follows that MRI techniques designed for assessing living tissue in the body can be applied to scaffold monitoring and tissue engineering. Scaffold MRI can provide spatial and temporal information regarding the date of scaffold and the formation of tissue *in vitro* and *in vivo*. However, MRI is costly and requires long-acquisition imaging sequences on the order of a few seconds to minutes and thus is limited with regards to real-time imaging. Additionally, technical expertise is needed to perform complex imaging sequences, and the magnetic nature of this modality is problematic for patients with metallic implants or devices. Despite these minor drawbacks, MRI has found widespread use in the clinic and regenerative medicine research. A comparison of MRI to other modalities with regards to properties essential for tracking scaffolds are summarized in Table **1.2**. For these reasons, we believe MRI is the ideal modality for tracking scaffolds and, consequently, cells, discussed further in section 1.4. Adapting MRI to scaffold imaging has become an active and important area of research. The following sections will examine how MRI has been utilized to measure scaffold properties for use in tissue engineering, with an initial focus on the fundamentals of MRI for tissue imaging and then contrast enhancement with molecular contrast agents. Key MRI studies and methods for imaging scaffolds will be discussed and critically assessed.

Imaging Technique	Resolution*	Tissue Depth Penetration*	Sensitivity*	Possibility of longitudinal Studies*	Used generally in the clinic?
MRI	+++	+++	++	+++	Yes
SPECT	+	+++	++	+	Yes
PET	+	+++	+++	+	Yes
CT/ X-ray	+++	+++	+	+	Yes
US	++	++	+	+++	Yes
Fluorescence/ NIR	++	+	+++	++	No
2PLSM	+++	+	+++	++	No

Table 1-2: Comparison of imaging modalities with regards to properties essential for tracking scaffolds. 2PLSM, two-photon laser scanning microscopy; CT, computed tomography; MRI, magnetic resonance imaging; NIR, near-infrared imaging; PET, positron emission tomography; SPECT, single-photon emission computed tomography; US, ultrasound. *Strengths and weaknesses are given using a relative scale in which + = poor, ++ = moderate and +++ = excellent.[45,64]

1.3.4.1 Signal Generation and Quantitative MR Relaxometry of Scaffolds

MRI signal is produced primarily by the relaxation of water protons (^{1}H) after excitation with a radio frequency (rf) pulse in a stationary magnetic field. The magnetic moment associated with the ^{1}H nuclei in a water molecule aligns with the direction of the static magnetic field of an MRI scanner. These ^{1}H nuclei/protons can be shifted from this equilibrium state by excitation with the on-resonance rf pulse. After this pulse is removed, the protons begin to realign with the stationary magnetic field and "relax" to equilibrium. As they relax, these oscillating protons induce a transient voltage across a receiver antenna (MR coil), which constitutes the nuclear magnetic resonance (NMR) signal. The environment surrounding water protons greatly affects their degree of mobility, which in turn, alters their relaxation rate and, consequently, the MR signal. Different tissues with different structures, chemical compositions, densities, vascularity and cellularity will all have different local environments; thus, MR signal varies between tissues. This change in MR signal also holds true for different scaffold materials with varying structures, chemical compositions, densities and so forth. Furthermore, as these materials degrade and tissue in-growth occurs, these parameters will further change. This ability to visualize scaffolds and their interaction with host tissue due to endogenous differences in MR signal provides a solid foundation for MR

investigations of scaffolds in the body. Owing to this a plethora of MR tools and quantitative methods for scaffold assessment have been established.

The primary signal generated by the relaxation of water protons via MR imaging can be utilized to produce a three-dimensional image of a tissue. This image can be acquired within minutes of the scan and provides important anatomical information for clinical diagnoses. However, this signal is not only dependent on the inherent biophysical parameters of a tissue but also on multiple external factors such as the sensitivity of an MR system, the imaging acquisition method, and environmental conditions. For these reasons MR signal alone does not provide a reliable metric for assessing scaffolds in clinical trials; however, the exact water relaxation rates which produce the MR signal can be quantified. This quantification of water relaxation rates or times is accomplished with unique sequences of radiofrequency pulses and alterations in magnetic fields. This process is referred to as quantitative MR relaxometry. Quantitative MRI can extract different contrast mechanisms and parameters that make up the MR signal, irrespective of external factors. The primary quantitative contrast mechanisms that provide insight into a scaffold's and tissue's physiological characteristics are the relaxation times T_1, T_2 and T_2*. Each quantitative metric measures a different form of water proton relaxation; thus, each can inform us about a specific property or group of properties via a scaffold's interaction with water.

1.3.4.2 Quantitative T_1 Relaxometry

T_1 relaxation or otherwise referred to as longitudinal or spin-lattice relaxation is the relaxation of water protons after excitation with rf in the longitudinal axis. After the rf pulse is removed, the water protons will relax back into alignment with the stationary magnetic field of the MR scanner. This relaxation is not instantaneous but occurs over a period that is parametrized by a first-order time constant, T_1, hence the term T_1 relaxation time or the inverse, R_1 relaxation rate. Furthermore, as the protons relax and return to equilibrium, the magnitude of the net magnetic vector increases, and thus we see an increase in MR signal, which produces 'bright contrast'. For this reason, T_1 relaxation can be referred to as "positive" or "bright contrast". A quicker relaxation or short T_1 relaxation time within a particular pocket of water will yield a brighter MR signal than its surroundings and vice versa. This relaxation to equilibrium occurs via a release of energy from the protons to their environment, hence the term "spin-lattice relaxation". As the protons try to realign

with the main magnetic field, they will emit energy at the Larmor frequency (the rate of precession of the individual protons under the influence of the magnetic field). Many factors affect the rate of energy released to the environment; primary transfer occurs through interactions with other atoms.

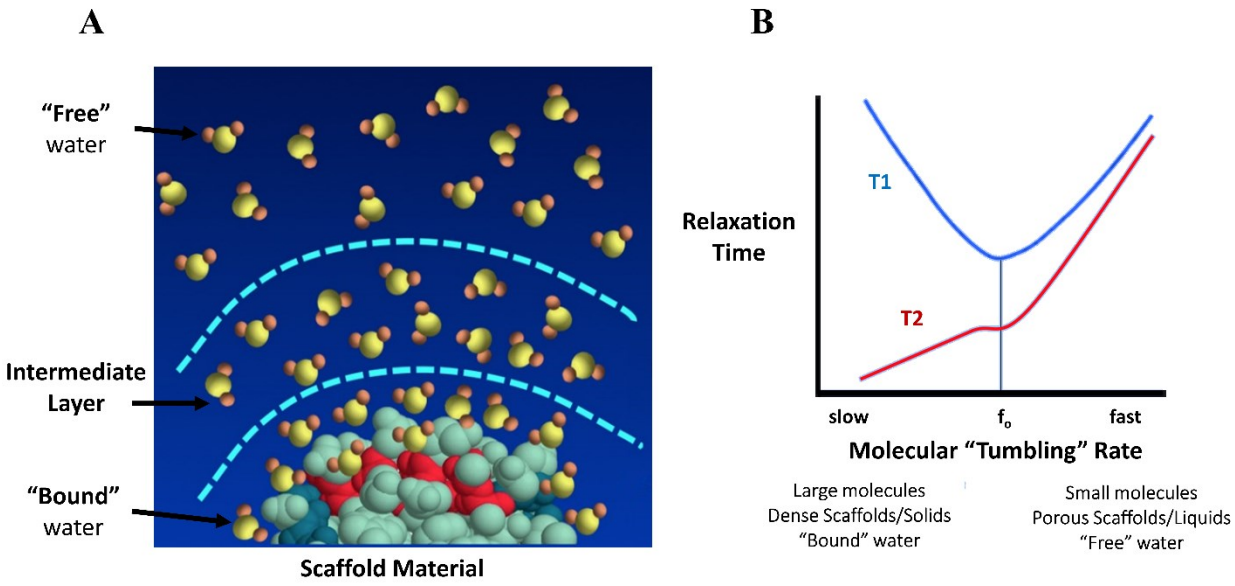

Figure 1.2: Water compartments and tumbling rate A) Illustration of the typical states or compartments of water in a scaffold or tissue. **B)** Graphical representation of the change in T_1 and T_2 relaxation times with molecular tumbling rate.

One important factor that affects the relaxation of water protons is the tumbling rate of the entire water molecule. As a water molecule tumbles, it changes the direction of the proton dipoles, which creates a fluctuating magnetic field. When the tumbling rate of the individual water molecules matches the precession frequency of the water protons around the stationary magnetic field (the Larmor frequency), then fast and efficient energy transfer will occur and result in a short T_1 time. This tumbling rate, however, will be dependent on the type of scaffold and its influence on a water molecule's state. If the scaffold is very dense (such as a synthetic bone scaffold) and restricts water motion, then the tumbling rate will be slow, resulting in a long T_1 time. If the material has an intermediate density, with more available space for water to rotate, such as a scaffold resembling soft tissue, then the T_1 will shorten. However, if the material is very porous and has a lot of empty space with free water motion, such as a scaffold resembling a larger vascular network, then it will have a very fast tumbling rate, which will result in a long T_1 again. These cases are demonstrated in Figure **1.2B**, where the change in T_1 is shown with respect to the change

in water tumbling rate. This quantitative metric demonstrates the potential to assess biomechanical properties of scaffolds via the state of the water molecules.

Furthermore, not only is there a change in the bulk relaxation rate between samples but there can also arise differences within a sample. This can occur due to the varied water compartments in a scaffold. As illustrated in Figure **1.2A**, water molecules can exist in different 'compartments' within a tissue; they can be highly immobilized near the surface of a scaffold, and more mobile or 'free' as they move away. This can result in distinct and varied multicomponent T_1 relaxation times within a sample. The bound or free water will relax faster or slower. In general most free water molecules tumble much faster than the Larmor frequency and thus bound water usually results in shorter T_1 times.[65,66] This can provide insightful information for differentiating materials that bind water more strongly and assess scaffold degradation via the release of bound water.

The T_1 relaxation time and the conditions that alter it have been correlated to many biophysical properties in scaffolds.[65–69] The change in this quantitative MR parameter has been used to assess and track scaffold properties such as degradation, loss of material results in less bound water; chemical composition, when scaffolds are made of different materials, they will bind water differently; and porosity/density.[65–69] Even complex biophysical properties such as young's modulus (a mechanical property that measures the stiffness of a material) have been shown to correlate strongly with a change in T_1 relaxation time.[66] Scaffolds grown by cells through deposition of extracellular matrix proteins resulted in stiffer scaffolds overtime.[66] When quantitatively imaged, the measured T_1 times exhibited a strong inverse correlation with scaffolds that had greater stiffness as measured by their Young's modulus.[66] This could be rationalized by the increasing presence and density of proteoglycans and collagen molecules produced by the cells. As the quantity of these macromolecules increased, the percentage of bound water increased as well, causing a reduction in T_1 time. Additionally, with more bound water and macromolecular content, there is the potential for proton exchange between them, which would also enhance the reduction in T_1 time.[65] This strong correlation between T_1 relaxation times and biophysical scaffold properties provides a unique MR profile that can be used to assess scaffolds.

1.3.4.3 Quantitative $T_{1\rho}$ Relaxometry

Another quantitative MR parameter that has been used to measure macromolecular/scaffold content more directly is $T_{1\rho}$. $T_{1\rho}$ is measured in the same manner as is T_1; however, in these acquisitions, a long duration and low power radiofrequency pulse is left on during the relaxation measurement. In this case, $T_{1\rho}$ is very sensitive to relaxation occurring at much lower frequencies than T_1 relaxometry. These low frequency processes are derived from interactions between water and macromolecular protons. This technique has been shown to accurately reflect changes in proteoglycan content in cartilage scaffold engineering. In various studies, cartilage grafts which were enzymatically degraded or proteoglycan content was reduced, resulted in significant increases in $T_{1\rho}$.[70–73] Furthermore, in the development of cartilage grafts harvested from cell culture, $T_{1\rho}$ was highly sensitive to both changes in proteoglycan content, but also, collagen content which was shown by a bimodal distribution of $T_{1\rho}$ values with higher amounts of collagen.[73] Additionally, as more collagen and proteoglycan content was produced both major $T_{1\rho}$ peaks decreased as expected.[73] The complementation of various strategies to assess similar changes in scaffold properties provides greater confidence and accuracy in assessments.

1.3.4.4 Quantitative T_2 and T_2^* Relaxometry

In addition to T_1 and $T_{1\rho}$ relaxation, other quantitative MR metrics such as T_2 and T_2* have also been shown to correlate with scaffold biophysical properties. T_2* relaxation or otherwise referred to as transverse or spin-spin relaxation, is a result of the dephasing of the net magnetization of water protons after excitation in the transverse axis. When protons are excited and aligned away from the static magnetic field, they not only align in the longitudinal axis but also in the transverse axis, referred to as in-phase. Once the rf pulse is removed and the protons begin to return to equilibrium, they realign with the stationary magnetic pole in the longitudinal axis; however, there is no stationary pole in the transverse axis and thus, the protons begin to dephase across the transverse plane. The rate of dephasing follows a simple exponential decay curve with a time constant of T_2*. As the protons return to a random statistical arrangement, the magnitude of their net magnetic vector decreases and thus we see a drop in MR signal, producing ‘dark contrast’. T_2 relaxation occurs via the same mechanism; however, T_2 relaxation reflects the relaxation due to

only natural atomic and molecular mechanisms, while T_2* reflects the total observed relaxation due to all external variables such as inhomogeneities in the magnetic field. These parameters can be measured independently with MR acquisition methods. In both cases, the dephasing of the water protons during relaxation is primarily dependent on the interaction between each other (hence the term "spin-spin relaxation") as well as neighboring molecules. Each proton and molecule's nuclei cause a change in the local magnetic field, this magnetic field is experienced by a relaxing proton which will either increase or decrease the rate of its relaxation. Each proton may experience different local environments and thus will relax at a different rate.

As described above different scaffold structures and compositions will alter factors such as the bound state and tumbling rate of water molecules. This also alters T_2 relaxation but does so in a more progressive manner than observed with T_1 relaxation (Figure **1.2B**). In a very dense scaffold where the water is highly immobilized, the local magnetic effects each proton experiences from its neighbors and from the material will be relatively constant over time; thus, all the protons will quickly relax at a relatively uniform rate. However, as the water protons become freer, they can now move away or towards each other resulting in fluctuating interference (both constructive and/or destructive). This fluctuation will result in an overall slower and thus longer net relaxation of the bulk water signal. With increasing mobility, the relaxation rate will continue to lengthen resulting in varying contrast between dense and more porous scaffolds.

Furthermore, as seen with T_1 relaxation, the rate of T_2 relaxation varies between samples and spatially within a sample due different water compartments. In fact T_2 and T_2* have been shown to be even more precise to slight changes in water compartments than T_1 measurements.[68,69] This can result in distinct and varied multicomponent T_2 relaxation times within a sample. Bound water will relax faster resulting in short T_2 times, while free water will relax more slowly, resulting in longer T_2 times. This can provide insightful information for differentiating materials and assessing changes as a material degrades. This multicomponent assessment of water compartments has been analyzed for a variety of tissues and scaffolds.[67–69,74] In a study of multi-material cartilage scaffolds, not only, was it shown that there can exist multiple T_2 components, but also, as the scaffolds degrade, T_2 relaxometry can identify which material degraded the most.[74] This analysis can also measure spatial heterogeneity within a scaffold, where superficial regions of cartilage scaffolds exhibit shorter T_2 times due to highly organized collagen fibers, whereas random arrangement of collagen deeper within the scaffold have longer T_2 times. [75,76] Additionally, the

presence of cells, the degree of cellularity, and their regional dispersion can also be assessed by multicomponent T_2 analysis, because cells represent an additional water fraction (intracellular vs. extracellular) and have been shown to exert changes on T_2 relaxation times.[77] It is important to note that studies that have assessed multiple changes in a scaffold, such as degradation, cell seeding and mineralization have sometimes shown contradictory results to theoretical trends in T_2. This can occur due to the complex interaction of water in tissues and the multi-factor dependency of T_2; however, many other MR techniques (discussed in section 1.3.4.6) have been developed to limit the confounding factors and provide greater accuracy for assessing scaffolds *in vivo*. Overall, multiple T_2 components in many of these instances provide information about the various layers or heterogeneity in a scaffold and the formation of tissue.[76]

1.3.4.5 Diffusion MRI

In addition, to measuring the bound state of water and the information it provides regarding scaffold content and composition, MRI can also be used to assess functional scaffold parameters such as water diffusion. Diffusion MRI takes advantages of the strong effect of local magnetic fields on the rate of proton dephasing. To image diffusion in a scaffold, local magnetic gradients are switched on in an area of interest at a particular time, which causes water molecules in that area to dephase at an accelerated rate. Later, an inverse magnetic gradient is applied which should refocus the phase of any of the water protons remaining in that area; resulting in no net phase change and thus no change in MR signal. However, if new protons from an outside area with a different phase, move into the area of interest, this will alter the net phase of the bulk water and result in MR signal. Overall, the amount of signal correlates positively with the rate of diffusion. This signal can be measured in multiple planes to get a better picture of how diffusion is occurring in 3D space. The geometric mean of this signal from each plane and at different magnetic field gradient strengths is then plotted as an exponential curve, from there a quantitative diffusion parameter known as the Apparent diffusion coefficient (ADC) or diffusion (D) coefficient can be determined. These coefficients can be measured pixel-by-pixel and thus plotted across a region of interest analogous to an image displaying T_1 or T_2 values across a tissue. This process is called diffusion mapping and it can be used to assess changes in scaffold properties, such as swelling and enhanced cellularity and porosity while in a patient.

One of the major uses of diffusion analysis in scaffold engineering is the ability to compare scaffold designs with endogenous tissue *ex vivo* to determine which have ideal properties for use *in vivo*. In the case of cartilage, there is no naturally present vasculature, so the ability for nutrients to diffuse throughout a scaffold is important for supporting cell growth and survival. In the development of novel scaffolds, diffusion MRI has shown that ECM scaffolds harvested from different organs and cell cultures have varying diffusion characteristics. [78] Being able to assess this functional parameter non-invasively and quantitatively provides tissue engineers with useful information that can be used to create synthetic alternatives.

In addition to the comparison of diffusion between tissues and scaffolds, diffusion can also vary within a scaffold, like T_1 and T_2 relaxation, and provide information regarding scaffold structure and content. Diffusion is highly dependent on water compartments, and thus multicomponent diffusion coefficients can be determined in complex scaffolds and tissues. For example, bound water inside a cell would diffuse much more slowly than free water. These differences can be measured by determining and fitting the degree of the diffusion exponential curve, analogous to multicomponent T_1 and T_2 measurements. Based on the complexity of the tissue the curve can be fitted to mono-, di-, or tri-exponential signal decay; from this, the number and type of compartments (i.e. Slow and fast) can be determined. The change in the slow and fast diffusion coefficients can provide tissue engineers with information regarding biophysical parameters such as degradation, change in chemical composition and cellularity. For example, when scaffolds are grown in cell culture, the content of collagen and proteoglycans, which change with time, has been correlated with diffusion MRI measurements.[66]

1.3.4.6 Magnetization and Chemical Exchange Saturation

Most of the methods presented thus far probe the scaffold or its water population indirectly. While these methods are relatively easy, they can be difficult to interpret due to multiple confounding factors. This can be mitigated by using MR methods that probe the different water populations and the macromolecular protons directly. Magnetization transfer (MT) contrast directly assesses the influence of bound water on the signal produced from free water. This is accomplished by selectively saturating the bound water with an off-resonance radio-frequency pulse. As these protons exchange or 'transfer' with the protons on free water, the signal from the bound water can

be determined via the magnetization transfer ratio (MTR). Since the bound water directly reflects macromolecular content, MTR is a sensitive method for assessing scaffold content changes. In scaffolds that contain collagen and proteoglycans, materials which bind a lot of water, we'd expect to see a large MTR, which would decrease with degradation.[79] Within bone engineering MTR has been highly utilized to assess the change in mineralization due to the positive correlation with bound water. [80]

Utilizing the same fundamental process for MTR contrast we can also directly measure the protons on the macromolecular backbone of a scaffold. This process is known as Chemical exchange saturation theory (CEST) imaging. There are two main requirements that must be met for CEST imaging to be possible. The first, is that the protons on the backbone of the scaffold must be able to chemically exchange with bulk water protons and the second, the protons need to have a chemical shift (frequency of excitation) distinct from that of water protons.[81] If a scaffold has such protons naturally present on its molecular backbone, then this technique is a powerful method that can directly measure scaffold content. If the protons on the scaffold have a unique frequency of excitation, then this method has the potential to track and assess scaffolds even in the presence of complex tissues, a problem that has been observed with the other methods discussed earlier. This is problematic for natural materials that are composed of the same molecular compounds found in the body. However, synthetic scaffolds, which are foreign, are ideal candidates for tracking with CEST imaging.[82,83] Scaffolds composed of multiple materials have also been tracked with CEST. [83] One study reported a strong correlation between the individual CEST signals measured and the degradation of each respective component/material.[83] Studies in vivo have tracked scaffolds injected subcutaneously in mice up to 89 days.[82] While these initial studies have shown promise for CEST MRI in biomedical research, the signal produced by CEST is significantly lower than the signal measured with traditional T_1 and T_2-weighted MRI methods. Consequently, to obtain the sensitivity required for CEST, non-clinical high field strength MR scanners, such as 7-11T are required. This hinders clinical adoption since most hospital MR scanners are typically 1-3T. However, continued developments in CEST signal enhancement are being explored and clinical applications may be possible in the future. Nonetheless, this technique provides unique capabilities in the research setting to directly monitor specific scaffolds and measure their content and degradation more accurately.

1.3.4.7 Molecular Labelling and Tracking of Scaffolds with MRI

The MR imaging methods described above have predominantly relied on the innate signal differences between scaffolds due to structure, density and chemical composition. These methods for MRI imaging were largely first developed for assessing diseased and injured tissues, and thus were highly transferable to scaffold imaging. However, these techniques, while versatile and quantitative, can suffer from sensitivity and/or selectivity issues. To enhance the source of MR signal, MR contrast inducing agents can be used. Traditional MR contrast agents catalytically shorten the relaxation times (T_1 or T_2) of the water protons within their vicinity, resulting in greater production of local MR signal. Typically, these agents are injected systemically in the body to enhance the MR contrast of particular tissues or injuries such as lesions for clinical diagnostic imaging; however, these agents can be modified and bound to a scaffold. Binding of an MR contrast agent to a scaffold produces greater MR signal at the site of the scaffold and permits longitudinal tracking. This approach also alleviates previous challenges with imaging natural-based scaffold materials that suffer from MR specificity and sensitivity *in vivo*.

To track a scaffold with exogenous contrast agents, two main factors must be considered. The first pertains to the type of contrast agent/label used, and the second pertains to the method of labelling/conjugation to the scaffold. With regards to the contrast agent, primarily three main types have been explored for scaffold MRI. The first, referred to as T_1-agents or bright/positive contrast agents, are complexes of paramagnetic transition metals (mainly Mn^{II} and Fe^{II}) or lanthanides (Gd^{III}) with unpaired electrons in their valence shell. They increase the T_1 relaxation rate of surrounding water protons by enhancing energy transfer between the proton and its environment through electron-nuclear spin-spin coupling from the unpaired valence electrons of the metal.[84] The enhanced relaxation rate results in a faster return of MR signal producing bright/positive contrast in a MR image. The second, referred to as T_2-agents or dark/negative contrast agents, include large bundles of paramagnetic metals (mostly based on superparamagnetic iron oxide particles) which enhance T_2 relaxation of water protons by producing strong local magnetic inhomogeneities that drive proton dephasing. The enhanced rate of proton dephasing results in a faster loss of MR signal which produces dark/negative contrast in an MR image. The third, referred to as CEST-agents, are organic or synthetic chemical compounds that contain exchangeable protons, which can be imaged by CEST MRI as described previously in Section 1.3.4.5.[85]

When assessing contrast agents for scaffold tracking, the primary factor that has been the major focus of the field is the sensitivity of the agent. In the past two decades, superparamagnetic iron oxide (SPIO) nanoparticles, discussed in greater detail in Section 1.4.2.1, have been shown to be highly efficient and sensitive T_2 contrast agents [86,87]. Furthermore, due to the extensive work in nanoparticle chemistry a wide range of coatings and conjugation reactions have been developed to target and/or link nanoparticles to various surfaces and materials[86]. These favourable properties have made iron oxide nanoparticles the preliminary contrast agent of choice for scaffold tracking. [88–92] In one study, the incorporation of ultrasmall super-paramagnetic iron oxide (USPIO) nanoparticles into collagen scaffolds permitted MRI visualization and degradation tracking of the scaffolds in rats for 22 days.[88] One complication that was observed was the distortion of the scaffold size and shape due to the high concentration of the iron oxide agents. The mechanism by which iron oxides product contrast, distortion in the magnetic field, can result in significant blooming artifacts or negative voids that can hinder the anatomical accuracy of visualization and quantitative assessment of labelled scaffolds. [92] Furthermore, as the scaffold degrades, and the concentration of the contrast agent decreases, so too will the MR signal. This makes it difficult to visualize scaffolds until complete degradation. This is further exacerbated for T_2-enhanced scaffolds owing to the endogenously dark signal (low T_2 times) of many tissues, such as muscle (~30ms) and cartilage (~40ms), rendering the contrast invisible at low concentrations. [77,92–96] Additional and parallel issues regarding the use of SPIOs for imaging in tissue engineering are discussed in greater detail in Section 1.4.2.1 on T_2-imaging of cells where SPIOs have been extensively explored.

Contrast agent sensitivity is an important aspect of molecular imaging; however, additional factors that need to be considered are safety and clearance of the contrast agent following scaffold degradation. The long lifetimes (weeks to months) that scaffolds are present in the body need to be considered when designing the ideal contrast agent for scaffold monitoring. With this in mind, the safety and clearance of an agent will be a major question for clinical approval. In regards to iron oxide agents, multiple reports have explored their toxicity and deemed them to be biocompatible at low doses with a variety of tissues and cell types.[85,97] Cells, such as macrophages, in fact easily engulf SPIOs with no adverse effects on cell viability[97]; however, this uptake and retention is problematic for signal quantification and accurate detection of scaffold degradation overtime. [97] This retardation in clearance and the potential for retention at the site of scaffold

implantation presents a significant limitation of iron oxide-based scaffold labelling approaches. Lastly, due to the large size of iron oxides (20-100nm) compared to traditional unimolecular MRI contrast agents (<1 kDa), they can cause structural and mechanical issues if they are incorporated during scaffold formation.[92] Comparisons in scaffold labelling with T_2 enhancing iron oxide agents and T_1 enhancing gadolinium (Gd) chelates for tracking bone scaffolds, have shown that incorporation of iron oxide particles (30nm) hinder scaffold formation and mechanical strength, while smaller (<1kDa) gadolinium agents do not. [92]

These limitations are being addressed in the larger field of iron-oxide based contrast agents, however, their occurrence has spurred interest in alternative agents such as T_1 and CEST-based. Both classes of agents provide a means of producing signal that is differentiable in the body and can be quantified. In the case of T_1 agents, they provide greater confidence (i.e. specificity) in the origin of MR signal and can be used to track scaffolds quantitatively and long-term as seen in recent reports.[98–101] Of the few studies reporting on bright-contrast enhancement of scaffolds, they have primarily utilized gadolinium-based contrast agents (GBCAs). [98–101] This is primarily because gadolinium chelates are the most widely used contrast agents for clinical MRI, with over three decades of development and application. The paramagnetic Gd^{III} ion present in GBCAs has the largest possible number of unpaired electrons, seven, in its valence shell and thus acts as an efficient T_1 agent.[84] Despite their clinical approval and vast use, recent developments have shown potential toxic side effects due to the release of Gd^{III} ion from clinical chelates and subsequent build-up in brain and bone tissues.[102–104] Gadolinium is foreign to the body and toxic at low levels[105,106]; for these reasons, some Gd agents have been pulled from commercial shelves and restrictions have been imposed to limit the quantity and number of doses per individual per year. [102,107,108] This discovery has prompted new research in the larger field of MRI contrast agents and greater interest into manganese (Mn) based contrast agents.[109,110] Manganese ions are efficient T_1-agents, and chelates can be designed to produce greater contrast enhancement than traditional Gd^{III}-based agents[111,112]. Furthermore, the Mn^{II} ion is an essential micronutrient in the body and can be eliminated safely in low concentrations[113]. Additionally, Mn-chelates are traditionally under 1kDa [114] and can easily diffuse through tissues and cells, resulting in enhanced clearance by both the renal and hepatic systems.[115,116] For these reasons, manganese holds great promise as an ideal T_1-agents for scaffold tracking. Since manganese-based CAs are utilized throughout this

dissertation, the next section 1.3.4.7 elaborates further on the origins and development of Mn-agents for MRI imaging.

In addition to considering the appropriate contrast agent for molecular scaffold tracking, the labelling method and corresponding linker must also be carefully considered to ensure adequate stability, ease of conjugation and safety. One of the first methods explored in scaffold labelling, has been passive incorporation of a MR agent into the structure of a scaffold during scaffold synthesis. [92] In this case, the contrast agent associates with the scaffold passively via non-covalent interactions. This labelling method is simple and straightforward; however, it does not directly link the agent to the scaffold material and thus could result in a false-negative signal from premature wash out of the agent. For this reason, direct labelling of scaffolds has also been explored. In this context, a contrast agent is chemically conjugated/linked to the molecular backbone of a scaffold. Direct conjugation ensures that the change in the signal of the agent represents the change in content. The method of conjugation must be efficient but also gentle to ensure natural material-based scaffolds, such as collagen or ECM, are not denatured in the process. As this field grows, many different types of bonds and chemical techniques are being explored for covalent linkage to scaffolds. Currently, most methods employ standard techniques that are facile and quick but terribly inefficient and lack versatility.[88,98] Future research in versatile MR probes and conjugation techniques is needed to develop more efficient, unique and universal methods for scaffold labelling and tracking with MRI.

1.3.4.8 Manganese-based Contrast Agents

The recent safety concerns with gadolinium based contrast agents among other issues discussed previously and in later sections (Section 1.4.2.4), have prompted new research in the larger field of MRI contrast agents and greater interest into manganese (Mn) based agents [114]. Manganese ions, like gadolinium, have unpaired electrons and thus act as efficient T_1 agents on MRI producing bright positive contrast [114,117]. However, unlike gadolinium, Mn is an essential micronutrient in the human body, acting as a cofactor for enzymatic reactions[118] and is usually acquired through food, with daily recommendations of 2-5 mg/kg body-weight [113]. Upon ingestion, manganese is rapidly absorbed in the gastrointestinal (GI) tract and then distributed into different tissues through the circulatory system.[113] Mn plays essential roles in many organs, including the liver, pancreas,

kidney, brain and bone and in various processes such as development, digestion, reproduction, antioxidant defence, energy production, immune response and regulation of neuronal activities [113]. After absorption and distribution in the body, the liver primarily regulates Mn storage, redistribution and elimination; however, if excess Mn is present, it can also be eliminated via the kidneys [119,120]. Due to these natural processes that manage Mn in the body, it is safe at low levels, unlike gadolinium, however excess Mn can be neurotoxic at high doses and has been linked to Parkinson's-like symptoms.[118,121,122] For this reason Mn-based agents for MRI are often chelated with ligands, similar to Gd agents, to retain the metal ion and limit its interaction and release in the body. However, due to the lower charge on Mn^{II}, in comparison to Gd^{III}, traditional chelators, such as diethylenetriamine pentaacetate (DTPA), form unstable complexes [114]. Furthermore, Mn^{II} agents have fewer sites for water coordination and fewer unpaired electrons, which limit their relaxivity and sensitivity as an MR contrast agent.[117] To address these challenges the development of Mn-based contrast agents remains an active area of research with novel chelates[117], macromolecules[123] and nanoparticle formulations[124,125] to improve relaxivity and reduce in vivo dissociation of the Mn ion. One promising platform is the development of manganese (III)-porphyrins (MnPs), which have been considered as alternatives to Mn^{II}- and Gd^{III}-chelates due to their superior relaxivity and thermodynamic stability[126]. Since MnPs are utilized throughout this dissertation, the section below highlights their general properties and propensity for use in medical applications and molecular tracking of scaffolds.

1.3.4.9 Manganese Porphyrins

Manganese (III)-porphyrins were first discovered as potential positive-contrast agents in the late 1970s[126]. They consist of a tetrapyrrolic macrocycle, porphyrin, that chelates a single Mn^{III} ion as seen in Figure **1.3**. The porphyrin chelator itself represents a class of naturally occurring molecules with many important biological functions.[127] Porphyrins are ubiquitous throughout our environment and body. In plants, they make up chlorophyll and bind magnesium needed for electron transport in photosynthesis.[128] In the body, they make up the heme group needed to bind iron in red blood cells and facilitate oxygen storage and transport. [127]. These unique properties are a result of their structure. Porphyrins are highly conjugated aromatic molecules that create an electron shielded inner cavity with four pyrrolic nitrogen atoms. This cavity has the appropriate size and geometry to bind a variety of metallic cations with different oxidation states.

Consequently, they easily form organic metallo-macrocycles as demonstrated in nature. However, specific cations with a radius of 55-80 pm fit ideally into the inner plane of the porphyrin. They sit within the porphyrin and coordinate to the pyrrolic nitrogen atoms creating thermodynamically and kinetically stable complexes. Larger ions can also coordinate within the porphyrin ring; however, they sit above the porphyrin plane and thus are less stable and more likely to dissociate[129].

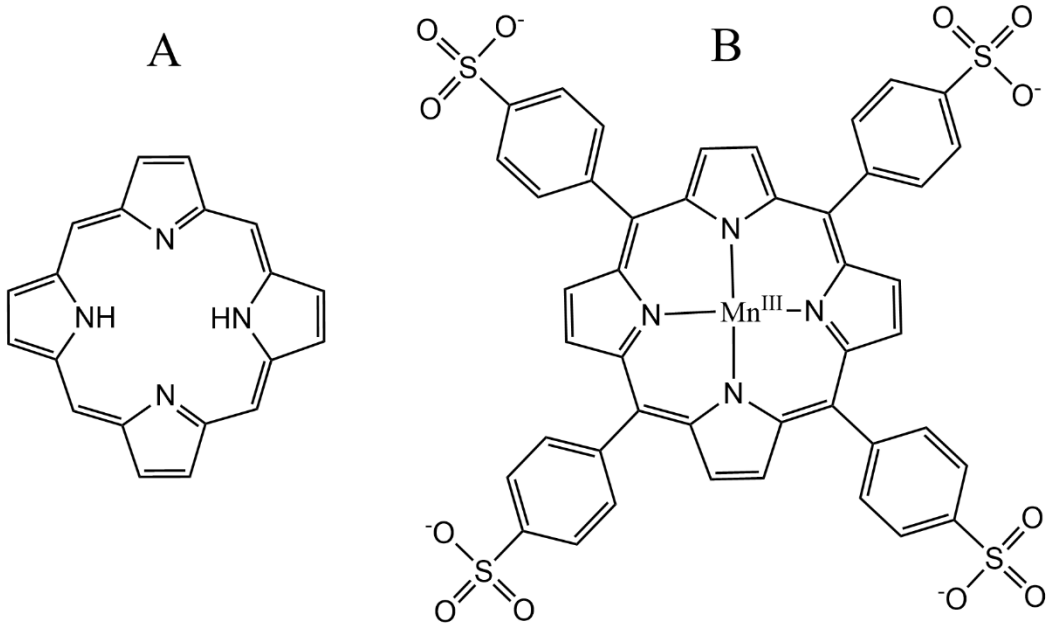

Figure 1.3: Porphyrin structure A) Highly aromatic cyclic ring with four pyrollic nitrogen atoms for metal ion binding/chelation **B)** Structure of $MnTPPS_4$.

The stability of the chelated complex is important to consider with regards to manganese ion because their smaller ionic radii and lower charge results in unstable complexes with traditional linear and macrocyclic chelators. However, the characteristics of the Mn ion make it ideal for chelation with porphyrins. In one study, where the stability of porphyrins chelated with Mn, Gd or Iron (Fe) was evaluated, the Mn-porphyrins exhibited superior kinetic inertness with no demetallation even after nine days in physiological conditions, whereas Gd and Fe were rapidly lost due to dissociation [115]. While more extensive studies are required to determine their stability over longer time periods common in tissue engineering applications (months to years), these preliminary findings provide strong support for the utility of porphyrins as ideal Mn chelators. Furthermore, these preliminary studies also reported the first water-soluble MnP, manganese (III)

meso-tetra (4-sulfonatophenyl)porphyrin ($MnTPPS_4$, Figure **1.3B**), which exhibited an unexpectedly high relaxivity of 10.4 $mM^{-1}s^{-1}$ at low field strength [111,115]. In comparison to free Mn^{II} ions and clinical GBCAs, which exhibit relativities of ~7 and 3-7 $mM^{-1}s^{-1}$, [130,131] respectively [130,131], this MnP was far superior. In theory, the oxidized Mn^{III} in $MnTPPS_4$ has only four unpaired electrons compared to the seven in Gd^{III} [132] and thus should exert a weaker effect on the T_1 relaxation of surrounding protons; however, the opposite was found to be true. While this phenomenon and other relaxometric properties of MnPs are still an active research question, the most current rationale is that the rigidity of the porphyrin chelator slows the degree of molecular tumbling, which in combination with dual water binding sites results in a stronger interaction between the Mn ion and water protons. [133–136] This stronger interaction facilitates efficient energy transfer between the two atomic species resulting in an enhanced T_1 relaxation rate.[133–136] More interestingly, this "anomalously" high relaxivity was observed to grow with magnetic field strength, unlike Mn^{II}-chelates, which typically decrease in sensitivity [111]. Similar decreasing trends in relaxivity have also been observed with standard small GBCAs. While high field strength scanners are still not widespread clinically, many large hospitals and research facilities have upgraded their systems for the higher sensitivity and resolution afforded by 3-11 Tesla scanners, with 8 Tesla currently being the highest field strength permitted by the FDA for routine clinical practice.

In addition to the superb relaxivity and stability of $MnTPPS_4$, its small size (~1 kDa) and hydrophilic pendant groups ($-SO_3^{-1}$ pendant groups) enhance rapid clearance from the body. Biodistribution studies in healthy mice following $MnTPPS_4$ injection exhibited initial signal enhancement in the kidney and urine, and minimal secondary enhancement in the liver, with complete return to baseline within 48 hours.[115,137] This demonstrates dual clearance routes with primary renal and secondary hepatic pathways. [115] While the body can handle low levels of hepatic Mn, it is preferred that contrast agents are cleared primarily by renal routes to limit interaction and retention in the body. Due to the efficient clearance of $MnTPPS_4$ from the body [115,137] and the high stability[115] of the metallic complex, this compound has exhibited favourable safety profiles *in vivo*. Several reports have observed no toxic side effects after intravenous injection in rat and mouse models with high doses of 0.4-0.5 mmol/kg[138,139]. It is worth noting that one report by Lyon et al. measured an LD_{50} of 0.5mnol/kg in animal tumour models.[115] However, this experiment was only reported in a personal communication (by H.J. Weinmann to Lyon) that was never published.

Furthermore, animal tumour models are known to have high rates of animal mortality and are not ideal toxicological study models for a systemic agent that is known to accumulate in tumours (discussed further below). Despite these confounds, this study has been cited frequently in papers concerning MnTPPS[140–142], even though the toxicity of the agent may have been overestimated. Therefore, the LD_{50} for MnTPPS remains to be determined in healthy animals. Furthermore, these values represent the concentrations for systemic injection, in the context of scaffold tracking where implants for humans have volumes of 1-10ml with CA quantities of 0.1-1 umol, this would result in a dosing of 0.1-1 ug (assuming 1kDa CA) per a 70-kg individual or 0.0014 umol/kg body weight; multiple orders of magnitude lower than what is reported above.

An interesting property observed in the cancer imaging models is the strong affinity of $MnTPPS_4$ for tumours[115,138,140,142,143]. This agent accumulated within a tumour when systemically injected and was retained for several days[142]. The ability to selectively enhance tumours with low doses (0.025 mmol/kg) for prolonged periods of time allows for greater insight regarding the physiology of the tumour. To better understand the mechanism of interaction with tumours, several mechanistic studies were carried out.[144–149] These studies discovered that this agent can adhere to extracellular matrix (ECM) proteins, materials that are highly abundant in tumours. While this unique property can be exploited for clinical use, it also can be used for scaffold tracking. One of the most widely used scaffolds in tissue engineering are collagen and ECM based materials. ECM proteins are highly conserved and found throughout the entire human body in all connective tissues. For this reason, these materials, as discussed earlier in Section 1.1.2, have been extensively utilized for tissue engineering applications. The innate abundance of collagen in the body, however, makes it difficult to distinguish exogenous implants from native tissue. Additionally, due to the vast amount of conditions that alter collagen graft mechanical properties, it is difficult to determine how modified grafts will behave in the body and the reproducibility between laboratories. For these reasons, a facile method for assessing extracellular matrix and collagen implants *in vivo* is needed. The demonstration of $MnTPPS_4$ binding and retention to tumours *in vivo* provides a promising efficient, and sensitive labelling agent for collagen and ECM based scaffolds.

Lastly, the unique properties observed with $MnTPPS_4$ are highly dependent on the porphyrin macrocycle and its composition. The porphyrin structure and external pendant groups can be easily modified with various functional moieties to confer different properties. With regards

to $MnTPPS_4$, the degree of sulfonation alters its clearance rate and as well as its affinity for tumours.[144,145,148,149] In literature, MnPs have also been modified for other applications such as albumin binding to achieve prolonged blood pool circulation for MR angiogigraphy[150]. The porphyrin macrocycle's amenable natural to structural modification can be exploited for specific conjugation to various scaffold materials. The pendant groups can be intelligently chosen to permit conjugation while also maintaining favourable solubility and clearance properties for *in vivo* use. For these reasons, MnP-based agents have great potential for molecular tracking and imaging applications in tissue engineering.

1.4 Cell Tracking

Discussed earlier, the pillars of tissue engineering and regenerative medicine are cells and scaffolds. While scaffolds can be used independently or in conjunction with cells in regenerative therapies, sole cellular injections have also shown promise for the treatment of multiple medical conditions such as diabetes[151], cardiovascular disease[152], cancer[153], and degenerative muscular[154] and neuro disorders[155]. In these cases, the ability to track and assess the cells rather than the scaffold is imperative to gleaning clinical insights.[156,157] The common requirement for the development of nearly all cell therapies is a means to visualize the biodistribution of cells following injection. However, traditional assessments of transplanted cells with gross tissue dissection and histological analysis are not feasible for clinical use and limits longitudinal monitoring in animals for biomedical research. Consequently, it is ideal to track the implanted cells non-invasively and independently in each patient as discussed in Sections 1.1.3 and 1.2. Non-invasive imaging of the cells would confirm injection location and extent of distribution spatially and temporarily, as with scaffolds, but also provide additional information regarding the viability and proliferation of the cells once in the body. Tracking cells non-invasively, however, poses greater challenges than scaffold tracking. In cell tracking, the methods and conditions to label and probe cell fate must be innocuous before and after injection into the body. While scaffolds can be processed with a range of conditions and tools, the fragility of a living cell restricts the use of harsh industrial methods and scalable processes. Furthermore, the quantity of bulk material in cellular injections is significantly lower in comparison to scaffold injections, and thus poses a greater challenge for sensitive detection. For these reasons, tracking selected groups of cells requires intracellular uptake of biocompatible contrast agents or tracers. This ensures direct tracking of the

injected cells and permits quantitative assessment of cell distribution. When developing a cell imaging method two main factors must be considered. The first is the type of tracer and the second is the labelling method.

1.4.1 Cell Imaging Modalities and Tracers

Analogous to scaffold tracking, a variety of modalities and tracers have been employed for imaging cells in real-time. Optical imaging (OI), as discussed for scaffold tracking in Section 1.3.1, has also been at the forefront of cellular imaging due to its superior sensitivity and resolution [158] and its established library of fluorescent probes [159,160] that can be linked to a variety of cell structures and proteins. [158] However, as was the case for scaffold imaging, it is significantly limited to use *in vitro* or subcutaneous/near-surface *in vivo* animal models due to the loss of signal from light scattering and attenuation through tissue. [59] Consequently, the field of *in vivo* cellular imaging has followed a similar trajectory as did scaffold tracking and adopted conventional medical imaging modalities to overcome this limitation and confer clinical utility. The same modalities, X-ray/CT, PET, SPECT and US, have all been trialled and continue to be actively researched with interesting developments such as genetically encoded cellular-microbubbles for US imaging [161,162] and genetic PET tracers for tracking T-cell immunotherapies[163,164]; however, the limitations discussed in sections 1.3.2-1.3.3 remain, such as the use of ionizing radiation and limited anatomical information with PET/SPECT imaging; and low spatial resolution and poor tissue contrast with US imaging. Consequently, MRI proves to be the most promising modality for cellular tacking in regenerative medicine as it does for scaffold monitoring due to its superior soft-tissue contrast and spatial resolution without the need for ionizing radiation. Even in the development and clinical testing of other cell tracking modalities such as PET or CT, MR imaging is always conducted due to its ability to demarcate fine anatomical features throughout the body. Contrast-enhanced MRI, with various intracellular MR tracers/contrast agents, further enhance the utility of MRI for sensitive and specific cellular tracking.[42,85,165–168] For these reasons, significant development in the field of cellular MRI has occurred, with promising clinical trials and the potential future widespread translation to the clinic.[42,165,169]

1.4.2 MRI Contrast Agents for Cell Tracking

Traditional MRI techniques, such as quantitative relaxometry, can be utilized to image the general site of cellular implantation and the change in tissue composition as cells proliferate and lay down new extracellular matrix[170]; however, visualizing selected groups of cells and quantitative measurements of viability and biodistribution requires direct tracking made possible with contrast agents or tracers for cellular tagging. For this reason, among others, MRI cell tracking has seen greater development in contrast agent-based methods than scaffold tracking, which has lagged. When assessing contrast agents for cellular tracking, both the sensitivity of the agent and the biocompatibility must be considered. In traditional applications of contrast-enhanced MRI, the contrast agents are usually present at concentrations of a few hundred micromolar; thus, a region of interest that is hundreds to thousands of millilitres in the body or in a bioreactor can have roughly $10^{17} – 10^{19}$ contrast agents. In tissue engineering, cells are typically seeded/injected on the order of a few million to billion, significantly lower than traditional concentrations of contrast agents. Thus cellular MRI requires sensitive contrast agents and efficient cellular uptake of said agent.

With regards to MRI contrast agents, four main types have been extensively explored in this field, as seen in Table **3**. These types include chemical agents that contain paramagnetic metals that enhance the T_1 and/or T_2 relaxation rate of surrounding water protons, compounds that contain Fluorine-19 atoms which can be excited and produce distinct MRI signal (^{19}F MRI) separate from water protons (^{1}H MRI), and agents which contain CEST-active protons. Currently, the most widely used CAs for MRI cell imaging have been T_2/T_2* based agents, particularly iron oxide particle formulations, due to their high sensitivity in comparison to clinical gadolinium and other paramagnetic T_1 agents. Directly excitable probes such as CEST and ^{19}F-based agents, while less sensitive as well, have gained greater interest in recent years due their unique properties and, the later, have even been investigated in clinical cell trials. The sensitivity and detection principle of each technique and contrast agent with regards to cellular tracking is shown in Table **3** and further explored in the below sections.

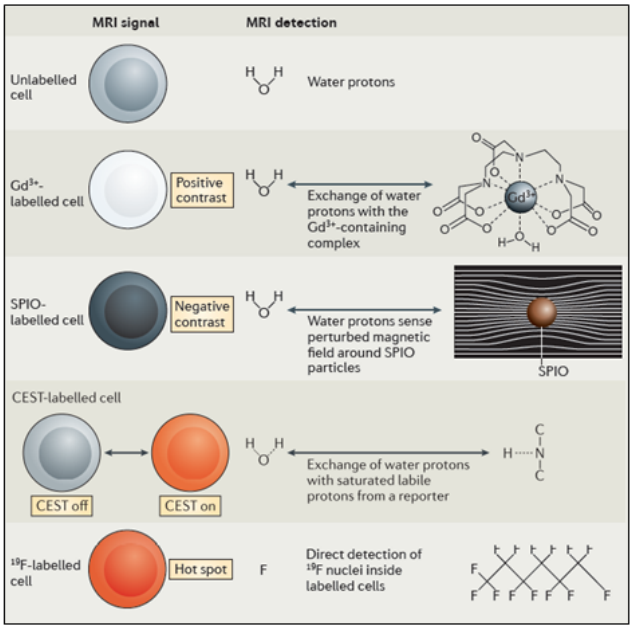

Probe	Cell detection limit	Quant. cell number	Clinical trial?
Gd^{3+}, Mn^{2+}	~ 1,000	No	No
SPIOs	1	No	Yes (EU, China, Israel)
^{1}H CEST	10,000	No	No
^{19}F	1,000 – 100,000	Yes	Yes (USA)

Table 3: Overview of classes of contrast agents utilized for cellular MRI and their corresponding detection principle. Adapted with permission from Ahrens, E.T., & Bulte, J. W. *Nat. Rev. Immunol.,* 2013, 13, 755. Copyright (2013) Springer Nature.

1.4.2.1 T_2-MRI Contrast Agents

Multiple formulations of iron oxide agents are commercially available[171] and have been extensively explored for use in pre-clinical and clinical cell tracking. [85,172–174] These particles, as their name suggests, are made up of an iron oxide core, that contains multiple individual crystal regions that act as independent magnetic domains. In a magnetic field, each domain becomes oriented and generates a magnetic dipole greater than the sum of the individual atoms, resulting in a superparamagnetic state. The large magnetic moment generated by these superparamagnetic iron oxide (SPIO) particles disrupts the homogeneity of the local magnetic field felt by surrounding water molecules, which enhances their T_2/T_2* relaxation rate, and produces a negative void/dark contrast at and near the site of the particle. These agents are engulfed by cells via endocytic processes and are retained intracellularly due to their large size, charge, and adsorption onto other biomolecules in the cell and the cell membrane.[175] Uptake and retention of these agents intracellularly confers dark contrast to the cell permitting direct cell imaging and homing.

These particles are primarily categorized based on size, which includes ultrasmall particles (<20nm), SPIOs (20-100nm) and micron-sized particles (≥1um). The largest particles exhibit the

highest T_2 relaxivity[176], due to greater iron atom loading per particle; however, they suffer from inefficient cellular uptake. The particles can also be coated with a variety of organic or synthetic polymers and macromolecules to enhance stability, biocompatibility, intracellular uptake and chemical/biological targeting. Several of these agents are commercially available[171] and have been evaluated in clinical studies[41]. The first-generation clinical SPIO formulations included Ferridex® (Berlex Labratories, Montville, NJ) and Endorem® (Guerbet, Aulnay-sous-Bois, France) which consisted of ferumoxide particles coated with a polysaccharide, dextran, and had diameters of 120-180nm and 80-150nm, respectively. Other formulations such as Resovist (Bayer Schering, Pharma, Berlin, Germany) and Sinerem (Guerbet, Villepinte, France) consisted of ferucarbotran particles coated with carboxydextran and had diameters of 60nm and 15-30 nm, respectively. The first clinical trials with Endorem®[165] and Ferridex®[177] demonstrated the ability to successfully label therapeutic cells with SPIOs and monitor their migration *in vivo*. These initial trials utilized MRI-guided cell injection[178,179] with a temporal resolution on the order of seconds[180] for real-time imaging and parameter adjustment of injection speed and volume, and catheter positions to ensure cell delivery to the target site.[169,181]. Furthermore, these studies were directly compared against clinically approved SPECT cell tracking with (^{111}In)-oxine-labelled cells, which revealed the superiority and accuracy of MRI-based cell tracking. MRI tracking of SPIO-labelled cells was able to accurately determine off-target/mis-injection rates in patients, while SPECT tracking was not, which was surprising considering over 50% of the clinical cohort were mis-injected. The discovery of such high mis-injection rates in a clinical cell therapy trial also demonstrated the need for real-time injection guidance[165]. The sensitivity of SPIOs coupled with the high anatomic resolution and soft-tissue contrast of MRI has proved vital for the assessment of early injection success of cell therapies. Following this preliminary success, over nine clinical trials to date[41], constituting the majority of clinical cell tracking trials with MRI, have been conducted with SPIOs. A range of cell types including dendritic cells,[165] pancreatic islet cells[182–184], blood mononuclear cells[185] and neural[177,186,187], bone marrow[188] and mesenchymal[189] stem cells have been tracked clinically to determine injection success, cell retention, and *in vivo* biodistribution[190]. These studies as well as an immense body of preclinical work[97,191–198] have also demonstrated the safety and biocompatibility of MRI tracking with SPIO-labelled cells. While a few studies have shown negative effects of SPIO labelling on specific differentiation pathways of mesenchymal stem cells[199–201], and cytokine production of macrophages[202], majority have shown cyto-safety at low

doses with a variety of cell types [85,97,175]. This is largely due to the endogenous presence of iron and the ability for biodegradation in the liver[203]. A comprehensive clinical study, with SPIO-labelled blood mononuclear cells, found them to be safe and exhibit no adverse effects on cellular parameters and patient health[185].

While these pre-clinical and clinical studies have shown promise for MRI cell tracking with SPIOs, there are, however, several major limitations that have been discovered with T_2-based cellular MRI. Firstly, these particles are in general cell-impermeable and can only be up-taken by cells via phagocytosis or macropinocytosis[165,182]. While cell uptake can be enhanced utilizing a variety of transfection methods (discussed in greater detail in section 1.4.3.1), this limitation has largely directed SPIO use for labelling phagocytic cells[165,182]. Furthermore, SPIO-based cell tracking has also experienced difficulty with accurate determination of cell volume and quantitative analysis of signal. The large magnetic susceptibility of the particles which produces strong signal also induces dark-void image artifacts that extend far beyond the volume of the particles and labelled cells[192,204–206]. This artifact as discussed in the context of scaffold tracking is common with T_2/T_2* contrast agents and is known as the "blooming effect". This effect can saturate pixels and distort spatial imaging, which hinders quantification and leads to loss of anatomical information needed for cell homing. T_2 agents also suffer in terms of specificity, due to the ambiguous origin of dark contrast voids in the body which occur in air spaces, tissue interfaces, hemorrhages and/or trauma, dead bone fragments, surgical implants, calcification or other imaging artifacts associated with magnetic susceptibility[206,207] This can lead to clinical misinterpretation, particularly in regenerative medicine and tissue engineering where patients with traumatic injuries have excessive blood pooling, irregular tissue interfaces and various implants or co-injected materials.[208] Traditional SPIO cell labelling methods also lack specificity for viable cells. Clinical and pre-clinical cell tracking investigations have reported prolonged hypointense T_2-weighted signal of dead cells at the sites of injection[209–214]. This was due to uptake and retention of the released SPIO nanoparticles by resident macrophages.[212–214]. The propensity for phagocytic cell uptake and high stability of the agent can result in significant accumulation following cell death or agent release which results in false-positive signal generation. Consequently, the detected MR signal at the transplant site will be a combination of the originally labelled cells and resident macrophages [209–214]. This renders quantification of signal useless and can lead to clinical misinterpretation in scenarios where all labelled cells are gone but signal persists. This is

particularly problematic in regenerative medicine where an influx of macrophages is traditionally observed during injury and following injection/implantation of cell grafts; which can complicate signal interpretation early on in select therapies, such as cardiac regeneration, which experience a large fraction of cell death, between 30-50%, within 24 hours of transplantation. [3]

In addition to technical challenges, SPIOs have also experienced commercial roadblocks that have significantly hindered their ability for clinical adoption. To date, the majority of clinical-cell tracking trials have utilized SPIOs; however, no SPIO has been approved by the FDA for cell-tracking purposes[41]. Furthermore, the SPIO agents that have been extensively tested and used for clinical cell labelling (ferumoxides; Ferridex® & Endorem® and ferucarbotrans; Resovist®) are no longer being manufactured and are discontinued as MRI contrast agents in the US because of economic considerations.[169] While other formulations have been generated and some have been approved for clinical use in intravenous iron therapy (ferumoxytol; Feraheme®, AMAG Pharmaceuticals, United States)[215], these current formulations have been less effective as cell-tracking agents due to inefficient cell uptake and inferior signal generation.[169,216,217] Furthermore, these second-generation clinical nanoparticles have not exhibited favorable biocompatibility and safety profiles as their previous counterparts. In 2015 the FDA issued a black box warning (the agency's most severe warning) for ferumoxytol, in response to several reports of severe and fatal adverse health events, including 18 fatalities[215,218–220]. Due to these technical, clinical and commercial challenges, the development of new CAs and methods for labelling and tracking cells is an important area of research.

1.4.2.2 ^{19}F-MRI Tracers

In addition to SPIOs, fluorine-19 (^{19}F) MRI with fluorinated contrast agents has also been explored for clinical cell tracking[221,222]. Fluorine-19 atoms have a unique atomic spin which can be specifically excited for direct detection. Furthermore, due to the lack of the atom's natural presence in the body, ^{19}F-MRI produces minimal to no endogenous background signal and thus exogenous compounds containing fluorine can be specifically detected and easily quantified *in vivo*[223]. The tracers commonly used for ^{19}F-cellular MRI are composed of perfluorocarbons (PFC) nanoemulsions such as perfluoropolyether (PFPE) or perfluoro-15-crown-5-ether (PCE)[158,224,225]. These compounds are mostly inert[226] and have shown to be highly stable in the body with no

significant adverse effects on cell viability[227]. Two clinical studies thus far have utilized ^{19}F-MRI for cell tracking[221,222], which, however, is much fewer in comparison to the nine trials with SPIOs[165,177,182,183,185–189]. These trails utilized the agent CS-1000, a commercially available reagent, to label and track cells in patients. While one of the trials is still ongoing, the completed study by Ahrens et al. demonstrated the ability to track and quantify the initial injection of labelled dendritic cells; however, due to the lower sensitivity of ^{19}F imaging, cell migration could not be tracked post injection as the cells and signal was dispersed[221]. Additionally, only large cell injections were imageable (1x10^7 cells) while lower doses in the order of 1x10^6 were beyond the limit of detection[221]. In addition to clinical trials, a multitude of preclinical studies have been conducted and shown promising applications for ^{19}F-cellular MRI. Cell labelling with high doses of PFC nanoemulsions have been used to enhance the limit of detection and visualize dendritic[228,229] and T-cell[230] migration in mice as well as quantification of cell accumulation at tumour sites for immunotherapies[229,231]. Additionally, PFC tracers can be designed with unique ^{19}F signal to potentially track multiple cell populations and follow cell-cell interactions in vivo[232].

Despite the unique properties and advantages of ^{19}F-MRI, there are several factors preventing widespread use of fluorine contrast agents for cellular tracking. First and foremost, the lower sensitivity of ^{19}F-MRI compared to traditional ^{1}H MRI (with paramagnetic contrast agents) is a significant hurdle that must be overcome to detect low quantities of cells and accurately determine cell persistence after mass death or migration. While ^{1}H MRI exhibits high SNR due to the abundance of local water protons, ^{19}F-MRI is limited by the local concentration and accumulation of exogenous fluorinated agents. To enhance the SNR and limit of detection for cellular ^{19}F-MRI, cells must internalize significant quantities of fluorine tracers[207]. To enhance cell uptake of PFCs, which are water insoluble and immiscible in cell membranes[226], they are incorporated into suspensions and nanoemulsions with charged moieties[233]. The high fluorine loading and stability of these agents enhance signal strength and long-term contrast retention; however, this can be problematic after cell death which may result in the transfer of the agents to resident phagocytes and produce false-positive signal, similar to what has been observed with SPIOs[229,231]. ^{19}F-MRI is also physically limiting due the requirement of specific hardware and higher field strength scanners which are not clinically widespread. The sensitivity of ^{19}F-MRI hardware also decreases exponentially with increasing tissue depth and thus requires substantially longer imaging times[234,235] to produce satisfactory SNR for image interpretation. The duration of

a clinical imaging session is further elongated by the need for secondary ^{1}H MRI anatomical imaging of cell localization, which is not acquired with a ^{19}F-MRI scan due to the lack of endogenous fluorine in the body. This makes time-efficient and clinically relevant ^{19}F MRI challenging in comparison to cellular MRI with traditional contrast agents which mark cells within their anatomic context, enabling real-time imaging.

1.4.2.3 CEST-MRI Contrast Agents

Despite its challenges, the main advantage of cell tracking with ^{19}F agents is the ability to directly track the probe's unique and differentiable signal. This attractive property has spurred research into other probes and methods such as CEST-based imaging. As described and explored with scaffold tracking (Section 1.3.4.5), chemical exchange caturation theory (CEST), excites specific hydrogen protons on a molecule and then measures the change in water signal due to proton exchange. While this method does not measure a probe molecule directly, it does utilize a unique excitation frequency that is distinct from the rf frequency used to excite ^{1}H nuclei on water. This method can track protons on endogenous macromolecules such as proteins and carbohydrates without the need for tagging with traditional MR contrast agents. These molecules can occur naturally in particular cell types[236–238] or can be exogenously synthesized and loaded into cells for MR tracking purposes, such as cationic polyamides, which are easily engulfed by cells and have traditionally been used as gene transport agents[239]. Whether the CEST-agent is endogenous or exogenous, cellular-CEST MRI for *in vivo* imaging is challenging due to the high background noise and low sensitivity of CEST, as discussed in Section 1.3.4.5. Additionally, first-generation CEST agents had relatively small differences in signal frequency from water protons and thus excitation could result in partial saturation of water,[240] which is particularly problematic *in vivo* where the water signal is broad. To address this limitation, a new class of paraCEST contrast agents have been developed. These agents contain paramagnetic lanthanide metallic ions chelated by a macromolecular ligand. The metallic ion shifts the signal of the ligand protons further from the water proton signal, which enhances signal differentiation *in vivo*. Traditional metallic ions include europium and ytterbium, among others, for their ability to enact large shifts in proton signal. [241–243] Various paraCEST agents have been tested for cell tracking purposes and have shown feasibility *in vivo* with tumour models[244,245] and cell therapies such as cardiac regeneration[241].

While these agents have increased the sensitivity and specificity of CEST-based imaging, they raise safety concerns regarding the use of lanthanide metals *in vivo,* which have no known biological role[236]. Supramolecular[246] and liposome based-CEST[247] agents have also been developed to enhance signal sensitivity; however, are still significantly less sensitive and exhibit lower spatial resolution in comparison to traditional MR contrast agents[236]. Despite these challenges, one attractive utility of CEST imaging for cell tracking is the capability to track multiple cell populations simultaneously with CEST agents that have unique and distinct proton signals.[244] While the potential of CEST-based imaging for specific and differentiable contrast has generated interest in this modality for biomedical research, no clinical cell tracking trials have been performed to date, which is likely due to the low sensitivity and spatial resolution of CEST as well as the need for higher field strength scanners.

1.4.2.4 T_1-MRI Contrast Agents

T_1 contrast agents, as discussed previously, are agents that contain paramagnetic metals with unpaired electrons which produce positive/bright-contrast on MRI. Positive contrast is generally preferred for clinical image interpretation because the signal of the target site is enhanced providing better resolution and easy detection[248], in comparison to negative T_2 contrast, which is dark and can render the target site invisible at times. Within this space, gadolinium-based chelates are the most widely used and accessible chemical agents for clinical contrast enhanced MRI[249]. There are currently nine commercially available gadolinium based contrast agents (GBCAs) for various medical imaging applications such as extracellular, hepatobiliary and MR angiography[130]. These agents are composed of macromolecular compounds that chelate a gadolinium ion (Gd^{3+}). Most of these agents are small and hydrophilic to facilitate rapid clearance and limit physiological toxicity[250]. Due to their widespread use in clinical MRI, GBCAs have also been tested as agents for labelling and tracking cells[199,251].While first-generation clinical GBCAs were composed of linear chelators, cyclic chelators have been studied more for cell tracking due their enhanced stability[250] particularly under harsh intracellular conditions[252,253]. These GBCAs are taken up by cells via endocytosis, similar to other exogenous agents, and have been shown to label a variety of cell types for *in vitro* and *in vivo* tracking[252,253]. However, these studies have shown low sensitivity compared to SPIOs, and require high concentrations (5-100mM) and long labelling times (12-24hrs) to sufficiently label cells. To enhance the sensitivity and cell loading of GBCAs, various

approaches and new agents have been developed. This issue has primarily been addressed by loading multiple Gd-complexes into nanocarriers[254,255], such as liposomes[256], virus capsids[257], and protein cargos[258] or synthesis of gadolinium-oxide nanoparticles with biocompatible coatings[259,260]. Cells labelled with particle-based Gd-agents and imaged with T_1-weighted MRI have been efficiently detected and tracked with no obscuring image artefacts, as seen with SPIOs and T_2-weighted imaging. Enhanced Gd loading, however, has additional concerns and limitations. Firstly, quenching of T_1 relaxivity is observed when large amounts of gadolinium ions are concentrated within a small intracellular space, and secondly, the potential toxicity side-effects with increased cellular loading and retention of gadolinium could be problematic. As discussed briefly in previous sections, there have been rising concerns regarding the safety of GBCAs in routine clinical MR imaging.

The gadolinium ion is completely foreign to the body and while clinical agents are designed to be rapidly cleared *in vivo* (within 24-48 hours), recent reports have discovered gadolinium retention in the brain, muscles, skin, and bones long after administration of the GBCA.[261–264] This is particularly problematic and poses health risks for patients with kidney and liver disease[265,266]. These patients have a reduced ability to efficiently clear the GBCAs from their body and thus are exposed to the agents for longer durations. Furthermore, the longer a gadolinium-chelate remains in the body the greater chance for gadolinium dissociation due to transmetallation with an endogenous cation ion such as zinc, calcium, iron or copper[267]. Once released the free Gd^{III} ion can bind to a variety of serum proteins (i.e. albumin), and endogenous anions (i.e. phosphates, hydroxides, carbonates, citrates) to form insoluble gadolinium salts which are deposited in the bone, liver, skin, heart, kidney, spleen and lymph nodes[249,268–270].The released gadolinium can also affect a number of physiological processes such as extravascular fibrillogenesis[268], calcium channel function[271] and has been linked to neurological and cardiovascular toxicity[272]. In the case of patients with reduced renal function, the accumulation of gadolinium can lead to severe and sometimes fatal nephrogenic systemic fibrosis (NSF)[273]. It is important to note that these toxicity issues have mostly occurred with the administration of linear GBCAs, which suffer from lower thermodynamic stability and greater gadolinium dissociation *in vivo*, in comparison to macrocyclic agents.[103] Due to these concerns, the FDA first issued a black box warning for GBCAs in 2007 [269] and in 2017 issued warning labels for all GBCAs indicating the possibility of gadolinium retention in the body[274]. Furthermore, in many European countries some GBCAs have been pulled from

commercial shelves and restrictions have been imposed to limit the quantity and number of doses per individual per year.[102,107,108]The safety concerns of clinical GBCAs present potential challenges for Gd use in regenerative medicine and long-term cell tracking. In this field, therapies will require continuous monitoring at early and late time points, often months or years along. The need for multiple doses or prolonged retention of gadolinium agents in the body could pose unnecessary health risks to patients. Furthermore, clinical GBCAs are injected intravenously and primarily cleared by the kidneys, thus it is unclear if and how Gd agents would be eliminated when administered directly into tissues with therapeutic cells. For these reasons it is unlikely that gadolinium-based agents will be used clinically for cell tracking.

Consequently, alternative manganese-based T_1-contrast agents are actively being explored for cellular MRI. As discussed above in Section 1.3.4.7, manganese is an essential micronutrient absorbed, transported and stored in the body[113]. Due to its endogenous presence many cell types can uptake Mn^{II} naturally, via various divalent metal transporters and channels [113]. The quick and facile cellular uptake of Mn^{II} prompted *ex vivo* dosing with free $MnCl_2$ as one of the first alternative methods for cellular MRI[275,276] and has permitted functional imaging of labelled cardiac muscles cells[275], neuronal cells[254,255], and immune cells (T and B lymphocytes)[275] *in vitro* and in animal models. While these studies demonstrated successful and facile labeling with no significant effects on cell viability or function, there remains concern for clinical application due to the known neurotoxicity of free Mn^{II} ions at high concentrations.[277] To address these concerns Mn has been loaded into various chelates[117], macromolecules[123], nanoparticles and nanocarriers [124,278–280], similar to GBCAs. The formulation of manganese-oxide particles [278] and loading of manganese into nanocarriers such as liposomes[281], protein nanocages[282] and silica particles [279] have improved the relaxivity and extracellular stability of Mn-based CAs for cellular tracking. However, like other particle-based CAs, Mn-particle agents suffer from limited cell uptake in non-phagocytic cells and the potential for non-specific signal retention *in vivo* due to agent release post-cell death and uptake by resident macrophages. To address these challenges active research in the formulation, coating and method of Mn-loading is ongoing to fine tune CA properties and enhance biocompatibility, relaxivity and pharmacokinetic profiles.

Mn-chelates are another Mn-based platform for cell tracking; however, as discussed in Section 1.3.4.7, traditional Mn-chelates have low thermodynamic stability and are kinetically labile in physiological conditions. Manganese porphyrins (MnPs) are an exception in this field and

form Mn^{III}-complexes with high thermodynamic stability and kinetic inertness[126], have tunable pharmacokinetics and high relaxivity[137]. Furthermore, porphyrins have been to shown to be biocompatible in the body and easily up-taken by cells[283]. The high T_1 relaxivity exhibited by MnPs is also maintained with increasing magnetic fields, unlike typical Mn^{II} agents, which exhibit a decrease in T_1 relaxivity[111]. With the adoption of higher field strength scanners for superior sensitivity and resolution with molecular imaging and cell tracking, this property will be advantageous in the future. Furthermore, at high concentrations typical Mn^{II}-agents exhibit both strong T_1 and T_2 effects which can produce negative signal voids masking the anatomical location of labelled cells[114,275,284]. However, this is not observed with MnPs and thus they are effective as efficient positive contrast T_1 agents[137]. These unique properties demonstrate great potential for various medical imaging applications and particularly cellular MRI.

1.4.3 Cell Labelling Methods

The two pillars of cellular tracking are the contrast agent and the method of cell labeling. While the agent produces trackable signal, the method of labelling confers that signal to the cell. The method utilized significantly impacts the quantity of agent associated with a cell and thus determines the sensitivity of the cell tracking system. Furthermore, the method controls which cells are labelled and thus impacts the specificity of the system as well. Due to the importance of the labelling method on both the sensitivity and specificity of a cell tracking system, a variety of approaches have been explored. These approaches fall under two main paradigms; in which cells are labelled *ex vivo* prior to injection into an animal or patient or they are targeted and labelled *in situ* within the body of a subject. These general approaches are illustrated in Figure **1.4**.

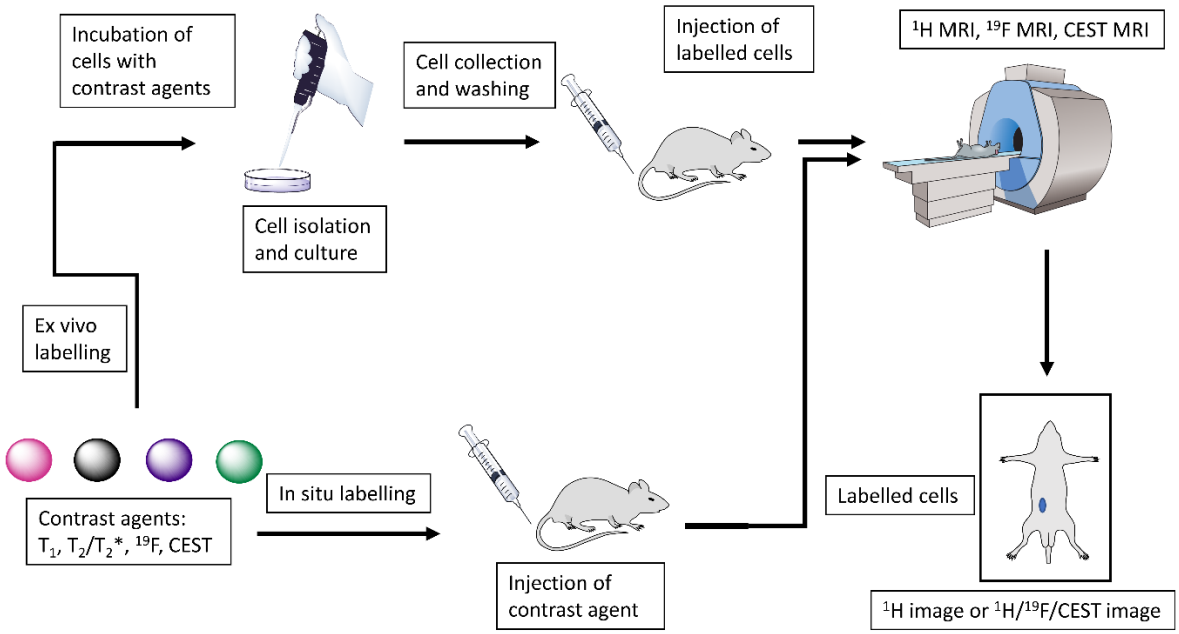

Figure 1.4: Cell labelling methods. Schematic showing ex vivo and in situ labelling of cells with magnetic resonance contrast agents

1.4.3.1 Ex Vivo Cell Labelling

Directly labelling cells with exogenous contrast agents prior to injection in a patient has been the most widely used approach for cellular MRI in preclinical and clinical studies due its ease and specificity[169]. *Ex vivo* labelling involves co-incubating pre-selected cells cultured in a laboratory with contrast agents. The cells are then labelled either by attachment of the agent to the cell membrane or intracellular uptake and retention. Cell membrane labelling was one of the first examples demonstrated, utilizing targeted antibodies and peptides to specific cell epitopes[285]; however, intracellular labelling has received greater attention in the field due its ease and enhanced contrast retention. In the later, contrast agents typically enter the cell via non-specific endocytic processes such pinocytosis or phagocytosis. This has been advantageous for highly phagocytic cells such as macrophages, microglia and immature dendritic cells[165,182]; however, it has been problematic for cells with a low level of phagocytosis or micropinocytosis activity; which includes many therapeutic cells used in regenerative medicine and tissue engineering. This limitation is particularly problematic for particle-based cellular tracking systems such as SPIOs [169], which are generally cell-impermeable due their foreign nature, large size and charge, and can only be taken

up by phagocytosis and pinocytosis. This issue has been partly addressed by complexing particles with cationic transfection agents[171,177]such as poly-L-lysine or protamine sulphate[286–288] simultaneously or prior to incubation with cells. The need for transfection agents, however, can be a hurdle for clinical use as they would require separate FDA approval. Furthermore, complexing negatively charged particles with positively charged transfection agents can cause aggregation and precipitation, which hinders endocytic uptake. Alternative approaches involve physical perturbation of the cell membrane, such as electroporation[280,289] or modification of the contrast agent itself to promote self-delivery[233,290–298]. The latter can be accomplished by modifying a CA's charge[233,291], or enhancing its lipophilicity to promote passive diffusion and uptake[296–298]. Additionally, CAs have also been functionalized with targeting moieties to promote receptor-mediated endocytosis, such as antibody-conjugates[290] or cell-penetrating peptides[292–295]. Utilizing these advancements, a variety of cells can be loaded with multiple CAs. After internalization of the CA, the cells are then harvested from culture, washed and administered to the patient. Owing to the simplicity of this method it has resulted in widespread use and holds potential for clinical approval due the standardization and control afforded by *ex vivo* approaches. However, due the assortment of techniques, CAs and cell types, the incubation period to reach optimal cell loading can vary significantly and thus needs to be experimentally determined for each scenario.

Despite the advancements in *ex vivo* delivery methods to enhance CA cellular uptake, a major unmet challenge is the inability to probe cell fate long-term. This is primarily due to the innate nature of *ex vivo* methods which have a limited temporal window for cell labelling and the lack of signal specificity once in vivo. With regards to the former, labelling cells prior to injection utilizes a finite quantity of CA; however, cell quantity is dynamic and will change once in the body. As cells proliferate and divide, the finite quantity of CA will be diluted among the daughter cells[299], resulting in a loss of signal as they disperse. Additionally, due the dynamic nature of a cell, CAs can also be lost due to active exocytosis[300], further decreasing signal. To address this limitation, many CA formulations, particularly particle-based, have been developed to enhance cellular retention. [169,198,301] However, this has created a secondary problem with signal specificity. Many particle-based CAs, particularly observed with SPIO trials, are retained at the site of injection even after cell death, due to uptake by resident macrophages. This confounds signal specificity and quantification[187,212–214]. These issues occur due to the limiting nature of physically coupling a contrast agent to a cell. The contrast agent and the signal it produces is not biologically

linked to the cell and thus it is challenging to report or respond to biological phenomenon such as cell division or death. For these reasons alternate labelling methods and techniques have been developed to probe cell fate longitudinal and provide greater insight *in vivo*. However, the immediate utility of *ex vivo* labelling cannot be completely dismissed, for it is a facile platform that is highly translatable, can provide early information regarding injection site success, and is well poised for clinical adoption.

1.4.3.2 In Situ Cell Labelling

To enhance the longitudinal capability of cellular tracking, cells can be targeted and labelled *in vivo*. *In situ* labelling involves the targeting, labelling and generation of cellular contrast in endogenous cells, or exogenous cells post injection in a patient. In the former, a labeling agent is systemically injected and then intrinsically taken up by cells in the body. Due to the large abundance of phagocytic immune cells in the reticuloendothelial (RES) system, which filters the circulatory system, systemically injected contrast agents are naturally engulfed. The immune cells in this system are involved in inflammatory responses and accumulate at sites of inflammation; thus, when labelled *in situ* can provide information regarding the host immune response to various treatments and procedures. Systemic *in situ* labelling with T_2 [302–305] and ^{19}F [305–308] contrast agents has been applied to image various inflammatory responses in biomedical research and regenerative medicine[310–312]. This approach has provided important insight regarding the recruitment, trafficking and dispersion of immune cells in clinically relevant models such as central and peripheral nervous system inflammation[217,313,314], multiple sclerosis[305,315,316], pulmonary inflammation[317], inflammatory bowel disease[307], bacterial infections,[308] organ ischemia[318] identification of atherosclerotic plagues[304] , and in regenerative medicine with organ[309,319] and cell transplant rejections[320–322]. Particle-based contrast agents have largely been employed in this context due to their prolonged circulation and preferential uptake by phagocytic cells; however, these ideal properties also result in off-target accumulation in the liver, spleen and lymph nodes which produces non-specific background signal and confounds research and clinical observations[323,324]. Furthermore, it is difficult to restrict uptake by other cells, such as neutrophils or dendritic cells, thus limiting this approach for broad applications that image “all” cells involved in systemic physiological events. The lack of specificity has partly been addressed by direct

injection of a CA into a target tissue, which promotes preferential uptake by local immune cells. This technique has been used for tracking tumor migration or immune cell homing from tumor sites to lymph nodes[302].

Overall, endogenous cell tracking with *in situ* labelling can be conducted longitudinally by reinjection of a CA and has demonstrated utility in niche applications that monitor physiological cellular responses. However, this approach lacks cell specificity and suffers from the limitations associated with the use of an exogenous labelling agent. The signal produced by exogenous agents does not always represent viable cells and is lost with cellular division. To achieve specific and longitudinal cell tracking reflective of cell state, the agent must be coupled biologically with the cell. New developments in genetic engineering have sought to accomplish this task by coupling the production of MR contrast with cellular processes.

1.4.3.3 Genetic Cell Labelling

To translate regenerative cell therapies into the clinic, *in vivo* tracking of injected cells over time is critical. Most preclinical and clinical trials have only provided information on immediate cell delivery and short-term cell retention due to the inherent limitations of *ex vivo* labelling and the use of exogenous agents. While first-generation *in situ* targeting systems with CAs have tried to address this, they lack the specificity for accurate cell detection and homing. To obtain cell-specific longitudinal imaging, more emphasis has been directed towards genetic labelling approaches. Genetic *in situ* labelling involves transfecting cells with a reporter gene construct to produce an endogenous protein, transporter, enzyme or receptor-based platform that generates cellular contrast and enables live cell bioimaging; an overview of this approach is illustrated in Figure **1.5**. Such methods present an opportunity to develop superior cell-tracking systems which do not suffer from signal loss due to cell division but rather exhibit a positive correlation between signal intensity and proliferating cells. Genetic labelling also ensures that contrast generation is active and inducible only in living cells, providing greater specificity in the origin of MR signal. The later point is of specific importance, due to the issues discussed earlier regarding non-specific contrast agent uptake by inflammatory cells following cell death, which results in a false positive readout of cell persistence. Furthermore, genetic-cell labelling provides greater utility beyond cell tracking and opens the door for investigations of gene and protein expression.

Clinically, only PET/SPECT based genetic cell-tracking systems thus far have been trialled. While these systems have shown early success and utility of genetic-based imaging approaches, they suffer several limitations. Firstly, PET/SPECT-based imaging does not provide anatomical information and therefore requires co-registration with CT or MRI, which increases methodological complexity and cost of an imaging session. Also, the use of radioactive tracers is a concern for cell toxicity and prolonged use in regenerative medicine. These limitations have stimulated the development of MRI-based genetic reporter systems.

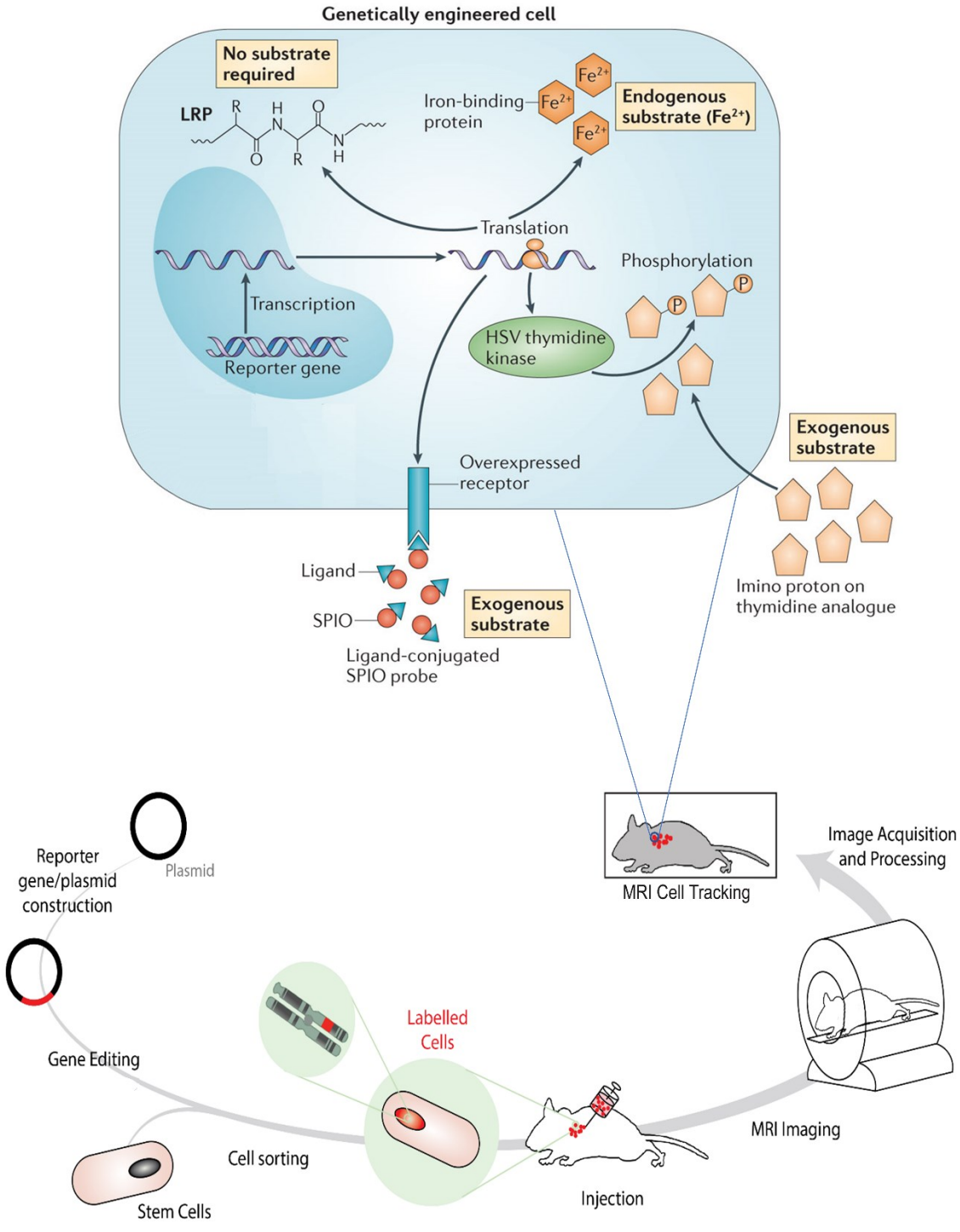

Figure 1.5: Schematic and overview of MRI genetic reporter systems. The process of genetic cell labelling begins with the insertion of a reporter gene into a vector such as a plasmid. The plasmid is then inserted into the genome of a cell. The labelled cells are selected based on stable reporter gene expression before injection in an animal. Once inside the body, the labelled cells produce *in situ* cellular contrast detectable with MR imaging. Inside the cell a transcribed reporter

gene results in the overexpression of endogenous proteins and macromolecules which act on a variety of exogenous or endogenous substrates to produce intracellular contrast. Certain reporters require no substrates and thus produce contrast innate. One class of reporters generate cell contrast by encoding cell surface receptors which bind exogenous contrast agents, such as SPIOs, conjugated with the receptor ligand. Other systems utilize enzyme-mediated processes to phosphorylate exogenous agents which traps them in the cell. Over-time enough agent is accumulated to produce visible MR contrast. The second class of reporters bind and accumulate endogenous substrates such as paramagnetic ions (i.e. iron) to generate intracellular contrast. Lastly, the third class of reporters require no substrate. The gene product of CEST reporters such as lysine-rich protein, produces contrast innately due to its CEST-active amide protons that can be excited and detected. Adapted with permission from Ahrens, E.T., & Bulte, J. W. *Nat. Rev. Immunol.,* 2013, 13, 755. Copyright (2013) Springer Nature.

MRI genetic reporters for cell tracking can be categorized by the substrate they act on and the gene product they create. The substrate is the inherent material (paramagnetic ion, ^{19}F-compound, or CEST ligand) which will generate contrast, and the gene product is a cellular actor which either accumulates or activates the substrate. Substrates can be endogenously available or exogenously supplemented and the gene product can be a variety of cellular macromolecules including enzymes, receptors, metalloproteins/protein-chelators, and transporters.

Enzyme-based reporters were one of the first systems developed for cellular tracking. They were originally applied for optical and PET imaging using an herpes simplex virus thymidine kinase (HSV-tk) reporter gene[163,325]. In this system transduced cells overexpress the foreign HSV-thymidine kinase which phosphorylates circulating exogenous thymidine analogues and promotes their cellular accumulation. This system has been recently adopted for MRI by utilizing a thymidine analogue that is CEST-active[326] and has been used to track the survival of mesenchymal stem cells for cardiac regeneration[327]. Other MRI enzyme-substrate reporter systems utilize tyrosinase [328,329] or B-galactosidase [330,331] overexpression in conjunction with paramagnetic substrates. In brief, overexpression of tyrosinase catalyzes the production of melanin which can bind and accumulate circulating paramagnetic ions[252]. In other systems, overexpression of B-galactosidase can activate paramagnetic-chelates functionalized with blocking B-galactose ligands. Cleavage of the B-galactose ligand exposes water binding sites on the paramagnetic metal which produces MR contrast. [253] Most enzymatic reporter genes are endogenous to humans and thus clinically safe; however, their natural presence can result in off-target signal and elevated

background[332]. Furthermore, the degree of genetic expression can vary based on cellular environments which hinder accurate signal detection and quantification.

In addition to *in situ* labelling by enhancing cellular enzymatic activity, cells *in vivo* can also be targeted and labelled with receptor-ligand systems. In these systems, cells are genetically modified to express specific membrane receptors that bind exogenous contrast agents functionalized with the corresponding ligand. The most common systems utilize genetic overexpression of transferrin receptor (TfR)[333,334] or biotin [335], in conjunction with contrast agents bound to transferrin or streptavidin, respectively. While these systems have shown the potential for specific cellular targeting, they primarily suffer from inefficient delivery of exogenous contrast agents to the target site in the body. However, recent studies with cells overexpressing TfR have removed the need for exogenous agents due to the natural uptake of endogenous iron. The uptake of this abundant substrate results in an increased T_2-relaxation rate and the production of corresponding dark contrast[336–339]. The ability to uptake endogenous paramagnetic ions is highly advantageous and is the primary method of contrast generation for metalloprotein reporter systems discussed below.

Several distinct technologies have been developed to produce MR contrast with endogenous substrates. The most studied systems are based on metalloprotein reporter genes that bind iron, particularly those in the ferritin family[340–348]. In these systems, the ferritin protein, which is overexpressed in target cells, sequesters endogenous iron, and forms an intracellular iron oxide crystal with a ferritin-protein shell. This iron core is superparamagnetic and thus produces strong T_2-weighted contrast, analogous to SPIO nanoparticles. The formation of these iron-ferritin nanoparticles is a natural and safe method for iron storage in cells. For these reasons the ferritin-iron reporter gene system has been extensively studied and explored for tracking a variety of cell types including pluripotent stem cells[342], mesenchymal stem cells[349] skeletal myoblasts[350], dendritic cells[351], neural progenitors[345,352], hepatocytes[353] and has even been applied in transgenic whole animal models[353,354]. However, due to the innate dark T_2-signal of most tissues and the low endogenous level of iron, many of these systems require additional iron supplementation[353,355] to increase the quantity of ferritin-particles and enhance intracellular contrast. Additionally, the utilization of T_2-contrast for cell tracking suffers many limitations, discussed previously in Section1.4.2.1, that hinder accurate cell monitoring.

To confer greater confidence in anatomical cell visualization and image interpretation, genetic reporter systems have also been developed to produce bright T_1-cellular contrast with endogenous substrates. This has been primarily been achieved with genetic expression of membrane channel proteins which enhance the transport of endogenous paramagnetic metal ions, such as Mn^{II}, into a cell[356]. In one approach, cells were transduced with human divalent metal transporter-1 (DMT-1), which increased cellular uptake of Mn^{II} ions and produced bright T_1-cellular contrast. This reporter system exhibited rapid uptake and clearance of Mn^{II} which created a small window for imaging *in vivo* after systemic $MnCl_2$ injection[356]. It is important to note that ion transport and clearance is highly variable between cell types and environments thus the window of imaging for transporter-based systems will be as well[357]. This is further complicated by the biodistribution of ions between different tissues, and thus these systems require significant optimization for *in vivo* applications. Furthermore, the elevated concentrations of intracellular free ions can have adverse effects on cell viability and function due to disruption of membrane potentials and ionic equilibriums which drive many cell processes[357]. Additionally, in the scenario when free ion supplementation is required, appropriate pharmacological studies must be conducted to determine safe systemic doses; however as discussed earlier, iron and manganese are endogenous substrates with clinically recommended daily amounts.

Most genetic reporter systems have two components, the gene product and substrate, however, there is one class of genetic reporters that is an exemption because its gene product is also its substrate. This class of cellular reporters produce MR contrast innately and are exclusively CEST-based[358]. With these systems cells are genetically modified to overexpress CEST-active macromolecules and proteins[359]. The first demonstration of a CEST reporter gene produced a lysine-rich protein (LRP) in labelled rat 9L-glioma cells and demonstrated the ability to track tumors formed by the labelled cells. The LRP reporter gene produced enhanced signal above background proteins due to its many amide protons, which are excitable within a small signal range and exhibit faster exchange kinetics than endogenous amide protons[359]. Lysine polymers, however, are foreign to the body and can occasionally trigger inflammatory responses[360,361]. To address this, human-based CEST reporter systems, such as human protamine-1, have also been developed.[326] CEST reporters offer unique capabilities for cell tracking, as discussed previously, such as on-demand signal generation and visualization of multiple cell populations[362,363]. However, they

exhibit low signal *in vivo* and lack the ability for real-time detection. For this reason most genetic reporter systems rely on paramagnetic substrates for superior contrast enhancement[330,340,364].

While genetic reporter systems can produce accurate and cell specific contrast, they suffer from inherently low sensitivity, multiple orders of magnitude less than exogenous labelling methods[365–367]. To enhance cellular contrast many systems express high levels of the MR gene product, as high as 60-fold overexpression from native cells.[340,368–370] Such high expression levels may have adverse effects on cell function over-time due to unwanted energy utilization or cascade signalling. Another important consideration when genetically modifying a cell is the risk of unintended off-target mutations and alteration of vital cell functions. It is desirable to limit not only the number of insertions but also the locations of insertions. These technical issues are common across the field of genetic engineering and not isolated within the smaller field of MR reporter genes. Thus, as the field advances so will MR genetic labelling approaches. Despite these general concerns, there is potential for clinical application of these systems, considering many genetically engineered cell therapies are undergoing clinical trials[371,372] and multiple have been approved for clinical use such as Yescarta and Kymriah; a genetically modified autologous T-cell immunotherapy for treatment of lymphoblastic leukemia[373] and Luxturna™; a gene therapy for inherited retinal disease.[371] Currently in the US, there are over 17 approved cellular and gene therapy products with more in the pipeline.[374]

Overall, the genetic reporter systems discussed above demonstrate the potential to probe cell fate directly and achieve longitudinal tracking with higher diagnostic accuracy for cell-based therapies. While the development of safe and sensitive systems is an active research area, the specificity of genetic-based cell imaging will make it a powerful tool for guiding clinical practice and scientific development. These platforms open the door for in-depth investigations that can answer important questions regarding how cells behave in vivo and their impact on clinical success.

Chapter 2 : Motivation and Central Aims of Research

2.1 Rationale and Global Objective

Tissue engineering is an emerging field which has rapidly expanded in the past decade with the development of multiple biomaterial-based scaffolds and cellular therapies striving to regenerate almost every tissue and organ of the body. However, despite the advances in this field, very few scaffold or cell-based therapies have been approved for clinical use due to the vast changes and unexpected outcomes that can occur as therapies transition from the laboratory bench to the body of a patient. Implanted scaffolds suffer from placement shifting and incorrectly tuned degradation rates while injected cells suffer from mis-injection, uncontrolled migration and significant death at early and late timepoints in a therapy. Despite the distinct nature of these materials, the issues faced by their respective therapies have a shared commonality: lack of spatial and temporal monitoring *in vivo*.

To address this challenge, the principle aim of this thesis was to develop non-invasive, non-ionizing, and biocompatible imaging techniques with MRI to track scaffolds or cells intended for regenerative medicine and tissue engineering applications. With the correct imaging tools, implants can be accurately visualized and assessed with high spatial and temporal resolution *in vivo*. The methods developed were designed to be facile and efficient so that they can be readily applied to any scaffold or cell therapy protocol and workflow. Their utility and translatability will enhance the optimization of regenerative therapies and provide greater diagnostic accuracy in the clinic. To achieve sensitive and safe contrast enhancement, manganese-based positive contrast agents were selected as a general platform due their high T_1 sensitivity and the biocompatibility of the Mn ion, an essential micronutrient, at low doses in comparison to the foreign and toxic gadolinium ion. Furthermore, Mn-positive contrast is clinically preferred to negative "dark" T_2/T_2* contrast generated by SPIOs which suffer from susceptibility artifacts and difficultly with accurate visualization *in vivo* due to confounding sources of hypointense regions in the body such as blood clots and tissue-air interfaces particularly present in injury models relevant to regenerative medicine.

2.2 Scope and Aims of Research

The first part of this thesis sought to address the lack of sensitive and non-invasive methods for tracking extracellular matrix (ECM) based scaffolds, a highly regenerative and widely utilized material in both research and clinical settings. The material's natural origins and innate abundance in the body make it an ideal scaffold but also difficult to distinguish from native tissue with traditional MR imaging. This is complicated further as a scaffold degrades and becomes integrated into host tissue; rendering the scaffold indistinguishable from its surroundings. Owing to the difficulty of imaging natural materials and their sensitivity to chemical processing, the application of a gentle scaffold labelling approach with a contrast agent at physiological conditions was desirable. To create a highly sensitive yet facile method for labelling ECM-based materials, a positive-contrast manganese porphyrin (MnP) was exploited for its high T_1 relaxivity and its known ability to strongly associate with ECM-rich tumors in vivo. Furthermore, MnPs exhibit high thermodynamic and kinetic stability an important safety consideration in regenerative medicine where implants directly engage with cells and tissues for prolonged periods of time. Passive labelling of ECM materials with the MnP would permit non-invasive visualization of scaffolds *in vitro* and *in vivo*.

While passive or non-covalent labelling is an attractive approach due its simplicity and ease of clinical adoption, it inherently suffers from limited long-term retention and the potential for signal flux non-representative of scaffold changes. Thus, to achieve enhanced accuracy, specificity and long-term monitoring of biomaterials, the second part of this thesis aimed to develop and compare a covalent binding approach for direct labelling and monitoring of scaffolds with MRI. To enhance clinical translation, commercially sourced collagen hydrogels were selected as a prototypical scaffold that can be injected and thermally formed in the body for minimally invasive therapies. To achieve direct conjugation, a manganese-porphyrin (MnP) compound was designed and chemically functionalized with a single nucleophilic end group, but otherwise unaltered to maintain desirable qualities such as small size (<1kDa) and water solubility. Furthermore, due to the thermo-sensitivity of collagen hydrogels and their incompatibility with organic solvents, an atypical conjugation approach was designed with a bio-inspired adhesive, polydopamine, that is self-activating in aqueous solution. Methods utilizing this conjugation approach with the MnP agent would be explored to determine the most efficient, safe and facile scheme for scaffold

labelling. Development of direct biomaterial labeling with a 'bright'-MnP-contrast agent would create highly distinguishable grafts with the potential for long-term tracking of scaffold content *in vivo*.

Another significant and challenging area in regenerative medicine is tracking and assessing cell-based therapies. The ability to visualize the biodistribution of cells following injection is the common requirement for the development of nearly all cell therapies. Owing to the enhanced MRI sensitivity and biocompatibility observed with MnP contrast agents and previous literature that has shown cellular uptake of porphyrins, the previously synthesized MnP agent was tested for its potential to directly label and track regenerative-specific cells with MRI. Labelling cells *ex vivo* by co-culture with the MnP contrast agent would confer positive-contrast to the cell for non-invasive MR visualization. The facile nature of this labelling method could be readily applied to any cell therapy protocol and circumvents the difficulties of targeting specific cells *in vivo*. Furthermore, to enhance academic and clinical adoption we sought to limit the synthesis protocol and enhance its scalability by utilizing a commercial precursor starting material. Overall, we sought to develop a non-invasive, biocompatible and translatable positive-contrast method to visualize and track cells post implantation *in vivo* with MRI.

Labelling cells *ex vivo* with an exogenous contrast agent is highly adoptable due to its simplicity and ease of use; however, it is limited as a longitudinal cell tracking method because the MR signal is not inherently linked to cell fate and thus can suffer from signal loss due to cell division or agent release. Consequently, the final section of this thesis aimed to develop a genetic based method for producing bright endogenous cellular contrast with the potential for long-term cell tracking. To design a safe yet sensitive system, we utilized a CRISPR/Cas9 genetic approach for targeted and controlled expression of an endogenous metalloprotein, ferritin. Ferritin is known for binding and storing iron in the body; however, we theorized that this protein could bind other cationic metals such as manganese and potentially create intracellular manganese nanoparticles for positive-contrast MR imaging. The formation of manganese particles linked to live-cell expression would produce a specific intracellular MRI 'bright'-contrast system with the potential for longitudinal cell tracking *in vivo*.

Chapter 3 : MRI method for labeling and imaging decellularized extracellular matrix scaffolds for tissue engineering

This work has been published in *Magnetic Resonance in Medicine* Volume 83, Issue 6, pp.2138-2149, (2020) and has been reproduced with permission from the respective publishers.[375] Article listed below:

Szulc D.A., *et al.* MRI method for labeling and imaging decellularized extracellular matrix scaffolds for tissue engineering. *Magn Reson Med*. 2020;83(6):2138-2149. doi:10.1002/mrm.28072

3.1 Abstract

Purpose: To develop a facile method for labeling and imaging decellularized extracellular matrix (dECM) scaffolds intended for regenerating 3D tissues.

Methods: A small molecule manganese porphyrin, $MnPNH_2$, was synthesized and used to label dECM scaffolds made from porcine bladder and trachea and murine whole lungs. The labeling protocol was optimized on bladder dECM, and imaging on a 3T clinical scanner was performed to assess reductions in T_1 and T_2 relaxation times. In vivo MRI was performed on dECM injected in the rat dorsum to verify sensitivity of detection. Toxicity assays for cell viability, metabolism, and proliferation were performed on human umbilical vein endothelial cells. The incorporation of $MnPNH_2$ and its long-term retention in dECM were assessed with transmission electron microscopy and ultraviolet absorbance of eluted $MnPNH_2$ over time.

Results: All tissues, including thick whole 3D organs, were uniformly labeled and demonstrated high signal-to-noise on MRI. A nearly 10-fold reduction in T_1 was consistently obtained at a labeling dose of 0.4 mM, and even 0.2 mM provided sufficient contrast in vivo and ex vivo. No toxicity was observed up to 0.4 mM, the maximum tested. Binding studies suggested nonspecific association, and retention studies in the labeled whole decellularized lungs revealed less than 20% $MnPNH_2$ loss over 30 days, the majority occurring in the first 3 days after labeling.

Conclusion: The proposed labeling method is the first report for visualizing dECM on MRI and has the potential for long-term monitoring and optimization of dECM-based organ tissue engineering.

3.2 Introduction

The ultimate goal in tissue engineering and regenerative medicine is building complex, 3D tissue structures, even entire organs, for transplantation to obviate the need for donor transplant. Growing tissue with a defined geometry, however, requires a framework, or scaffold, for 3D support and growth. Scaffolds made from a variety of synthetic materials have been investigated over the decades with limited success, and attention quickly turned to natural materials. Amongst these, tissue-specific decellularized extracellular matrix (dECM) was recognized as a viable option, with the first demonstrations shown for building vascular grafts.[376] The key advantage to using dECM, one that no nonbiological alternative can replicate, is biological integration and retention of desired mechanical properties, structure, and biochemistry. Over the past 2 decades, the dECM approach has been studied for regenerating a plethora of tissues and organs, including heart valves[377], bladder[378], skeletal muscle[379], liver[380], cartilage[381], trachea[382], lungs[383], and myocardium[384]. Most recently, the dECM approach has found traction in 3D bioprinting, with several investigators reporting success using dECM gel as a bioink over collagen, alginate, or other more common bioink substrates[385]. The interesting implication here is that, even if we do not use the structural and morphological cues provided by an intact dECM, the biochemistry of the dECM alone imparts a more physiologically realistic environment for 3D tissue regeneration.

Whenever scaffolds are used, the need for non-invasive in vivo scaffold imaging remains for understanding time-course behavior and optimizing regeneration. The capability for in vivo scaffold tracking allows one to assess scaffold degradation, host-tissue interactions, and restoration of tissue functions. Many scaffold materials, such as ceramics and synthetic polymers, can be differentiated from native tissue on imaging due to stark differences in material properties. In the case of dECM, however, innate contrast differences between dECM and host tissue are negligible, because their biochemistry and structure are so similar.

What becomes necessary is a method to label the dECM scaffold to enhance its image contrast and allow for clear, unambiguous identification in vivo. In the scenario where only a part of an organ needs to be replaced, the ability to visualize the location and distribution of injected or implanted scaffold, and distinguish it from native tissue, is essential. With time, the ability to determine implant success or failure is also critical to allow intervention if and when required. This type of long-term monitoring relies on sustained contrast for accurate evaluation of scaffold

biodegradation as tissue regenerates. Direct scaffold labeling also affords a fair degree of immunity to contrast "blending" as local cells and tissue ingrowth occurs. Equipped with a non-invasive ability to monitor remodeling and biodegradation, we can effectively optimize the scaffold and introduce material modifications (i.e., biological composites, cross-linking) or treatment modifications (i.e., growth factor loading, cell seeding, repeated injection/implantation) to ensure the rate of biodegradation is ideally matched to support cell infiltration and tissue growth.

A second scenario is when an entire decellularized organ is implanted, in which case labeling the implant would serve not to enable visualization (standard MR imaging suffices) but to permit monitoring of scaffold structure and content as it gets modified and degraded during integration. Whether we aim to replace part of or an entire organ, a potentially useful approach for labeling dECM material is one taken to label biomaterial gels with imaging contrast agents, with recent examples described for imaging collagen gels[88,386] and gelatin hydrogels[387] on MRI. To date, a method to label and visualize dECM scaffolds noninvasively on MRI has not been investigated.

This study is, to our knowledge, the first report of a method for labeling and imaging dECM scaffolds on MRI. A positive-contrast manganese porphyrin ($MnPNH_2$) contrast agent is exploited for its efficient contrast enhancement and thermodynamic and kinetic stability[388,389], the latter being an especially key safety consideration. The synthesis and labeling methods presented herein are facile and represent a flexible platform for further refinement and modification. We present the feasibility of our approach for labeling and imaging a range of decellularized tissue types currently investigated for regeneration using the dECM approach, including the bladder, lungs, and tracheal smooth muscle and cartilage.

3.3 Materials and Methods

3.3.1 Materials

Manganese chloride ($MnCl_2$), concentrated sulfuric acid (H_2SO_4), N,N-diisopropylethylamine (DIPEA), acetonitrile (ACN), 4-(2-hydroxyethyl)piperazine-1-ethanesulfonic acid (HEPES), dimethylformamide (DMF), sodium bicarbonate ($NaHCO_3$), ammonium acetate (NH_4OAc), hydrochloride (HCl), Tris-HCl, Dulbecco's modified eagle's medium-high glucose (DMEM), dopamine hydrochloride, phosphate buffered saline (PBS), ethylenediaminetetraacetic acid

(EDTA), benzonase nuclease, 3-[(3-cholamidopropyl)dimethylammonio]-1-propanesulfonate hydrate (CHAPS), Pefabloc Plus, Triton X-100, penicillin/streptomycin, potassium chloride (KCl), sodium dodecyl sulfate (SDS), sodium deoxycholate (SDC), 10% formalin, ethanol, paraformaldehyde (PFA), and glutaraldehyde, were purchased from Sigma Aldrich (Steinheim, Germany).

CyQuant Direct Cell Proliferation Assay C35011 was purchased from Thermo Fisher Scientific (MA, USA), calceinacetoxymethyl (Calcein AM) and ethidium homodimer-1 (EthD-1) from Invitrogen (CA, USA), primary human umbilical vein endothelial cells (HUVECs), single donor, in EGM-2 from Lonza (Basel, Switzerland), and VascuLife VEGF Endothelial Medium from Lifeline Cell Technologies (MD, USA). The 5-(4-aminophenyl)-10,15,20-(triphenyl)porphyrin was purchased from PorphyChem (Dijon, France). Pretreated regenerated cellulose dialysis tubing (MWCO: 1 kD) was purchased from Spectrum Labs (OH, USA). Ion-exchange resin (amberlite IR120, H form) was purchased from ACROS Organics. All chemicals were of appropriate analytical grade and were used without further purification.

3.3.2 Synthesis of $MnPNH_2$

Manganese 5-(4-aminophenyl)-10,15,20-(tri-4-sulfonatophenyl)porphyrin ($MnPNH_2$) was synthesized using a modified protocol[390]. In brief, the precursor 5-(4-aminophenyl)-10,15,20-(triphenyl)porphyrin was dissolved in concentrated sulfuric acid and heated at 75°C to form the intermediate product 5-(4-aminophenyl)-10,15,20-(tri-4-sulfonatophenyl)porphyrin (Apo-PNH_2). Apo-PNH_2 was purified by dialysis (Regenerated cellulose, MWCO: 1 kD). After purification Apo-PNH_2 was dissolved in DMF and reacted with $MnCl_2$ and DIPEA at 135°C for 3 h to form $MnPNH_2$. The reaction was monitored by UV analysis to determine the degree of metalation. The product, $MnPNH_2$, was purified by ion-exchange chromatography (Amberlite IR120, H form resin) and dialysis (Regenerated cellulose, MWCO: 1kD). $MnPNH_2$ was lyophilized with a VirTis BenchTop Freeze Drier and stored at −20°C.

3.3.3 Characterization of $MnPNH_2$

$MnPNH_2$ purity was determined by high performance liquid chromatography (HPLC), ultraviolet-visible (UV-Vis) spectroscopy, flame atomic absorption spectroscopy (FAAS), and mass

spectroscopy. HPLC was run using a continuous ramping protocol with a gradient mix of ACN to 10mM NH_4OAc on a PerkinElmer Series 200 system, Supelco Supercoil LC 18 column, and with UV/Vis detection at 469 nm. Elution occurred at 2.20 min with 99.86% purity. UV/Vis absorption spectra were measured in HEPES buffer at 25°C, $\lambda_{max} = 469$ nm, $\varepsilon = 93552\ M^{-1}cm^{-1}$ (Agilent 8453 Spectrometer). Mass spectroscopy was conducted with an Agilent 6538 Q-TOF system in electrospray ionisation mass spectrometry (ESI MS) negative mode. ESI MS found m/z = 459.5138 [M^+], calculated for $C_{44}H_{26}MnN_5O_9S_3^{-2}$, m/z = 459.5142. FAAS was conducted with a PerkinElmer AAnalyst 100 spectrometer and a Manganese Lamp. The concentration of the product determined by UV/vis was compared to the concentration of Mn to confirm the 1:1 ratio and the absence of any residual Mn salt.

3.3.4 $MnPNH_2$ labeling of dECM scaffolds and gels

Decellularized ECM scaffolds were prepared according to a published protocol[391]. In brief, porcine bladders were harvested from outbred Yorkshire male pigs (3 months old; 28-35 kg) and then decellularized in a series of solutions. All bladder collections were performed in accordance with the "Principles of Laboratory Animal Care" defined by the National Society for Medical Research and the "Guide for the Care of Laboratory Animals" issued by the National Institutes of Health. Harvested bladders were rinsed with sterile PBS before gross sectioning and immersion in a hypotonic cell-lysing solution (5 mM EDTA, 10 mM Tris-HCl, pH 8.0, 1% Triton X-100, 0.1 mg/mL Pefabloc Plus^{TM} and penicillin/streptomycin) and then a hypertonic protein-denaturing solution (5 m M EDTA, 10 mM Tris-HCl, pH 8.0, 1% Triton X-100 and 1.5 M KCl) for 48 h each at 4°C with stirring.

The bladder sections were then washed with HBSS and incubated with benzonase (0.16 mU/mL) at 37°C for 12 h to degrade residual DNA and RNA components. Afterward, the bladders were immersed in a nondenaturing detergent solution (0.25% CHAPS, 50 mM Tris-HCl, pH 8.0, 1% Triton X-100, and penicillin/streptomycin) at 4°C for 48 h before final rinsing with double-distilled water and lyophilization with a VirTis BenchTop Freeze Drier. For dECM bladder gels, the bladder sections were processed according to published protocols[392–396]. The dried dECM bladder sections were ground into a powder; 1 gm of powder was then digested with 50 mg of pepsin in 50 mL of 0.1 M HCl for 48 h at room temperature with stirring to produce a solution of 20 mg/mL.

The resultant viscous solution was adjusted with 0.1 M HCl after digestion to account for any volume loss due to evaporation, before neutralization with 0.8M sodium bicarbonate at 4°C. dECM gel solutions were stored at 4°C until further processing.

To label the dECM bladder scaffolds with $MnPNH_2$ a protocol using a bio-inspired adhesive, polydopamine (PDA), discussed in Chapter 4 was used and modified[386]. The scaffolds were first immersed in either PBS (1×; pH 7.4) or Tris-HCl (10 mM; pH 9.6) before addition of dopamine hydrochloride (0, 0.1, 1.0, 5.0 mg/mL) for 24 h at room temperature with shaking. The scaffolds were then rinsed with PBS (1×; pH 7.4) and incubated with $MnPNH_2$ (0.4 mM or 4 mM) in PBS (1×; pH 7.4) at 37°C overnight with shaking. The scaffolds were then sufficiently washed with PBS (1×; pH 7.4) to remove any unbound chemicals before further experimental studies.

$MnPNH_2$-labeled dECM bladder gels were prepared by a modified protocol from the approach described above. Neutralized dECM solutions were diluted with PBS (1×; pH 7.4) to 10 or 1 mg/mL before mixing with $MnPNH_2$ (0.4 mM) in PBS (1×; pH 7.4) overnight at 4°C with stirring. The solutions were thermally cross-linked to form gels by incubation at 37°C for 12 h. The gels were then sufficiently washed with PBS (1×; pH 7.4) to remove any unbound chemicals before any characterization or experimental studies.

3.3.5 $MnPNH_2$ labeling of decellularized trachea and lungs

Tracheas were harvested from outbred Yorkshire male pigs (3 months old; 28-35 kg) involved in other projects at the University Health Network (Toronto, Canada). Tracheal collection was done soon after the animal was killed. All experiments were performed in accordance with the "Principles of Laboratory Animal Care" defined by the National Society for Medical Research and the "Guide for the Care of Laboratory Animals" issued by the National Institutes of Health. For decellularization, fresh tracheal samples were harvested and placed in Falcon tubes (50 mL) and subjected to 48 h in 1 % (w/v) SDS (in deionized H_2O) solution at 4ºC on rocking platforms at 60 rpm. The solution was changed after 24 h. After 48 h of decellularization, tracheal samples were washed thrice (15 min) in PBS to remove excess SDS and stored in PBS supplemented with 1 % (v/v) penicillin-streptomycin (Gibco, Gaithersburg, MD, USA) at 4ºC until experiment.

For decellularization of mouse lungs, heart-lung blocks were removed from male C57Bl/6 male mice (14-16 weeks; Jackson laboratories). Decellularization was done according to previously published protocols[397,398]. Briefly, the trachea and right ventricle were cannulated and the heart-lung block was stored in distilled water (dH_2O) at 4ºC for 1 h. The vasculature and airways were subsequently washed using dH_2O and stored in 0.1% Triton X-100 solution at 4ºC overnight. The block was then placed in 2% SDC solution at 4ºC for 24 h, in sodium chloride solution at room temperature and DNase (0.1 mg/mL, Sigma) solution at room temperature for an additional hour with dH_2O washes of vasculature and airways in between each step.

Before labeling with 0.2 mM $MnPNH_2$, all decellularized organs underwent serial solvent exchange with PBS (1×; pH 7.4). Different samples of trachea were prepared: control (no labeling), interior labeling, and complete labeling. To label only the interior of the trachea, $MnPNH_2$ in PBS (1×; pH 7.4) was loaded into the trachea, and the ends were sealed with rubber stoppers. The entire trachea was then immersed in additional PBS (1×; pH 7.4) solution to fully submerge the tissue. To label the entire tissue, the dECM organ (trachea or heart/lung block) was fully submerged in the $MnPNH_2$ solution. All samples (control, interior labelling and complete labelling) were then kept in an incubator overnight at 37°C with shaking. The labeled organs were then sufficiently washed with PBS (1×; pH 7.4) to remove any unbound chemicals before MRI or further testing.

3.3.6 In vitro, in vivo, and ex vivo MRI

In vitro experiments were conducted to optimize the dECM-labeling protocol for adequate sensitivity of detection on MRI. $MnPNH_2$-labeled scaffolds were prepared from porcine-derived bladder dECM and loaded into polystyrene phantoms and immersed in either DMEMx1 or PBSx1 at physiological pH and salt concentrations. Imaging was performed on a clinical 3T clinical MRI scanner (Achieva 3.0T TX, Philips Medical Systems, Best, The Netherlands) using a 32-channel transmit/receive head coil. T_1-weighted images were acquired using a 2D inversion recovery (IR) turbo spin-echo (TSE) sequence: repetition time (TR) = 3000 ms, echo time (TE) = 18.4 ms, 120 mm field-of-view (FOV), 3 mm slice thickness, 0.5 mm × 0.5 mm in-plane resolution, turbo factor = 4, and number of signal averages (NSA) = 1. T_2-weighted images were acquired using a 2D TSE sequence: TR = 3000 ms, TE = 80 ms, NSA = 2, echo train length = 8. Quantitative T_1 mapping was performed by repeating the IR-TSE sequence for inversion times

(TI) = [50, 100, 250, 500, 750, 1000, 1250, 1500, 2000, 2500] ms. Quantitative T_2 mapping was performed using a multi-echo SE sequence: 32 echoes with TE spacing = 7.63 ms, TR = 2000 ms. MRI data were transferred to an independent workstation for quantitative data analysis using in-house software developed in Matlab (v.9.3) (MathWorks, Natick, MA, USA). Calculations of T_1 and T_2 times were performed on a pixel-by-pixel basis in each scaffold as described previously[399,400].

In vivo experiments were performed to validate sensitivity of dECM detection on MRI. Live animal experiments were approved by the institutional animal care committee (protocol #36668), and all procedures were conducted in accordance with the national Council on Animal Care. An adult female Sprague Dawley rat (Charles River Laboratories International, Inc., Wilmington, MA, USA) was anesthetized on 3% isoflurane in 100% oxygen delivered at a flow rate of 2 L/min. Injections of 1.5 mL porcine dECM bladder gels 10 mg/mL labeled with $MnPNH_2$ (0 0.2 mM) were administered on the dorsum by means of a 21-gauge needle. The following day and the day after, MRI was performed on the 3.0T scanner with an 8-channel receive-only wrist coil. The rat was anesthetized on 3% isoflurane (with 2 L/min flow rate of 100% oxygen at 50 psi).

Once anesthetized, it was transferred to the wrist coil and maintained on 2% isoflurane. The rat was placed prone, head first into the scanner and kept warm on a water-blanket heated by Heat Therapy Pump (HTP-1500, Andriotmedical) set at 41°C. To visualize anatomic details, sagittal high-resolution T_1-weighted and T_2-weighted spin echo images were acquired. T_1-weighted images were acquired using a 2D SE sequence with fat suppression: TR = 2173 ms, TE = 13.6 ms, 130 mm FOV, 3-mm slice thickness, 0.6 mm × 0.6 mm in-plane resolution, and NSA = 3. T_2-weighted images were acquired using a 2D turbo SE sequence: TR = 4000 ms, TE = 75 ms, NSA = 2, and similar resolutions as for T_1-weighted imaging.

Ex vivo imaging on decellularized porcine trachea and murine heart/lungs was performed on the same 3.0T scanner using an 8-channel receive-only wrist coil. T_1-weighted images were acquired using a 3D fast field echo sequence: TR = 11.2 ms, TE = 5.84 ms, flip angle = 20°, 30 mm FOV, 1-mm slice thickness, 0.25 mm × 0.25 mm in-plane resolution, and NSA = 3.

3.3.6 Toxicity analysis

To investigate the potential toxicity of $MnPNH_2$-labeling to cells, both qualitative and quantitative assays were performed. Gels derived from dECM bladder were prepared as stated earlier in 24-well plates. HUVECs were chosen as an ideal human cell type for testing due to their extensive usage in tissue engineering applications with decellularized scaffolds to promote angiogenesis and tissue regeneration[401–403]. HUVECs were seeded at a density of 40,000 cells per well and cultured for 72 h. For live-dead staining and microscopy, cells were incubated with 2 μM Calcein AM live stain and 4 μM EthD-1 dead stain in PBS (1×; pH 7.4) with calcium and magnesium for 45 min at 37°C. Imaging was performed on a Leica DMi8 inverted epifluorescence microscope using a green fluorescent protein (GFP) and Texas Red (TXR) filter cube to visualize the live and dead stain, respectively.

Quantitative assays for cell metabolism and proliferation were also conducted. Scaffolds were prepared in 96-well plates, and HUVECs were seeded at 4000 cells per well and cultured for 72 h. To assess metabolic activity of the seeded cells, culture medium was removed from each well and replaced with fresh media containing WST-1 reagent (1:10 dilution) for 1 h before measuring absorbance at 450 nm with a PerkinElmer Envision 2104 Multilabel Plate Reader (MA, USA). To assess live cell proliferation, CyQuant Direct Nucleic acid live stain and background suppressor dead stain (1:5 ratio) was prepared in cell culture medium and incubated with each well for 2 h before measuring fluorescence with a PerkinElmer Envision 2104 Plate Reader equipped with a FITC filter set.

3.3.8 Transmission electron microscopy

Transmission electron microscopy (TEM) was performed to determine how the $MnPNH_2$ agent was incorporated and distributed in the dECM scaffold network. Pepsin solubilized dECM bladder was deposited onto formvar/carbon supported grids G200H-Ni (Electron Microscopy Sciences, Hatfield, PA, USA) and neutralized with ammonia vapor. After air drying, the grids were fixed with glutaraldehyde and washed with distilled water before staining. Grids with and without dECM fibers were then incubated with $MnPNH_2$ (0.2 and 0.4 mM) in PBS (1×; pH 7.4) at 37°C overnight. After extensive washing with PBS (1×; pH 7.4), all grids were imaged on an FEI Tecnai 20 TEM (FEI Company, OR, USA) at 100 kV.

3.3.9 $MnPNH_2$ binding and retention in dECM scaffolds

Binding of $MnPNH_2$ to dECM, was determined as follows. Pepsin solubilized dECM bladder was neutralized with sodium bicarbonate (0.8 M) and diluted to 1 mg/mL with PBS (1×; pH 7.4) at 4°C. The solution was then incubated at 37°C for 24 h to form gels. Various concentrations of $MnPNH_2$ (0, 2, 5, 10, 20, 50, 70, 100, and 200 μM) were then incubated in vials with or without dECM bladder gels for 4 h with shaking. The concentration of unbound $MnPNH_2$ was measured on UV absorbance at 469 nm.

The retention and stability of $MnPNH_2$ in dECM scaffolds was assessed in labeled decellularized murine lungs. The decellularized murine lungs were labelled with 0.2 mM $MnPNH_2$ as described previously. Over a span of 30 days after labeling, the PBS buffer in which the tissue was immersed was removed daily for measurement of free $MnPNH_2$ with an Agilent 8453 UV-visible spectroscopy system. Fresh buffer was replenished daily. The lungs were kept at 37°C on a shaker inside the incubator for the entire duration of the experiment.

3.3.10 Histology

Native and decellularized tissues and organs were fixed with 4% PFA, embedded in paraffin, and then prepared as 5-μm sections before mounting on glass slides. After deparaffination, sections were stained with hematoxylin and eosin (H&E), imaged by an Aperio slide scanner and then assessed for the presence of cell nuclei (Supporting Information Appendix A-Figure **A1**)

3.3.11 Statistical analysis

A two-way analysis of variance (ANOVA) was used to determine significant changes in the T_1 and T_2 relaxation times, with the variables being $MnPNH_2$ concentrations and the dose of dopamine. A one-way ANOVA was used to determine significant changes in the metabolic and proliferation assay measurements, with the variable being $MnPNH_2$ concentration. A Tukey-Kramer test was used for post hoc analysis. Significance is reported at a *P*-value of 5%.

3.4 Results

Figure **3.1** depicts the different tissue types investigated in this study for labeling with $MnPNH_2$. The porphyrin contrast agent imparts a distinctive greenish color, which provides a convenient visual signature to labeled tissues.

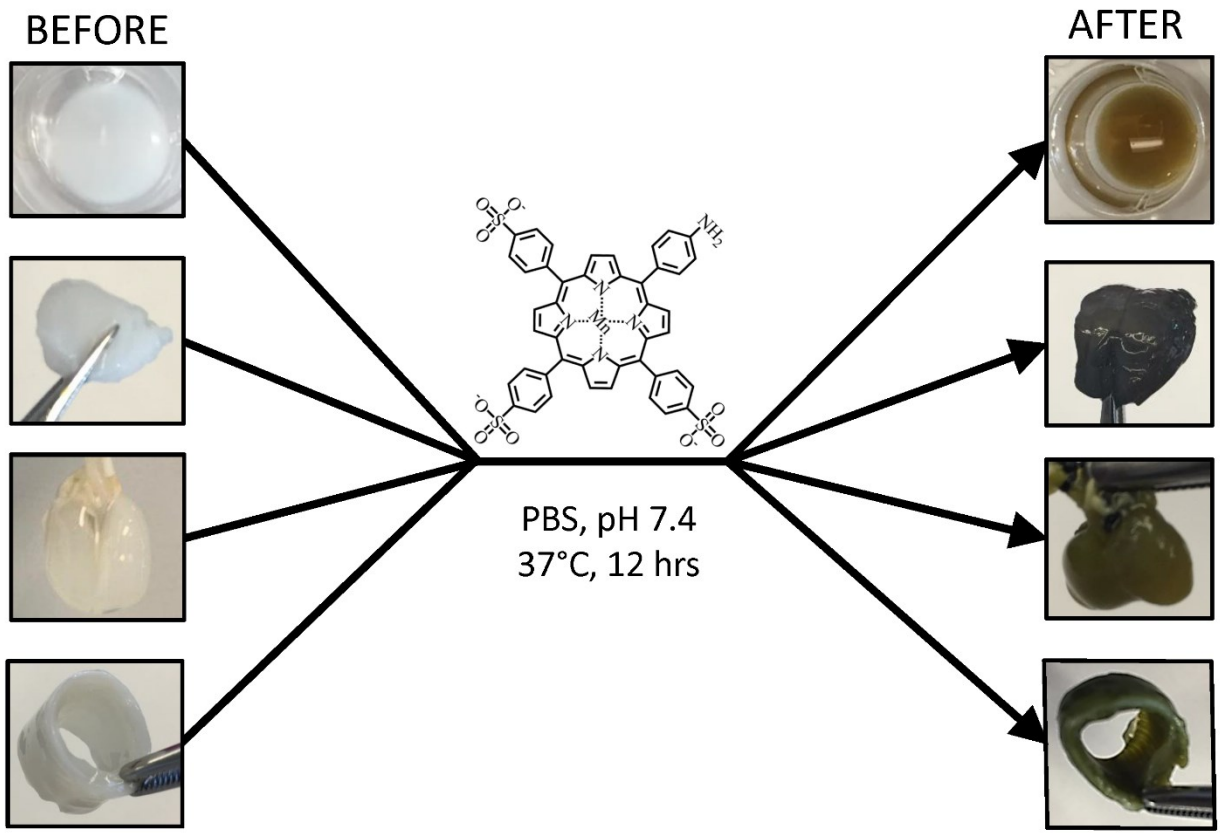

Figure 3.1: dECM scaffold labeling scheme. The protocol for labeling dECM scaffolds with $MnPNH_2$ is illustrated for the 4 different tissue types chosen for investigation in this study (top to bottom): (1) porcine bladder dECM gel, (2) porcine bladder dECM scaffold, (3) murine whole lungs, and (4) porcine trachea. Note the characteristic greenish hue imparted by the porphyrin.

In vitro results from optimizing the labeling protocol are shown in Figure **3.2** and Supporting Information-Appendix A Figure **A2**. Both T_1-weighted images (Figure **3.2**) and T_2-weighted images (Supporting Information-Appendix A Figure **A2**) are illustrated for bladder dECM scaffolds that were prepared with increasing levels of $MnPNH_2$ (different columns) and PDA (different rows). Corresponding T_1 maps and T_2 maps are included to show absolute changes in MR relaxation times. A significant decrease in both T_1 and T_2 was observed with higher

$MnPNH_2$ doses ($P < 0.05$), but the incorporation of PDA had no significant effect. Gels prepared from bladder dECM and labeled with $MnPNH_2$ as described above exhibited similar reductions in relaxation times.

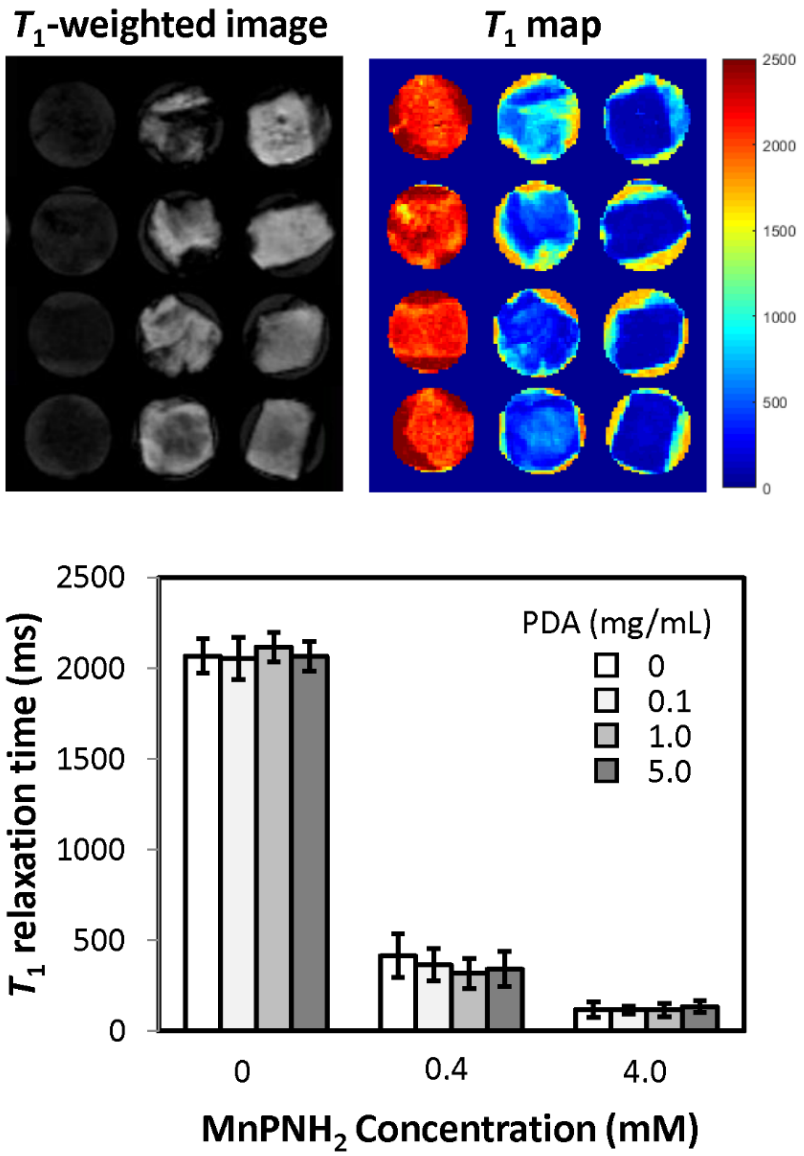

Figure 3.2: Optimization of labeling dECM scaffolds. Porcine bladder dECM scaffolds were labeled with varying concentrations of $MnPNH_2$ (0, 0.4, and 4.0 mM, in images from left to right within each row) and PDA (0, 0.1, 1.0, and 5.0 mg/mL, in images from top to bottom within each column). Representative T_1-weighted inversion recovery turbo spin-echo image (top left) and corresponding T_1 map (top right), and mean changes in T_1 (bottom center). A significant change in T_1 is observed only for different $MnPNH_2$ concentrations ($P < 0.05$) but not for PDA. Shown are mean values and SDs.

Sensitivity of in vivo scaffold detection on MRI is shown in Figure **3.3**. Yellow arrows indicate the location of the rat dorsum where dECM bladder gels labeled with 0.2 mM of $MnPNH_2$ were injected and gelled in situ. Three consecutive imaging slices are included to highlight the intrinsic capability of MRI to track the shape of the dECM at different slice locations both 1 day and 2 days post-injection. Note that a very large contrast enhancement was achieved, despite using a much lower dose of $MnPNH_2$ compared to the range tested in vitro.

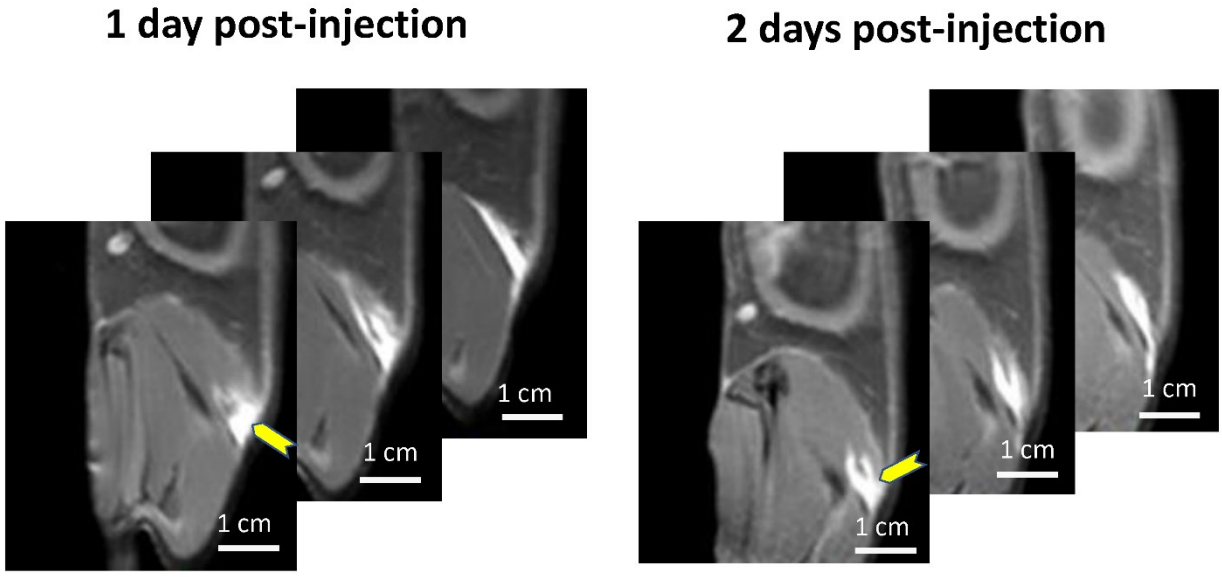

Figure 3.3: In vivo MRI of dECM gels in rats. Fat-saturated T_1-weighted spin-echo images of rats injected with porcine bladder dECM gel labeled with 0.2 mM $MnPNH_2$ only. Yellow arrow indicates site on rat dorsum where dECM was injected.

Figures **3.4** and **3.5** illustrate whole tissue and organs that were decellularized and labeled with the proposed approach. Photographs and MR images of the labeled decellularized porcine trachea (Figure **3.4**) and labeled decellularized murine lungs (Figure **3.5**) are shown. On the trachea, labeling was investigated for the entire organ and for specific tissue regions only. When only the interior was labeled, MRI clearly demarcated the boundary between the inner surface and the deeper layers. Labeling the whole trachea was also feasible, as was labeling the entire lungs of a mouse. Notice in Figure **3.5A** that, because the unlabeled lungs were immersed in solution in a bioreactor, they displayed iso-intensity and not the typical susceptibility-induced signal void associated with air/tissue interfaces in the lungs. Consecutive imaging slices through the intact lungs revealed spatially resolved details that could be depicted because of full penetration of the labeling agent into the organ.

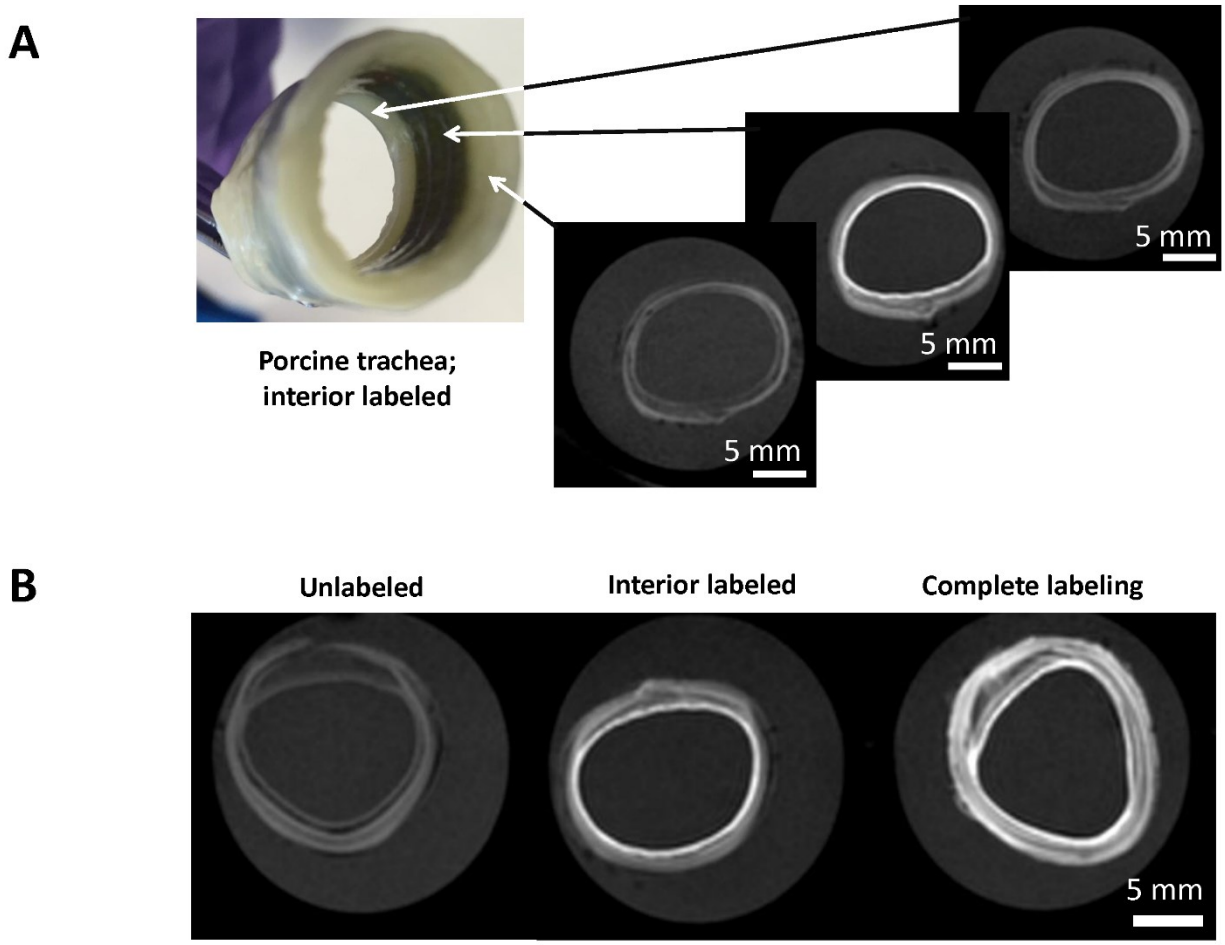

Figure 3.4: Ex vivo MRI of the labeled trachea. **A**, The decellularized porcine trachea takes on a greenish hue where labeling with $MnPNH_2$ occurs. **B**, MRI clearly demarcates the labeled regions, whether it is the interior of the trachea only or the entire organ

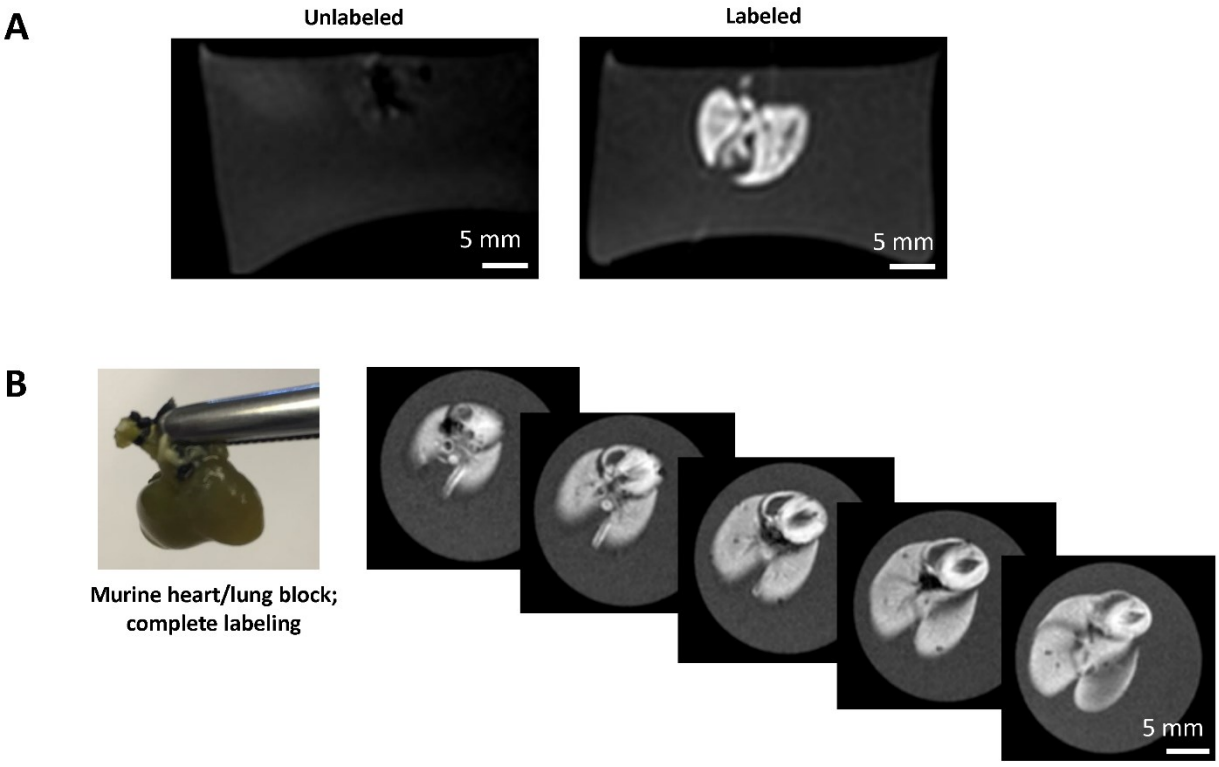

Figure 3.5: Ex vivo MRI of the labeled lungs. The decellularized murine lungs completely take on a greenish hue after labeling with $MnPNH_2$. **A**, The heart/lung block were immersed in solution in a bioreactor when MRI was performed and were visible only when labeled. **B**, High-resolution MRI reveals fine anatomical structures, which indicate thorough penetration of the labeling agent into the decellularized organ.

The cytotoxicity of labeled dECM bladder scaffolds is assessed in Figure **3.6**. Fluorescent live/dead images were taken at 24 and 72 h after culturing HUVECs on $MnPNH_2$ scaffolds labeled at varying concentrations up to 0.4 mM; no deleterious effects on cell viability were seen visually at the tested concentrations. Quantitative assays for metabolic and proliferative activity also suggest that $MnPNH_2$-labeled scaffolds are biocompatible with the conditions used in this study.

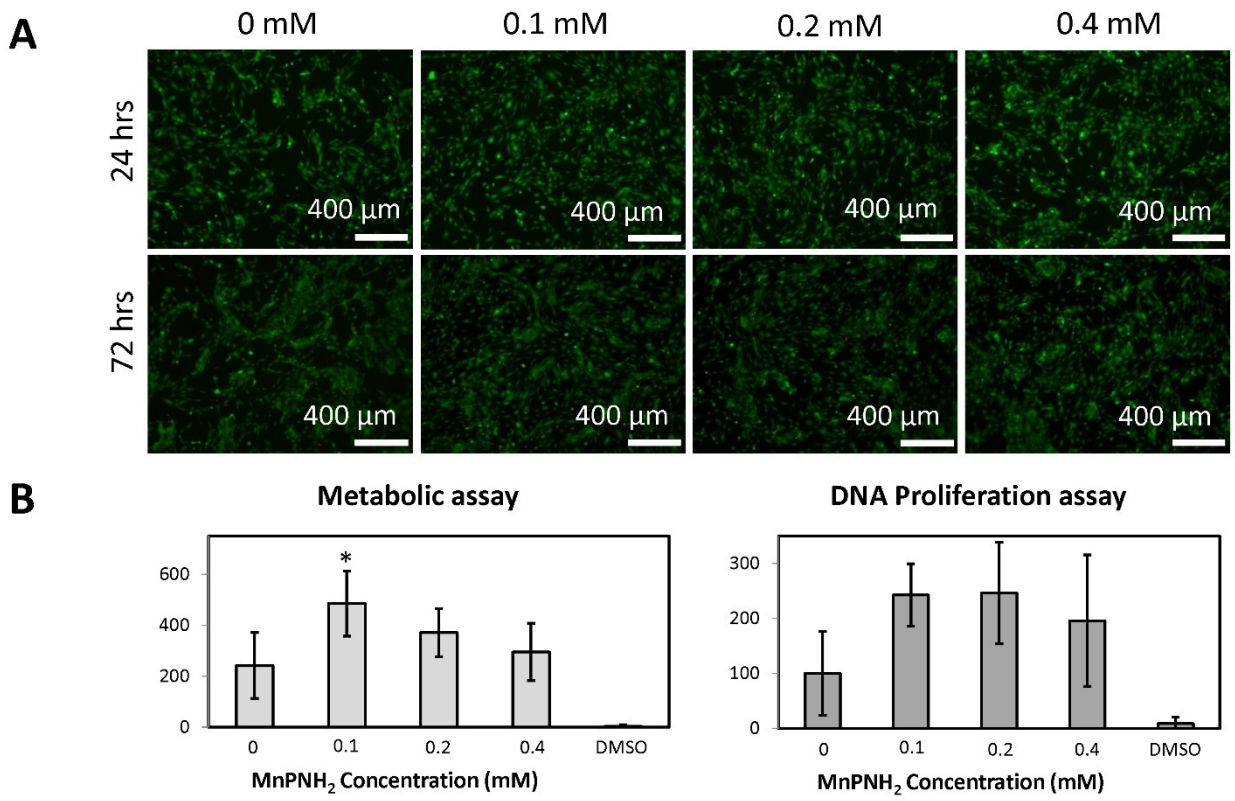

Figure 3.6: Biocompatibility of labeled dECM scaffold. **A**, Live (green)/dead (red) fluorescent assay on HUVECs reveals minimal cell death from growing cells on dECM scaffolds labeled with $MnPNH_2$ up to 0.4 mM. **B**, Metabolic (WST-1) and DNA proliferation (CyQuant Direct Nuclei acid stain) assays further suggest the biocompatibility of the labeled dECM scaffolds. Dimethyl sulfoxide (DMSO) controls were treated with 5% DMSO. A significantly higher metabolism was observed only for HUVECs grown on dECM labeled with 0.1 mM $MnPNH_2$ ($P < 0.05$)

How the labeling agent $MnPNH_2$ is incorporated in the dECM bladder scaffold is illustrated on TEM in Figure **3.7**. The labeling agent is seen to adhere to the fibers in dECM deposited on carbon grids and aggregate as dark clumps of varying sizes (highlighted by red arrows). The blank grid served as a positive control and verified that no labeling agent remained after extensive washing. Binding studies on dECM were also carried out and confirmed the incorporation of $MnPNH_2$ into dECM gels, with a binding efficiency of approximately 50% and no evidence of saturation up to concentrations of 0.2 mM (Supporting Information-Appendix A Figure **A3**). The stability and retention of $MnPNH_2$ in labeled dECM lungs was also assessed. Measurements of free $MnPNH_2$ from labeled whole lung dECM revealed minimal $MnPNH_2$ release, with daily changes under 1% by the fourth day and less than 20% total over 30 days (Figure **3.8**).

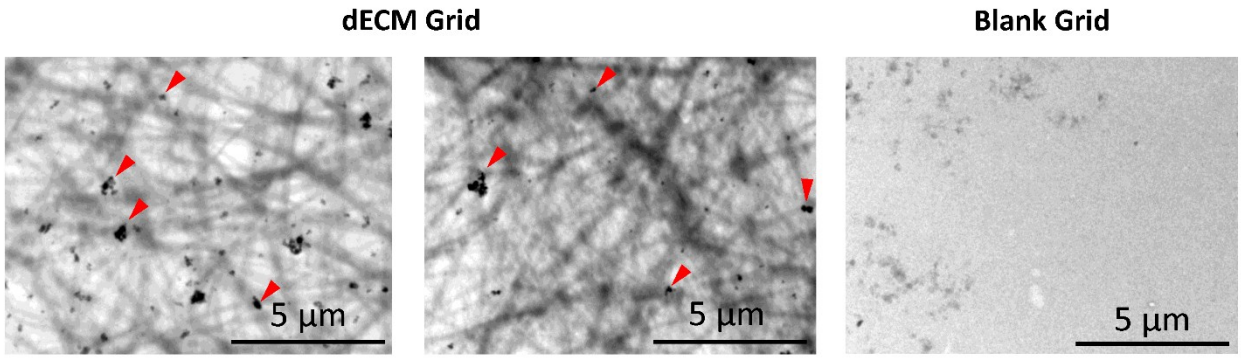

Figure 3.7: TEM of labeled dECM scaffold. Carbon grids with dECM scaffolds (left and center) and without (right) were labeled with $MnPNH_2$ (0.4, 0.2, and 0.2 mM, respectively). The labeling agent is seen to adhere to the dECM fibers and aggregate as dark clumps of varying sizes (red arrows). Adherence of agent to the blank grid was absent, as expected.

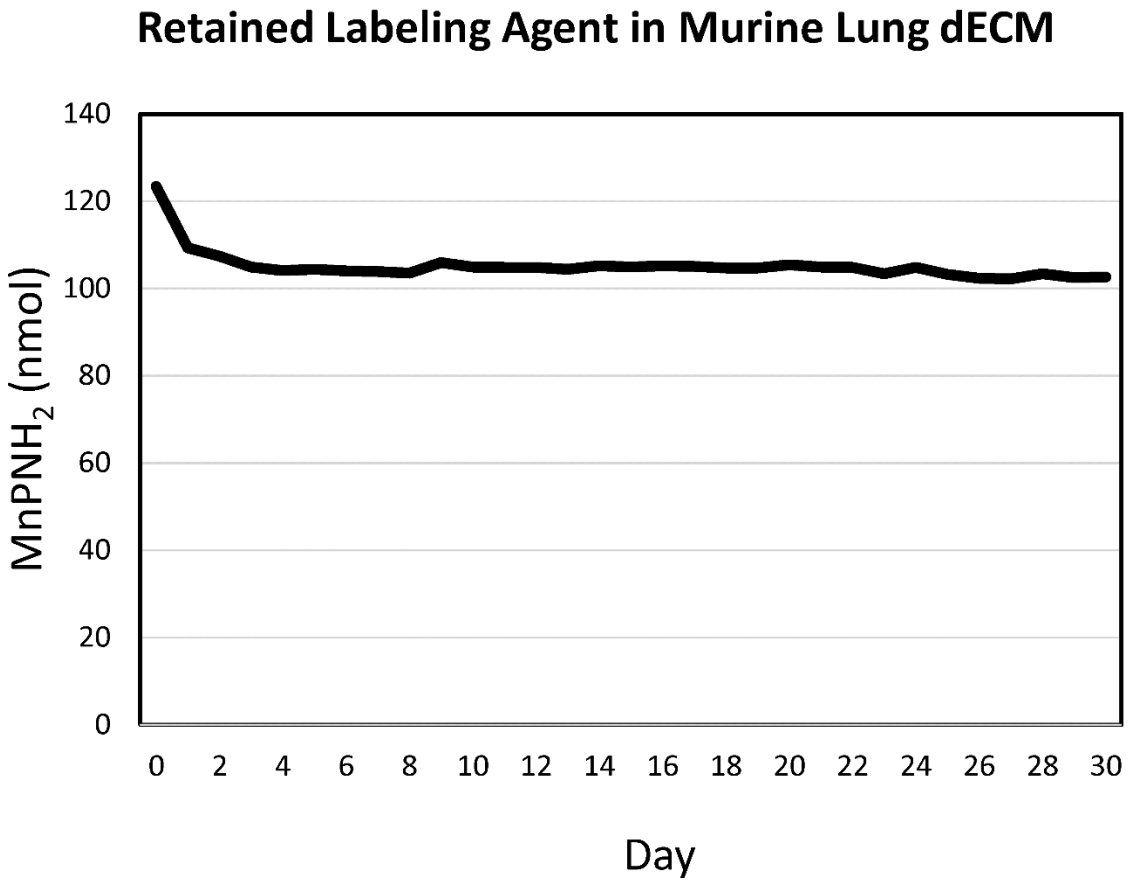

Figure 3.8: Stability and retention of contrast agent in labeled lung dECM. Amount of $MnPNH_2$ retained in a murine lung dECM labeled at 0.2 mM is shown over a time span of 30 days post-labeling. Less of 20% of the agent incorporated initially is released over the 1-month interval, with the majority of the release occurring in the first 3 days.

3.5 Discussion

Because dECM scaffolds and gels were ushered into the field of tissue engineering over 2 decades ago, investigators have steadily applied the concept of using decellularized natural matrices to grow tissues and organs as a substitute for donor transplant. The realization of supplanting donor organs with dECM-derived materials remains a distant goal, but the current revival of interest and earnest research efforts into engineering a wide variety of tissues using dECM, including vital organs such as the heart, lungs, and liver, is testament to the promise of this regeneration paradigm. As with any scaffold material for regeneration, however, one central difficulty to optimizing dECM structure and composition is our limited ability to identify the dECM scaffold in vivo given its similarity to native tissue. A method to image the implanted dECM noninvasively in vivo would be desirable for identification and monitoring. In this work, we report a facile method for labeling dECM scaffolds and gels and demonstrate its efficacy for several tissue types and organs, including bladder, trachea, and whole lungs.

Our optimization study demonstrated the reproducibility of achieving substantial contrast enhancement of labeled dECM scaffolds, with T_1 reductions of almost 10-fold at a $MnPNH_2$ labeling concentration of 0.4 mM. In vivo and ex vivo imaging confirmed that, even at half the dose, 0.2 mM, very bright contrast was achieved, suggesting that adequate signal-to-noise can be easily attained if further dose reduction were desired. Another important result is the ability of $MnPNH_2$ to permeate throughout thick 3D tissues and, thereby, uniformly label whole dECM organs and not merely superficial layers. This advantage is particularly important for whole organs that have no intrinsic contrast, such as the lungs, and for distinguishing 3D tissues intended to replace part of a diseased organ, as such the heart.

In addition to identification, we now are also equipped to potentially track dECM degradation in vivo, a parameter one cannot assess otherwise using cell-tracking techniques. Although dECM is not required to degrade completely, unlike synthetic materials, it is nonetheless important to understand the dynamics of degradation as new tissue growth and matrix deposition occur and how these dynamics differ between successful and failed regeneration. Lastly, as seen in Figure **3.6**, cultured mammalian cells directly exposed to the labeled dECM for 3 days exhibited no adverse changes in proliferation or metabolic activity with respect to control dECM, suggesting

non-cytotoxicity of the contrast agent and labeled material at the tested concentrations. Biocompatibility is particularly critical in scaffold labeling, because the labeling agent is intended to linger for a substantial portion of the scaffold's lifetime.

It is instructive to compare the results obtained in this study and those from work on labeling pure collagen hydrogels demonstrated and discussed later in Chapter 4. Both dECM scaffolds and collagen gels underwent significant reductions in T_1 from labeling; however, PDA was found unnecessary for labeling dECM scaffolds in the current study. In fact, TRs were unaltered with the addition of PDA. One possible explanation is that the organized and denser matrix of dECM provided an anchor for $MnPNH_2$ and removed the need for adhesives. Another possibility is that the utility of PDA for binding $MnPNH_2$ to the scaffold would be seen only at much lower concentrations of $MnPNH_2$ (less than the minimum concentration of 0.4 mM tested), where increased retention aided by an adhesive would rise above saturation and become significant. Aside from this notable difference, other observations were similar: excellent contrast enhancement in vivo and no cell toxicity.

The decellularized bladder, tracheal, and lung models used to exemplify our proposed labeling and monitoring approach were chosen because of their immediacy *and* relevance in the field of tissue engineering. Research centers around the world are investigating ways using dECM materials to regenerate the bladder[404], trachea[382,405], and lungs[406,407], amongst the many other tissue types not covered in this study. Because these efforts are largely in the infant stages of development, where optimal cell types, for example, have yet to be uncovered, the application of our labeling method to study regeneration in vivo would yield the greatest insight when the regeneration approach itself has matured further to a stage where new tissue growth is confirmed but how to optimize that growth needs to be answered.

One notable observation from this study is the manner in which $MnPNH_2$ appears to bind dECM. When dECM scaffolds were labeled with various concentrations of $MnPNH_2$, the binding efficiency remained constant at approximately 50%. If $MnPNH_2$ had bound a specific protein pocket or receptor, one would expect the binding efficiency to be very high initially, then saturate and drop drastically, producing a characteristic S-shape binding curve. The absence of such a phenomenon indicates lack of specificity of this agent. TEM of labeled dECM fibers confirmed

this nonspecific association, as electron-dense $MnPNH_2$ appeared to aggregate nonspecifically on dECM fibers rather than intercalate and selectively bind protein pockets. This nonspecific behaviour is likely attributed to the amphiphilic characteristics of the porphyrin core, which has been shown to associate with ECM-rich tumours in vivo, and the anionic sulfonate pendant groups, which have been shown to strongly bind to ECM proteins such as collagen by means of electrostatic and hydrogen bond interactions[141,144,149,408].

With the assumption of nonspecific binding, the observed retention of contrast in the decellularized whole murine lungs over 30 days is remarkable. Although the retention experiment was not performed most realistically in the in vivo environment, we did maintain the tissues at physiological conditions and provided continuous 24/7 shaking to mechanically dislodge loosely bound $MnPNH_2$. With less than 20% loss of initial contrast concentration over a span of 30 days, the decrease in contrast enhancement on MRI would be minimal.

Lastly, while the fluorescence data, metabolic assay, and DNA proliferation assay all indicated the absence of cell toxicity up to a labeling concentration of 0.4 mM $MnPNH_2$, it is interesting to note a significantly higher cell metabolism at 0.1 mM compared with no labeling. This result may be attributed to potentially a higher number of attached cells due to the presence of $MnPNH_2$. In addition to the absence of toxic effects, $MnPNH_2$ might improve cell attachment, thereby increasing absolute cell numbers and, consequently, measures of metabolism and proliferation. The mechanism behind enhanced cell attachment is unknown and needs to be explored in future studies.

3.6 Conclusion

We have reported on a new method and contrast agent to label and image dECM scaffolds on MRI. Excellent sensitivity was achieved both in vitro and in vivo at 3T using labeling concentrations that had no negative effects on cell viability, proliferation, or metabolism. Examples using porcine trachea and bladder and whole murine lungs demonstrated the efficacy of the proposed approach for uniformly labeling thick 3D tissues and organs and visualizing the labeled scaffolds with high sensitivity and exquisite detail. Binding and retention studies indicated nonspecific association but

extraordinarily long retention, which lays the foundation for long-term in vivo monitoring in future dECM regeneration investigations.

3.7 Contributions

H.-L.M. Cheng contributed to: overall direction of study, design of MR acquisition protocol and data acquisition protocol, *in vitro* and *in vivo* MRI, development of software for analyzing quantitative MRI data, analysis and interpretation of data, writing the manuscript, final approval of the manuscript. D.A.S. contributed to: conceptualization and design of study, synthesis, characterization and quantification of $MnPNH_2$ harvest of porcine bladder, decellularization of porcine bladder and histology, preparation of porcine dECM solutions and gels, labelling of dECM scaffolds stability and retention studies, cell biocompatibility assays, assistance with transmission electron microscopy, in vitro, ex vivo and in vivo MRI, analysis and interpretation of data, writing and final approval of manuscript. M. A. contributed to: harvest and supply of murine lung/heart blocks, decellularization of murine lung/heart blocks and histology. F. G. A. contributed to: harvest and supply of porcine trachea, decellularization of porcine trachea and histology. G. K contributed to: writing of manuscript, final approval of manuscript. T.K.W contributed to: supply of dECM scaffolds, discussion of appropriate dECM scaffolds and final approval of manuscript

Chapter 4 One-Step Labeling of Collagen Hydrogels with Polydopamine and Manganese Porphyrin for Non-Invasive Scaffold Tracking on Magnetic Resonance Imaging

This work has been published in *Macromolecular Bioscience* Volume 19, Issue 4 (2019) and has been reproduced with permission from the respective publishers.[386] Article listed below:

Szulc DA, Cheng HM. One-Step Labeling of Collagen Hydrogels with Polydopamine and Manganese Porphyrin for Non-Invasive Scaffold Tracking on Magnetic Resonance Imaging. *Macromol Biosci*. 2019;19(4):e1800330. doi:10.1002/mabi.201800330

4.1 Abstract

Biomaterial scaffolds are the cornerstone to supporting 3D tissue growth. Optimized scaffold design is critical to successful regeneration, and this optimization requires accurate knowledge of the scaffold's interaction with living tissue in the dynamic in vivo milieu. Unfortunately, non-invasive methods that can probe scaffolds in the intact living subject are largely underexplored, with imaging-based assessment relying on either imaging cells seeded on the scaffold or imaging scaffolds that have been chemically altered. In this work, the authors develop a broadly applicable magnetic resonance imaging (MRI) method to image scaffolds *directly*. A positive-contrast "bright" manganese porphyrin (MnP) agent for labeling scaffolds is used to achieve high sensitivity and specificity, and polydopamine, a biologically derived universal adhesive, is employed for adhering the MnP. The technique was optimized in vitro on a prototypic collagen gel, and in vivo assessment was performed in rats. The results demonstrate superior in vivo scaffold visualization and the potential for quantitative tracking of degradation over time. Designed with ease of synthesis in mind and general applicability for the continuing expansion of available biomaterials, the proposed method will allow tissue engineers to assess and fine-tune the in vivo behavior of their scaffolds for optimal regeneration.

4.2 Introduction

Scaffolds are an essential ingredient in many tissue engineering strategies. Whether they are synthetic or derived from natural materials, scaffolds help support tissue formation in three dimensions and are pivotal to growing thick tissue. They allow cells to penetrate, attach, and migrate; they retain biochemical factors conducive to tissue growth; and they biodegrade over time at a rate ideally matched to that of new extracellular matrix production as new tissue forms. One of the major challenges facing scaffold development, however, is proper optimization for desired in vivo function. Accurate characterization of in vivo behavior and especially kinetics cannot be predicated on in vitro degradation studies, since the transition from an in vitro to an in vivo setting often results in vast changes in a material's structure, properties, and function. Thus, accurate in vivo imaging techniques for scaffold monitoring are crucial for optimizing tissue-engineered scaffolds in the intended biological environment. However, imaging applications to date have focused largely on implants with an innate, stark contrast difference relative to native tissue. For natural scaffolds that are more difficult to distinguish due to similar contrast levels, scaffold monitoring has been tackled indirectly. For example, one method has been to image the cells that are seeded onto a scaffold[409,410], but this approach provides no information on the evolving scaffold structure and is inappropriate for acellular matrix-based regeneration methods. The ability to image the implanted scaffold *directly* in vivo remains largely unexplored, but would yield critical information on degradation, host-tissue interactions, and restoration of tissue function.

Non-invasive imaging technologies such as magnetic resonance imaging (MRI) hold significant potential for scaffold monitoring in tissue engineering. MRI provides fine spatial resolution, deep tissue penetration, and superior soft-tissue contrast. To enable direct monitoring of scaffolds in vivo, we adopt a different approach using MRI. We do not image labeled cells in the scaffold or rely on intrinsic contrast differences from native tissue arising from biochemical and structural differences. Instead, we directly label the scaffold with a “bright” MRI contrast agent to provide scaffold identification regardless of its biochemical makeup. Unlike the handful of existing reports that attempt to track scaffolds directly using iron oxide-based “dark” imaging[88,98,387], we adopt a positive-contrast “bright” method. Positive-contrast imaging offers the benefit of greater specificity in where the signal comes from and the potential to quantify contrast agent concentration, and therefore scaffold content, in absolute terms. This potential for quantification

is a must if we need to monitor degradation in meaningful units. To achieve strong "bright" scaffold imaging, we utilize manganese (Mn), an endogenous MRI-active metal that is significantly less toxic than gadolinium (Gd) in free ionic form. The Mn ion is coordinated in a porphyrin ring to produce a manganese porphyrin (MnP) structure that yields excellent contrast enhancement[388]. The porphyrin ring binds the Mn ion with high thermodynamic and kinetic stability, thus conferring safety. Importantly, the ring also allows facile chemical functionalization[112] to enable labeling a wide variety of scaffold materials. To create a flexible labeling strategy, we sought to develop a simple labeling method that did not rely on the chemical make-up of the scaffold. For this, we turned to polydopamine (PDA), a bio-inspired polymer that has been found to coat various surfaces ranging vastly in material properties and composition[411]. The versatility, facile synthesis, and biocompatibility of PDA made it an ideal candidate for use in a universal labeling method[412]. We report here the first approach using MRI and positive-contrast MnP to directly label scaffolds via a universal adhesive for non-invasive scaffold monitoring.

4.3 Materials and Methods

4.3.1 Materials

N,*N*-diisopropylethylamine (DIPEA), manganese chloride ($MnCl_2$), dimethylformamide (DMF), dimethyl sulfoxide (DMSO), concentrated sulfuric acid (H_2SO_4), 4-(2-hydroxyethyl)piperazine-1-ethanesulfonic acid (HEPES), Dulbecco's modified eagle's medium – high glucose (DMEM), sodium bicarbonate ($NaHCO_3$), hydrochloride (HCl), dopamine hydrochloride, collagenase from clostridium histolyticum (Type 1), ethtlenediaminetetraacetic acid (EDTA), phosphate buffered saline (PBS), Proliferation Reagent WST-1, and manganese standard for ICP were purchased from Sigma Aldrich (Steinheim, Germany). Nutragen (Bovine Collagen Solution, Type 1, 6 mg mL^{-1}), PureCol (Bovine Collagen Solution, Type 1, 3 mg mL^{-1}), and FibriCol (Bovine Collagen Solution, Type 1, 10 mg mL^{-1}) were purchased from Cedarlane Labs (Ontario, Canada). CyQuant Direct Cell Proliferation Assay C35011 was purchased from Thermo Fisher Scientific (MA, USA). Calceinacetoxymethyl (Calcein AM) and ethidium homodimer-1 (EthD-1) were purchased from Invitrogen (CA, USA). Primary human umbilical vein endothelial cells, single donor, in EGM-2 from Lonza (Basel, Switzerland). VascuLife VEGF Endothelial Medium from Lifeline Cell

Technologies (MD, USA). Pretreated regenerated cellulose dialysis tubing (MWCO: 1 kD) was purchased from Spectrum Labs (OH, USA). Ion-exchange resin (amberlite IR120, H form) was purchased from ACROS Organics. 5-(4-Aminophenyl)-10,15,20-(triphenyl)porphyrin was purchased from PorphyChem (Dijon, France). All chemicals were of appropriate analytical grade and were used without further purification.

4.3.2 Synthesis of MnPNH2

Manganese 5-(4-aminophenyl)-10,15,20-(tri-4-sulfonatophenyl)porphyrin trisodium chloride ($MnPNH_2$) was synthesized following the protocol described in section 3.3.2.

4.3.3 Characterization of Apo-PNH_2 and $MnPNH_2$

Apo-PNH_2 and $MnPNH_2$ identity and purity was determined by UV–visible spectra, ^1H NMR, HPLC, FAAS, and mass spectroscopy. UV–visible spectra were recorded on an Agilent 8453 UV–visible spectroscopy system. Absorption spectra of Apo-PNH_2 and $MnPNH_2$ were measured in HEPES buffer at 25 °C, λ_{max} = 415 nm and λ_{max} = 469 nm, ε = 93 552 $M^{-1}cm^{-1}$, respectively (Figure **B2**, Supporting Information-Appendix B). ^1H NMR spectra were recorded on a Bruker US 500 MHz system (Figure **B1**, Supporting Information-Appendix B). HPLCspectra were recorded using a PerkinElmer Series 200 system with UV/Vis detectors recording at 469 nm and using an acetonitrile and 10 mM ammonium acetate (NH_4OAc) gradient mix. Elution occurred at 2.20 min with 99.86% purity (Figure **B3**, Supporting Information-Appendix B). A Supelco Supercosil LC-18 column with dimensions 25 cm × 4.6 mm and 5 um beads was used. FAAS were recorded on a PerkinElmer AAnalyst 100 system with a Manganese Lumina Hollow Cathode Lamp. The Mn concentration determined by UV was compared to Mn concentration determined by FAAS to confirm that all excess Mn was removed. Mass spectroscopy was conducted on $MnPNH_2$ with an Agilent 6538 Q-TOF system in ESI MS Negative mode. ESI MS found m/z = 459.5138 [M^+], calculated for $C_{44}H_{26}MnN_5O_9S_3^{-2}$, m/z = 459.5142 (Figure **B4**, Supporting Information-Appendix B).

4.3.4 Synthesis of $MnPNH_2$ Labeled Collagen Scaffolds

Acid purified bovine type 1 collagen (Cedarlane, Canada) at concentrations 3, 6, or 10 mg mL^{-1} were mixed with DMEM (containing glucose and phenol red) and neutralized with sodium bicarbonate at 4 °C. This solution was then mixed either with $MnPNH_2$ only or $MnPNH_2$ and dopamine hydrochloride at different time points (0 or 24 h) and concentrations ($MnPNH_2$: 0, 0.1, 0.2 or 0.4 mM and dopamine hydrochloride: 0, 0.25, 0.5, or 2.5 mM). The solutions were then kept stirring at 4 °C for an additional 24 h. Afterward, the solutions were cross-linked to form gels by warming them up to room temperature for 1 h and then heating at physiological temperature 37 °C for 12 h. To remove any unbound chemicals, all scaffolds were then washed for 3 days in phosphate buffered saline at physiological pH. The buffer was exchanged every 3 h. Day 1 and day 3 of washing occurred at room temperature, while day 2 was conducted at the physiological temperature of 37 °C. After washing, gels were incubated in DMEMx1 for one day before any characterization or experimental studies.

4.3.5 Scanning Electron Microscopy

To assess changes in fiber morphology and density, scaffolds were flash frozen with liquid nitrogen and then freeze dried with a VirTis BenchTop Freeze Drier. The specimens were then sputter-coated with platinum and imaged using an environmental field emission scanning electron microscopy (Quanta FEG 250 ESEM, FEI Company, OR, USA) at 10 kV in a high-vacuum environment.

4.3.6 Magnetic Resonance Imaging

For in vitro MRI measurements, scaffolds were loaded into polystyrene phantoms and immersed in either DMEMx1 or PBSx1 at physiological pH and salt concentrations. MR relaxometry of the scaffolds was performed on a clinical 3.0-Tesla whole-body MR scanner (Achieva 3.0T TX, Philips Medical Systems, Best, the Netherlands) using a 32-channel transmit/receive head coil. High-resolution T_1-weighted images were acquired using a 2D spin-echo (SE) sequence: repetition time (TR) = 100 ms, echo time (TE) = 14.1 ms, 120 mm field-of-view (FOV), 3 mm slice thickness, 0.5 mm × 0.5 mm in-plane resolution, and number of signal averages (NSA) = 8.

High-resolution T_2-weighted images were acquired using a 2D turbo spin-echo sequence: TR = 3000 ms, TE = 80 ms, NSA = 2, echo train length = 8.

Quantitative T_1 relaxation times were measured using a 2D inversion-recovery TSE sequence: inversion times (TI) = [50, 100, 250, 500, 750, 1000, 1250, 1500, 2000, 2500] ms, TR = 3000 ms, TE = 18.5 ms, TSE factor = 4, and the same voxel resolution as above. Quantitative T_2 relaxation times were measured using a multi-echo SE sequence: 32 echoes with TE spacing = 7.63 ms, TR = 2000 ms.

MRI data were transferred to an independent workstation for quantitative data analysis using in-house software developed in Matlab (v.8.3) (MathWorks, Natick, MA). Calculations of T_1 and T_2 times were performed on a pixel-by-pixel basis in each scaffold as described previously[399,400]. Relaxation times were then averaged over all pixels in each scaffold and reported as mean values and standard deviations.

4.3.7 Collagenase Assay and Characterization

Collagen scaffolds with and without $MnPNH_2$ and dopamine hydrochloride were prepared as before and immersed in PBSx1 (pH 7.4) with calcium and magnesium. Varying concentrations (4, 8, and 16 U mL^{-1}) of collagenase from clostridium histolyticum, Type 1 (Steinheim, Germany) were added to the scaffolds to induce enzymatic degradation. The scaffolds were incubated in these mixtures for 4 h at 37 °C. Afterward, enzymatic activity was quenched via the addition of 1 mL of 0.01 M EDTA. The scaffolds were then washed three times with 10× excess volume of PBSx1. The scaffolds were imaged by MRI using the sequences and analysis techniques described above. UV–vis analysis was carried out on the residual degradation solutions to determine the release profile of $MnPNH_2$ from the degraded scaffolds (Figure **B5**, Supporting Information-Appendix B). Scaffolds were prepared and assayed over three individual trials (n = 3).

4.3.8 Contraction Assay and Characterization

Collagen scaffolds with $MnPNH_2$ and dopamine hydrochloride were prepared as before but were solidified in triangular molds to aid with the identification of change in shape that may be due to degradation versus contraction. The gels were then immersed in PBSx1 (pH 7.4) without calcium

and magnesium before contraction in a solution of 0.1 M HCl. The scaffolds were incubated in this mixture for 4 h at 37 °C. Afterward, the scaffolds were then washed three times with 10× excess volume of PBSx1. The scaffolds were imaged by MRI using the sequences and analysis techniques described above.

4.3.9 Cell Culture for Biocompatibility Analysis

For all biocompatibility assays, scaffolds were prepared as before and then seeded on top with primary human umbilical vein endothelial cells, single donor, in EGM-2 (Basel, Switzerland). The seeded cells were cultured in VascuLife VEGF Endothelial Medium (MD, USA). The DMSO control samples were cultured with medium containing 5% DMSO to provide a cell death positive control for all assays.

4.3.10 Live-Dead Staining and Microscopy

Scaffolds were prepared as stated before in 24 well plates. After gelation and washing, cells were seeded at a density of 40 000 cells per well and then cultured for 48 h. Prior to imaging, cells were incubated with 2 μM calceinacetoxymethyl (Calcein AM) live stain and 4 μM ethidium homodimer-1 (EthD-1) dead stain in PBSx1 with calcium and magnesium for 45 min at 37 °C. Stained cells were then imaged by fluorescence microscopy with a Leica DMi8 inverted epifluorescence microscope using a GFP filter cube to visualize the live stain and a TXR filter cube to visualize the dead stain.

4.3.11 Live Cell DNA Proliferation and Cytotoxicity Assay

Scaffolds were prepared as stated before in 96 well plates. After gelation and washing, cells were seeded at a density of 4000 cells per well and then cultured for 48 h. CyQuant Direct Nucleic acid stain and background suppressor stain (1:5 ratio) were then prepared in cell culture medium and added to each well. The wells were then incubated for 2 h at 37 °C before fluorescence was measured with a FITC filter set on a PerkinElmer Envision 2104 Multilabel Plate Reader (MA, USA). The fluorescence intensity directly corresponded to live cell DNA content due to the cell permeable nucleic acid stain and the dead cell background suppressor stain. This ensures that this

assay measures both cell proliferation and cytotoxicity. Scaffolds were prepared and assayed over six individual trials (n = 6).

4.3.12 Metabolic Activity Assay

Scaffolds were prepared as stated before in 96 well plates. After gelation and washing, cells were seeded at a density of 4000 cells per well and then cultured for 48 h. Culture medium was then removed from each well and replaced with fresh media containing WST-1 reagent at a 1:10 dilution. The wells were then incubated for 1 h at 37 °C, after which the WST-1 containing medium was removed, and its absorbance at 450 nm was measured by a PerkinElmer Envision 2104 Multilabel Plate Reader (MA, USA). Scaffolds were prepared and assayed in triplicate (n = 3).

4.3.13 In Vivo Evaluation

All animal experiments were approved by the institutional animal care committee (protocol #36 668), and all procedures were conducted in accordance with the National Council on Animal Care. Five Sprague Dawley rats (Charles River Laboratories International, Inc., Wilmington, MA, USA) were used in a pilot study to evaluate the safety and efficacy of the labeled scaffolds. All methods of labeling were tested, and both $MnPNH_2$ and dopamine solutions were used as controls. Rats were injected subcutaneously with various solutions of $MnPNH_2$ (0, 0.1, or 0.2 mM), dopamine hydrochloride (0, 0.25, or 0.5 mM), neutralized un-cross-linked chilled collagen solution (3, 6, and 10 mg mL^{-1}), and neutralized un-cross-linked chilled collagen solutions labeled with dopamine (0, 0.25, or 0.5 mM) and/or $MnPNH_2$ (0, 0.1, or 0.2 mM). This set of conditions was chosen to determine the safety of the different compounds and the ideal labeling procedure for the most efficacious in vivo visualization of collagen scaffolds. All injections were conducted subcutaneously on the dorsal side of the animal at the following injection sites: base of the neck, right and left front limbs, and right and left hind limbs while the rat was under anesthesia at 3% isoflurane. After injection, the animal was kept under anesthesia at 2% isoflurane for an additional hour to ensure the collagen solutions were given adequate time to thermally cross-link in vivo at an internal temperature of 37 °C.

At days 1, 2, 3, 5, 7, 9, 16, and 22 post-implantation, MRI of the implanted scaffolds was performed on the 3.0-Tesla scanner with a 16-channel receive-only wrist coil. Rats were anethesized on 3%

isoflurane (with 2 L min^{-1} flow rate of 100% O2 at 50 psi). Once anesthetized, rats were transferred to the receiving coil and maintained on 2% isoflurane. Rats were placed prone, head first into the scanner and kept warm on a water-blanket heated by Heat Therapy Pump (HTP-1500, Andriot Medical Systems) set at 41 °C. To visualize anatomic details, sagittal high-resolution T_1-weighted and T_2-weighted spin echo images were acquired. T_1-weighted images were acquired using a 2D SE sequence with fat suppression: TR = 2173 ms, TE = 13.6 ms, FOV = 130 mm, slice thickness = 3 mm, in-plane resolution is 0.6 mm × 0.6 mm, and NSA = 3. T_2-weighted images were acquired using a 2D turbo SE sequence: TR = 4000 ms, TE = 75 ms, NSA = 2, and similar resolutions as for T_1-weighted imaging.

Animals were sacrificed after 16 days for the animal bearing only control injections and after 22 days for all other animals. An incision was made to expose the collagen implants, which were then photographed and excised for gross analysis. The dimensions of the explants were noted.

4.3.14 Statistical Analysis

A two-way ANOVA was used to determine significant changes in the T_1 and T_2 relaxation times, with the variables being either the method of labeling and $MnPNH_2$ concentrations or the dose of dopamine and $MnPNH_2$ concentrations. For the degradation study, a one-way ANOVA was used to determine significant changes in UV absorbance, scaffold volume, or T_1/T_2 relaxation times as a function of collagenase concentration. A Tukey–Kramer test was used for post-hoc analysis. Significance is reported at a p-value of 5%.

4.4 Results and Discussion

The feasibility of in vivo scaffold monitoring depends a great deal on the sensitivity provided by the contrast agent used for labeling. In our approach, we use Mn for positive contrast enhancement, as it provides a key advantage over Gd-chelates traditionally used for bright imaging: lower toxicity. Manganese is a vital mineral naturally found in the human body and plays a role in many intracellular activities such as bone mineralization, enzyme activation, metabolism, and cellular protection from free radical species[122]. Manganese amounts in the body range from 10 to 20 mg distributed amongst many tissues with primary accumulation in the blood and liver[122]. Epidemiological studies have shown that doses as high as 11–15 mg per day cause no

adverse effects in adult humans, with excess Mn being excreted via feces and trace amounts via urine[122,413,414]. In our study, very low doses of Mn (5.49×10^{-3} to 2.196×10^{-2} mg per scaffold) were required to achieve significant MRI signal and, thus, posed no safety threat. Furthermore, blood-pool Mn can be shuttled around the body by transferrin, and at the cellular level Mn enters cells via assisted passive transport by specific transporters such as the divalent metal transporter-1 to act as a co-factor for many different enzymes and metabolic processes[122]. In contrast, Gd is not an endogenous metal and its accumulation has been linked to toxicity in both immediate and long term exposures in human patients[108,269,388,415]. While many Gd-based contrast agents (GBCA) are still clinically used, the recent bioaccumulation and toxicity findings have led to legal bans and the removal of some GBCA's from the market while others have been restricted in their clinical use[108]. In addition to its enhanced safety novel, Mn chelates have been designed so that they exhibit a greater number of water binding sites, resulting in greater contrast enhancement than traditional Gd-chelates[388]. Collectively, these attributes have made Mn-based compounds a very promising new class of positive-contrast MRI agents. Within the class of Mn agents exists a subclass known as MnPs, which consist of a Mn core chelated by a porphyrin ring. An MnP contrast agent, $MnPNH_2$, was designed and synthesized in this study as per the reaction scheme shown in Figure **4.1A**. The structure and purity of the intermediates and final product was determined by ultraviolet (UV)-visible spectra, ^1H nuclear magnetic resonance (NMR), high perform liquid chromatography (HPLC), flame atomic absorption spectroscopy (FAAS), and mass spectroscopy (Figures **B1–B4**, Supporting Information-Appendix B).

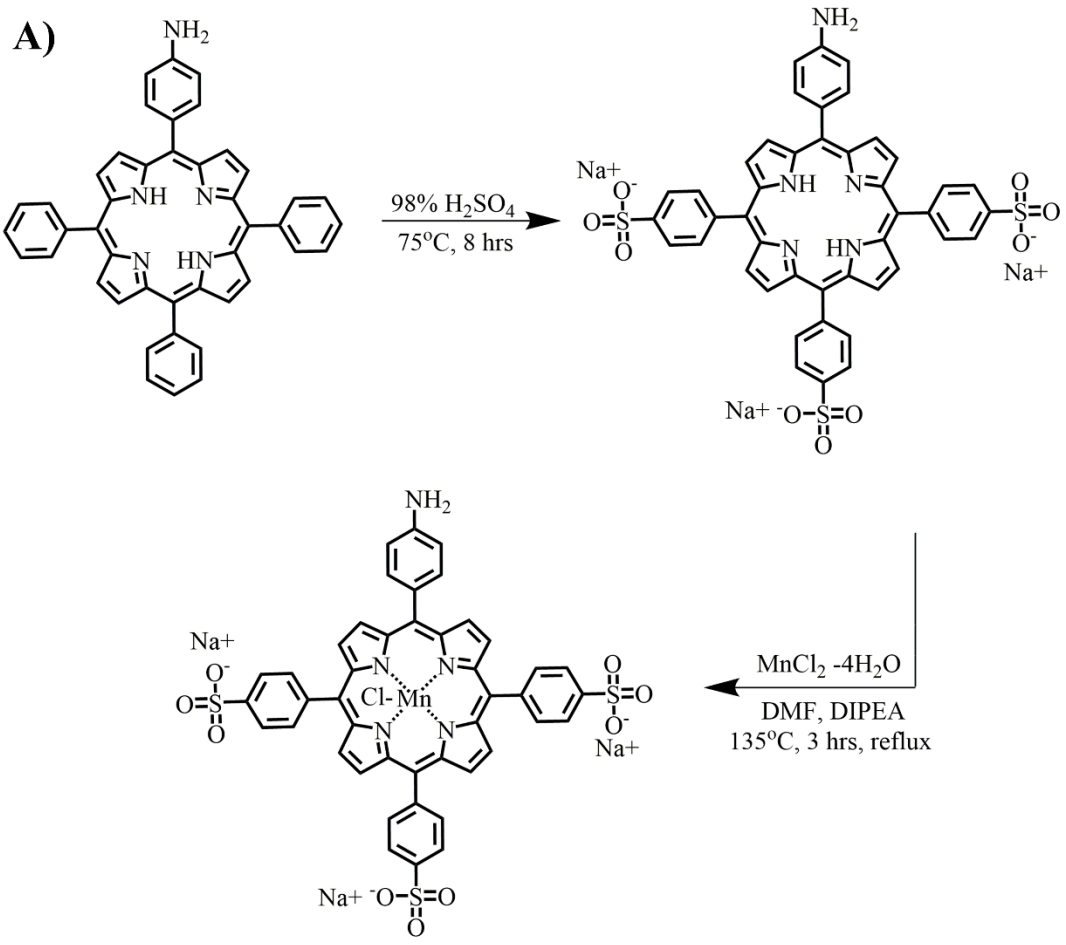
A)
NH2
NH
N
N
HN
98% H2SO4
75°C, 8 hrs
Na+
O-
O=S=O
Na+ -O-S=O
MnCl2 -4H2O
DMF, DIPEA
135°C, 3 hrs, reflux
Cl-Mn

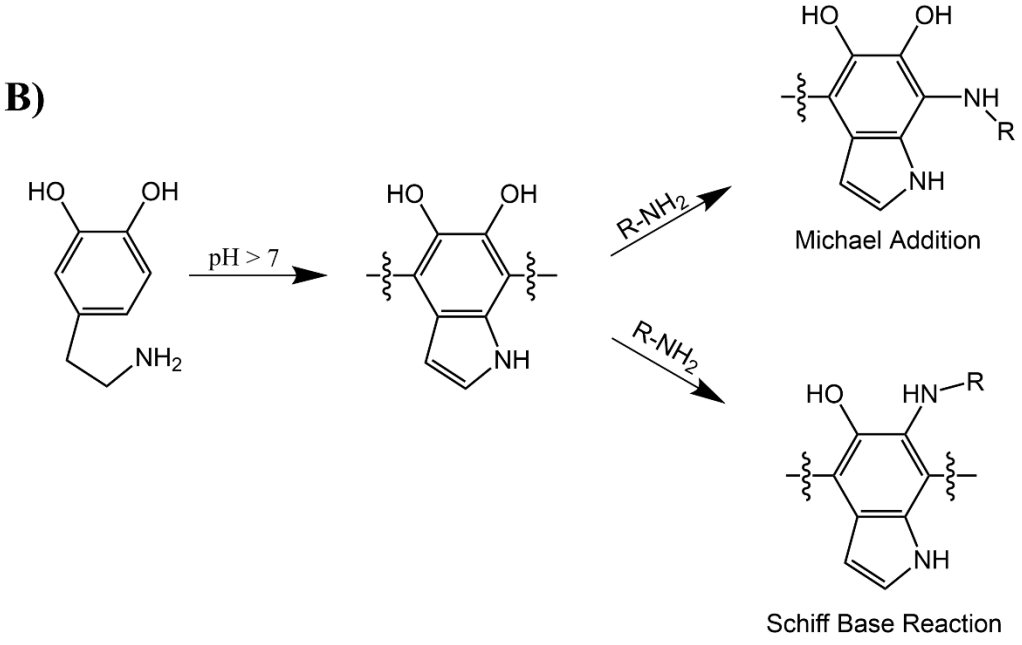
B)
HO
OH
NH2
pH > 7
NH
R-NH2
Michael Addition
HN-R
Schiff Base Reaction

Figure 4.1:**Reaction scheme illustrating the synthesis of $MnPNH_2$, PDA and PDA's secondary functionalization routes**. **A)** $MnPNH_2$ was synthesized from a porphyrin precursor. The precursor was then functionalized with peripheral sulfates groups and subsequently a primary amine group. **B)** Dopamine self-polymerizes at slightly basic conditions resulting in PDA, which can be functionalized with amine-containing compounds via Schiff base reaction and Michael-type additions.

The porphyrin ring of the contrast agent not only chelates the Mn metal, inhibiting demetallation in the body, but also allows for facile chemical modification and, thus, control of its chemical reactivity. To create a contrast agent ideal for scaffold labeling in vivo, the porphyrin ring was modified to enhance its excretion and its ability to be chemically linked to other compounds for labeling and tracking purposes. To meet these requirements, the porphyrin ring was functionalized with a single nucleophilic amine group and three highly hydrophilic sulfate groups. The single amine group acts as a chemical point of attachment. Amine functionalized molecules are used extensively in biological conjugation reactions, because they contain an active lone pair of electrons on the electronegative nitrogen atom. This makes amines very nucleophilic and easily conjugated to a variety of other chemical groups[416]. The three sulfate groups increase the porphyrin's water solubility, which is essential for the agent to be transported via the circulatory system[109,417]. In summary, the structure of the $MnPNH_2$ contrast agent was designed to facilitate both easy conjugation to a scaffold's molecular backbone and excretion from the body after the scaffold degrades.

In addition to providing sensitive detection, safety, and biocompatibility, the scaffold labeling approach must also be simple and applicable to a wide variety of materials. To meet these requirements, we utilized a bio-inspired adhesive polymer, PDA, to adhere the MRI contrast agent to a scaffold. Polydopamine is easily formed by the self-polymerization of dopamine in slightly basic physiological solutions. It deposits and adheres to a variety of biomaterials and demonstrates favorable biocompatibility[418]. Another relevant feature is the strong conjugation of PDA coatings with amine-functionalized compounds, whereby the amine compound covalently attaches to the PDA monomers via a Schiff base reaction or a Michael-type addition (Figure **4.1B**)[419]. These properties favor PDA as an ideal platform for adhering $MnPNH_2$ to a variety of scaffold materials for in vivo tracking.

As proof-of-principle, collagen hydrogel, a biomaterial that is highly tunable and used extensively in tissue engineering, was used as a prototype scaffold[27–33]. Collagen hydrogels have a molecular structure that promotes cell attachment and growth, and its physical properties can be easily modified with a variety of cross-linking agents. To determine the most ideal method of scaffold labeling, three facile, efficient, and versatile protocols were tested for passive and active incorporation of $MnPNH_2$ into collagen scaffolds (**Figure 4.2**). Two of these protocols use dopamine, which is known to polymerize in the presence of collagen while maintaining its adhesive character[420–422].

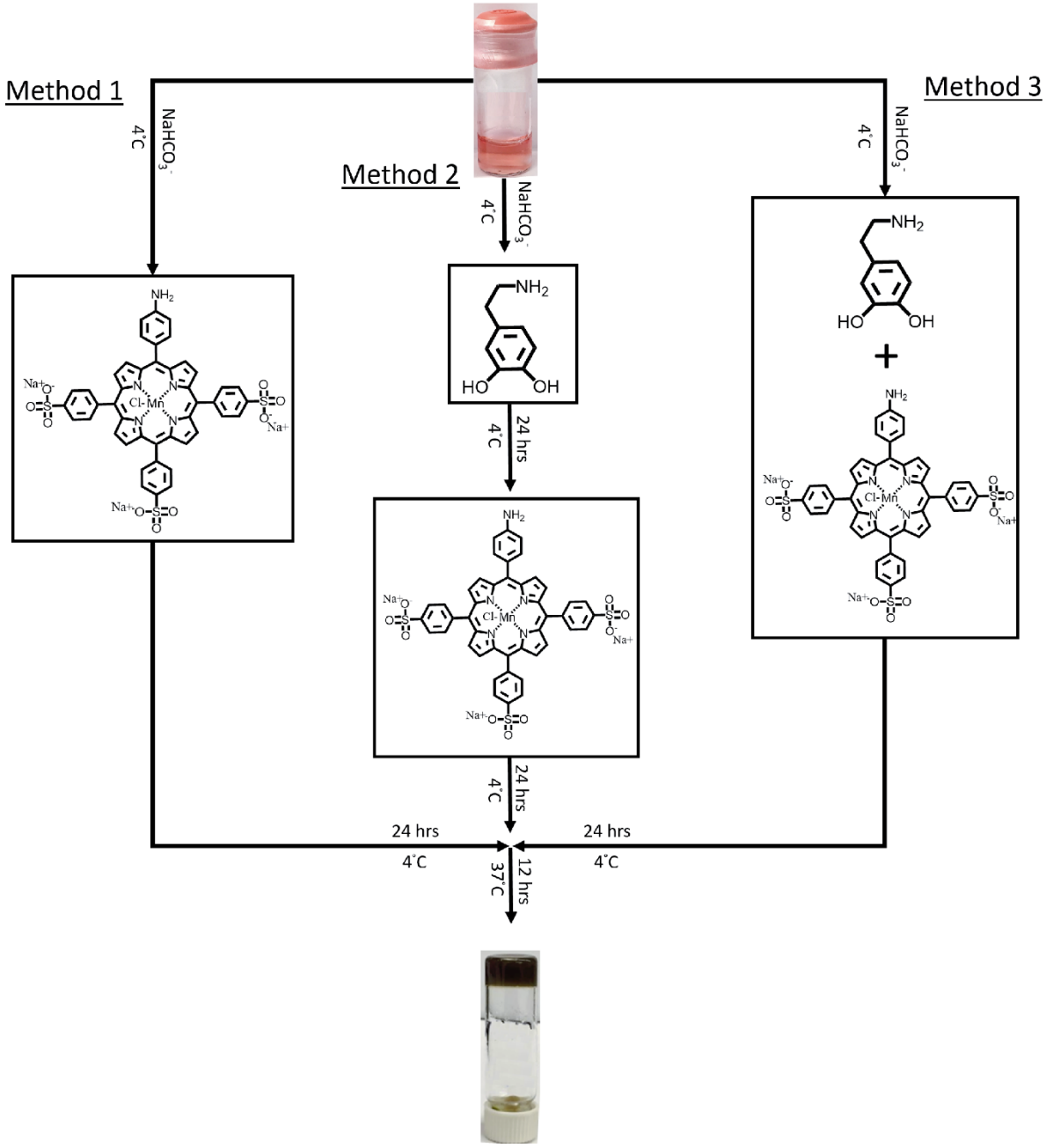

Figure 4.2: **Collagen hydrogel labeling reaction scheme.** Three different methods were tested. Method 1 involved passively incorporating $MnPNH_2$ into a neutralized (pH 7.4) collagen solution prior to thermal cross-linking/gelation. Method 2 involved mixing collagen with dopamine and then $MnPNH_2$ prior to gel formation. Method 3 involved mixing collagen with dopamine and $MnPNH_2$ in one pot prior to gel formation.

Method 1 passively entraps $MnPNH_2$ into the collagen scaffold prior to thermal cross-linking and gelation. Method 2 actively incorporates $MnPNH_2$ into the scaffold by conjugation to a PDA-collagen gel, analogous to similar methods for the formation of collagen-PDA scaffolds and collagen-PDA scaffold functionalization[421,423]. Method 3 actively incorporates $MnPNH_2$ into the scaffold by the simultaneous reaction of dopamine and $MnPNH_2$ in one pot with collagen. Method 1 was developed to determine if $MnPNH_2$ would itself bind non-covalently to the scaffold. Methods 2 and 3 examined the need for a temporal separation between collagen-PDA formation and $MnPNH_2$ conjugation. This was done to determine the simplest yet most efficient method of labeling the scaffold. After labeling, gelation, and sufficient washing, the gels were imaged on a clinical 3-Tesla MRI scanner. T_1- and T_2-weighted images were acquired (Figure **4.3A,B**), and quantitative T_1 and T_2 relaxometry maps were measured (Figure **4.3C,D**). A reduction in T_1 and T_2 relaxation times for labeled scaffolds relative to unlabeled scaffolds could be detected in all three methods and $MnPNH_2$ concentrations tested, as expected for a T_1 agent. A maximum T_1 reduction of six-fold relative to control and a maximum T_2 reduction of fourfold were achieved for the conditions tested (Figure **4.3E,F**). This is consistent with literature[137], where MnP derivatives act primarily as positive-contrast T_1 agents but also exert dual activity as moderate T_2 agents. Comparison amongst all three labeling protocols demonstrated that Method 3 exhibited the largest reductions in T_1 times at all $MnPNH_2$ concentrations and, thus, the greatest positive signal (Figure **4.3A,E**). Furthermore, the uniformity of the bright signal throughout the gel (Figure **4.3A**) indicates uniform dispersion and attachment of the contrast agent. There are multiple potential reasons for the enhanced reductions achieved by Method 3; however, we hypothesize that it is simply due to the availability of coupling sites between PDA and $MnPNH_2$. As dopamine reacts and becomes PDA, it will interact with any free amines (present both on collagen and on $MnPNH_2$). Thus, in Method 2, since PDA is formed in the presence of collagen first, it can bind many coupling sites, leaving fewer available for binding to $MnPNH_2$. This results in higher T_1 values and also binding saturation, which is seen at higher $MnPNH_2$ loading concentrations for Method 2. However, in Method 3, $MnPNH_2$ is present as the PDA forms; thus, there is more competition for binding sites and more $MnPNH_2$ can bind, which is evident by the enhanced contrast and larger reductions in T_1 at all labeling concentrations. These results provide solid proof-of-principle evidence for the ability to label and visualize collagen gels by MRI, with the highest signal and lowest T_1 times produced by the one-pot labeling approach (Method 3). It

is worth noting that the passive approach (Method 1) resulted in significant contrast enhancement also; however, this enhancement may not be sufficient for visualizing a scaffold as it degrades in the body and further lowers signal contrast.

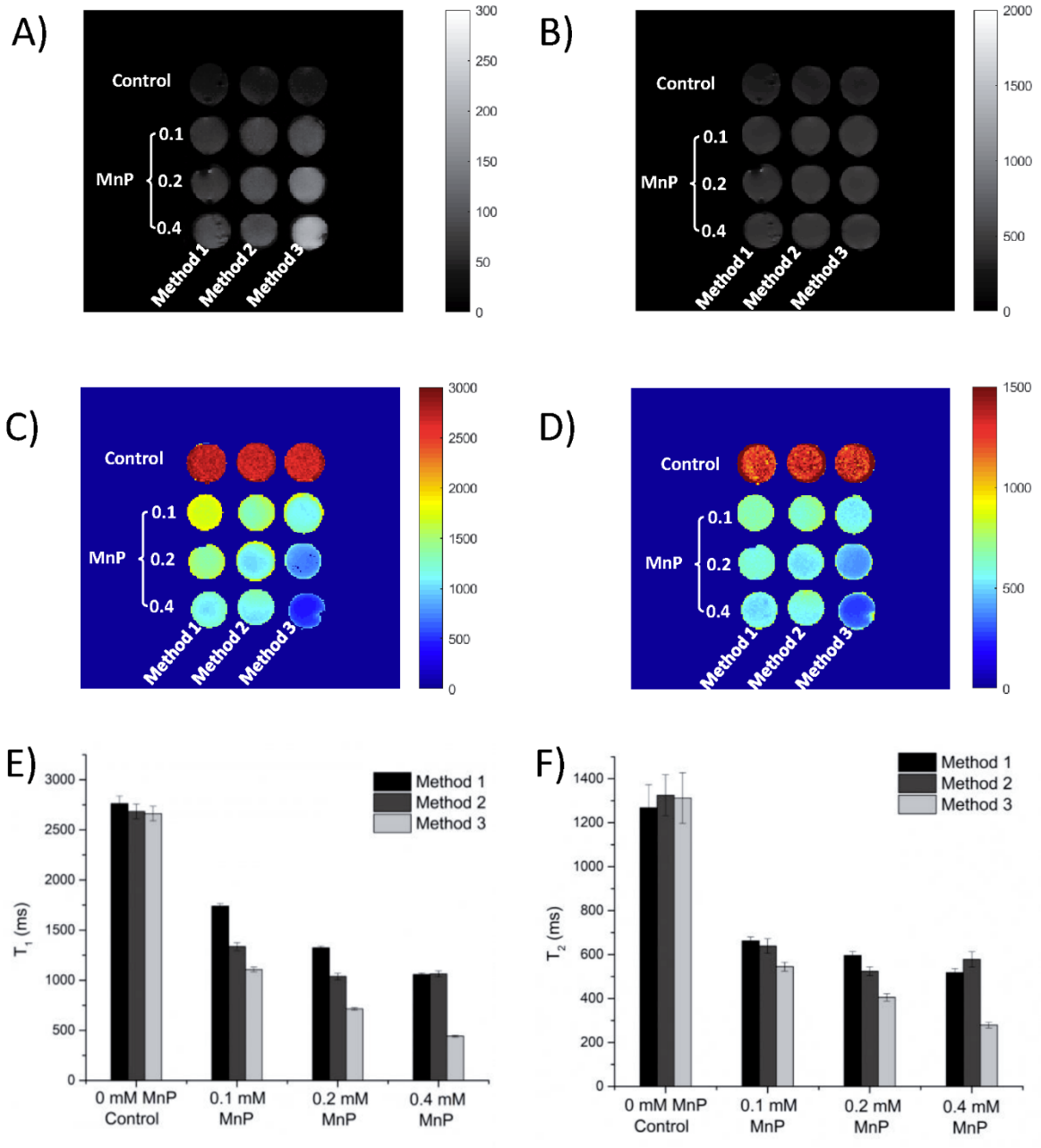

Figure 4.3: **Comparison of methods for labeling collagen hydrogel scaffolds on MRI.** Scaffolds labeled using different methods and concentrations of $MnPNH_2$ (0, 0.1, 0.2, and 0.4 mM) are shown on a **A)** T_1-weighted image, **B)** T_2-weighted image, **C)** map of T_1 relaxation times, and **D)** map of T_2 relaxation times. Methods 2 and 3 incorporated 0.25 mM of dopamine-hydrochloride. **E,F)** Graphs of T_1 and T_2 relaxation times show a significant difference

in T_1 and T_2 across different $MnPNH_2$ concentrations ($p < 0.05$). However, while T_1 was significantly different amongst all methods, T_2 was different only for Method 3 ($p < 0.05$). Shown are mean values and standard deviations.

Upon identifying Method 3 as the most effective for scaffold labeling, an additional range of dopamine concentrations (0–2.5 mM) and $MnPNH_2$ concentrations (0.1–0.4 mM) were tested to determine the optimal ratio of $MnPNH_2$:PDA for labeling. Labeled scaffolds were scanned on MRI as before. A reduced T_1 and T_2 was observed with either increasing $MnPNH_2$ concentrations or increasing PDA concentrations, or both, with a 1.53 to 4.2-fold T_1 reduction and 1.2 to 2.76-fold T_2 reduction from passively labeled (no PDA) to actively labeled scaffolds (with PDA) (Figure **4.4**). It is important to note that a large reduction in T_1 versus control was observed even with the lowest concentration of $MnPNH_2$ and PDA, thus demonstrating the capability of Method 3 to produce large contrast enhancement with very small amounts of labeling agents. This data provides a useful scale for determining the ideal $MnPNH_2$:PDA ratio required to achieve optimal contrast on MRI in any specific in vivo setting. However, since the T_1 of the labeled scaffold (250–750 ms) is considerably lower than the range of T_1s of different organs (brain gray matter T_1 = 1615 ± 149 ms, skeletal muscle T_1 = 1509 ± 150 ms, myocardium T_1 = 1341 ± 32 ms at 3.0 Tesla[424]), it is relatively straightforward to achieve extremely high contrast for the labeled scaffold in vivo in nearly all tissues in the body.

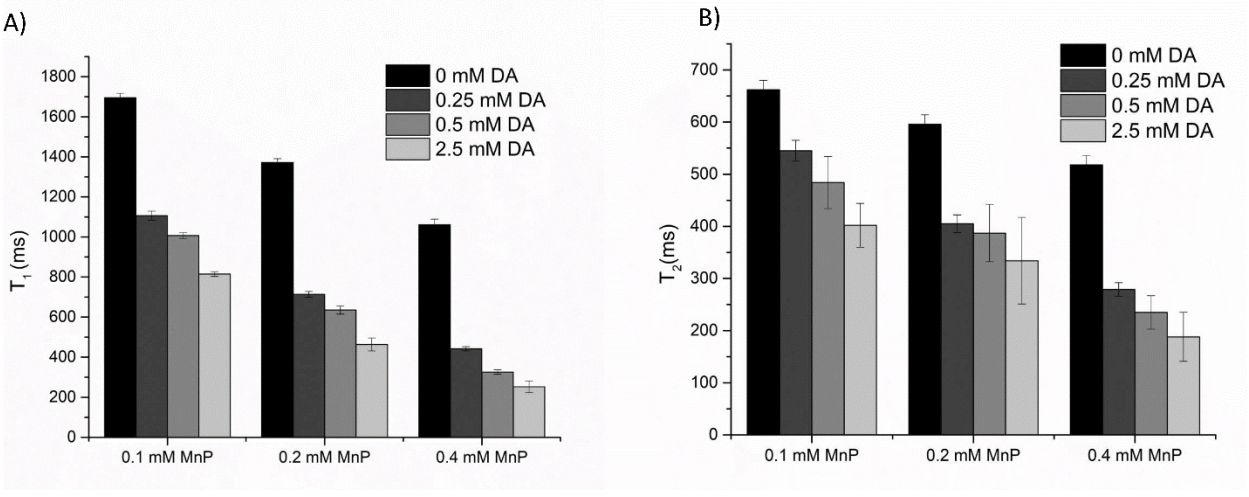

Figure 4.4: **Effect of dopamine (DA) and $MnPNH_2$ concentration on labeling**. **A)** T_1 and **B)** T_2 relaxation times of collagen hydrogels labeled with $MnPNH_2$ using Method 3 demonstrate the T_1- and T_2-reducing effects of increasing concentrations of either $MnPNH_2$ or the adhesive.

Samples were extensively washed before imaging. Significant differences in T_1 and T_2 exist across different DA and $MnPNH_2$ concentrations ($p < 0.05$). Shown are mean values and standard deviations.

Initial proof-of-principle studies for monitoring scaffold degradation was conducted by degrading labeled and unlabeled gels enzymatically with collagenase in vitro (Figure **4.5**). Gels were prepared and degraded with different concentrations of collagenase for the same amount of time (4 hrs) to prevent differences arising from hydrolytic degradation. Degradation was assessed by MRI of the gel and UV absorbance of the degraded solution (Figure **4.5A–F**). The characteristic absorbance profile of $MnPNH_2$ was only observed in degraded solutions containing $MnPNH_2$-conjugated gels (Figure **B5**, Supporting Information-Appendix B), and the absorbance intensity at λ_{max} (468 nm) correlated positively with gels loaded with more collagenase, indicating greater degradation as expected (Figure **4.5E**). UV absorbance intensities were also highly consistent within a sample group, and between groups, exhibiting a stable and controlled release profile rather than a burst model, indicative of strong binding to the collagen gel. The degradation trend was further confirmed by volumetric MRI, which provided an accurate volumetric analysis of labeled gels and indicated significant surface degradation, with a negative correlation between gel size and collagenase loading (Figure **4.5F**). Potential bulk degradation throughout the scaffold was assessed on quantitative T_1 and T_2 maps. The interiors of scaffolds were minimally degraded, as judged by a relatively constant signal between sample groups on MRI; however, the small increase in T_1 and T_2 and the corresponding decrease in signal-to-noise ratios was statistically significant, indicating the possibility to detect with MRI slight changes in density in labeled scaffolds (Figure **4.5D**). This is possible as the signal measured by MRI is directly proportional to contrast agent concentration. Since in our case the contrast agent is adhered to the collagen fibers, the local concentration now reflects the density of the scaffold/fibers. This observation was confirmed qualitatively on scanning electron microscopy (SEM) by porosity and fiber density of the degraded scaffolds. After MRI, the scaffolds were flash frozen and lyophilized to maintain their structure. They were then imaged by an environmental SEM to visualize changes in pore size. SEM images in Figure **4.5G** show that all scaffolds maintained a similar pore size and fiber density, corroborating the finding of minimal bulk degradation. The sensitivity of MRI to microstructural alterations was further validated with a collagen contraction model. In this model, it was expected that as the collagen fibers contracted, the conjugated $MnPNH_2$ molecules would move with them; thus, as the density of collagen increased, so would the local concentration of $MnPNH_2$, creating

a spatially isolated area of high concentration and high signal. As seen in Figure **5H**, the contracted gel exhibited a much higher signal indicative of a higher $MnPNH_2$ concentration. Further validation is required to assess the capability of this technique to accurately measure scaffold changes in fiber density; however, this result serves as a testament to the sensitivity of MRI for non-invasive scaffold monitoring.

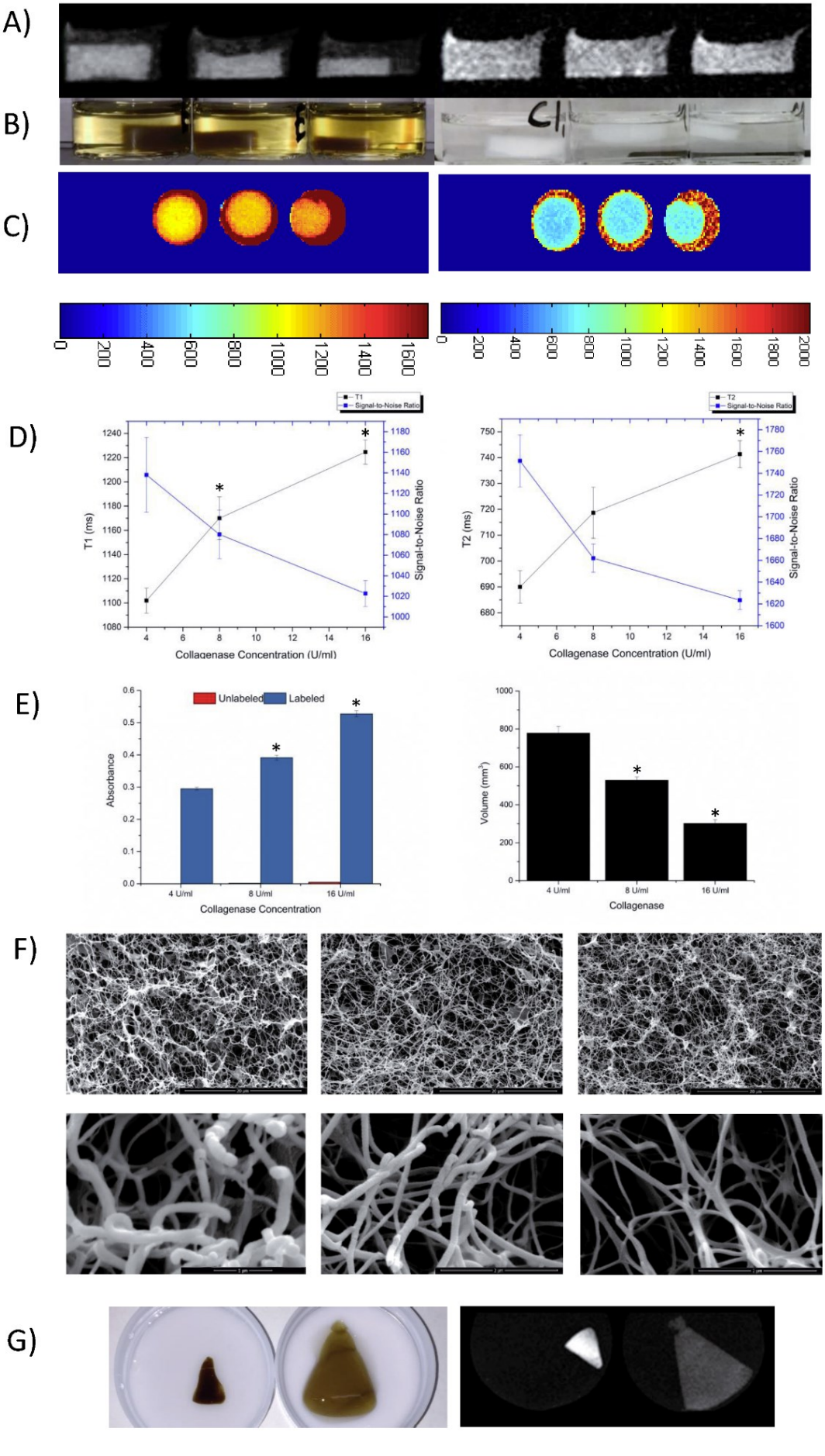
A)
B)
C)
0
200
400
600
800
1000
1200
1400
1600
0
200
400
600
800
1000
1200
1400
1600
1800
2000
D)
T1
Signal-to-Noise Ratio
T1 (ms)
Signal-to-Noise Ratio
Collagenase Concentration (U/ml)
T2
Signal-to-Noise Ratio
T2 (ms)
Signal-to-Noise Ratio
Collagenase Concentration (U/ml)
E)
Unlabeled
Labeled
Absorbance
4 U/ml
8 U/ml
16 U/ml
Collagenase Concentration
Volume (mm³)
4 U/ml
8 U/ml
16 U/ml
Collagenase
F)
G)

Figure 4.5: **Monitoring in vitro degradation with MRI**. Collagen gels degraded enzymatically for a fixed time interval with varying amounts of collagenase (4, 8, and 16 U mL^{-1}) were assessed on MRI and UV. **A)** T_1-weighted MR images of labeled (left) and unlabeled (right) collagen gels degraded with 16, 8, and 4 U mL^{-1} collagenase from left to right. **B)** Corresponding photographs of degraded gels. **C)** Maps of T_1 and T_2 relaxation times (ms) of the labeled gels and **D)** corresponding mean values and signal-to-noise ratios (SNR). E) UV analysis of the degraded gel solution with peak absorbance at 468 nm (left) and MRI volumetric analysis of the labeled gels (right). **F)** SEM of degraded gels with 4, 8, and 16 U mL^{-1} of collagenase from left to right. **G)** Photographs of contracted and non-contracted gels (left) and the corresponding T_1-weighted image on MRI (right). *Denotes significant differences ($p < 0.05$).

To evaluate the biocompatibility of the labeled collagen gels, a series of scaffolds were assessed for their ability to promote cell attachment and growth. Scaffolds were prepared with various ratios of dopamine and $MnPNH_2$ as before and seeded with primary human umbilical vein endothelial cells (HUVEC). The cells were grown for 48 h and then assayed for metabolic activity, live cell DNA content, and live/dead staining (Figure **4.6**). HUVEC cells were chosen as a prototypical cell type for their application in tissue engineering and regenerative medicine, where they have been utilized extensively with collagen scaffolds to promote endothelialization and angiogenesis[425,426]. Scaffolds prepared with both high and low amounts of dopamine and $MnPNH_2$ exhibited statistically similar levels of live cell DNA content and metabolic activity compared to control collagen scaffolds (Figure **4.6B,C**). This demonstrated that both labeled and unlabeled scaffolds promoted similar rates of cellular proliferation and metabolism. Furthermore, live/dead staining of the cells under all conditions, except for the dimethyl sulfoxide (DMSO) negative control, showed very low to no dead cells (Figure **4.6A**), further supporting the biocompatibility and nontoxic properties of the labeled scaffolds. Additionally, on all scaffolds a flatten and spread cell morphology as opposed to a rounded shape was found. This is distinctive for healthy proliferating cells and indicative of the ability of the scaffolds to promote cell adhesion. Despite the absence of statistical differences, it is worth noting the slightly elevated averages in metabolic activity and DNA cell content, which correlates well with the perceived live cell density in the live/dead stained fluorescence micrographs. This enhanced cell number could be due to the adhesive properties of PDA that have been shown to preferentially binds cells and promote proliferation[421].

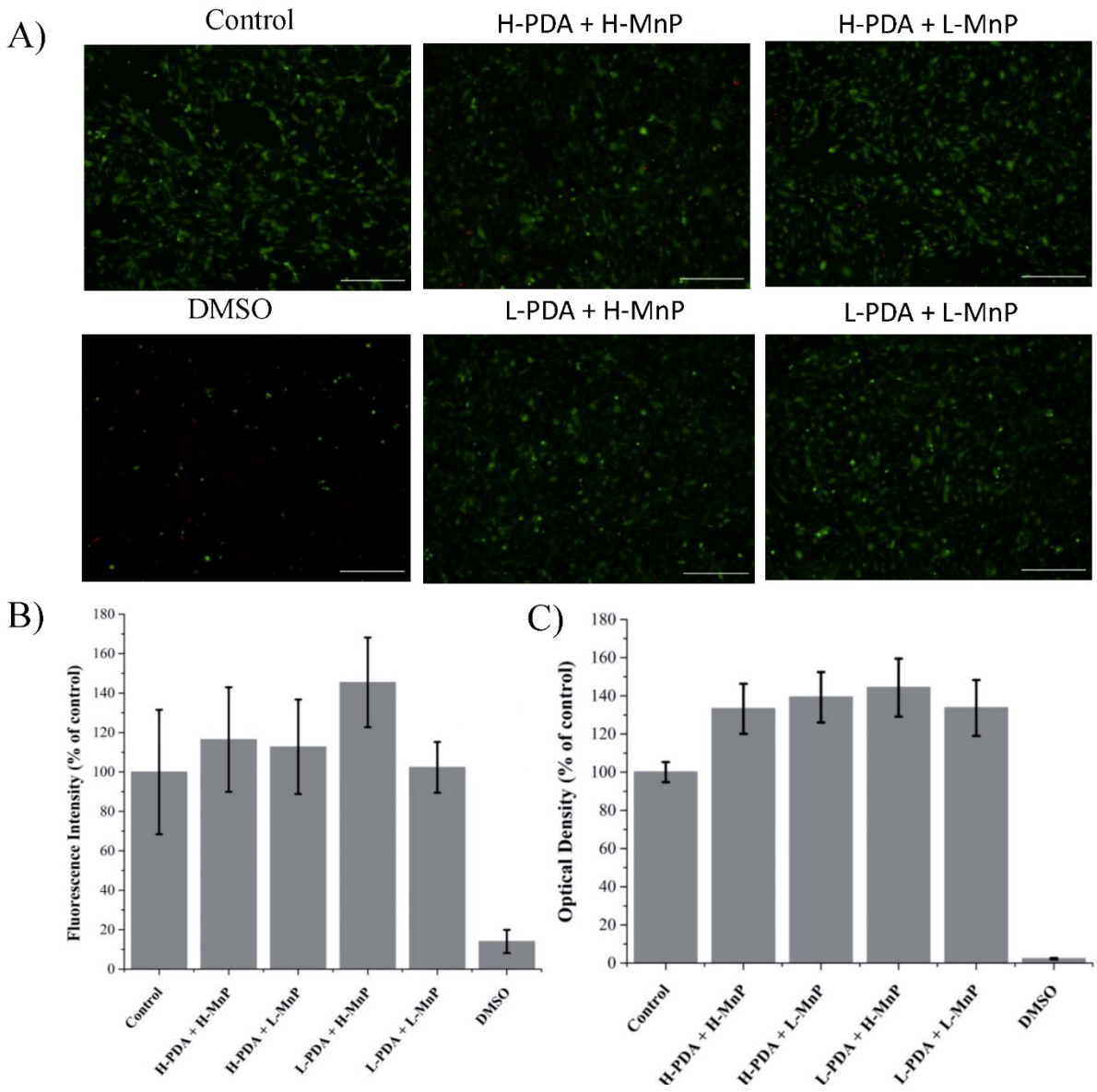

Figure 4.6: **Biocompatibility of labeled scaffolds.** HUVEC cells were seeded and cultured on collagen gels for 48 h before **A)** live (green) and dead (red) staining, scale bar 400 um, **B)** live cell DNA proliferation assay, and **C)** WST-1 metabolic activity assay. H-PDA and L-PDA represent high (2.5 mM) and low (0.25 mM) dopamine labeling, while H-MnP and L-MnP represents high (0.4 mM) and low (0.1 mM) MnP-NH2 labeling. DMSO controls were treated with 5% DMSO.

To determine the feasibility of non-invasively imaging and monitoring labeled scaffolds in a living animal, an in vivo study was conducted on a series of scaffolds. Labeled and unlabeled collagen hydrogels were formed in situ by subcutaneous injection in female Sprague Dawley rats. The scaffolds were monitored longitudinally on MRI up to 22 days post-implantation, and all

animals were sacrificed for gross dissection (Figures **4.7**). $MnPNH_2$-PDA scaffolds could be accurately tracked and visualized for the full 22-day period using T_1-weighted MRI. The labeled scaffolds degraded over time, which was evident by a significant reduction in scaffold size, visualized by MRI and confirmed on gross pathology. Furthermore, a decrease in signal contrast from the interior of the scaffold was observed over the study period. This loss in signal and change in size can be attributed to bulk and surface degradation, respectively, indicating that as the scaffold degraded, the $MnPNH_2$ contrast agent was flushed away, resulting in signal loss. Gross dissection confirmed the accuracy of MRI in spatially delineating graft size and geometry even at 22 days (Figure **4.7A**). In contrast, unlabeled collagen gels were not visible on MRI, except on Day 1 due to initial high water content (Figure **4.7B**). Similarly, distinct hyperintensity from labeled collagen scaffolds was observed in all animals, demonstrating the robustness of our labeling approach for in vivo monitoring and assessment of biomaterial scaffolds.

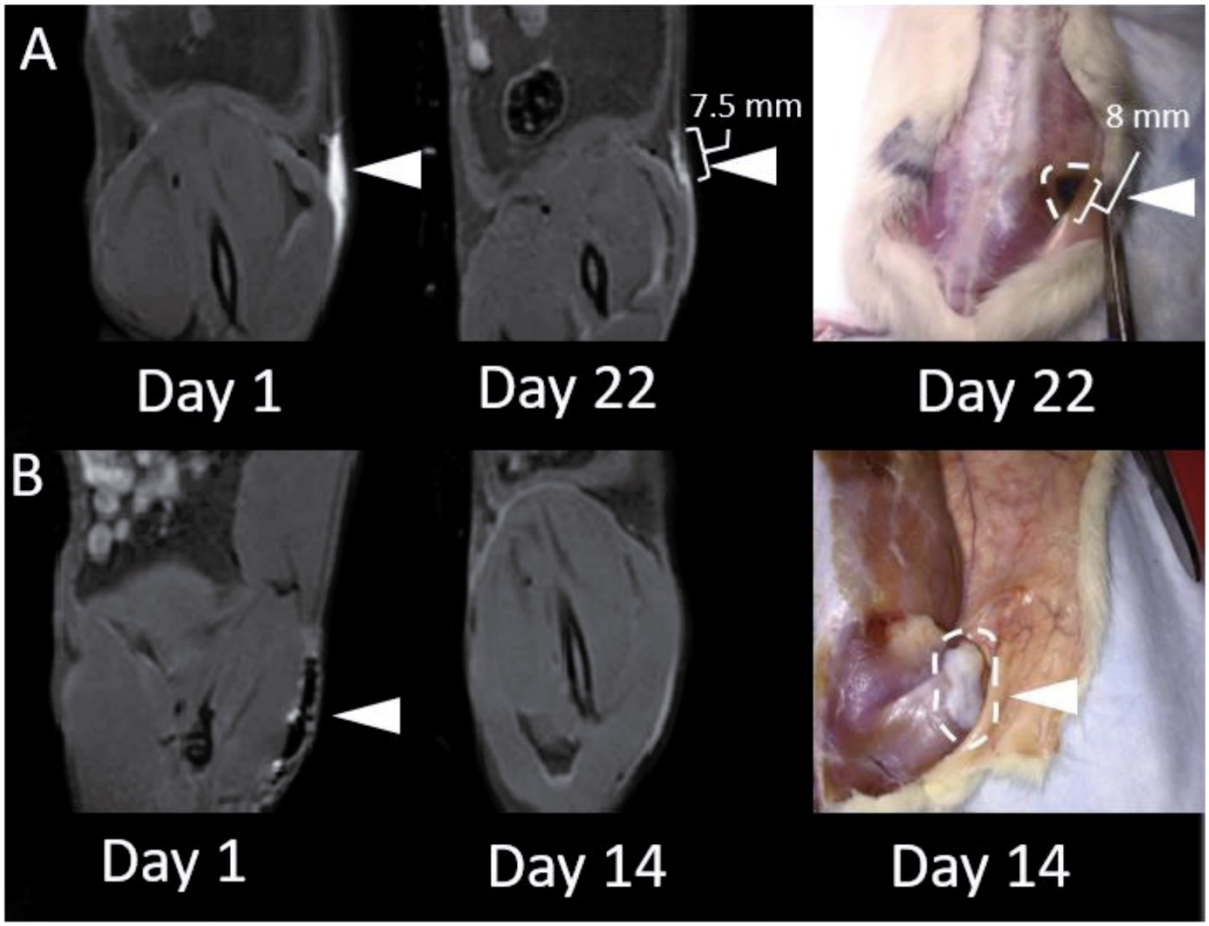

Figure 4.7: In vivo MRI monitoring of scaffold degradation. Fat-saturated T_1-weighted spin echo images over time and gross dissection of rats injected with **A)** 3 mg mL^{-1} collagen gel labeled with 0.2 mM $MnPNH_2$ and 0.25 mM PDA, and **B)** 10 mg mL^{-1} collagen gel unlabeled. MRI accurately delineated graft dimensions, as confirmed post-mortem on gross pathology on Day 22. Unlabeled gels were visible on MR on Day 1 but not on Day 14, when post-mortem confirmed the gel was still present.

4.5 Conclusion

This work demonstrates a promising proof-of-principle method for creating biocompatible collagen scaffolds that are "trackable" on MRI. Multiple methods, including both passive and active binding, were investigated to label collagen scaffolds with a positive contrast-generating agent $MnPNH_2$. The active binding methods based on a PDA adhesive resulted in the highest contrast retention and signal enhancement. Labeled collagen scaffolds were visualized with excellent sensitivity both in vitro and in vivo. The superb sensitivity even permitted monitoring until nearly complete scaffold degradation in vivo, thus creating the potential for in vivo longitudinal monitoring of degradation rates. Although collagen was chosen as the prototype scaffold, our approach can, in principle, be readily extended to a variety of biomaterials. The proposed simple yet effective technique for scaffold labeling and monitoring lays the foundation for future investigations of biomaterial response in the body and for the creation of non-invasive, clinically oriented monitoring systems for patients.

4.6 Contributions

H.-L.M. Cheng contributed to: overall direction of study, design of MR acquisition protocol, *in vitro* and *in vivo* MRI, development of software for analyzing quantitative MRI data; analysis and interpretation of data, writing and final approval of the manuscript. D.A.S. contributed to: conceptualization and design of study, synthesis, characterization and quantification of Apo-PNH_2 and $MnPNH_2$, synthesis and labelling of collagen scaffolds, collagen scaffold characterization, degradation, and contraction studies, cell biocompatibility assays, scanning electron microscopy, in vitro and in vivo MRI, analysis and interpretation of data, writing and final approval of manuscript.

Chapter 5 A manganese porphyrin-based T_1 contrast agent for cellular MR imaging of human embryonic stem cells

This work has been published in *Scientific Reports* Volume 8, Article number: 12129 (2018) and has been reproduced with permission from the respective publishers.[389] Article listed below:

Venter*, A., Szulc*, D.A., Loai*, S. et al. A manganese porphyrin-based T1 contrast agent for cellular MR imaging of human embryonic stem cells. *Sci. Rep.* 8, 12129 (2018). https://doi.org/10.1038/s41598-018-30661-w

5.1 Abstract

MRI for non-invasive cell tracking is recognized for enabling pre-clinical research on stem cell therapy. Yet, adoption of cellular imaging in stem cell research has been restricted to sites with experience in MR contrast agent synthesis and to small animal models that do not require scaled-up synthesis. In this study, we demonstrate the use of a gadolinium-free T_1 contrast agent for tracking human embryonic stem cells. The agent, $MnPNH_2$, is an easily synthesized manganese porphyrin that can be scaled for large cell numbers. MRI was performed on a 3 T clinical scanner. Cell pellets labeled at different $MnPNH_2$ concentrations for 24 hours demonstrated a decrease in T_1 relaxation time of nearly two-fold ($P < 0.05$), and cellular contrast was maintained for 24 hours ($P < 0.05$). Cell viability (Trypan blue) and differentiation (embryoid body formation) were unaffected. Cell uptake of Mn on inductively coupled plasma atomic emission spectroscopy corroborated MRI findings, and fluorescence microscopy revealed the agent localized mainly in cell-cell boundaries and cell nuclei. Labeled cells transplanted in rats demonstrated the superior sensitivity of $MnPNH_2$ for *in-vivo* cell tracking.

5.2 Introduction

Human stem cells have the unique potential of renewing themselves and differentiating into tissue-specific cells with specialized function, thus representing a clinically relevant cell source in regenerative medicine[427,428]. Embryonic stem cells (ESCs), derived from the inner cell mass of the blastocyst, are favored for their potential to treat a variety of diseases and injuries, including heart disease, stroke, diabetes, and bone and cartilage deterioration[429]. However, despite continued

advances in stem cell-based regeneration strategies, a number of critical barriers related to cell delivery and tracking must still be overcome. There is an urgent need for novel methods to non-invasively track ESCs *in vivo*. Currently, we are completely blind as to the fate of cells post-transplantation and must await histology to confirm successful engraftment. The ability to label and visualize ESCs *in vivo* would help ensure their appropriate distribution within the tissue during initial delivery, and it would allow assessment of graft cell death and function over time (e.g. informing the need for additional cell injections and/or modulated immunosuppression).

Magnetic resonance imaging (MRI) is a sensitive and non-irradiative approach for non-invasive cell tracking *in vivo*[208]. Over the years, various applications have been reported, the majority of these utilizing iron-oxide nanoparticles for cell labeling[430]. However, the non-specificity of a dark signal, which can arise from the iron-labeled cells or from endogenous T_2 sources (e.g. blood clots) or from macrophages that have ingested iron released from dying cells[431], has prompted efforts to use bright contrast instead for cell labeling. To this end, both gadolinium and manganese have been explored as potential T_1 agents for cell labeling and tracking[432,433]. While toxicity issues exist with gadolinium[265], manganese (Mn) is naturally found in the body and any excess at low concentrations can be eliminated safely. Therefore, while manganese should not be used in its ionic form (e.g. $MnCl_2$), when bound tightly, the Mn ion can exert its T1 effects without posing risks to the body.

In this study, we propose a Mn-based contrast agent for cell labeling, one that is easy to synthesize and has high thermodynamic stability[434], both important factors for eventual clinical translation. The proposed agent, hereafter termed $MnPNH_2$, is a monomeric Mn porphyrin modified with a single amine group for enhanced cell uptake. We have previously investigated the relaxation properties of this agent in solution and found it to be far superior to gadolinium agents used clinically, with $r1 = 9.33\ mM^{-1}s^{-1}$ and $r2 = 12\ mM^{-1}s^{-1}$ [435]. Here, we investigate the efficacy of $MnPNH_2$ for labeling human ESCs and confirm the absence of adverse effects on cell viability, colony formation, suspended cell aggregation behavior, and differentiation. We also provide the first characterization of the agent's subcellular distribution and efficacy *in vivo*. Our overall goal is to advance MRI contrast agents that are not only safe and provide sensitive cell detection *in*

vivo but also are easy to synthesize for scalability, to enable studies in larger animal models and eventually patients receiving stem cell treatment.

5.3 Materials and Methods

5.3.1 Chemicals for Synthesis

All reagents and deuterated solvents used for synthesis were of reagent grade or better and were used without further purification unless stated otherwise. Starting materials, reagents and deuterated solvents were purchased from Sigma Aldrich, and all other solvents were purchased from Caledon Laboratories. The PNH_2 precursor, 5-(4-aminophenyl)-10, 15, 20-(tri-4-sulfonatophenyl)porphyrin triammonium, was purchased from PorphyChem. All reactions were carried out under argon. Thin layer chromatography was carried out on pre-coated aluminum plates of Silica Gel 60 F254 from Merck. Column chromatography was performed using Caledon Silica Gel 60. Dialysis was performed with Biotech CE dialysis tubing (MWCO 100–500 Da). Cation exchange was performed using an Aberlite IR120 H resin. All spectroscopic data for structural characterizations were obtained using the research facilities in the Department of Chemistry. NMR spectra were recorded on a Brucker-500 MHz. UV-visible spectra were recorded on an Agilent 8453 system. HPLC spectra were recorded on a PerkinElmer SERIES 200 system. FAA spectra were recorded on a PerkinElmer AAnalyst 100 system. Mass spectroscopy was carried out on a Agilent 6538 Q-TOF system.

5.3.2 Synthesis of $MnPNH_2$

The proposed contrast agent is a monomeric manganese tetraphenyl porphyrin with three sulfonate groups to afford water solubility and one amine group for improved cell permeability relative to the well-known manganese complex of 5, 10, 15, 20-tetra(sulfonatophenyl) porphyrin. The contrast agent, $MnPNH_2$, was synthesized by a modified protocol according to previously described procedures[436–438]; the full and scalable synthetic routes are shown in Figure **5.1**. The first step involved a condensation reaction between pyrrole and benzaldehyde carried out in dichloromethane with boron trifluoride etherate as the acid catalyst followed by oxidation with DDQ to provide compound 1, tetraphenyl porphyrin in 40% yield[436]. Subsequent nitration of the para-position of the phenyl ring with sodium nitrite in trifluoroacetic acid provided a mixture of

compound 2 and dinitroporphyrins[437]. This mixture was carried through to the hydrochloric acid-tin (II) chloride catalyzed reduction of the nitro groups to provide aminophenyl porphyrin, compound 3 in 56% yield. Finally, compound 3 was heated in concentrated sulfuric acid to provide 84% of the desired compound 4, PNH_2.[438] Mn was then inserted into compound 4 by metalation with $MnCl_2$ in dimethylformamide and N,N-Diisopropylethylamine with heat for 3 hours, to produce the final product, compound 5, $MnPNH_2$. This final step was also repeated with the purchased PNH_2, compound 4. The structures of compounds 1 and 3 were confirmed by ^1H NMR. Compound 4, PNH_2, was characterized by ^1H NMR, mass spectrometry, HPLC and UV-Visible spectroscopy matching the literature. Compound 5, $MnPNH_2$, synthesized from both the purchased and in-house produced compound 4, was characterized by mass spectrometry, UV-Visible spectroscopy, HPLC, and FAA spectrometry matching literature.

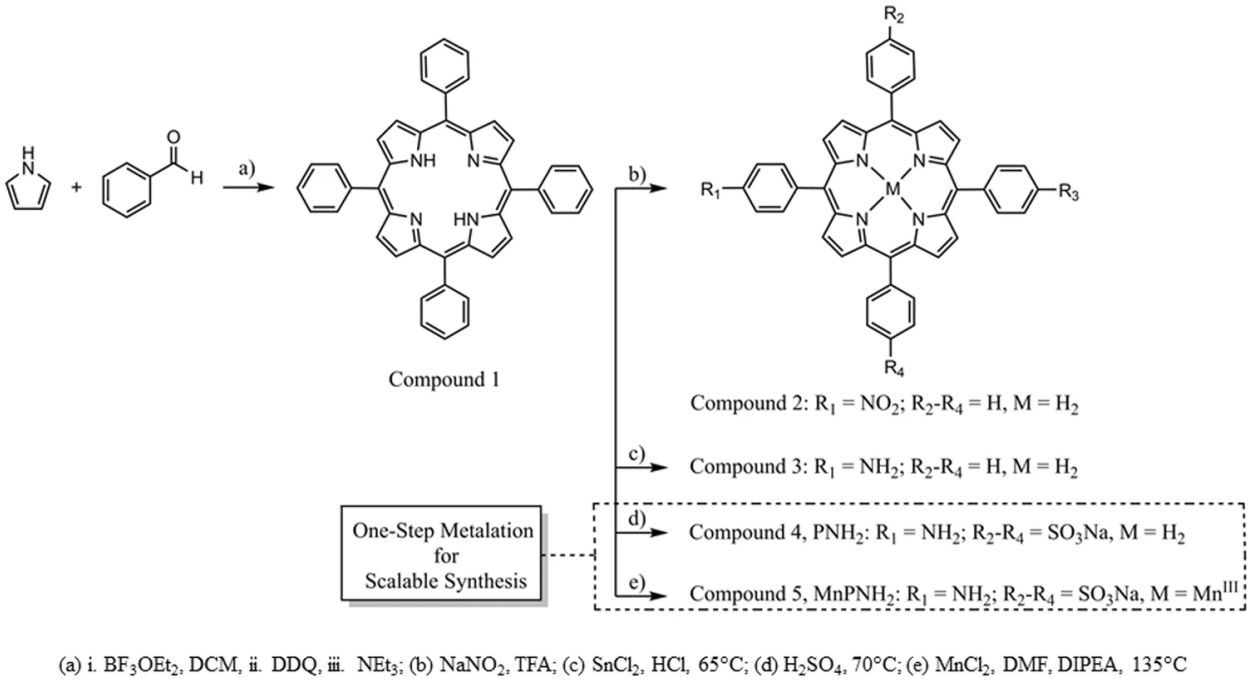

Figure 5.1:Schematic of chemical synthesis. The synthesis of $MnPNH_2$ from simple starting materials and the one-step metalation from the commercial precursor PNH_2 is shown.

5.3.3 Human Embryonic Stem Cell Line and Cell Culture

Human ESCs from the line ESI–017 (ESIBio, SKU: ES-700) were cultured in sterile conditions on tissue culture plates coated with Corning™ Matrigel™ Membrane Matrix (Fisher Scientific Catalog No.08-774-552) and kept in an incubator at 37 °C and 5% CO_2. Cells were grown in

colonies, maintained in mTeSR ™1 (STEMCELL Technologies Catalog # 85850), and passaged using enzyme-free dissociation to prevent differentiation and allow cells to remain in small colonies using Gentle Cell Dissociation Reagent (STEMCELL Technologies Catalog #07174) and mechanical cell scraper separation.

5.3.4 Cell Labeling Studies

Stock solution of $MnPNH_2$ at 10 mM dissolved in sterile distilled water under sterile conditions was created to label cells without significantly changing the volume of media. This stock solution was then heated at a low boil for 5 minutes to further ensure sterility. The contrast agent was added directly from the stock solution into the well containing cells that were to be labeled.

At the end of the cell labeling interval, the cell media was removed and cells were rinsed with room temperature DPBS (Thermofisher Catalog # 21600010) three times with gentle swirling of each rinse to ensure that most of the contrast agent not taken up by cells was washed off. The stem cells were then dissociated using a gentle cell dissociation protocol and then fully removed with a cell scraper. Cells were then resuspended in PBS and centrifuged at 300 g three times for five minutes each time to ensure all extracellular contrast agent was fully removed. The cells were then transferred into 115 × 5 mm Wintrobe sedimentation tubes (Kimble Chase, Vinelad, NJ), topped with mTeSR media, and transported on ice to the MRI scanner.

A range of contrast agent concentrations for cell labeling (0.1–0.5 mM) and two different labeling intervals (2 and 24 hours) were tested. The retention of contrast in labeled cells was also investigated up to 4 days post-labeling.

5.3.5 In-vitro MRI

Immediately after pelleting, the cell pellet-containing tubes were taken to MRI and placed in a custom-made ULTEM™ resin holder. Imaging was performed on a clinical scanner (Achieva 3.0 T TX, Philips Medical Systems) using a 32-channel head coil. T_1 mapping was performed using inversion recovery turbo spin echo: TR = 3000 ms, TE = 18.5 ms, 5 cm field-of-view, 3 mm slices, 0.5 × 0.5 mm in-plane resolution, and TI = [50, 100, 250, 500, 750, 1000, 1250, 1500, 2000 and 2500] ms. After image acquisition, the data was analyzed on a 3-mm deep cylindrical volume

within each cell pellet. T_1 values were calculated pixel-by-pixel (~50 pixels per vial) using in-house software developed in Matlab (ver. 8.1) following the method of ref.[399].

5.3.6 Quantification of Intracellular Manganese Content

To quantify manganese content on a per-cell basis, 0.2 mL aliquots of the previously imaged cell pellets were digested by the addition of one millilitre of 70% ultrapure analytical grade HCl and sonication at 40 °C for 30 minutes. The solution was then diluted to a final volume of 6 mL with ultrapure water. The final solution was run through a 0.22-µm filter to remove residual large protein, thus leaving a solution containing the $MnPNH_2$ that was taken up by cells. These samples were then run on an inductively coupled plasma atomic emission spectrometer ICP-AES (Optima 7300 DV ICP AES). ICP-AES passes this solution through a plasma flame to excite the manganese, which then emits a signal at 293 nm that is converted into parts-per-billion (ppb) of Mn in the solution. This value was then divided by the number of cells to give an approximation of the amount of Mn in one cell.

5.3.7 Cell Viability

To assess the effect on $MnPNH_2$ on cell viability, human ESCs were grown in 6-well plates until colonies reached 60% confluency. Wells were labeled with $MnPNH_2$ for 24 hours at 0, 0.1, 0.2, 0.3, 0.4, and 0.5 mM. Once labeling was complete, the contrast agent-containing media was aspirated, and cells were rinsed three times with room temperature PBS to eliminate residual extracellular contrast agent. Since human ESCs grow in colonies, complete dissociation into single cells was necessary to perform the trypan blue assay. The cells were then removed from the wells and suspended in 3 mL of PBS in 15-mL tubes for counting. Aliquots of 1 mL volume from each sample were then automatically mixed with trypan blue and counted on a Vi-Cell XR Cell Viability Analyzer (Beckman Coulter) with default image gating. Fifty separate images were taken and counted for viability. This trial was repeated three separate times to ensure statistical relevance.

5.3.8 Stem Cell Differentiation into Embryoid Bodies

The essence of using stem cells for therapy is their ability to differentiate into different cell types. Therefore, any contrast agent employed for cell labeling and tracking cannot adversely affect

differentiation potential. To confirm that labeled human ESCs maintained their innate ability to differentiate, four wells of a six-well plate with roughly 60% confluent human ESC colonies were labeled with $MnPNH_2$ for 24 hours, with two wells at 0.2 mM and two others at 0.5 mM. After labeling, the contrast agent-containing media was aspirated and cells were rinsed three times with room temperature PBS to eliminate residual extracellular contrast agent. The cells were then removed and plated into 12-well untreated, uncoated plates for suspension culture. Each original well was split into 6 of the 12-well plate wells with 2 mL of complete mTeSR media and incubated on a shaker spinning at 60 rpm and left for 5 days to assist aggregation.

Media was subsequently changed every four to five days with care not to disturb the embryoid bodies until day 14 for imaging. To prepare for imaging, the embryoid bodies were gently rinsed three times with PBS, fixed with 4% paraformaldehyde for 10 minutes at room temperature, and labeled with DAPI nuclear stain (Thermofisher Catalog # D1306).

5.3.9 Subcellular Contrast Agent Distribution

The subcellular distribution of a contrast agent determines the degree of contrast change obtained on imaging. To gain insight into where $MnPNH_2$ distributes intracellularly, we employed the apo-version, PNH_2, without the fluorescence-quenching Mn ion. This apo-version is a fluorescent compound with peak absorption around 415 nm and emission around 650 nm[439]. Human ESCs colonies were grown on glass cover slips to 60% confluency and labeled with mTeSR media containing 0.5 mM of $MnPNH_2$ for 24 h. After labeling, cells were rinsed three times with room temperature PBS and fixed with 4% paraformaldehyde at room temperature for 10 minutes. The cover slips were then mounted and imaged on a Leica DMi8 Inverted Microscope using the excitation filter of a DAPI filter cube (350/50 nm) and a DSRED emission filter (605/75 nm). A control sample of unlabeled human ESCs was also prepared as above.

5.3.10 *In-vivo* Rat Study

This study was approved by the Lab Animal Services of the Hospital for Sick Children (protocol #41181), and all procedures were conducted in accordance with the Canadian Council on Animal Care. Cells were labeled for 24 hours with $MnPNH_2$ at 0.22 mM, which is approximately less than

half the maximum concentration tested *in vitro*. Immediately after labeling, cells were collected, suspended in mTeSR media in Falcon tubes, and transported to the MR scanner. Female adult Sprague Dawley rats ($N = 2$) (Charles River Laboratories) weighing 200 g were anesthetized on 3% isoflurane (Forene, Abbott Labs, Baar, Switzerland) in pure oxygen (2 L/min flow rate). Approximately 10 million cells in 0.1 mL media was injected subcutaneously on the dorsal side close to the midline. One rat received an injection of labeled cells, and the other received an injection of unlabeled cells (control). Both rats were also given 0.2 mL saline injections as negative controls. Each rat was then placed prone in an 8-channel wrist coil, lying on a water blanket (HTP-1500, Adroit Medical Systems, Loudon, TN) set at 38 °C to maintain core body temperature. A maintenance dose of 2% isoflurane in pure oxygen was applied throughout imaging. Twenty 1-mm thick sagittal images slices were positioned centered at midline. A 2D T1-weighted spin echo sequence with fat suppression was acquired: repetition time (TR) = 724 ms, echo time (TE) = 13.6 ms, number of signal averaging (NSA) = 3, field of view (FOV) = 100 mm, and 0.6 × 0.6 mm in-plane resolution. To visualize the fluids in all injectate, a 2D T2-weighted turbo spin echo sequence was acquired with the same pixel resolution: TR = 4000 ms, TE = 75 ms, NSA = 2, echo train length = 16.

5.3.11 Statistics

Differences in T1 relaxation times were determined using Analysis of Variance (ANOVA). Changes in T1 with incubation concentrations and labeling interval were analysed with two-way ANOVA, while changes in T1 with post-labeling interval were analysed with one-way ANOVA. Post-hoc analysis was based on the Tukey-Kramer test. Significant changes in cell viability were determined using a two-tailed Student's t-test. Significance was reported at a p-value of 5%.

5.4 Results

Figure **5.2** shows that the success of labeling cells with $MnPNH_2$ can be qualitatively observed by the color of the cell pellets. A gradient of color from white (i.e. unlabeled cell pellets) to progressively darker green can be seen, correlating well with the $MnPNH_2$ concentration used for labeling. The staining can be discerned even on a cellular level.

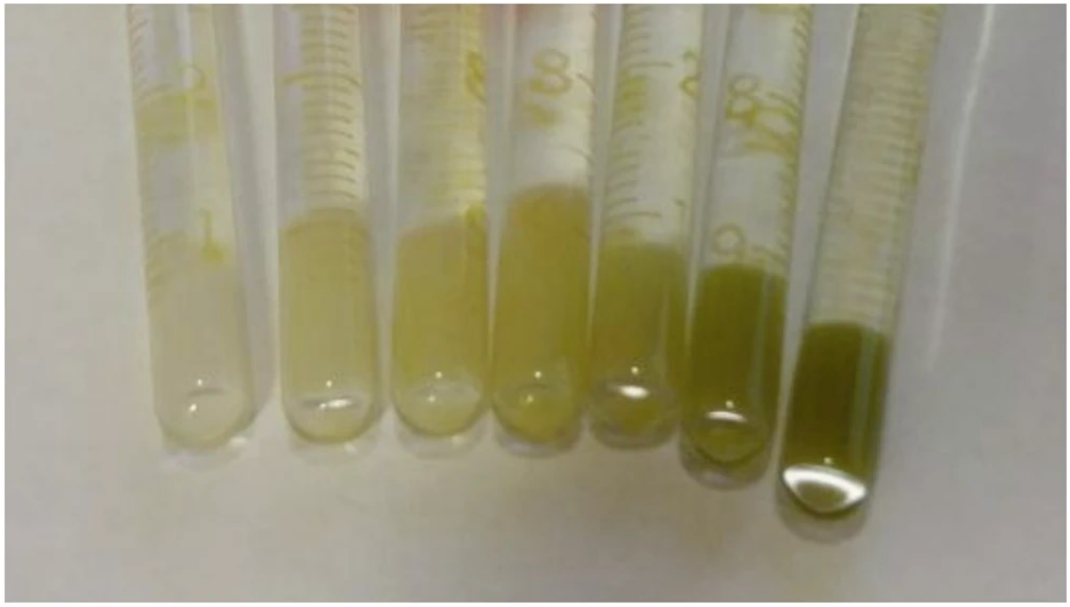

Figure 5.2: Labeled human embryonic stem cells prepared for MR imaging. Cell pellets in borosilicate glass tubes show characteristic dark green of the porphyrin contrast agent. A darker green corresponds to increased contrast uptake.

The efficacy of $MnPNH_2$ as a T_1 contrast agent is shown in Figure **5.3**. Significant decreases in T_1 relaxation times were achieved even for short labeling intervals and low incubation concentrations. The decreases in T_1 in all labeled cells were significantly different from unlabeled controls ($P < 0.05$), and there was a significant difference between the two labeling intervals of 2 and 24 hours ($P < 0.05$). However, the anticipated dependence of T_1 on incubation concentration was observed only for a labeling interval of 24 hours but not 2 hours. Table **5.1** summarizes intracellular Mn quantification from ICP-AES, which is seen to corroborate T_1 relaxivity measurements. A retention study of cells labeled at 0.5 mM $MnPNH_2$ for 24 hours revealed that substantial contrast remained within the first 24 hours post-labeling but thereafter decreased towards baseline levels, with insignificant T_1 contrast after 2 days (Figure **5.4**).

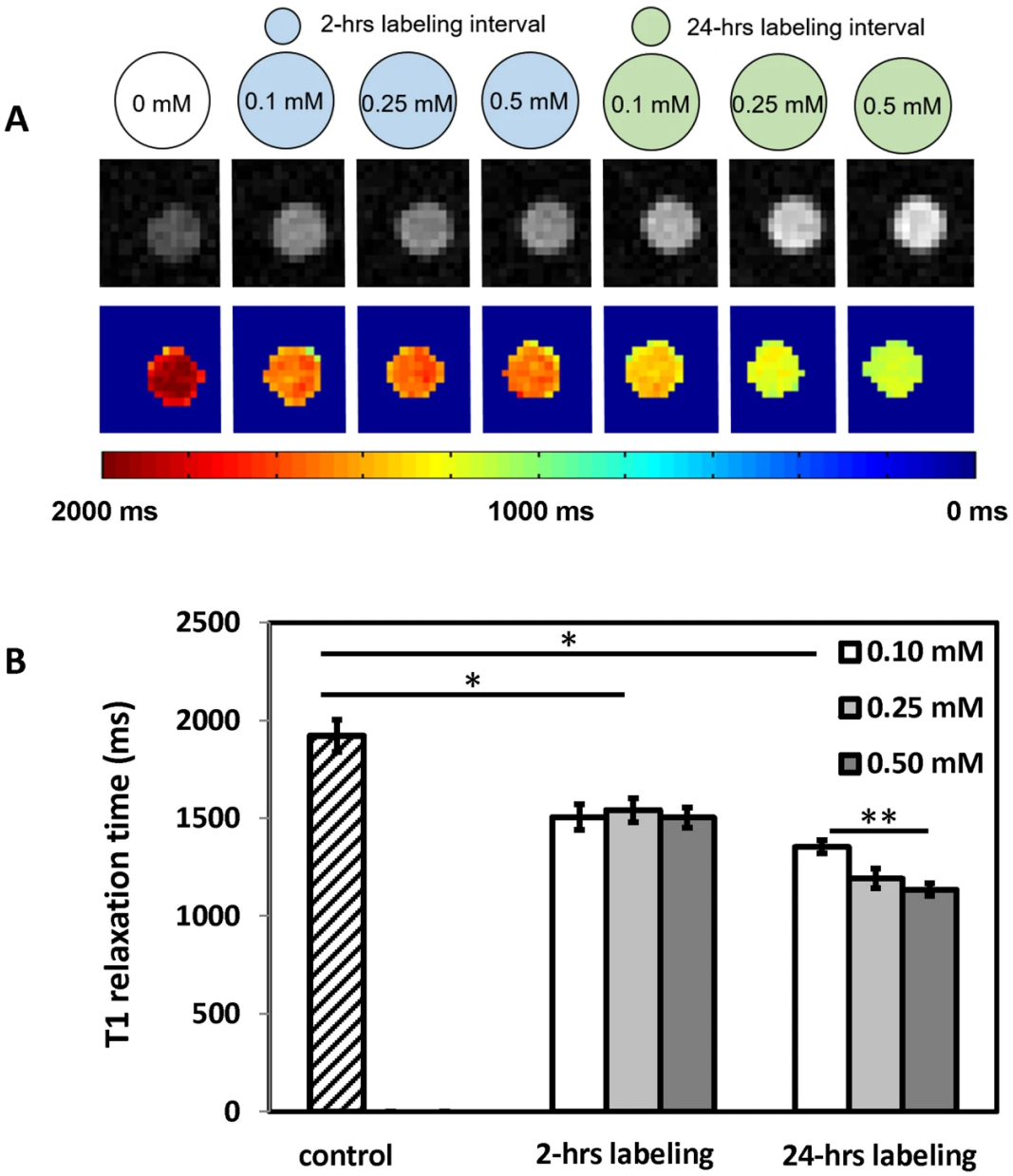

Figure 5.3: Impact of labeling conditions on reductions in T_1 relaxation times (**A**) MRI of labeled human embryonic stem cells on 3-Tesla scanner. T_1-weighted inversion-recovery images of cells labeled for different time intervals (2 and 24 hours) and various incubation concentrations (top row), and corresponding T_1 map (bottom row). (**B**) Mean T_1 relaxation times for unlabeled cells and human embryonic stem cells labeled under different conditions. Error bars represent standard deviation. *Denotes significant difference ($P < 0.05$) between control and different labeling intervals. **Denotes significant difference ($P < 0.05$) with contrast concentration within the same labeling interval.

Sample	Mn Concentration/pellet (ppb)	Mn Concentration/cell (mol)
Control	BDL	BDL
2-hour labeling interval		
0.10 mM	8.82	1.05e-11
0.25 mM	13.5	1.61e-11
0.50 mM	19.1	2.28e-11
24-hour labeling interval		
0.10 mM	12.4	1.47e-11
0.25 mM	18.0	2.14e-11
0.50 mM	46.9	5.59e-11

BDL: below detection level.

Table 5-1: Manganese content in cell pellet digests as measured on ICP-AES.

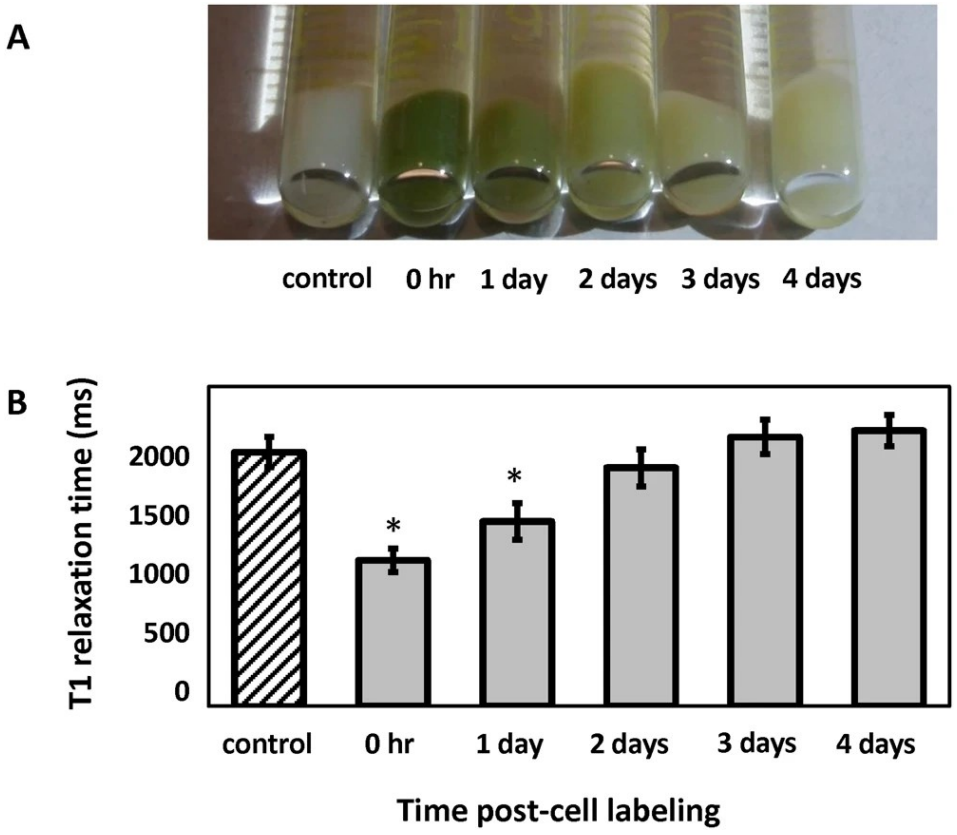

Figure 5.4: **Retention of contrast in labeled human embryonic stem cells**. (**A**) Cell pellets visibly lose the green color imparted by the porphyrin contrast agent with longer intervals post-labeling. (**B**) T_1 relaxation times for unlabeled control cells and cells labeled at 0.5 mM $MnPNH_2$ for 24 hours at different times post-labeling. T_1 has returned to baseline levels by 48 hours. Error bars represent standard deviation. *Denotes significant difference ($P < 0.05$) between control and different post-labeling intervals.

Figures **5.5-5.7** demonstrate that the contrast agent had no adverse effects on cell colony morphology, cell survival, proliferation, and differentiation potential. In Figure **5.5**, bright-field microscopy images of representative colonies are shown for unlabeled control cells and cells at 24, 48, and 72 hours after a 24-hour labeling interval. Colonies at 96 hours post-labeling show similar morphology. These images illustrate that other than a slight coloration of cells from $MnPNH_2$, the labeling itself had no effect on colony size, shape, and distribution. Cell viability was also unaffected, even for the longest labeling interval of 24 hours (Figure **5.6**). To further confirm the absence of adverse effects on cell behavior and function, labeled human ESCs were successfully differentiated into embryoid bodies. Every well containing labeled ESCs developed into embryoid bodies, and these all displayed the same size and appearance regardless of their origin (i.e. whether they were differentiated from labeled or unlabeled human ESCs) (Figure **5.7**).

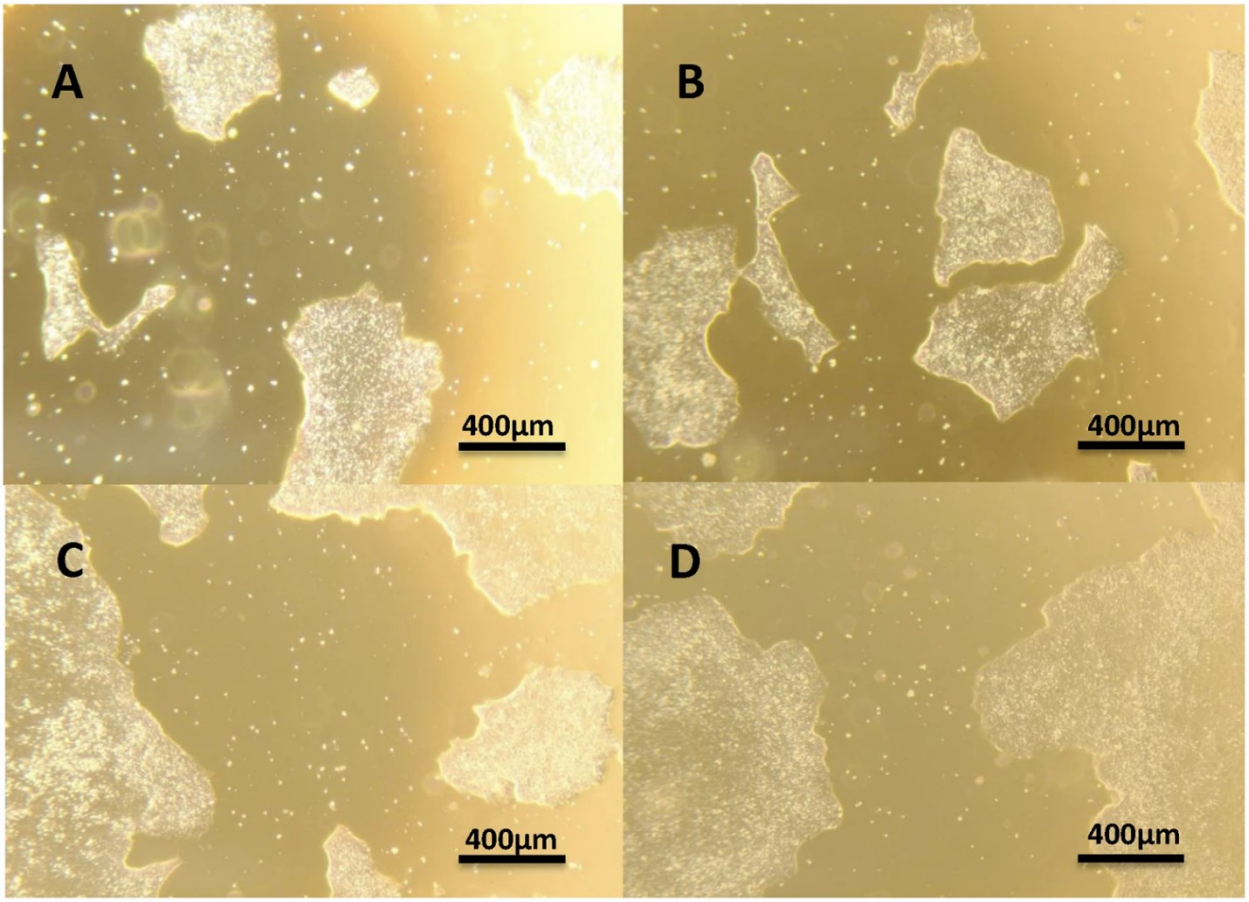

Figure 5.5: Phenotype of human embryonic stem cells on microscopy. Representative bright-field images showing human embryonic stem cell colonies before labeling and at 24, 48, and 72 hours after labeling at 0.5 mM $MnPNH_2$ for 24 hours. Cell morphology and colony shape are unchanged (4× magnification).

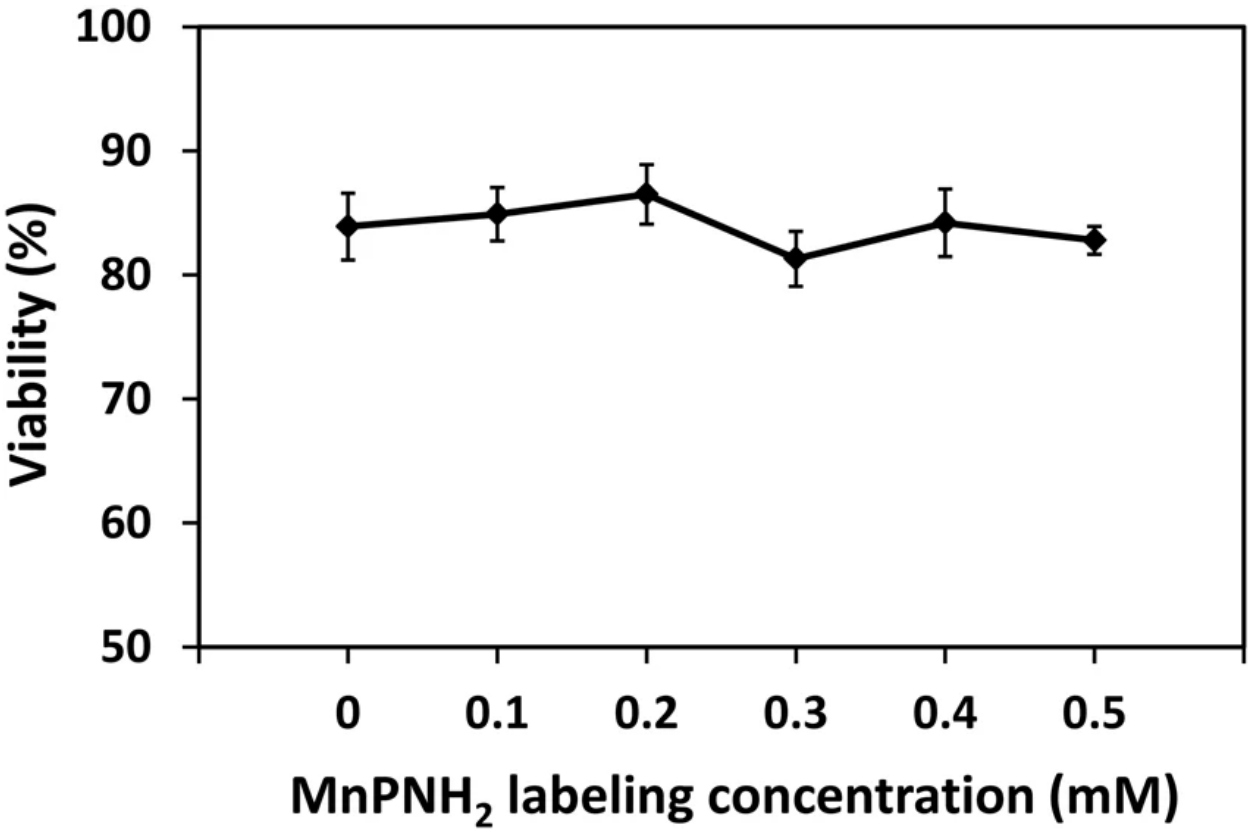

Figure 5.6: Cell viability. Viability assessed on trypan blue assay for different incubation concentrations and 24-hour labeling. Shown are mean values and standard deviation ($N = 3$).

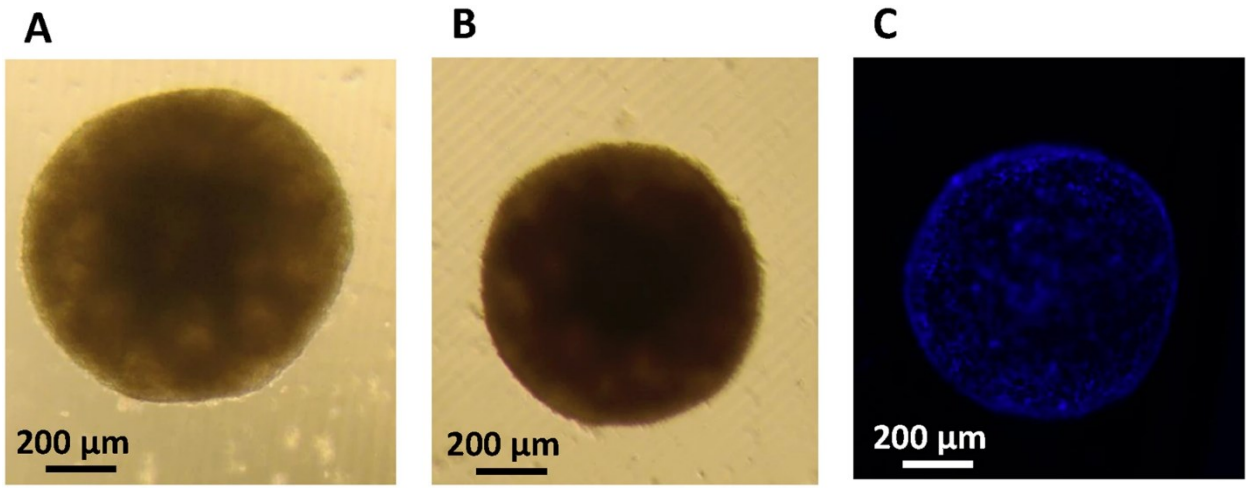

Figure 5.7: Embryoid body formation. (**A**) Brightfield image of a 21 day-old embryoid body derived from unlabeled human embryonic stem cells (10× magnification). (**B**) An embryoid body 21 days after stem cells were labeled at 0.5 mM $MnPNH_2$ for 24 hours and (**C**) corresponding DAPI nuclear stain fluorescence image. Shown in each panel is a single embryoid body formed from thousands of embryonic stem cells; individual cells are seen on the fluorescence image.

Using the non-metalated version of $MnPNH_2$ for labeling human ESCs, we were able to map the subcellular distribution of the contrast agent on fluorescent microscopy. Fluorescence was detected throughout the cells, but a stronger signal was observed as clumps near the cell periphery and in the nucleus (Figure **5.8**). These observations suggest that the contrast agent is, indeed, internalized and not simply bound to edges of the cell membrane, with preferential localization in the nucleus.

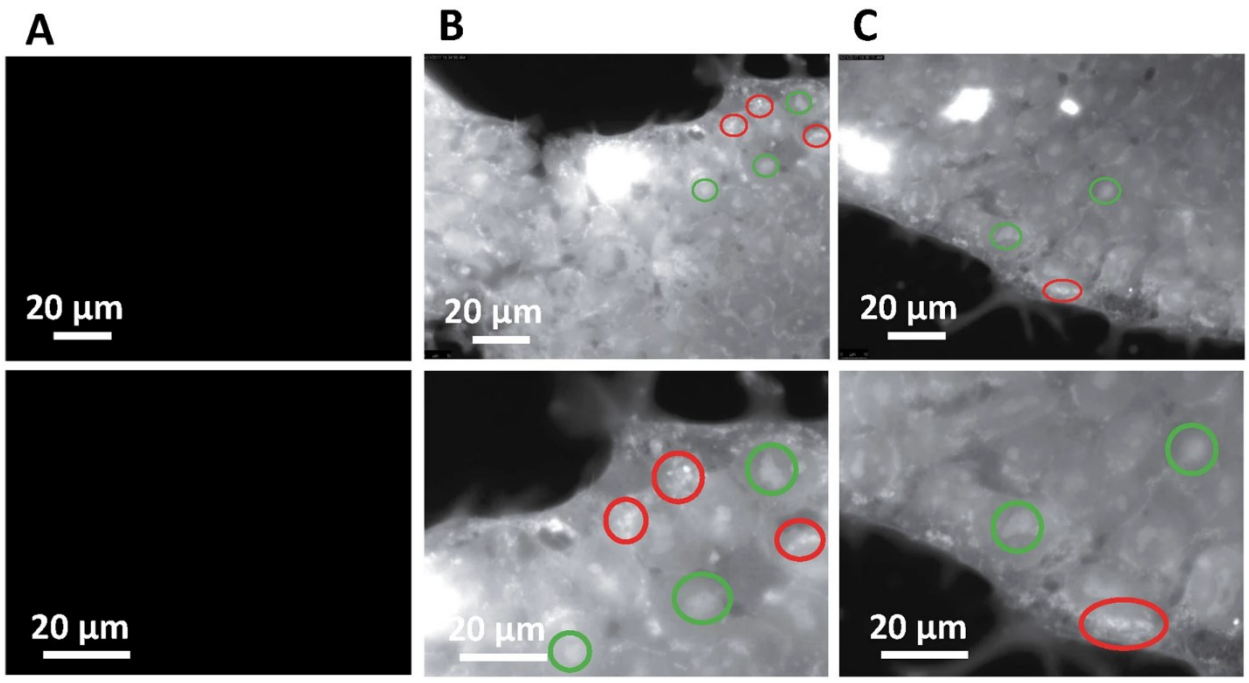

Figure 5.8: Subcellular distribution of contrast agent. Fluorescence imaging reveals the subcellular distribution of PNH2 after a 24-hour labeling interval. (**A**) Unlabeled cells show no fluorescent signal (63× magnification). (**B**) Cells labeled with 0.5 mM of the apo-porphyrin for 24 hours (63× magnification) with (**C**) further digital zoom. Red circles indicate numerous bright accumulations around the cell periphery and inter-connective space of the colony. Green circles highlight increased signal from higher porphyrin concentration in the nucleus.

In-vivo imaging of rats injected with labeled and unlabeled human ESCs demonstrated superior detection sensitivity afforded by $MnPNH_2$ (Figure **5.9**). Labeled cells can be clearly seen as a brightly enhancing volume at the site of injection on T_1-weighted spin-echo images, whereas unlabeled cells and saline are both isointense, as expected. T_2-weighted images are shown only to demonstrate their inability to delineate cells, as hyperintensity represents the fluid in which cells are suspended.

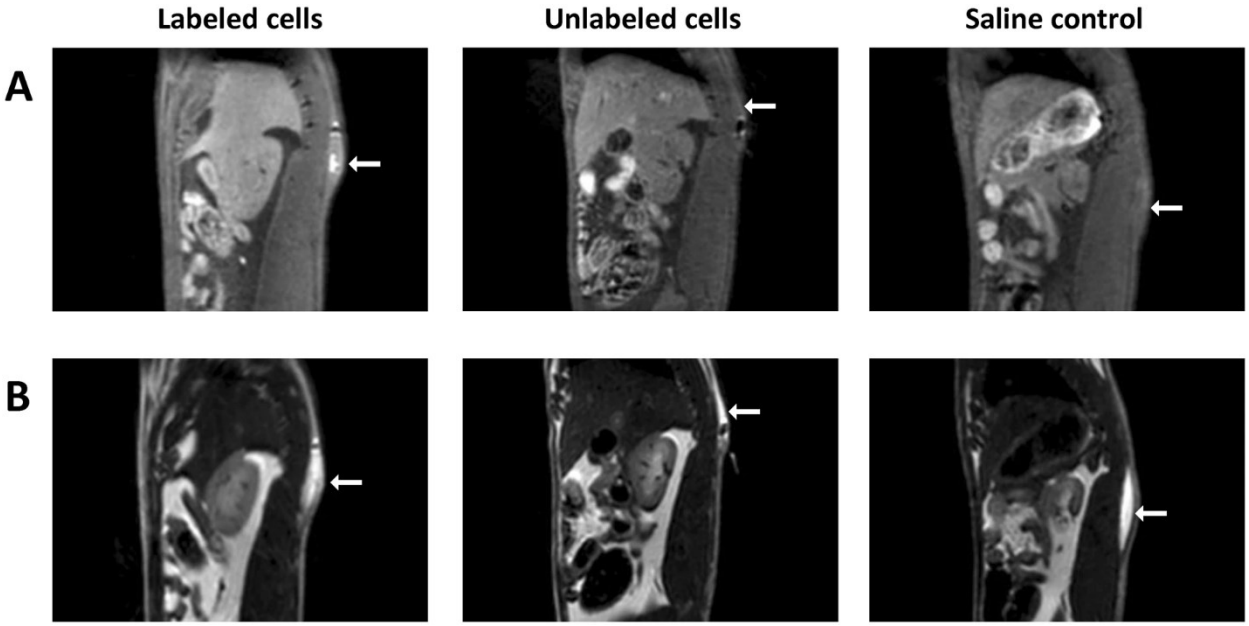

Figure 5.9: *In-vivo* MR imaging of implanted human embryonic stem cells in rat. Cells labeled at 0.22 mM $MnPNH_2$ for 24 hours were injected subcutaneously on the dorsal side of adult rats. T1-weighted spin-echo images with fat suppression (**A**) clearly show an enhancing volume where the labeled cells were injected, whereas unlabeled cells and saline were isointense against native tissue. T2-weighted turbo spin-echo images were acquired to localize the fluid in all injections, independent of whether or not cells were present.

5.5 Discussion

The main driving motivation for this work was to create an efficient cell-labeling T_1 contrast agent with good potential for clinical translation. This requirement meant that the agent had to be both safe and easily synthesized. We have shown that $MnPNH_2$ is easy to synthesize and requires a simple one-step chemical reaction to produce the final functional agent. The single step of metalating the porphyrin can be readily carried out in labs that are not specialized in MR contrast agent chemistry[440], thus representing a viable alternative for many research groups who are interested in employing MR contrast agents for cell tracking. Another advantage of our agent is that no complicated procedure to assist cell uptake is required (e.g. electroporation), as the agent need only be dissolved in the media in which cells are cultured.

The other major consideration of safety is even more important for any cell-labeling contrast agent intended for meaningful *in-vivo* pre-clinical studies or eventual clinical translation. Meeting this

requirement of safety cannot be more critical than in regenerative medicine, where the labeled stem cells are the source for new tissue growth. The labeling agent cannot exert adverse effects on cell function: this includes cell viability, proliferation, and, most importantly for stem cells, differentiation potential. We have shown the safety of $MnPNH_2$ on a cellular level through a panel of morphological and functional assessment: light microscopy, trypan blue viability assay, proliferation and embryoid body differentiation[441]. While more extensive testing can be performed, this panel represents the key initial indices that need to be probed to confirm safety.

In regard to T_1 efficiency as a cell-labeling contrast agent, $MnPNH_2$ produced nearly a two-fold reduction in T_1 relaxation times, which enabled high signal-to-noise contrast for labeled cells. The one interesting observation we made was related to the absence of significant T_1 changes with incubation concentration when the labeling interval was 2 hours. This implies that the rate of absorption of $MnPNH_2$ was too slow and was likely the rate-limiting step for short labeling intervals. To reap the benefit of higher incubation concentrations, a 24-hour labeling interval was necessary. However, notice that changes in T_1 did not scale with intracellular Mn content. It is entirely possible that the contrast agent aggregated in the cytoplasm initially, which led to a plateau in T_1 despite a higher absolute ion content. With time, aggregation lessened and the agent exerted a greater T_1 effect.

To gain an appreciation for $MnPNH_2$–induced contrast on MRI, the intracellular distribution of the fluorescent version, PNH_2, was observed for a labeling interval of 24 hours and an incubation concentration of 0.5 mM. This was done to ensure maximum fluorescence signal. Peak brightness was detected as clumps at the edges of cells, indicating that PNH_2 aggregated potentially in vacuoles in the cytoplasm. Also, the nucleus appeared brighter than the cytoplasm, indicating overall denser nuclear accumulation, in agreement with a previous study that confirmed nuclear penetration of the apo-porphyrin[442]. Since the agent is present in the nucleus, chromosomal assay or DNA sequencing can be performed in future work to show it is not negatively interacting with the cell's DNA. Furthermore, real-time microscopy in living cells would give better insight into the dynamics of the agent's uptake and distribution in cells and possibly shed light on the impact of different labeling intervals.

Further increases in T_1 contrast of labeled cells may be desired. To determine the maximum achievable contrast, a much larger range of incubation times and contrast concentrations need to be tested. It would be necessary when testing higher doses to implement more extensive and detailed assays to ensure off-target effects in cells are absent. For example, in addition to the trypan blue exclusion test for cell membrane integrity[443], we would also perform a TUNEL assay to rule out apoptotic cell death[444]. The potential for genetic or long-term alterations on cell function also need to be ruled out using chromosomal karyotyping, or DNA sequencing, although genetic alternations are not anticipated. Lastly, full differentiation into the desired mature cell type would be performed to ensure both structure and function is maintained.

As with all exogenous contrast agents used for cell labeling, the contrast agent will be diluted as cells divide and the agent becomes distributed amongst daughter cells. Depending on the rate of cell division, one can expect the contrast from labeled cells to be retained over the course of a few days, perhaps even up to a week for slowly dividing cells. In addition to the dilution effect, however, contrast agents will leak back out across the cell membrane unless a complex mechanism is employed to "lock" the agent in[280,435]. Our retention study showed that labeled cells maintained significant contrast within the first 24 hours post-labeling. For many regenerative medicine applications, the first 24 hours post-cell transplantation represents the most challenging interval for cells to survive through. Being able to monitor cell survival and, in moving tissues like the heart, cell retention during this time span is key to informing on whether additional cell injections are needed and where.

Given the preponderance of MR contrast agents utilized for cell tracking, with none approved for clinical use, it is important to compare our agent with other ones that have been employed in the past. Negative contrast iron oxide nanoparticles represent the vast majority of cell-tracking applications. However, they cannot be compared to small molecule T_1 agents due to differences in mechanisms of cell uptake and affinity for macrophages. In truth, there is no easily accessible T_1 agent for MR cellular imaging. Clinically approved gadolinium-based agents are not designed for labeling cells, as their hydrophilicity renders them impermeable to the cell membrane. Different formulations of T_1 agents reported in the literature require specialized chemistry for their synthesis, which render them immediately inaccessible to most labs[280,445].

A more subtle issue with potential toxicity pertains not to the labeled cells but to the organism receiving the cell transplant. Although manganese is present at low levels physiologically, it is a neurotoxin at high concentrations in the body. Many early studies on neuroimaging have reported toxicity of manganese chloride ($MnCl_2$)[446,447]. However, note that these studies used *free* Mn ion, which is very different from the Mn-porphyrin complex we report here. The porphyrin ring provides extremely strong thermodynamic stability of the bound Mn ion, which puts this compound in a league different from $MnCl_2$ and Mn nanoparticles. Unlike gadolinium, which is toxic even in minute amounts, Mn is toxic only at high level. In rats, LD50 of $MnCl_2$ has been calculated to be 7.5 mmol/kg[445]. If we assume we inject 10 million cells into a 300 g rat (and this is a very high number of cells), each cell carrying the maximum level of Mn we measured at 5.59×10^{-8} mmol/cell, we have equivalently 1.86 mmol/kg, which is well below the LD50 level for *free* Mn. So, in the greatly exaggerated scenario where *all* the Mn ions dissociate from the porphyrin ring, we are still administering safe levels of Mn.

Finally, detection sensitivity is the single most important parameter ascribed to any contrast agent, especially for T_1 agents that are less sensitively detected than negative-contrast iron oxide nanoparticles. This concept of detection sensitivity goes beyond simply knowing the relaxivity of the agent but considers also the number of cells in a typical imaging voxel, noise level, and so on. In our *in-vitro* studies, there were approximately 75,00 cells per voxel with a volume of $0.5 \times 0.5 \times 3$ mm^3. A rigorous study of the minimum number of detectable cells is beyond the scope of this manuscript and would require titrating the cell density in cell suspensions *in vitro* and investigating the contrast-to-noise as a function of anatomical location *in vivo*. To answer the question of adequate detection sensitivity for our contrast agent, we took a pragmatic approach and performed an *in-vivo* study in rats. When labeled cells are injected in an animal, cell density is governed naturally by how easily the cells could occupy native tissue, which is very different from the artificial scenario of being densely packed in a cell pellet. Our rat imaging results clearly demonstrate the high detection sensitivity provided by a modest dose of $MnPNH_2$ for cell tracking *in vivo*.

There are a number of avenues to explore in future work. One of these is to optimize labeling with respect to contrast agent concentration and labeling interval for human ESCs and to repeat this

optimization for several different mature cell types of interest for regeneration. Karyotyping will also be performed now that the key indices of cell function (i.e. viability, proliferation, differentiation) have been shown to be unaffected by labeling. *In-vivo* studies are also planned for preclinical models of stem-cell therapy in relevant anatomical locations for regeneration, such as the heart muscle wall subsequent to a myocardial infarction.

5.6 Conclusion

This study has presented a MRI contrast agent for T_1-based cellular imaging and tracking of human embryonic stem cells. We achieved efficient labeling of human ESCs using a manganese-based contrast agent that is simple to synthesize and can be readily adopted in research labs that wish to employ MRI agents for cell labeling. No adverse effects on cell viability or differentiation potential were observed, and subcellular assessment revealed that the agent passed through the cell membrane and even accumulated in the nucleus. Cellular contrast was maintained for 24 hours post-cell labeling, and *in-vivo* imaging of transplanted cells in rats demonstrated superior sensitivity of detection. Future studies will extend this contrast agent to other cell types for tissue regeneration, such as for spinal cord and muscle.

5.7 Contributions

H.-L.M. C contributed to: overall direction and conception of study, design of MR acquisition protocol and data acquisition, analysis and interpretation of data, *in-vivo* rat study, writing the manuscript, and final approval of the manuscript. A.V. contributed to: cell study design, cell culture and assays, cell microscopy, cell labeling studies, analysis and interpretation of data, writing manuscript, and final approval of manuscript. D.A. S. contributed to: synthesis, characterization and quantification of MnPNH2, cell labeling studies, cell retention studies, *in-vivo* rat study, writing manuscript, and final approval of manuscript. S.L. contributed to: cell retention studies and *in-vivo* rat study. T.G. contributed to: *in-vivo* rat study. I.E.H. contributed to synthesis of PNH2, writing manuscript, and final approval of manuscript.

Chapter 6 : Bright ferritin - a reporter gene platform for on-demand, longitudinal cell-tracking on MRI

This work has been published in *iScience* Volume 23, Issue 8, Article Number 101350, (2020) and has been reproduced with permission from the respective publishers.[448] Significant portions of this chapter have also been published in the patent listed below.

Szulc DA, Lee XA, Cheng HY, Cheng HL. "Bright ferritin - a reporter gene platform for on-demand, longitudinal cell-tracking on MRI," *iScience.* 2020; 23 (8): 101350.
doi: *10.1016/j.isci.2020.101350*

Cheng HLM, Szulc DA, Cheng HYM, "Ferritin for cellular tracking utilizing T1-weighted MRI", United Kingdom. Application No.2004892.2. Filed April. 2, 2020.

6.1 Abstract

A major unresolved challenge in cell-based regenerative medicine is absence of non-invasive technologies for tracking cell fate in deep tissue and with high spatial resolution over an extended interval. MRI is highly suited for this task, but current methods fail to provide longitudinal monitoring or high sensitivity, or both. In this study, we fill this technological gap with the first discovery and demonstration of in-vivo cellular production of endogenous bright contrast via a MRI genetic reporter system that forms manganese-ferritin nanoparticles. We demonstrate this technology in human embryonic kidney cells genetically modified to stably overexpress ferritin, and show that in the presence of manganese, these cells produce far greater contrast than conventional ferritin overexpression with iron or manganese-permeable cells. In living mice, diffusely implanted bright-ferritin cells produce the highest and most sustained contrast in skeletal muscle. The bright-ferritin platform has potential for on-demand, longitudinal, and sensitive cell tracking in vivo.

6.2 Introduction

In-vivo cell tracking is valuable across a multitude of applications ranging from stem cell therapy to studies of cancer metastasis. To visualize and distinguish the cells of interest, we must impart

to them a differential contrast against background tissue. The simplest approach is to label the cells directly, prior to injection or implantation, with an image modality-specific contrast agent, such as iron oxides for magnetic resonance imaging (MRI)[449] or 18F-FDG for nuclear medicine imaging[450]. This exogenous labeling approach, however, works well only for short-term studies and cannot attain the desired capability for monitoring over the long term. Multiple factors underlie this shortcoming, foremost of which are label dilution upon cell division, leakage of contrast agent from cells[389], and non-specific labeling of macrophages that take up contrast agents released from dying cells[431]. Longitudinal cell tracking requires a method that provides sustained contrast specific to the viable cells of interest. To date, the most promising solution to longitudinal cell tracking in vivo is via reporter genes.

A variety of reporter genes have been proposed over the years for use with different imaging modalities. Of note are firefly luciferase for bioluminescence imaging[451], herpes simplex virus-1 thymidine kinase for nuclear medicine[452], and ferritin for MRI[350]. Amongst the modalities suitable for cell tracking, MRI is particularly attractive, because it uniquely affords flexible background tissue contrast, unlimited tissue penetration depth, absence of radiation, and superior spatial resolution compared to nuclear medicine and bioluminescence imaging[453]. Ferritin, a polymeric iron storage protein, is the most widely used amongst MR reporters[341,454], as other MR gene reporter systems are less accessible due to very low sensitivity or the requirement for specialized coils tuned to different nuclei[455,456]. Despite the success achieved with ferritin for cell tracking, however, there remain a number of technical challenges. The change in MR relaxation time is frequently small and the resulting signal drop modest[366,367], very high levels of ferritin and/or iron are required to achieve the requisite detection sensitivity[457,458], and the onset of signal change is slow as iron requires days to accumulate[368]. Sensitive and longitudinal cell tracking remains an unmet need.

In this work, we describe a “bright-ferritin” mechanism for sensitive, longitudinal cell tracking in vivo. This approach uses the cell’s ferritin machinery to self-assemble manganese (Mn) nanoparticles, which confer a positive contrast on MRI. While previous work in the 1990s had shown the in-vitro nucleation and growth of Mn particles in the cavity of extracted ferritin protein under harsh chemical conditions[459–461], we report herein, for the first time, the in-vivo self-assembly of endogenous Mn nanostructures. The bright contrast gleaned from Mn-ferritin

nanoparticles can overcome many limitations associated with conventional negative contrast from ferritin overexpression. The main advantages are: (1) higher specificity, as negative contrast cannot be clearly distinguished from intrinsically dark sources (e.g. tissue/air interface, microbleeds); (2) higher sensitivity, especially in intrinsically dark background tissues (e.g. skeletal muscle); (3) accurate delineation of cell distribution (i.e. no "blooming" artifact); and (4) the potential for quantitation. Our comparison of "bright-ferritin" against conventional "dark-ferritin" cell imaging both in vitro and in vivo confirmed a substantially greater sensitivity of cell detection for the former. "Bright-ferritin" is also shown to rival the sensitivity derived from another positive-contrast reporter gene, the divalent metal transporter-1 (DMT-1), a membrane channel protein whose overexpression leads to increased transmembrane transport of free Mn ions[356]. Our exploitation of the cell's machinery for endogenous production of bright-contrast Mn-ferritin nanoparticles presents a paradigm shift in the utilization of ferritin for on-demand, longitudinal and sensitive in-vivo cell tracking in cell-based therapeutics.

6.3 Materials and Methods

6.3.1 Experimental design

In designing our MR reporter gene system, we sought to adhere to design criteria that would maximize the potential of our system for future translational work. With this in mind, we introduced our ferritin transgene using non-viral CRISPR technology for a single, targeted insertion at the "safe-harbor" locus. Once stable integration was attained, the next task was to optimize in vitro the labeling conditions (i.e. with metal ion supplementation) that would confer sensitivity of detection at the lowest possible dose. This, again, is consistent with our general philosophy of using the lowest overexpression, dosing, etc. necessary to achieve sensitivity of cell detection. In-vivo testing in immune-compromised mice was undertaken to demonstrate the practicality of the bright-ferritin system. Finally, extensive validation experiments were designed and undertaken to provide a biophysical understanding of how "bright-ferritin" contrast arises in cells.

6.3.2 DNA cloning, amplification, and purification

Gene synthesis of human ferritin heavy chain 1 (FTH1) and human ferritin light chain 1 (FTL1), codon-optimized for expression in human cells, was conducted by Genscript (Piscataway, NJ). The FTL1 gene fragment was subcloned into the pcDNA3.1(+)-P2A plasmid, upstream of and in-frame with the sequence for the P2A self-cleaving peptide. The Kozak sequence GCCACC was introduced before the start codon of FTL1 to promote protein expression. The FTH1 gene fragment was cloned downstream of the P2A sequence. The FTL1-P2A-FTH1 transgene sequence was then cloned downstream of the CAG promoter in a pzDonor plasmid. The final construct, pzDONOR-CAG-FTL1-P2A-FTH1-PGK-eGFP-BleoR, expresses FTL1-P2A-FTH1 under the control of the CAG promoter and the fusion of eGFP and the bleomycin resistance gene under the control of the PGK promoter (Figure **6.1A**).

Gene synthesis of mouse DMT-1 carrying an internal HA tag[462] codon-optimized for expression in human and mouse cells, was likewise carried out by Genscript. Kozak and Shine Dalgarno sequences were added to increase the efficiency of translational initiation. The DMT-1 transgene was first subcloned into the pcDNA6/V5-His A plasmid and then cloned into the pzDonor plasmid to generate the final construct, pzDONOR-CAG-DMT-1-PGK-eGFP-BleoR (Figure **C1A**, Supporting Information-Appendix C).

For propagation of plasmids, DH5α *E. coli* cells were transformed and grown in Lysogeny Broth (LB) media supplemented with antibiotic. Plasmids were purified using Qiagen HiSpeed Plasmid Maxi kits (#12662). DNA concentration and purity were assessed quantitatively by UV absorbance at 260 and 280 nm using the NanoDrop™ 2000 UV Spectrometer (Thermo Scientific). Plasmids were verified by sequencing as well as restriction digestion analysis.

6.3.3 Stable cell line generation

All cell lines were generated with a non-viral CRISPR/Cas9 system for targeted integration into the AAVS1 safe-harbor locus. HEK293 cells were cultured in Dulbecco's minimal essential medium (DMEM) with 10% fetal bovine serum (FBS) and 1% penicillin/streptomycin (P/S). Cells were co-transfected with the AAVS1-T2-CRISPR vector (Addgene, #7283) along with either pzDONOR-CAG-FTL1-P2A-FTH1-PGK-eGFP-BleoR or pzDONOR-CAG-DMT-1-PGK-

eGFP-BleoR constructs, resulting in CRISPR/Cas9 targeting of the reporter transgenes to the AAVS1 locus in human cells. Cells were transfected using a 3:1 ratio of polyethyleneimine (PEI) to vector DNA for 24 hours. Cells were then sorted for eGFP expression with a BD FACSAria II flow cytometer before expansion of single colonies to produce monoclonal cell lines. Clones were screened by polymerase chain reaction (PCR) to confirm integration of the reporter transgene into the genomic DNA and by immunoblotting to confirm transgene protein overexpression.[463] Only those clones that exhibited the highest level of overexpression of DMT-1 or ferritin relative to wild type were selected for further tests.

6.3.4 Polymerase chain reaction

Genomic DNA was extracted from select clones and analyzed by polymerase chain reaction (PCR) for the presence of the correct transgene. To detect the presence of the DMT-1 transgene, forward and reverse primers recognizing HA and DMT-1, respectively, were used in the PCR amplification reaction (HA-fwd:5'-CCCTATGACGTGCCTGATTACGC-3'; DMT-1-rev: 5'-CATCCCAGGTAGAACACGAAGGTC-3'). To detect the presence of the ferritin transgene, forward and reverse primers recognizing P2A and FTH1, respectively, were used (P2A-fwd: 5'-GGAGCTACTAACTTCAGCCTGCTG-3'; FTH1-rev: 5'-CTTCCGCAGATTGGTCACGTGATC-3'). Samples were electrophoresed on agarose gels and imaged with a Bio-Rad Gel Doc XR+. The pzDONOR-CAG-FTL1-P2A-FTH1-PGK-eGFP-BleoR and pzDONOR-CAG-DMT-1-PGK-eGFP-BleoR plasmids were used as template in positive control PCR reactions, whereas water and DNA extracted from wild type HEK cells were used as negative controls.

6.3.5 Western blotting

Cultured cells were washed twice in PBS and lysed in RIPA lysis buffer supplemented with protease inhibitors through gentle trituration through a 23-gauge needle. Lysates were centrifuged at 20,000 g and supernatants were collected and quantified for protein concentration using the Bradford assay. Proteins were resolved by SDS-PAGE and blotted onto PVDF membranes. Membranes were blocked with 5% skim milk in TBS-T (0.05%) for 1 hour at room temperature

(RT), and incubated overnight at 4 °C with the following primary antibodies at 1:1000 dilution: anti-ferritin (Abcam, ab75973); anti-DMT-1 (Abcam, ab55735); anti-2A peptide (Novus Biologicals, NBP2-59627); alpha-tubulin (Abcam, ab2144); and anti-HA (Sigma Aldrich, #11867423001). The next day, membranes were washed 5 x 5 min in TBS-T and then incubated for 1 hour at RT in HRP-conjugated secondary antibody. Chemiluminescent signals were visualized with a Bio-Rad ChemiDoc™.

6.3.6 Transmission electron microscopy

Cells were examined with transmission electron microscopy (TEM) for confirmation of nanoparticle formation and subcellular localization, as described in previous reports for tracking exogenous nanoparticles[464]. Cells were cultured with 0.2mM manganese chloride ($MnCl_2$) for 24 hours before harvesting. Cells were washed three times with complete media for 10-minute durations at 37°C to remove excess Mn. Cells were gently centrifuged for 5 minutes at 300g and re-suspended to remove residual Mn or aggregates before fixation. Primary fixation was carried out in 1% glutaraldehyde and 4% formaldehyde in 0.1M phosphate buffer (pH7.2) for 1 hour at RT. The fixative solution was then replaced, and the sample was left at 4°C overnight. Cells were then washed three times for 30-minute durations with 0.1M phosphate buffer at RT before secondary fixation. Samples were post-fixed with 1% osmium tetroxide in phosphate buffer for 1 hour at RT in the dark and then washed three times in 30-minute durations. Samples were then dehydrated by serial immersion in ethanol solutions of 30, 50, 80 and 95% for 20-minute intervals until 100% for 45 minutes at RT. A final wash with propylene oxide was conducted twice for 15-minute durations. The samples were then infiltrated with epoxy resin using a graded series of epoxy-propylene oxide before solidification with heat (60°C) for 48 hours. Thin sections of 90-100nm were then cut and stained with uranyl acetate and Reynold's lead citrate before imaging on a FEI Talos L120C TEM system with an accelerating voltage of 80kV at the Faculty of Medicine, University of Toronto (Toronto, Canada). TEM imaging was also conducted on purified ferritin extracts from cells labeled with Mn as described above. After washing and harvesting cells, intact ferritin particles were extracted and purified by a gentle immunoprecipitation protocol modified to preserve complexed ferritin nanoparticles. In brief, collected cells were lysed with mild lysis buffer (50mM Tris-HCl pH 7-8.5, 150 mM NaCl, 1% NP-40, 0.1% sodium deoxycholate, and 10%

protease inhibitor) with physical trituration through a 23-gauge needle. Lysates were then spun down at 20,000 g for 10 minutes at 4°C. The remaining pellets were incubated with 1ug of anti-ferritin antibody (ab75973) overnight at 4°C with rocking. Following antibody binding, protein A/G beads were added for 4 hours with rotation. Beads were then collected by centrifugation and washed 3 times in the aforementioned lysis buffer with the addition of 0.1% bovine serum albumin (Bioshop, ALB001). Purified ferritin protein was then eluted with 200mM Glycine-HCl pH 3 at RT and then neutralized with 1M Tris-HCl, pH 9.5. Purified ferritin extracts were then immediately deposited on carbon-film coated grids (CF300-Cu, Electron Microscopy Sciences) that were glow discharged with a PELCOeasiGlow^{TM}. Grids were then washed three times with ultrapure water. Grids were dried by solvent wicking and imaged on a FEI Talos L120C TEM with an accelerating voltage of 120kV at the Faculty of Medicine, University of Toronto (Toronto, Canada).

6.3.7 Inductively coupled plasma atomic emission spectroscopy (ICP-AES)

Manganese presence and content was determined analytically by inductively coupled plasma atomic emission spectroscopy (ICP-AES). Purified ferritin extracted from Mn-labeled cells as previously described was digested with concentrated nitric acid (HNO_3) with TraceSELECT (Fluka Analytical) at 50°C with sonication for 7 hours[301]. Samples were then diluted to 2% w/v HNO_3 before analysis on an Optima 7300 DV ICP-AES spectrometer at the Department of Chemistry, University of Toronto (Toronto, Canada).

6.3.8 Cellular toxicity analysis

To investigate the potential toxicity from overexpressing ferritin or DMT-1, or from iron and manganese supplementation, we assessed metabolic activity, proliferation, and viability of all cells. The WST-1 assay utilizes an UV convertible salt that is activated by cellular esterases. The degree of activation quantitatively measures the rate of enzymatic activity in metabolically viable cells which provides an indication of cell proliferation and metabolic rate. All cells were seeded at an initial density of 2000 cells per well of a 96-well plate and then cultured for 96 hours so that the assay would emphasize any impact on cell proliferation. After 24 hours from plating, cells

were dosed with Mn (0.2mM) for 24 hours or iron (0.9mM) for 72 hours (the optimal labeling conditions required for MR contrast). All cells were washed after supplementation. Prior to imaging, culture medium was removed from each well and replaced with fresh medium containing WST-1 reagent (1:10 dilution) for 1 hour before measuring absorbance at 450 nm with a PerkinElmer Envision 2104 Multilabel Plate Reader (MA, USA).

Cell viability was further assessed by the live/dead viability/cytotoxicity kit for mammalian cells (Molecular Probes, Invitrogen), whereby live cells are stained fluorescent 'green' with a cell permeable/enzymatically activatable dye (Calcein AM, Ex/Em: 494/517nm) and dead cells are stained 'red' by a cell impermeable/DNA binding dye (Ethidium homodimer-1, Ex/Em: 528/617nm). A third cell permeable/DNA binding dye (Hoescht 33342, Ex/Em: 345/460nm, Sigma Aldrich) was utilized for nucleus staining to aid cell counting measurements. All cells were seeded at an initial density of 20,000 cells per well of a 24 well plate and then cultured for 96 hours. After 24 hours from plating, cells were dosed with Mn (0.2mM) for 24 hours and iron (0.9mM) for 72 hours, same as above. All cells were washed after supplementation. Prior to imaging cells were incubated with 2 μM Calcein AM live stain, 4 μM EthD-1 dead stain, and 1ug/ml Hoescht nuclear stain in PBS (1×; pH 7.4) with calcium and magnesium for 45 min at 37°C. Imaging was performed on a Leica DMi8 inverted epifluorescence microscope using a green fluorescent protein (GFP), Texas Red (TXR) and DAPI filter cube to visualize the live, dead, and nuclear stain, respectively.

6.3.9 In-vitro cellular MRI

To assess the capability of each reporter gene for MRI contrast generation, cells were dosed with free iron (ferric ammonium citrate) or manganese before live cell imaging with MRI. Ferritin-overexpressing cells were dosed with either Mn (0 – 0.2mM) or iron (0 – 0.9mM) for 24, 48, or 72 hours until significant contrast was observed. DMT-1-overexpressing cells were dosed with Mn (0 – 0.9mM) for 1 hour. Labeling concentrations and times were chosen based upon standard doses used in live animal imaging and previous reports[356,368]. After dosing, cells were washed with complete media three times to remove excess supplement and then trypsinized, pelleted, and washed again. Washed cells were then transferred into 115x4m Wintrobe sedimentation tubes (Kimble CHASE, Vinelad, NJ) and centrifuged gently at 300g for 5 minutes. Complete media was

added without disturbing the pellet. The cells were then taken immediately on ice to the MRI scanner. Cell pellets were loaded into a custom-made ULTEM^{TM} resin holder and imaged in a 32-channel head coil on a clinical 3T MR scanner (Achieva TX, Philips Medical Systems) at the Hospital for Sick Children (Toronto, Canada). High resolution T_1-weighted images were acquired using a two-dimensional (2D) spin-echo (SE) sequence: repetition time (TR) = 100 ms, echo time (TE) = 14.1 ms, 60 mm field-of-view (FOV), 2 mm slice thickness, 0.5 mm × 0.5 mm in-plane resolution, and number of signal averages (NSA) = 8. T_1 mapping was performed using inversion recovery turbo SE: TR = 3000 ms, TE = 18.5 ms, 60 mm FOV, 2 mm slices, 0.5 × 0.5 mm in-plane resolution, and inversion time (TI) = (50, 100, 250, 500, 750, 1000, 1250, 1500, 2000, and 2500) ms. After image acquisition, the data were analyzed on a 2 mm deep cylindrical volume within each cell pellet. T_1 values were calculated on a pixel-by-pixel basis using in-house software developed in Matlab (v. 8.1)[465]. Quantitative T_2 relaxation times were measured using a 2D multiecho SE sequence: TR = 2000 ms, 32 echoes with minimum TE = 7.6 ms and 7.6 ms echo spacing, 60 mm FOV, 2 mm slice thickness, and 0.5 mm × 0.5 mm in-plane resolution.

6.3.10 In-vivo cell-tracking with MRI

This study was approved by the Lab Animal Services of the Hospital for Sick Children (protocol #36770), and all procedures were conducted in accordance with the Canadian Council on Animal Care. Five-week old female NOD/SCID mice (N = 10, Charles River Laboratories) weighing 22-25g, were injected with $3x10^6$ cells in serum-free media intramuscularly in each inner leg. Nine experimental animals had cell reporter lines (bright-ferritin, dark-ferritin, and DMT-1, N = 3 per line) and wild type cells injected I.M. in contralateral legs and imaged. One control animal (N = 1) was injected with ferritin- and DMT-1-overexpressing cells in contralateral legs and supplemented with saline. The bright-ferritin and DMT-1 experimental groups were injected with 0.4mmol/kg $MnCl_2$ subcutaneously on the dorsum 24 hours after cell injection. MRI imaging was conducted on Day 1 (pre-contrast prior to $MnCl_2$ injection) and Day 2, 4, 5, and 7. One DMT-1 animal was injected twice with $MnCl_2$ subcutaneously at 24- and 96-hours post-cell injection to test the recovery of bright contrast. The dark-ferritin experimental group did not receive any supplement for the first 48 hours to assess the ability of ferritin to produce contrast from endogenous iron sources. Afterward 48 hours, each mouse was orally supplemented with 2

mmol/kg of iron (ferric ammonium citrate) once daily. One of the three mice died during oral gavage. These mice were imaged on Day 1, 2, 5, and 7 to observe pre-contrast signal, endogenously induced contrast, and supplement-induced contrast. Following day 7, all mice were sacrificed, and inner leg muscles were harvested and fixed with 4% paraformaldehyde. Fixed tissues were then embedded in paraffin and prepared as 5µm sections before mounting on glass slides. After de-paraffination, sections were stained with hematoxylin and eosin (H&E) and assessed for the presence of morphologically distinct HEK cells distributed within leg skeletal muscle (Figure **C2**, Supporting Information-Appendix C).

MRI imaging was conducted on mice placed in a prone position inside an 8-channel wrist coil on a clinical 3T MR scanner (Achieva TX, Philips Medical Systems). Mice were induced on 5% isoflurane and maintained on 2% isoflurane (Forene, Abbott Labs, Baar, Switzerland) in pure oxygen (2 L/min flow rate). Body temperature was maintained by placing under the animal a water blanket (HTP-1500, Adroit Medical Systems, London, TN) set at 41°C. Mice were imaged using two T_1-weighted sequences: (1) 2D SE sequence with fat saturation with TR=507ms, TE=17.6ms, NSA=2, FA=90°, FOV=100mm, 1 mm slice thickness, and 0.3 mm x 0.3 mm in-plane resolution, and (2) non-fat saturated 3D fast field gradient echo (FFE) sequence with TR=10.07ms, TE=5.21ms, NSA=3, FA=30°, FOV=100mm, and similar resolutions as the 2D SE. Quantitative T_1-mapping was performed using a variable flip-angle method[465]. To capture T_2- and T_2^*-weighted contrast, a T_2-weighted 2D turbo SE sequence with TR=3000ms, TE=50ms, NSA=3, FA=90°, and echo train length (ETL)=8, and a T_2^*-weighted 2D FFE with TR=500ms, TE=20ms, NSA=3, FA=20° and echo train length of 1 was used, respectively. Quantitative T_2 and T_2^*- mapping was performed using a 2D multi-shot turbo SE sequence with ETL=6, minimum TE=13ms, TR=2000ms, and a 2D multi-shot FFE with ETL=32, minimum TE=4.4ms, TR=99.6ms, and FA=20°, respectively.

6.3.11 Statistical analysis

Descriptive statistics and data plotted are represented as mean ± SEM, except for in-vitro and in-vivo T_1/T_2 and R_1/R_2 values, which are shown as mean ± SD. All immunoblots shown are representative blots from a minimum of three independent replicates. Normally distributed data

were analyzed using a two-way analysis of variance (ANOVA) followed by a Tukey-Kramer test for post-hoc analysis. Significance is reported at a *p*-value of 5%.

6.4 Results

In-situ manganese encapsulation by ferritin-overexpressing cells

To demonstrate the bright-ferritin technology, we chose to overexpress the human ferritin protein using a non-viral CRISPR/Cas9 system for targeted integration into the AAVS1 "safe-harbor" locus in human embryonic kidney (HEK293) cells (Figure **6.1A**). Monoclonal cell lines selected for enhanced levels of ferritin expression demonstrated stable gene and protein levels relative to wild type cells (Figure **C1**, Supporting Inforamtion-Appendix C).

The bright-ferritin effect, as will be shown shortly, results from endogenous self-assembly of Mn-ferritin nanoparticles. To confirm this mechanism of intracellular particle formation, stable HEK cell lines overexpressing ferritin were supplemented with free Mn in culture prior to intracellular imaging with transmission electron microscopy (TEM) (Figure **6.1B**). Whole-cell TEM sections of mutant cells revealed visibly distinct aggregates of nanoparticles accumulating in vesicles, which themselves reside in lysosome-like structures (Figure **6.1C**), an observation consistent with previous reports of subcellular localization of ferritin nanoparticles[466]. In contrast, wild-type cells contained minimal nanoparticles with no visible aggregates (Figure **C2A**, Supporting Information-Appendix C). Furthermore, cell lysates were collected and immunoprecipitated with ferritin monoclonal antibody to extract and purify the intracellular ferritin. TEM of the ferritin protein purified from mutant cells post-Mn incubation revealed electron-dense metallic particles with discrete mineral cores averaging 5.4 ± 0.3 nm in diameter (Figure **6.1D**), similar in size to endogenous ferritin-iron nanocages measured by TEM[467,468]. Ferritin extracts purified prior to Mn incubation, however, contained no electron-dense metallic nanoparticles (Figure **C2B**, Supporting Information-Appendix C). To confirm the identity of the metallic core, elemental analysis for Mn was conducted on the purified ferritin particles via inductively coupled plasma atomic emission spectroscopy (ICP-AES). Ferritin-overexpressing cells had over twice the Mn-ferritin content (Figure **6.1E**) and twice the ferritin protein expression levels (Figure **6.1F**) relative to wild type cells.

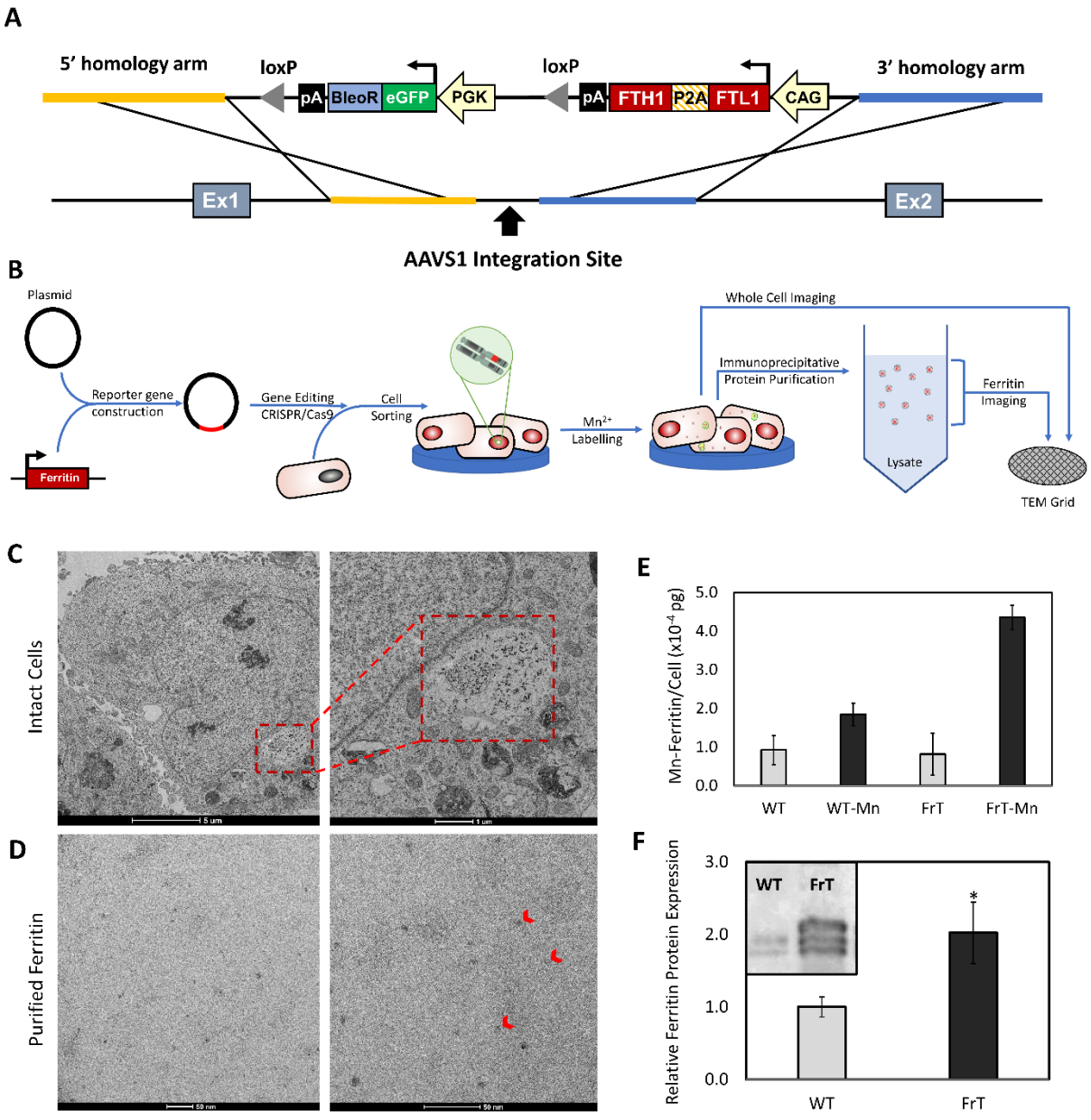

Figure 6.1: **Engineering of mammalian bright-ferritin reporter gene system**. **(A)** Plasmid vector diagram for CRISPR/Cas9 gene editing for insertion of the human ferritin transgene at the AAVS1 locus. **(B)** Schematic of stable cell line generation and assay for intracellular nanoparticle formation. Representative TEM of **(C)** ferritin nanoparticle subcellular localization and **(D)** purified electron-dense ferritin nanoparticles (red arrowheads) extracted from ferritin-overexpressing cells supplemented with 0.2mM $MnCl_2$ for 24 hours. **(E)** Cellular manganese content from purified ferritin nanoparticles in wild type (WT) and ferritin-overexpressing (FrT) cells with or without Mn supplementation. **(F)** Relative ferritin protein level normalized to α-tubulin in WT and FrT cells. Mn-incubated WT and FrT cells have different ferritin protein expression levels (* $P < 0.05$). Data in subfigures (E) and (F) are represented as mean ± SEM. See also Figure **C1** and **C2**, Supporting Information-Appendix C.

Cellular expression of ferritin provides efficient bright-contrast on MRI

In-vitro MRI reveals substantial contrast enhancement from stable ferritin-overexpressing cells that assemble Mn-ferritin nanoparticles intracellularly. Figure **6.2** illustrates live-cell imaging on a clinical 3T MR scanner. Ferritin-overexpressing and wild type cells, both with and without Mn supplementation, were imaged in glass tubes using conventional T_1-weighted imaging to visualize bright contrast and T_1 mapping to quantify contrast-induced longitudinal relaxation effects (Figure **6.2A**). At baseline, ferritin-overexpressing and wild type cells displayed similar contrast levels. Upon Mn supplementation, ferritin-overexpressing cells exhibited a T_1 that was ~2.5-fold lower than that of wild type cells (Figure **6.2B**), thus rendering a higher signal on T_1-weighted scans. For this reason, we dub this MRI reporter gene complex "bright-ferritin", a nomenclature we shall use hereon to describe the turning "on" of bright contrast via the cell's ferritin machinery.

We next assessed the sensitivity of the bright-ferritin system relative to that achieved via other MR reporter gene systems (we used CRISPR/Cas9 targeting for all reporters; see Figure **C1**, Supporting Information-Appendix C). The contrast efficiency of bright-ferritin (Figure **6.2C**) was compared against conventional ferritin with iron supplementation (Figure **6.2D**) and against free Mn transport via DMT-1 overexpression (Figure **6.2E**). Illustrated in these graphs is the relationship between the change in relaxation rate ($R_1 = 1/T_1$ or $R_2 = 1/T_2$, depending on the MR reporter) and Mn or iron concentration. A steeper slope indicates a greater relaxivity associated with higher contrast efficiency. The bright-ferritin system had a high relaxivity of 17.7 mM^{-1} s^{-1}, exceeding those of engineered exogenous chemical agents and MR reporter gene gold standards[86,341,356,469,470]. By comparison, ferritin overexpression with iron supplementation, the most widely used MR reporter system to date[341], had a very low relaxivity of 2.15 mM^{-1} s^{-1}. Even when a high dose of 0.9 mM iron was used to supplement ferritin-overexpressing cells, a modest 1.2-fold change in R_2 relative to wild type was achieved. This low efficiency is the result of a lower ferritin protein overexpression from targeted CRISPR/Cas9 transfection, an approach we opted for over common non-targeted methods that entail undesired multiple insertions. To explore differences in signal generated from encapsulated Mn versus free Mn ions, we compared bright-ferritin against DMT-1. The DMT-1 system had a modest relaxivity of 7.1 $mM^{-1}s^{-1}$, most likely due to the challenge of cellular storage of free Mn. Clearly, bright-ferritin confers the highest contrast efficiency required for sensitive in-vivo cell tracking.

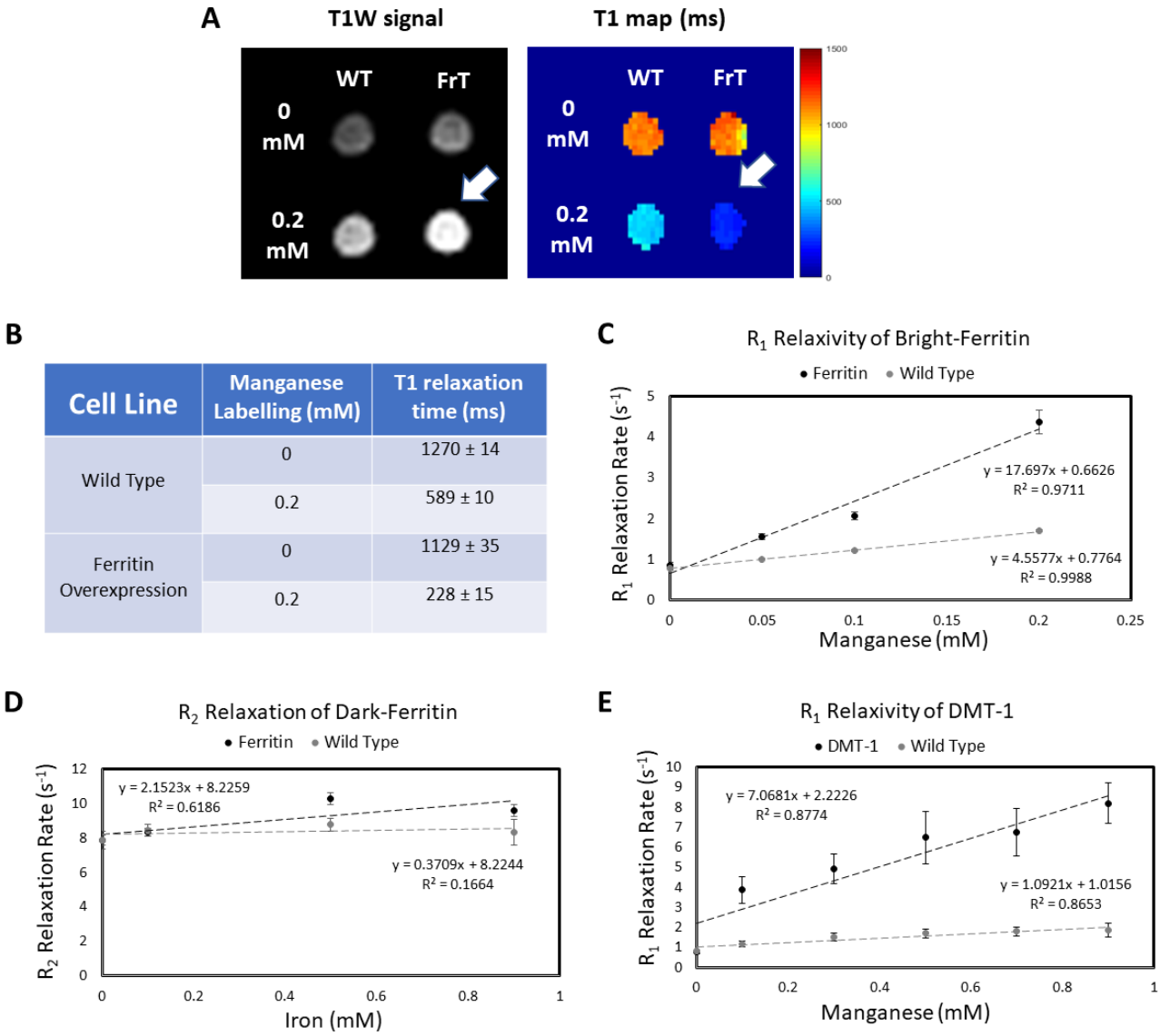

Cell Line	Manganese Labelling (mM)	T1 relaxation time (ms)
Wild Type	0	1270 ± 14
	0.2	589 ± 10
Ferritin Overexpression	0	1129 ± 35
	0.2	228 ± 15

Figure 6.2: **Bright-contrast efficiency in vitro on MRI**. **(A)** T_1-weighted spin echo image and T_1 map of wild type (WT) and ferritin-overexpressing (FrT) cells incubated with 0.2mM $MnCl_2$ for 24 hours. Arrow indicates the bright-contrast cell pellet. **(B)** Tabulated mean T_1 value ± SD. The contrast efficiencies of all MR gene reporter systems are compared by measuring relaxation rate versus metal concentration; data are represented as mean ± SD **(C-E)**.

Bright-ferritin is a non-toxic MR reporter gene complex

Absence of cellular toxicity is also very important in the setting of cell therapy. Not only must the cell-tracking technology be sensitive, but any modifications made to the therapeutic cells also cannot alter the cell's intended function to grow and replace tissue in the long-term. In our bright-

ferritin platform, we introduced two modifications: gene-editing for ferritin overexpression and Mn supplementation. To assess potential cytotoxicity associated with these modifications, we measured cell proliferation and metabolic activity for bright-ferritin and the other MR reporter systems at the optimal Mn or iron dose required for visible MR contrast. Cell viability and growth were assessed using a live/dead assay after dosing and expansion (Figure **6.3A**). Cells were stained with a cell permeable/enzymatically activatable 'green' fluorescent dye (Calcein AM) and a cell impermeable/DNA binding 'red' dye (EthD-1) to identify live and dead cells, respectively. Cell viability and growth were visually consistent at different time intervals between ferritin-overexpressing and wild type cells. Minimal cell death and similar cell densities were observed for all reporter systems and treatment groups (Figure **6.3B**). Cell metabolism assessed with WST-1 proliferation assay (Figure **6.3C**), which quantitatively measures enzymatic activity in metabolically viable cells, showed no difference amongst the different reporter systems and treatment groups, indicating the absence of genomic stress or cytotoxicity from Mn supplementation.

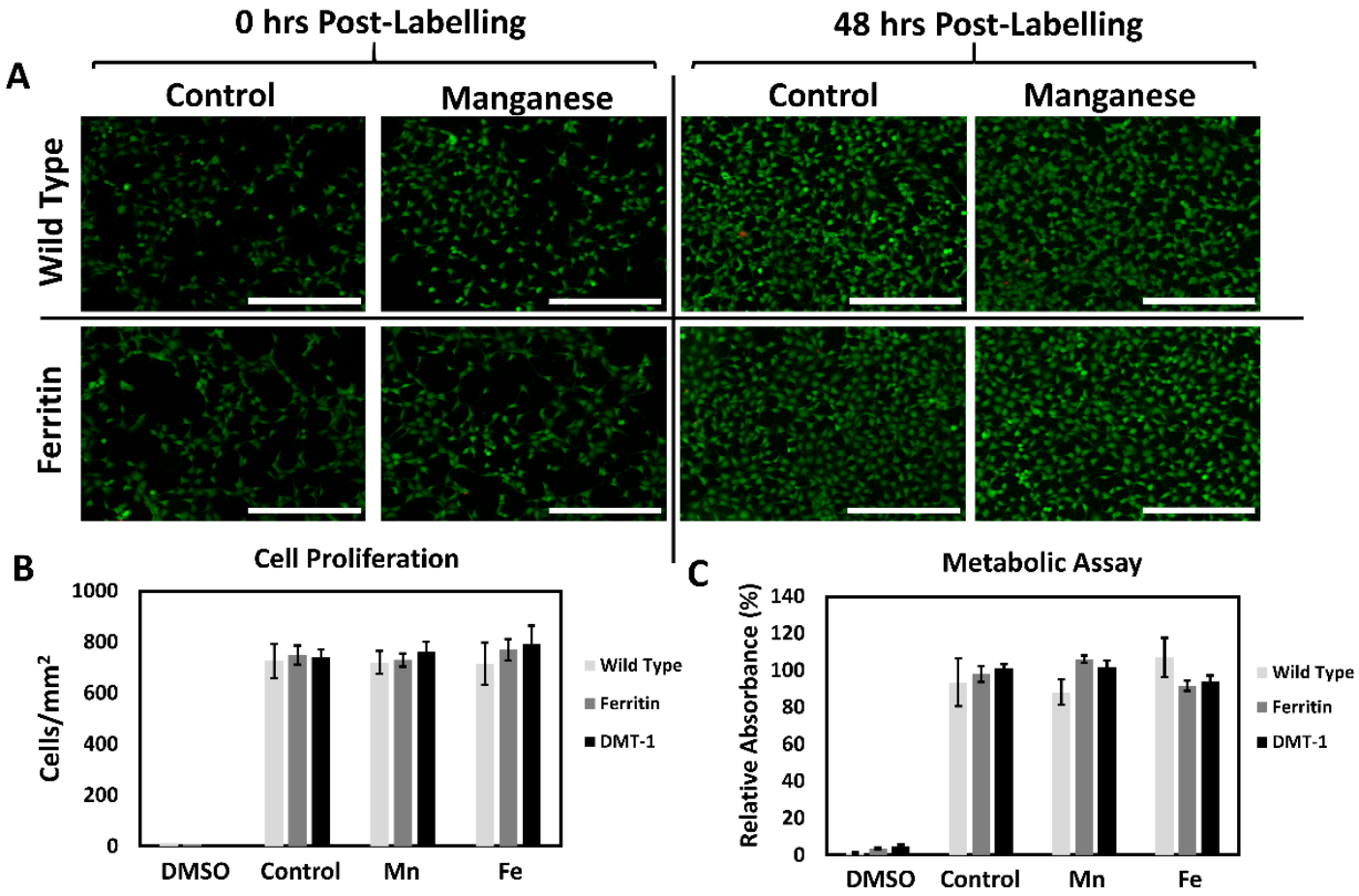

Figure 6.3: **Biocompatibility of genetic reporter systems**. **(A)** Live (green)/dead (red) fluorescent assay at 0 and 48 hours post-Mn supplementation revealed minimal cell death and minimal impact on cell growth from ferritin-overexpression and supplementation with 0.2mM Mn for 24 hours. Scale bar = 400 μm. **(B)** Cell proliferation measured by cell density at 72 hours after Mn supplementation (0.2mM Mn for 24 hours) or iron supplementation (0.9mM Fe for 72 hours). **(C)** Metabolic (WST-1) assay for the same conditions as panel B. Positive controls were treated with 5% dimethyl sulfoxide (DMSO). Negative controls were cultured in standard growth media with no additional supplementation. Data are represented as mean ± SEM.

Bright-ferritin is a superior MR reporter gene for in-vivo cell tracking

Having validated the superior contrast efficiency of the bright-ferritin platform in vitro, our next challenge was to investigate its performance in vivo, where injected cells are likely to be diffuse and Mn exposure poorly controlled at the site of cell injection due to physiological variations. The performance of bright- ferritin, conventional "dark-ferritin", and DMT-1 in NOD/SCID mice was evaluated longitudinally on a 3T MR scanner using quantitative MR relaxometry. Cells carrying the genetic reporters were injected into the muscle of one leg, and wild type cells were injected in the contralateral leg. Histology confirmed the presence of viable cells distributed throughout the leg muscle (Figure **C3**, Supporting Information-Appendix C). For the bright-ferritin and DMT-1 systems, free Mn was administered S.Q. and allowed to accumulate for 24 hours. For the conventional 'dark-ferritin' system, in accordance with previous reports, no supplementation was given for the first 48 hours to allow for endogenous iron buildup, after which animals were given daily oral doses of iron for five consecutive days.

Prior to contrast administration (Day 1), none of the MR reporter systems presented differential contrast between the two legs (Figure **6.4A**, top row). After Mn injection (Day 2), bright contrast appeared in the leg containing bright-ferritin and DMT-1 cells relative to the contralateral leg containing wild type cells. Notably, the signal enhancement produced by bright-ferritin was sustained visibly for up to five days, while the signal produced by DMT-1 had diminished by this time. To restore bright signal in the DMT-1 cells, a re-injection of Mn was required. In contrast to bright-ferritin and DMT-1, conventional "dark-ferritin" imaging produced no visible contrast relative to the contralateral leg. This was true during the first few days without

iron supplementation (Days 1 and 2) and even at later times with oral iron supplementation (Days 5 and 7).

Quantitative MR relaxometry supported these visual findings. Both bright-ferritin and DMT-1 demonstrated a significant increase in R_1 after a single dose of Mn (Figure **6.4B**). A maximum R_1 increase of 3.5-fold, 2.3-fold and 1.5-fold relative to pre-contrast levels was achieved with the bright-ferritin, DMT-1, and WT systems, respectively. Enhanced relaxation rates were higher and maintained longer in the bright-ferritin system than in DMT-1. Unsurprisingly, the "dark-ferritin" system exhibited no temporal changes in R_2* (Figure **6.4C**). Note that R_2* is used here instead of R_1, because in the "dark-ferritin" system, contrast arises from susceptibility effects.

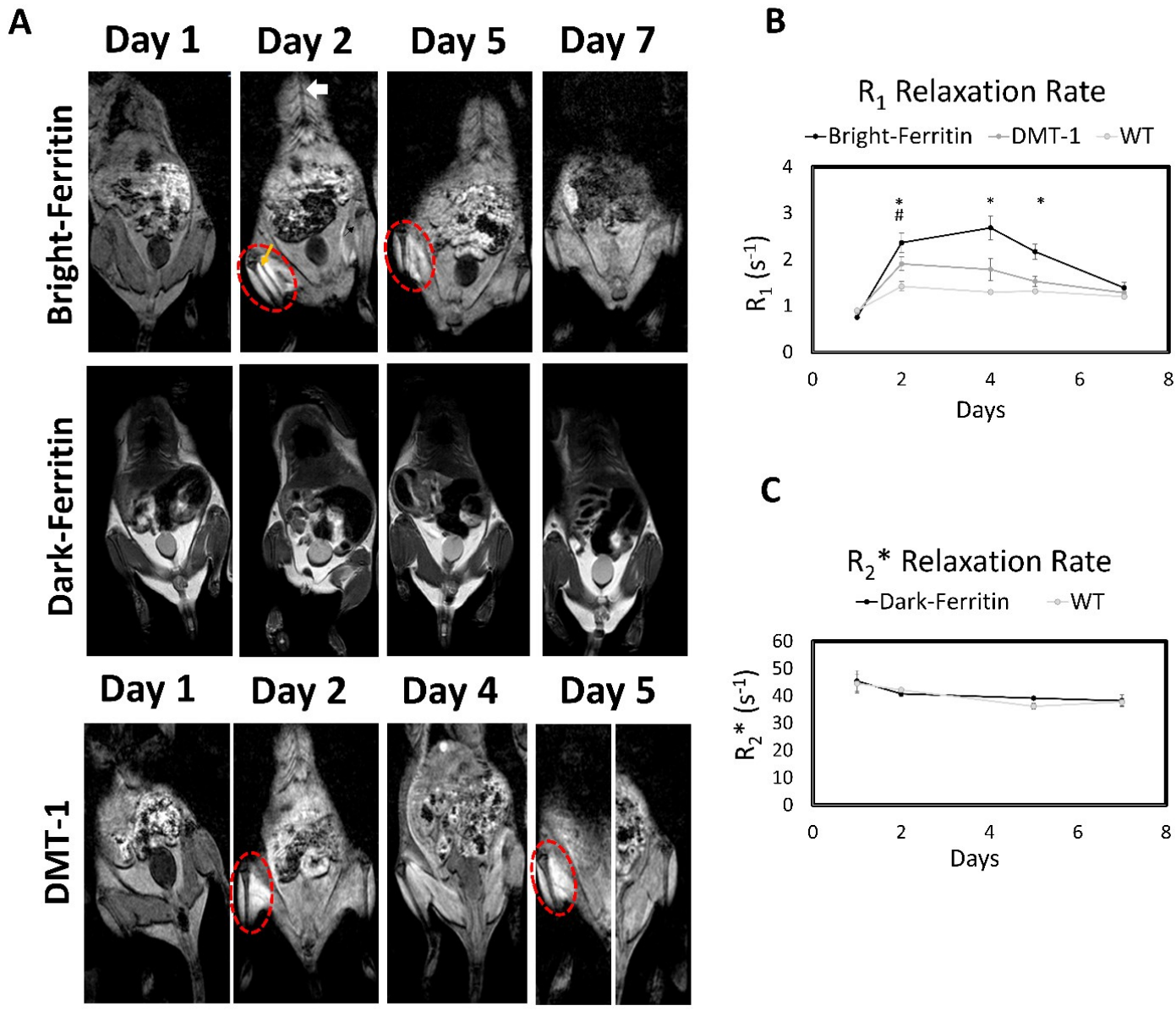

Figure 6.4: **In-vivo MRI of HEK cell injections in mice. (A)** MRI of NOD/SCID mice injected with ferritin or DMT-1 overexpressing cells in the left leg and wild type cells in the contralateral leg (site of cell injection indicated by yellow arrow). Subcutaneous $MnCl_2$ supplementation (administered subcutaneously at superior-inferior aspect indicated by white arrow) produced large signal enhancement in the leg containing bright-ferritin (top row) and DMT-1 (bottom row) overexpressing cells. To recover signal loss in DMT-1 cells after 4 days, $MnCl_2$ was re-applied to turn "on" signal. Dark-ferritin cells (middle row) showed no contrast change, both without (day 1 & 2) and with iron supplement (day 5 & 7); oral iron supplementation was given daily after Day 2. Quantitative relaxometry revealed **(B)** significant changes in R_1 in the bright-ferritin and DMT-1 legs relative to wild type but **(C)** minimal difference in R_2* on conventional dark-ferritin imaging. Difference in R_1 between bright-ferritin and DMT-1 is significant at all times (*

$P < 0.05$); difference in R_1 between DMT-1 and wild type is significant only at Day 2 (# $P < 0.05$). Data are represented as mean ± SD.

In addition to considering temporal contrast changes relative to pre-contrast levels, we also assessed changes in contrast ratios (i.e. ferritin:wild type or DMT-1:wild type), as this metric represents the "sensitivity" of the different MR reporter platforms in distinguishing the cells of interest against background tissue (Figure **6.5A**). Bright-ferritin provided the greatest change in relative contrast, with a maximum change in relative R_1 of ~2.0. By comparison, DMT-1 had a maximum change in relative R_1 of 1.3, and conventional "dark-ferritin" had negligible changes in relative R_2*. Based on literature and the observed results, we suggest in the following a potential mechanism for the bright-ferritin and DMT-1 systems (Figure **6.5B**). In the DMT-1 system, free Mn is transported into the cell via DMT-1 and other endogenous pathways[471]. DMT-1 is an active proton-coupled metal ion symporter, which means it catalyses the co-transport of H^+ protons and divalent metals (e.g. Mn^{2+}). At neutral pH, it symports one proton for every divalent metal cation, and its import capabilities is enhanced by increasing the extracellular proton concentration[472,473]. As more Mn^{2+} and H^+ enter a cell, it is reasonable to expect the intracellular pH to decrease, thus reducing the proton gradient force that drives Mn uptake. The result is a plateau in Mn-induced signal, which we observed between days 2 and 4. As the extracellular concentration of Mn continues to drop, the rate of Mn uptake falls below that of Mn elimination, thus reducing intracellular Mn and bright contrast. It is important to emphasize that this postulation is difficult to validate completely, given our current understanding of the mechanisms underlying proton-coupled transporters is incomplete[474]. It is also important to note that unlike most previous reports utilizing I.V. and I.P. administration of Mn [356], we take advantage of S.Q. injection for its slow release kinetics to achieve higher contrast and longer signal retention.

In the bright-ferritin system, Mn again enters the cell via endogenous mechanisms[471]. Once inside a cell, Mn does not remain in its ionic form but is sequestered by excess ferritin protein inside a mineral core. The sequestration slows the transition towards equilibrium (of free Mn), thus maintaining a gradient that drives Mn uptake into the cell over a prolonged interval. We postulate that Mn-ferritin particles do not remain indefinitely in the cytosol; rather, they are eventually engulfed in autophagosomes and the ferritin is ultimately degraded by lysosomal proteases. This hypothesis would be consistent with our observations on TEM, where we saw numerous dark

puncta within a smaller vesicle found inside a lysosome-like structure. As the extracellular concentration of Mn continues to decrease, a point is reached where the rate of Mn-ferritin synthesis falls below the rate of ferritin turnover and Mn excretion. The result is a decline of intracellular Mn content and bright contrast.

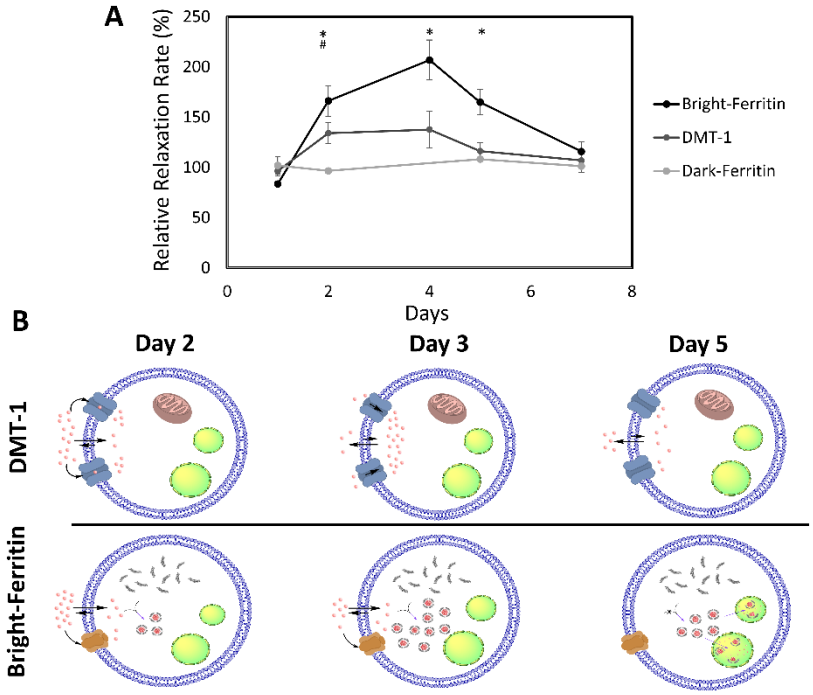

Figure 6.5: **In-vivo relative contrast for different MR reporter gene systems**. **(A)** Normalization of relaxation rates of the three gene reporter systems against wild type HEK cells in vivo. Difference in relative R_1 between bright-ferritin and DMT-1 is significant from Day 2 to 5 (* $P < 0.01$); difference in relative R_1 between DMT-1 and dark-ferritin is significant at Day 2 (# $P < 0.05$). Data are represented as mean ± SD. **(B)** Proposed mechanisms of contrast generation in the bright-ferritin and DMT-1 systems. Manganese transport and storage vary with time. Red dots represent Mn ions. Green organelles represent lysosome-like bodies.

6.5 Discussion

We report here the first utilization of a cell's own machinery for in-vivo cellular synthesis of endogenous Mn-ferritin nanoparticles to enable sensitive and non-invasive bright-contrast cell tracking over long intervals. This MRI platform, which we call bright-ferritin, seeks to attain the long-sought goal of longitudinal cell tracking in regenerative medicine, and it does so via the use of reporter genes for endogenous contrast generation in viable cells. To compete with the

sensitivity provided by short-lived exogenous cell labeling methods, the bright-ferritin system must break the low sensitivity ceiling that had hindered MR reporter gene systems. In this work, we proved in vivo and in vitro the superior sensitivity and contrast efficiency of bright-ferritin relative to other MR reporters, including conventional dark-contrast imaging using iron-ferritin particles and bright-contrast cell imaging using DMT-1 overexpression. Importantly, we achieved high detection sensitivity without introducing genomic stress and using low, non-toxic levels of exposure to Mn supplementation. The new bright-ferritin platform meets the key requirements for a practical cell-tracking technology in regenerative medicine: longitudinal monitoring capability, no ionizing radiation or radioactive tracers, unlimited depth penetration, high spatial resolution, high sensitivity to the viable cells of interest, high specificity to exclude non-targeted cells, and absence of cytotoxicity.

An important consideration with genetic modification is the potential for unintended off-target mutations and alteration of vital cell functions. We must limit not only the number of insertions but also the locations of insertions. It is for this reason that we adopted CRISPR/Cas9 to perform a single, targeted insertion at the "safe-harbor" AAVS1 locus. While our approach minimizes the risk of deleterious effects, it also reduces the protein expression level, and, therefore, the amount of available contrast, compared to common non-targeted insertions that achieve very high overexpression (up to 60-fold) of MR genetic reporters[356,368,370,458,475]. This difference – single, targeted versus multiple, non-targeted insertions – may explain why we obtained negligible contrast with conventional dark-ferritin when many have reported modest contrast changes. The fact that our bright-ferritin system was able to furnish large contrast changes at low ferritin levels is exceedingly beneficial, as high protein overexpression commonly employed can create cellular stress and non-targeted systems are very unlikely to enter the clinical domain. These "safety" attributes of our bright-ferritin platform are essential attributes in any system intended for integration in the body for tissue regeneration.

The attainable sensitivity of a cell-tracking system can be determined only in an in-vivo setting, where the diffusion and migration of injected cells against a background of non-uniform tissue, which are absent in a controlled in-vitro setting, together with limited control over Mn distribution to the cell injection site, can substantially diminish the contrast achievable. Despite these in-vivo challenges, our bright-ferritin system could readily identify and track diffuse cell

populations over days in the mouse leg and with a high degree of detection sensitivity. It is equally important to emphasize that the capability for targeted imaging afforded by our system overcomes a longstanding limitation of exogenous nanoparticles and traditional cellular imaging methods[476]. Our system now lays the foundation for enhanced non-invasive cell monitoring, with the ability to assess cell death in the early days post-injection, cell migration throughout tissue over time, and continued cell growth from the original injected population. Furthermore, our use of bright contrast (as opposed to dark contrast with traditional ferritin) opens the door to cell-tracking in inherently low-signal tissues such as skeletal and cardiac muscle[350]. Although not investigated fully in this work, the possibility exists with bright- contrast mechanisms for quantification of cell numbers. On this point, it is interesting to note the consistency we observed in ferritin protein overexpression (2-fold increase), cellular Mn-ferritin content (2.2-fold increase), in-vitro change in R_1 (2.3-fold increase), and in-vivo change in R_1 (2-fold increase). This high degree of correlation between ferritin overexpression, Mn content, and MR contrast changes, strongly indicates a robust and controllable platform with quantitative cell-tracking capabilities.

One seemingly peculiar phenomenon is why, at low concentrations, Mn is able to provide a large change in contrast while iron cannot. The answer lies in the inherent difference by which Mn and iron nanoparticles alter MR relaxation rates underlying contrast changes. Iron nanoparticles, when aggregated at high concentrations, can effectively distort the local magnetic field, thus creating a change in the transverse relaxation rate R_2* that produces dark signal. However, to effect a significant distortion of the local field, there must be an abundance of iron nanoparticles. With our low level of ferritin overexpression, we did not reach the particle concentration required for a measurable R_2* effect. On the other hand, Mn nanoparticles produce contrast changes by altering the R_1 relaxation rate of the water protons with which the particles interact. High concentrations of Mn particles are not required for a large pool of water molecules to interact with the Mn ion, because water exchanges very rapidly at a rate of approximately one million times per second.

Another consideration on the topic of contrast efficiency is the impact of the environment on the effective relaxivity of Mn. We measured a longitudinal relaxivity of 17.7 $mM^{-1}s^{-1}$ per Mn ion in our invitro cell studies, which is over two times higher than an average of 6.2 $mM^{-1}s^{-1}$ reported for Mn-loaded ferritin in solution without cells[469]. This difference is partly due to the

rotational diffusion of the complex, which is expected to be slower inside a cell than it is solution, thus, accounting for slower tumbling and increased relaxivity. Furthermore, our measured relaxivity is representative of the entire cellular system, which includes not only ferritin-bound Mn but also free Mn in the cytosol and Mn ions bound to organelle membranes. This latter portion, which is ascribed to non-ferritin Mn, can be approximated by the effect measured in wildtype cells (Figure **6.2B**). However, the precise proportion of bound versus free Mn cannot be derived from T_1 changes alone, because relaxation effects differ between free and bound Mn, as the free ion pool has a smaller effect from rotational diffusion but exchanges very rapidly with water.

There is also the question of what bright-contrast mechanism is best for a particular application. In this work, we characterized the performance of both bright-ferritin and DMT-1. Bright-ferritin produces contrast via the endogenous synthesis of Mn particles, while DMT-1 produces contrast via enhancing cellular uptake of free Mn ions. The choice of one over the other ultimately depends on whether a differential toxicity threshold exists between the two. For some cells, there may be no difference. For other cell types, there may be lower compatibility with one mechanism versus the other, because Mn in its ionic form affects cells differently compared to Mn stored in a particle. Neural cells, for example, which are highly sensitive to free ion concentrations, are unlikely to work well with DMT-1, given the vast literature evidence on Mn-related neural toxicity[477]. The utility of bright-ferritin across a wide array of cell types remains to be explored.

The immediate next step is further pre-clinical investigation of the bright-ferritin technology in different cell therapy platforms. The relatively low cost of requisite materials means the method is easily and repeatedly accessible. Conceivably, any desired cell type can be tracked and against any background tissue, including low-signal tissues that previously failed to provide contrast differences relative to injected cells[345,366,478,479]. More detailed longitudinal studies are needed in animal models to characterize the mechanism of particle elimination, test and retest the turning on of bright signal from the target cells, and uncover differences (if any) in tissue regeneration relative to wild type cells. At a cellular level, mechanistic studies that provide precise characterization of relaxation effects will be valuable. Building on analogous studies in iron-ferritin systems[480,481], these future investigations would involve cell systems in which the ferritin-bound Mn fraction is separated out; Mn binding location and loading factor within the nanocage would also be determined. Additionally, the influence of Mn in other cellular compartments such

as the cytosol and organelles, whether bound or free, and their influence on relaxation, would be elucidated to provide system insight. Translation into the clinical domain, however, would require further technical and safety characterization and optimization. Rigorous genomic testing is required to ensure the cells are completely safe for injection. We may wish to tailor the mode of administering Mn supplement, such as localized delivery to the injection site or oral supplementation, thus providing an opportunity for further dose reduction. While these questions remain to be answered, we do have insight on the answers to some questions. For example, our Mn-ferritin nanoparticles had standard core diameters. Particle size is an important parameter, because it dictates a particle's function, permeability, and uptake/degradation[482,483]. By maintaining the size of native ferritin, the particle has a high likelihood of behaving naturally like endogenous ferritin and undergoing similar routes of formation and degradation. Also, there is evidence from in-vitro studies performed in solution that Mn can initially bind to ferritin with a stoichiometry of 8 ions per molecule[484], and with specific binding to the ferroxidase centre[485]; following this, a Mn oxyhydroxide (β-MnOOH) core is formed with various loading amounts from 500 to 4000 Mn atoms per protein[460,461].

6.6 Conclusion

We report the first in-vivo MRI cell tracking system that exploits ferritin in combination with manganese supplementation for the endogenous production of highly efficient bright contrast with greater sensitivity and retention than current MR reporters. This bright-ferritin system opens the door for accurate longitudinal monitoring of cell fate, available on demand, across a broad spectrum of applications in regenerative medicine.

6.7 Contributions

H.-L.M.C. contributed to: overall direction, conceptualization, and design of study; design of *in vitro* and *in vivo* MRI experiments; design and implementation of MRI protocols; development of software for analyzing quantitative MRI data; *in vitro* and *in vivo* MRI; and quantitative MRI analysis. D.A.S. contributed to: conceptualization and design of study,

generation of stable cell lines, western blot and densitometric analysis, cellular Mn uptake studies, design and execution of protein extraction and purification, electron microscopy sample preparation and imaging, analytical manganese content analysis, toxicity assays and histology, *in vitro* and *in vivo* MRI, and statistical analysis of MRI data. H.-Y.M.C. contributed to: design and generation of targeting constructs and PCR analysis. X.A.L. contributed to: generation of stable cell lines, western blot analysis, and protein purification. All authors contributed to manuscript drafting and approved the final version.

Chapter 7 : Concluding Remarks

7.1 Conclusions and Significance

The development of cellular and scaffold-based therapies is an important area of research that has made indispensable contributions to regenerative medicine and tissue engineering. While biomedical research in this field has increased exponentially, the techniques to properly monitor and assess these therapies have lagged behind. With a shift from depth-limited optical techniques, MRI is poised to be the choice modality for this field due to its fine spatial resolution and excellent deep soft tissue contrast in 3D space without the need for ionizing radiation. Progress in this area has developed a suite of CAs for molecular imaging that are important for visualizing implants and monitoring their fate once inside the body. However, further research into CAs and the methods of implant labelling is necessary to enhance widespread utility and translation of MR scaffold and cellular imaging in the clinics.

This thesis first attempted to develop a novel method and contrast agent for labelling and imaging dECM scaffolds on MRI. Chapter 3 describes the design, evaluation and application of a small water-soluble MnP positive contrast agent for labelling ECM scaffolds *ex vivo* and *in vivo*. A passive and efficient method was developed for efficacious and uniform labelling of a series of dECM scaffolds including gels, tissue grafts and whole organ constructs from porcine bladder and trachea and murine lungs and heart. The labelled scaffolds demonstrated high signal-to-noise on MRI with substantial reductions in T_1 relaxation time. The excellent sensitivity permitted accurate visualization and delineation of scaffold features otherwise non-distinguishable with traditional MRI. The substantial contrast enhancement with relatively low labelling concentrations had no negative effects on cell attachment, viability, metabolism and proliferation. Furthermore, the mechanism of MnP association with dECM was determined to be non-specific yet exhibited sufficient retention for early scaffold fate monitoring in vivo. With this work we are the first to report and demonstrate labelling and superior visualization of dECM scaffolds on MRI with the potential for *in vivo* monitoring and optimization of dECM-scaffold based tissue engineering applications.

Next, rational modification and optimization of the CA and labelling method was conducted to develop an active/covalent tagging approach for long-term monitoring of scaffolds with positive-contrast MRI. Chapter 4 explored the design of an asymmetric MnP and an atypical conjugation approach with polydopamine (PDA) for superior labelling and tracking of collagen hydrogels. As a molecular platform MnPs are amenable to structural modifications for versatile design and characteristic tunability. Consequently, a MnP was functionalized with a single nucleophilic end group and encircled by charged moieties for direct scaffold conjugation and high water solubility. Covalent labelling of collagen hydrogels with MnP via PDA in a one-step reaction achieved efficient labelling and greater scaffold MR signal enhancement compared to passively labelled gels. This substantial signal enhancement corresponded to a significant reduction in T_1 which enabled MR visualization and sensitive tracking of scaffold degradation *in vitro.* Furthermore, successful labelling at low temperatures and in neutral aqueous conditions permitted facile integration into the workflow of minimally invasive and clinically relevant implantation models where collagen solutions are injected and thermally gelled within a patient. When applied in a rodent model, injected scaffolds exhibited superb sensitivity of detection and long-term contrast retention necessary for scaffold visualization until nearly complete degradation. This simple yet effective technique for scaffold labelling and monitoring lays the foundation for future investigations in biomaterial research and clinical monitoring systems.

The demonstration of superb positive T_1 contrast coupled with high Mn-complex stability and biocompatibility in tissue engineering systems led to the investigation of MnP in Chapter 5 as an agent for MRI tracking of cells intended for regenerative medicine. The MnP agent was synthesized from a commercial precursor to achieve scalable and one-step synthesis for large cell injections required in animal trials and translation across academic disciplines with limited chemical synthesis expertise and equipment. The agent was efficiently up taken within 24 hours by human embryonic stem cells which exhibited a two-fold reduction in T_1 relaxation time and high signal enhancement on MR. Cellular contrast was maintained for an additional 24 hours which permitted imaging of cells *in vivo* for monitoring cellular injection success. The high T_1 and low T_2 contrast of the agent allowed for accurate visualization and anatomical localization of cell depots without negative signal voids observed with typical manganese-based agents. Furthermore, no adverse effects on cell viability or differentiation potential was observed with labelled cells.

This work presents a sensitive MnP agent for positive-contrast cellular imaging and tracking with the potential for wide adoption in regenerative medicine and tissue engineering applications.

The final chapter of this thesis was aimed at developing a longitudinal cellular tracking system with greater accuracy and specificity in monitoring cell fate. Chapter 6 described the design of a MR genetic reporter platform for tracking cells with longitudinal and on-demand positive contrast. We report for the first time the discovery and use of the endogenous metalloprotein, ferritin, for *in situ* formation of manganese-ferritin nanoparticles to generate intracellular positive T_1 contrast. Safe and stable genetic modification of human embryonic kidney cells was accomplished with a non-viral CRISPR/Cas9 system for targeted integration of human ferritin gene constructs into the AAVS1 "safe-harbor" human locus. Genetically modified cells with minimal ferritin overexpression exhibited substantial contrast enhancement after incubation with manganese ion and superior relaxivity to traditional exogenous contrast agents and MR reporter gene systems. The ferritin overexpression and manganese incubation, integral to the bright-ferritin system, had no adverse effects on cell viability, metabolism and proliferation. When employed for *in vivo* cell tracking, the bright-ferritin system exhibited cell-specific signal enhancement with the highest T_1 relaxation rates and the longest contrast retention among current MR reporters. The bright-ferritin system holds the potential for accurate longitudinal monitoring of cell fate.

Overall, these studies have developed novel MR imaging approaches for monitoring scaffolds and cells for use in tissue engineering. The scaffold labelling techniques developed in this thesis are facile, efficient and biocompatible, allowing for widespread uptake and utility. The cellular tracking methods are efficient, highly versatile and offer great promise for longitudinal as well as cell-specific tracking. These developments will aid biomedical engineers in the assessment and optimization of novel strategies for regenerative medical therapies. This will greatly accelerate the pace of biomedical research and the translation of therapies into clinical trials.

7.2 Limitations and Future Directions

7.2.1 Positive-Contrast MRI of Scaffolds with Manganese Porphyrin

This thesis first demonstrated a facile and efficient method for labelling a variety of dECM materials with manganese porphyrin, which permitted accurate visualization and demarcation of scaffold features *in vitro* and *in vivo*. The MnP agent and approach, however, exhibited unspecific binding to ECM materials. While this property promoted uniform labelling and complete visualization of complex ECM scaffolds, it suffers certain limitations. Primarily, it is unable to label and track a specific macromolecule or protein in a multi-component scaffold. Specific labelling can provide scaffold engineers with important information regarding individual scaffold components and how they change under various conditions. However, the porphyrin molecule, which is amenable to structure modifications, provides a versatile platform for future design of CAs with tunable specificity. A potential future approach would involve the conjugation of targeting-peptides with affinity for different materials. Despite this limitation, the applications and utility of this method for whole scaffold tracking remain vast due to its facile and gentle nature. It can easily be integrated into a variety of workflows that process natural scaffolds in aqueous solutions and at physiological conditions. For these reasons, this approach is currently being employed to label and track natural scaffolds created with a commercial bioprinter. With commercial systems, it is difficult to incorporate complex chemical steps and conditions, thus simple addition of an MRI "dye" is ideal. Furthermore, these new scaffolds have very fine and intricate features which have been easily visualized and structurally monitored with this highly sensitive positive-contrast agent.

While the passive labelling approach has many benefits, one concern is the slow release of contrast agents over time, which may hinder the accuracy and ability of this method to report on long-term changes in scaffold content. To address the limitation of CA release, an active/covalent labelling approach with polydopamine was developed. This method exhibited stable labelling and visualization of scaffold content until nearly complete degradation. Furthermore, extensive literature has demonstrated polydopamine as a universal adhesive; thus, our approach in principle could be readily extended to a variety of biomaterials. However, the exact mechanism and kinetics of polydopamine formation is unclear and remains an active research area. Due to this, its synthesis

and resulting structure is difficult to control and predict, thus application with other materials and systems would require repeated optimization to achieve efficient labelling. Additionally, despite its inherent stability, its complex and inconsistent structure can result in variable biodegradation rates which could hinder its utility for tracking synthetic-based scaffolds that can last several months to years in the body, versus natural materials that are remodelled and degraded much faster. Furthermore, the timeframe of tissue regeneration is also an important aspect to consider for future applications of this technology. Depending on the formulation of the scaffold, the addition of growth factors, and the vascularity of the disease/injury site, tissue regeneration can occur across a variety of time frames from a couple of weeks to over a year. Future directions should assess both the utility of this method for labelling other materials and the capability for tracking over more substantial periods of time.

7.2.2 Manganese Porphyrin for Cellular MRI

This work also demonstrated the cross-capability of MnP as a contrast agent for T_1-based cellular imaging and tracking of human embryonic stem cells. MnP was easily synthesized at scale for animal studies and achieved safe and efficient cell labelling which permitted sensitive detection of cells post-injection *in vivo*. While immediate detection was possible, the lack of intracellular retention prevented long-term cell monitoring. However, intracellular uptake and retention is highly dependent on cell type and environment, thus future studies should explore various cell types, injection locations and dosage. Additionally, while longitudinal tracking is important for research optimization of new therapies and future personalized medicine, the short-term retention of this agent presents potential for immediate clinical use. Clinical cell therapies are plagued with high mis-injection rates and challenging regulatory approval of long-lasting exogenous agents. Retention of cellular contrast for 24 hours post-cell labelling ensures rapid clearance but permits real-time injection guidance or next-day imaging for flexible patient scheduling. Furthermore, another important future study would be to optimize the labelling conditions to determine the maximum cell loading capacity of MnP and consequently the minimum number of detectable cells. These studies as well as testing with a variety of cell types should be accompanied with exhaustive assessments of cell toxicity and function to ensure therapeutic cell profiles are not altered. With refined labelling conditions and determination of applicable cell types, this agent and facile method could be widely adopted.

7.2.3 Bright Ferritin Genetic Reporter Platform for Cellular MRI

The discovery and first demonstration of a ferritin-reporter gene for sensitive bright T_1-based cellular imaging opens the door for a plethora of applications and future investigations. While this platform demonstrated superior sensitivity and intracellular contrast generation in human embryonic kidney cells, future studies should assess the general value of this system with a variety of cell types. These studies should assess both the sensitivity and safety of this system *in vitro* and in large animal models to determine its utility for pre-clinical research. Additionally, while this work demonstrated the potential for longitudinal cell tracking, long-term monitoring over months and years was not conducted and should be considered in future trials with appropriate application-based time frames. For long-term studies an optimal dosing regimen should be determined to limit the quantity of Mn required; such as localized injections at the target site or slow release oral supplementation. It is also important to note that the widespread use of the current dark-ferritin platform creates a foundation and path for accelerated collaboration and testing of this new system. Furthermore, dissemination of our ferritin gene constructs compatible with CRISPR/Cas9 gene editing, should enhance the fidelity of experimental results between research laboratories and future studies.

References

1. Polak, D. J. Regenerative medicine. Opportunities and challenges: a brief overview. *J. R. Soc. Interface* **7 Suppl 6**, S777–S781 (2010).

2. *Advancing Gene, Cell, & Tissue-Based Therapies. Alliance for Regenerative Medicine Annual Report & Sector Year in Review: 2019*. (2020).

3. Aarntzen, E. H. J. G. *et al.* In vivo tracking techniques for cellular regeneration, replacement, and redirection. *J. Nucl. Med.* **53**, 1825–1828 (2012).

4. Hodgson, D. M. *et al.* Stable benefit of embryonic stem cell therapy in myocardial infarction. *Am. J. Physiol. Circ. Physiol.* **287**, H471–H479 (2004).

5. Wangde, D. *et al.* Allogeneic Mesenchymal Stem Cell Transplantation in Postinfarcted Rat Myocardium. *Circulation* **112**, 214–223 (2005).

6. Buttery, L. & Shakesheff, K. A brief introduction to different cell types. in *In Advances in tissue engineering* (eds. Pola, J., Mantalaris, S. & Harding, S. E.) 16–32 (Imperial College Press, 2008).

7. Reisman, M. & Adams, K. T. Stem cell therapy: a look at current research, regulations, and remaining hurdles. *P T* **39**, 846–857 (2014).

8. Mao, A. S. & Mooney, D. J. Regenerative medicine: Current therapies and future directions. *Proc. Natl. Acad. Sci. U. S. A.* **112**, 14452–14459 (2015).

9. Narushima, M. *et al.* A human beta-cell line for transplantation therapy to control type 1 diabetes. *Nat. Biotechnol.* **23**, 1274–1282 (2005).

10. Shiba, Y. *et al.* Human ES-cell-derived cardiomyocytes electrically couple and suppress arrhythmias in injured hearts. *Nature* **489**, 322–325 (2012).

11. Hare, J. M. *et al.* Comparison of allogeneic vs autologous bone marrow–derived mesenchymal stem cells delivered by transendocardial injection in patients with ischemic cardiomyopathy: the POSEIDON randomized trial. *JAMA* **308**, 2369–2379 (2012).

12. Bolli, R. *et al.* Cardiac stem cells in patients with ischaemic cardiomyopathy (SCIPIO): initial results of a randomised phase 1 trial. *Lancet (London, England)* **378**, 1847–1857 (2011).

13. Makkar, R. R. *et al.* Intracoronary cardiosphere-derived cells for heart regeneration after myocardial infarction (CADUCEUS): a prospective, randomised phase 1 trial. *Lancet (London, England)* **379**, 895–904 (2012).

14. Trounson, A. & McDonald, C. Stem Cell Therapies in Clinical Trials: Progress and Challenges. *Cell Stem Cell* **17**, 11–22 (2015).

15. Hosseinkhani, M. *et al.* Tissue Engineered Scaffolds in Regenerative Medicine. *World J Plast Surg* **33**, 3–7 (2014).

16. Laurencin, C. T., Ambrosio, A. M. A., Borden, M. D. & Cooper, J. A. Tissue Engineering: Orthopedic Applications. *Annu. Rev. Biomed. Eng.* **1**, 19–46 (1999).

17. Salgado, A. J., Coutinho, O. P. & Reis, R. L. Bone Tissue Engineering: State of the Art and Future Trends. *Macromol. Biosci.* **4**, 743–765 (2004).

18. Kim, K. D. & Wright, N. M. Polyethylene glycol hydrogel spinal sealant (DuraSeal Spinal Sealant) as an adjunct to sutured dural repair in the spine: results of a prospective, multicenter, randomized controlled study. *Spine (Phila. Pa. 1976).* **36**, 1906–1912 (2011).

19. Lee, J. E. *et al.* Surgical suture assembled with polymeric drug-delivery sheet for sustained, local pain relief. *Acta Biomater.* **9**, 8318–8327 (2013).

20. Malikmammadov, E., Tanir, T. E., Kiziltay, A., Hasirci, V. & Hasirci, N. PCL and PCL-based materials in biomedical applications. *J. Biomater. Sci. Polym. Ed.* **29**, 863–893 (2018).

21. Burke, J. F., Yannas, I. V, Quinby, W. C. J., Bondoc, C. C. & Jung, W. K. Successful use of a physiologically acceptable artificial skin in the treatment of extensive burn injury. *Ann. Surg.* **194**, 413–428 (1981).

22. di Summa, P. G., Kingham, P. J., Campisi, C. C., Raffoul, W. & Kalbermatten, D. F. Collagen (NeuraGen®) nerve conduits and stem cells for peripheral nerve gap repair. *Neurosci. Lett.* **572**, 26–31 (2014).

23. Guo, Y. *et al.* Hydrogels of collagen/chondroitin sulfate/hyaluronan interpenetrating polymer network for cartilage tissue engineering. *J. Mater. Sci. Mater. Med.* **23**, 2267–2279 (2012).

24. Hillel, A. T. *et al.* Photoactivated composite biomaterial for soft tissue restoration in rodents and in humans. *Sci. Transl. Med.* **3**, 93ra67 (2011).

25. Sharma, B. *et al.* Human cartilage repair with a photoreactive adhesive-hydrogel composite. *Sci. Transl. Med.* **5**, 167ra6 (2013).

26. Foster, L. J. R. & Karsten, E. A chitosan based, laser activated thin film surgical adhesive, 'SurgiLux': preparation and demonstration. *J. Vis. Exp.* (2012). doi:10.3791/3527

27. Glowacki, J. & Mizuno, S. Collagen scaffolds for tissue engineering. *Biopolymers* **89**, 338–344 (2008).

28. Parenteau-Bareil, R., Gauvin, R. & Berthod, F. Collagen-based biomaterials for tissue engineering applications. *Materials (Basel).* **3**, 1863–1887 (2010).

29. Lyons, F. G. *et al.* The healing of bony defects by cell-free collagen-based scaffolds compared to stem cell-seeded tissue engineered constructs. *Biomaterials* **31**, 9232–9243 (2010).

30. Köse, G. T. *et al.* Tissue engineered cartilage on collagen and PHBV matrices. *Biomaterials* **26**, 5187–5197 (2005).

31. Lu, Q., Ganesan, K., Simionescu, D. T. & Vyavahare, N. R. Novel porous aortic elastin and collagen scaffolds for tissue engineering. *Biomaterials* **25**, 5227–5237 (2004).

32. Freed, L. E. *et al.* Biodegradable polymer scaffolds for tissue engineering. *Biotechnology. (N. Y).* **12**, 689–693 (1994).

33. Chan, T. R., Stahl, P. J. & Yu, S. M. Matrix-bound VEGF mimetic peptides: Design and endothelial-cell activation in collagen scaffolds. *Adv. Funct. Mater.* **21**, 4252–4262 (2011).

34. Kaiser, N. J. & Coulombe, K. L. K. Physiologically inspired cardiac scaffolds for tailored *in vivo* function and heart regeneration. *Biomed. Mater.* **10**, 034003 (2015).

35. Hasan, A. *et al.* Injectable Hydrogels for Cardiac Tissue Repair after Myocardial Infarction. *Adv.*

Sci. **2**, 1–18 (2015).

36. Camci-Unal, G., Annabi, N., Dokmeci, M. R., Liao, R. & Khademhosseini, A. Hydrogels for cardiac tissue engineering. *NPG Asia Mater.* **6**, e99–e99 (2014).

37. Shi, C. *et al.* Stem-cell-capturing collagen scaffold promotes cardiac tissue regeneration. *Biomaterials* **32**, 2508–2515 (2011).

38. Zia, S. *et al.* Hearts beating through decellularized scaffolds: whole-organ engineering for cardiac regeneration and transplantation. *Crit. Rev. Biotechnol.* 1–11 (2015). doi:10.3109/07388551.2015.1007495

39. O'Brien, F. J. Biomaterials & scaffolds for tissue engineering. *Mater. Today* **14**, 88–95 (2011).

40. Williams, D. F. Challenges With the Development of Biomaterials for Sustainable Tissue Engineering. *Frontiers in Bioengineering and Biotechnology* **7**, 127 (2019).

41. Bulte, J. W. M. & Daldrup-Link, H. E. Clinical Tracking of Cell Transfer and Cell Transplantation: Trials and Tribulations. *Radiology* **289**, 604–615 (2018).

42. Bulte, J. W. M. In vivo MRI cell tracking: clinical studies. *AJR. Am. J. Roentgenol.* **193**, 314–325 (2009).

43. Mitrousis, N., Fokina, A. & Shoichet, M. S. Biomaterials for cell transplantation. *Nat. Rev. Mater.* **3**, 441–456 (2018).

44. Ringe, J. & Sittinger, M. Regenerative medicine: Selecting the right biological scaffold for tissue engineering. *Nat. Rev. Rheumatol.* **10**, 388–389 (2014).

45. Gil, C. J. *et al.* In Vivo Tracking of Tissue Engineered Constructs. *Micromachines* **10**, 474 (2019).

46. Kooreman, N. G. & Wu, J. C. Tumorigenicity of pluripotent stem cells: biological insights from molecular imaging. *J. R. Soc. Interface* **7**, S753–S763 (2010).

47. Campbell, N. G. & Suzuki, K. Cell delivery routes for stem cell therapy to the heart: current and future approaches. *J. Cardiovasc. Transl. Res.* **5**, 713–726 (2012).

48. Abdelwahid, E. *et al.* Stem cell death and survival in heart regeneration and repair. *Apoptosis* **21**, 252–268 (2016).

49. Appel, A. A., Anastasio, M. A., Larson, J. C. & Brey, E. M. Imaging challenges in biomaterials and tissue engineering. *Biomaterials* **34**, 6615–6630 (2013).

50. Ram-Liebig, G. *et al.* Regulatory challenges for autologous tissue engineered products on their way from bench to bedside in Europe. *Adv. Drug Deliv. Rev.* **82**–**83**, 181–191 (2015).

51. Weissleder, R. & Mahmood, U. Molecular Imaging. *Radiology* **219**, 316–333 (2001).

52. J, C. P. & K, R. G. Molecular imaging perspectives. *J. R. Soc. Interface* **2**, 133–144 (2005).

53. Naumova, A. V, Modo, M., Moore, A., Murry, C. E. & Frank, J. A. Clinical imaging in regenerative medicine. *Nat. Biotechnol.* **32**, 804–818 (2014).

54. Baker, M. Whole-animal imaging: The whole picture. *Nature* **463**, 977–980 (2010).

55. Wang, W. *et al.* Real-time and non-invasive fluorescence tracking of in vivo degradation of the

thermosensitive PEGlyated polyester hydrogel. *J. Mater. Chem. B* **2**, 4185–4192 (2014).

56. Kim, S. H. *et al.* Near-infrared fluorescence imaging for noninvasive trafficking of scaffold degradation. *Sci. Rep.* **3**, 1–7 (2013).

57. Puron, C. *et al.* In vivo and in vitro tracking of erosion in biodegradable materials using non-invasive fluorescence imaging. *Nat. Mater.* **10**, 704–709 (2011).

58. Artzi, N. *et al.* In vivo and in vitro tracking of erosion in biodegradable materials using non-invasive fluorescence imaging. *Nat. Mater.* **10**, 704–709 (2011).

59. Wang, L. *et al.* Visual in vivo degradation of injectable hydrogel by real-time and non-invasive tracking using carbon nanodots as fluorescent indicator. *Biomaterials* **145**, 192–206 (2017).

60. Xu, H., Othman, S. F. & Magin, R. L. Monitoring Tissue Engineering Using Magnetic Resonance Imaging. *J. Biosci. Bioeng.* **106**, 515–527 (2008).

61. Kim, K., Jeong, C. G. & Hollister, S. J. Non-invasive monitoring of tissue scaffold degradation using ultrasound elasticity imaging. *Acta Biomater.* **4**, 783–790 (2008).

62. Kim, K. & Wagner, W. R. Non-invasive and Non-destructive Characterization of Tissue Engineered Constructs Using Ultrasound Imaging Technologies: A Review. *Ann. Biomed. Eng.* **44**, 621—635 (2016).

63. Talukdar, Y., Avti, P., Sun, J. & Sitharaman, B. Multimodal ultrasound-photoacoustic imaging of tissue engineering scaffolds and blood oxygen saturation in and around the scaffolds. *Tissue Eng. Part C. Methods* **20**, 440—449 (2014).

64. Webber, M. J., Khan, O. F., Sydlik, S. A., Tang, B. C. & Langer, R. A Perspective on the Clinical Translation of Scaffolds for Tissue Engineering. *Ann. Biomed. Eng.* **43**, 641–656 (2015).

65. Watanabe, T., Murase, N., Staemmler, M. & Gersonde, K. Multiexponential proton relaxation processes of compartmentalized water in gels. *Magn. Reson. Med.* **27**, 118–134 (1992).

66. Miyata, S., Numano, T., Homma, K., Tateishi, T. & Ushida, T. Feasibility of noninvasive evaluation of biophysical properties of tissue-engineered cartilage by using quantitative MRI. *J. Biomech.* **40**, 2990–2998 (2007).

67. Cheng, H.-L. M., Loai, Y. & Farhat, W. A. Monitoring tissue development in acellular matrix-based regeneration for bladder tissue engineering: Multiexponential diffusion and T2* for improved specificity. *NMR Biomed.* **25**, 418–426 (2012).

68. Cheng, H.-L. M., Loai, Y., Beaumont, M. & Farhat, W. A. The acellular matrix (ACM) for bladder tissue engineering: A quantitative magnetic resonance imaging study. *Magn. Reson. Med.* **64**, 341–348 (2010).

69. Cheng, H.-L. M. *et al.* Quantitative Magnetic Resonance Imaging assessment of matrix development in cell-seeded natural urinary bladder smooth muscle tissue-engineered constructs. **16**, 10 (2010).

70. Duvvuri, U. *et al.* Human knee: In vivo T1(ρ)-weighted MR imaging at 1.5 T - Preliminary experience. *Radiology* **220**, 822–826 (2001).

71. Duvvuri, U. *et al.* T1ρ-relaxation in articular cartilage: Effects of enzymatic degradation. *Magn.*

Reson. Med. **38**, 863–867 (1997).

72. Kotecha, M., Klatt, D. & Magin, R. L. Monitoring cartilage tissue engineering using magnetic resonance spectroscopy, imaging, and elastography. *Tissue Eng. Part B. Rev.* **19**, 470–484 (2013).

73. Yin, Z., Schmid, T. M., Madsen, L., Kotecha, M. & Magin, R. L. Monitoring the Formation of Tissue-Engineered Cartilage in Scaffold-Free Pellet Culture Using Magnetic Resonance Imaging. *Ismrm* **20**, 7537 (2011).

74. Reiter, D. A., Lin, P.-C., Fishbein, K. W. & Spencer, R. G. Multicomponent T2 relaxation analysis in cartilage. *Magn. Reson. Med.* **61**, 803–809 (2009).

75. Saxena, V. *et al.* T1ρ Magnetic Resonance Imaging to Assess Cartilage Damage After Primary Shoulder Dislocation. *Am. J. Sports Med.* **44**, 2800–2806 (2016).

76. Maizlin, Z. V *et al.* T2 Mapping of Articular Cartilage of Glenohumeral Joint with Routine MRI Correlation---Initial Experience. *HSS J.* **5**, 61–66 (2009).

77. Saab, G., Thompson, R. T. & Marsh, G. D. Multicomponent T2 relaxation of in vivo skeletal muscle. *Magn. Reson. Med.* **42**, 150–157 (1999).

78. Ravindran, S. *et al.* Biological and MRI characterization of biomimetic ECM scaffolds for cartilage tissue regeneration. *Biomaterials* **71**, 58–70 (2015).

79. Potter, K. *et al.* Non-destructive studies of tissue-engineered phalanges by magnetic resonance microscopy and X-ray microtomography. *Bone* **38**, 350–358 (2006).

80. Chesnick, I. E. *et al.* Evaluation of bioreactor-cultivated bone by magnetic resonance microscopy and FTIR microspectroscopy. *Bone* **40**, 904–912 (2007).

81. Vinogradov, E., Sherry, A. D. & Lenkinski, R. E. CEST: From basic principles to applications, challenges and opportunities. *J. Magn. Reson.* **229**, 155–172 (2013).

82. Shazeeb, M. S. *et al.* Assessment of in vivo degradation profiles of hyaluronic acid hydrogels using temporal evolution of chemical exchange saturation transfer (CEST) MRI. *Biomaterials* **178**, 326–338 (2018).

83. Dorsey, S. M. *et al.* Visualization of Injectable Hydrogels Using Chemical Exchange Saturation Transfer MRI. (2015). doi:10.1021/ab500097d

84. Lauffer, R. B. Paramagnetic metal complexes as water proton relaxation agents for NMR imaging: theory and design. *Chem. Rev.* **87**, 901–927 (1987).

85. Srivastava, A. K. *et al.* Advances in using MRI probes and sensors for in vivo cell tracking as applied to regenerative medicine. *Dis. Model. Mech.* **8**, 323–336 (2015).

86. Alvares, R. D. A., Szulc, D. A. & Cheng, H.-L. M. A scale to measure MRI contrast agent sensitivity. *Sci. Rep.* **7**, (2017).

87. Bulte, J. W. M. & Kraitchman, D. L. Iron oxide MR contrast agents for molecular and cellular imaging. *NMR in Biomedicine* **17**, 484–499 (2004).

88. Mertens, M. E. *et al.* Iron oxide-labeled collagen scaffolds for non-invasive MR imaging in tissue engineering. *Adv. Funct. Mater.* **24**, 754–762 (2014).

89. Mertens, M. E. *et al.* USPIO-labeled textile materials for non-invasive MR imaging of tissue-engineered vascular grafts. *Biomaterials* **39**, 155–163 (2015).

90. Mertens, M. E. *et al.* FMN-coated fluorescent USPIO for cell labeling and non-invasive MR imaging in tissue engineering. *Theranostics* **4**, 1002–1013 (2014).

91. Mahmoudi, M. *et al.* Infection-resistant MRI-visible scaffolds for tissue engineering applications. *BioImpacts* **6**, 111–115 (2016).

92. Sun, Y. *et al.* Zero Echo Time Magnetic Resonance Imaging of Contrast-Agent-Enhanced Calcium Phosphate Bone Defect Fillers. *Tissue Eng. Part C Methods* **19**, 281–287 (2012).

93. Han, E. *et al.* In-Vivo T1 and T2 Measurements of Muskuloskeletal Tissue at 3T and 1.5T. *ISMRM Conf. Abstr.* **11**, 1 (2002).

94. Mosher, T. J. & Dardzinski, B. J. Cartilage MRI T2 Relaxation Time Mapping: Overview and Applications. *Semin Musculoskelet Radiol* **08**, 355–368 (2004).

95. Alam, M. H. *et al.* T1 at 1.5T and 3T compared with conventional T2* at 1.5T for cardiac siderosis. *J. Cardiovasc. Magn. Reson.* **17**, 102 (2015).

96. Gold, G. E. *et al.* Musculoskeletal MRI at 3.0 T: *Am. J. Roentgenol.* 343–351 (2004). doi:10.2214/ajr.183.2.1830343

97. Wang, P. C. & Shan, L. Essential Elements to Consider for MRI Cell Tracking Studies with Iron Oxide-based Labeling Agents. *J. Basic Clin. Med.* **1**, 1–6 (2012).

98. Liu, J. *et al.* Visualization of in situ hydrogels by MRI in vivo. *J. Mater. Chem. B* **4**, 1343–1353 (2016).

99. Karfeld-Sulzer, L. S. *et al.* Protein polymer MRI contrast agents: Longitudinal analysis of biomaterials in vivo. *Magn. Reson. Med.* **65**, 220–228 (2010).

100. Weerasekare, M. *et al.* Sol and gel states in peptide hydrogels visualized by Gd(III)-enhanced magnetic resonance imaging. *Biopolymers* **96**, 734–743 (2011).

101. Speidel, A. T. *et al.* Multimodal Hydrogel-Based Platform to Deliver and Monitor Cardiac Progenitor/Stem Cell Engraftment. *ACS Cent. Sci.* **3**, 338–348 (2017).

102. Swaminathan, S. *et al.* Cardiac and vascular metal deposition with high mortality in nephrogenic systemic fibrosis. *Kidney Int.* **73**, 1413–1418 (2008).

103. White, G. W., Gibby, W. A. & Tweedle, M. F. Comparison of Gd(DTPA-BMA) (Omniscan) versus Gd(HP-DO3A) (ProHance) relative to gadolinium retention in human bone tissue by inductively coupled plasma mass spectroscopy. *Invest. Radiol.* **41**, 272–278 (2006).

104. Gibby, W. A., Gibby, K. A. & Gibby, W. A. Comparison of Gd DTPA-BMA (Omniscan) versus Gd HP-DO3A (ProHance) retention in human bone tissue by inductively coupled plasma atomic emission spectroscopy. *Invest. Radiol.* **39**, 138–142 (2004).

105. Caillé, J. M., Lemanceau, B. & Bonnemain, B. Gadolinium as a contrast agent for NMR. *AJNR. Am. J. Neuroradiol.* **4**, 1041–1042 (1983).

106. Brücher, E. Kinetic Stabilities of Gadolinium(III) Chelates Used as MRI Contrast Agents BT - Contrast Agents I: Magnetic Resonance Imaging. in (ed. Krause, W.) 103–122 (Springer Berlin

Heidelberg, 2002). doi:10.1007/3-540-45733-X_4

107. Gadoliniumcontaining contrast agents. *World Health Organization* (2018).

108. Center for Drug Evaluation and Research. Drug Safety and Availability - FDA Drug Safety Communication: FDA evaluating the risk of brain deposits with repeated use of gadolinium-based contrast agents for magnetic resonance imaging (MRI). 4–6 (2015).

109. Nofiele, J. T., Haedicke, I. E., Zhu, Y. L. K., Zhang, X. A. & Cheng, H. L. M. Gadolinium-free extracellular MR contrast agent for tumor imaging. *J. Magn. Reson. Imaging* **41**, 397–403 (2015).

110. Cheng, W. *et al.* Complementary Strategies for Developing Gd-Free High-Field T1 MRI Contrast Agents Based on MnIII Porphyrins. *J. Med. Chem.* **57**, 516–520 (2014).

111. Koenig, S. H., Brown, R. D. 3rd & Spiller, M. The anomalous relaxivity of Mn3+ (TPPS4). *Magn. Reson. Med.* **4**, 252–260 (1987).

112. Cheng, W. *et al.* Complementary strategies for developing Gd-free high-field T1 MRI contrast agents based on MnIII porphyrins. *J. Med. Chem.* **57**, 516–520 (2014).

113. Chen, P., Bornhorst, J. & Aschner, M. Manganese metabolism in humans. *Front. Biosci.* 1655–1679 (2018). doi:10.1111/jnp.12069

114. Pan, D., Schmieder, A. H., Wickline, S. A. & Lanza, G. M. Manganese-based MRI contrast agents: past, present, and future. *Tetrahedron* **67**, 8431–8444 (2011).

115. Lyon, R. C. *et al.* Tissue distribution and stability of metalloporphyrin MRI contrast agents. *Magn. Reson. Med.* **4**, 24–33 (1987).

116. Nofiele, J. T. *et al.* Ultrashort echo time magnetic resonance imaging of the lung using a high-relaxivity T1blood-pool contrast agent. *Mol. Imaging* **13**, 1–6 (2014).

117. Drahoš, B., Lukeš, I. & Tóth, É. Manganese(II) Complexes as Potential Contrast Agents for MRI. *Eur. J. Inorg. Chem.* **2012**, 1975–1986 (2012).

118. Misselwitz, B., Mühler, A. & Weinmann, H. J. A toxicologic risk for using manganese complexes? A literature survey of existing data through several medical specialties. *Invest. Radiol.* **30**, 611–620 (1995).

119. Gunter, T. E. & Puskin, J. S. Manganous ion as a spin label in studies of mitochondrial uptake of manganese. *Biophys. J.* **12**, 625–635 (1972).

120. Daniel, G. *et al.* α-Synuclein-induced dopaminergic neurodegeneration in a rat model of Parkinson's disease occurs independent of ATP13A2 (PARK9). *Neurobiol. Dis.* **73**, 229–243 (2015).

121. Crossgrove, J. & Zheng, W. Manganese toxicity upon overexposure. *NMR Biomed.* **17**, 544–553 (2004).

122. Chen, P., Bornhorst, J. & Aschner, M. Manganese metabolism in humans. *Front. Biosci. (Landmark Ed.* **23**, 1655–1679 (2018).

123. Kueny-Stotz, M., Garofalo, A. & Felder-Flesch, D. Manganese-enhanced MRI contrast agents: From small chelates to nanosized hybrids. *Eur. J. Inorg. Chem.* 1987–2005 (2012). doi:10.1002/ejic.201101163

124. Xiao, J. *et al.* Ultrahigh relaxivity and safe probes of manganese oxide nanoparticles for in vivo imaging. *Sci. Rep.* **3**, 3424 (2013).

125. Chevallier, P. *et al.* Tailored biological retention and efficient clearance of pegylated ultra-small MnO nanoparticles as positive MRI contrast agents for molecular imaging. *J. Mater. Chem. B* **2**, 1779–1790 (2014).

126. Hambright, P. An acid solvolysis kinetic study of manganese(II)-tetra(2-N-methylpyridyl)porphine. *J. Inorg. Nucl. Chem. 39 (6), 1102-1103.* **39**, 1102–1103 (1977).

127. Porphyrins: Their Biological and Chemical Importance. *J. Am. Med. Assoc.* **157**, 1454 (1955).

128. Mauzerall, D. Porphyrins, Chlorophyll, and Photosynthesis BT - Photosynthesis I: Photosynthetic Electron Transport and Photophosphorylation. in (eds. Trebst, A. & Avron, M.) 117–124 (Springer Berlin Heidelberg, 1977). doi:10.1007/978-3-642-66505-9_5

129. Giovannetti, R. The Use of Spectrophotometry UV-Vis for the Study of Porphyrins. in *Macro To Nano Spectroscopy* (ed. Uddin, D. J.) 94-96. (Ed. InTech:, 2012). doi:10.5772/38797

130. Rohrer, M., Bauer, H., Mintorovitch, J., Requardt, M. & Weinmann, H.-J. Comparison of magnetic properties of MRI contrast media solutions at different magnetic field strengths. *Invest. Radiol.* **40**, 715–724 (2005).

131. Morgan, L. O. & Nolle, A. W. Proton Spin Relaxation in Aqueous Solutions of Paramagnetic Ions. II. Cr+++, Mn++, Ni++, Cu++, and Gd+++. *J. Chem. Phys.* **31**, 365–368 (1959).

132. Chen, C., Cohen, J. S., Myers, C. E. & Sohn, M. Paramagnetic metalloporphyrins as potential contrast agents in NMR imaging. *FEBS Lett.* **168**, 70–74 (1984).

133. Cheng, W. *et al.* Complementary Strategies for Developing Gd-Free High-Field T1 MRI Contrast Agents Based on MnIII Porphyrins. *J. Med. Chem.* **57**, 516–520 (2014).

134. Bloembergen, N. & Morgan, L. O. Proton Relaxation Times in Paramagnetic Solutions. Effects of Electron Spin Relaxation. *J. Chem. Phys.* **34**, 842–850 (1961).

135. Bloembergen, N. Proton Relaxation Times in Paramagnetic Solutions. *J. Chem. Phys.* **27**, 572–573 (1957).

136. Solomon, I. Relaxation Processes in a System of Two Spins. *Phys. Rev.* **99**, 559–565 (1955).

137. Cheng, H. L. M., Haedicke, I. E., Cheng, W., Nofiele, J. T. & Zhang, X. A. Gadolinium-free T1 contrast agents for MRI: Tunable pharmacokinetics of a new class of manganese porphyrins. *J. Magn. Reson. Imaging* **40**, 1474–1480 (2014).

138. Fiel, R. J., Mark, E., Button, T., Gilani, S. & Musser, D. Mechanism of the localization of manganese (III) mesotetra(4-sulfonatophenyl)porphine in mice bearing L1210 tumors. *Cancer Lett.* **40**, 23–32 (1988).

139. Patronas, N. J. *et al.* Metalloporphyrin contrast agents for magnetic resonance imaging of human tumors in mice. *Cancer Treat. Rep.* **70**, 391–395 (1986).

140. Els, T., Bockhorst, K. & Hoehn-berlage, M. Nmr contrast enhancement of brain tumours: comparison of the blood brain barrier tracer GdDTPA and the tumour-selective contrast agent MnTPPS. *Magma* **1**, 126–133 (1993).

141. Place, D. A., Faustino, P. J., van Zijl, P. C., Chesnick, A. & Cohen, J. S. Metalloporphyrins as contrast agents for tumors in magnetic resonance imaging. *Invest. Radiol.* **25 Suppl 1**, S69-70 (1990).

142. Place, D. A. *et al.* MRI contrast-dose relationship of manganese(III)tetra(4-sulfonatophenyl) porphyrin with human xenograft tumors in nude mice at 2.0 T. *Magn. Reson. Imaging* **10**, 919–928 (1992).

143. Wilmes, L. J. *et al.* In vivo relaxometry of three brain tumors in the rat: effect of Mn-TPPS, a tumor-selective contrast agent. *J. Magn. Reson. Imaging* **3**, 5–12 (1993).

144. Musser, D. A., Wagner, J. M. & Datta-Gupta, N. The Interaction of Tumor Localizing Porphyrins with collagen and elastin. **36**, 123–132 (1982).

145. Musser, D. A., Wagner, J. M., Weber, F. J. & Datta-Gupta, N. The binding of tumor localizing porphyrins to a fibrin matrix and their effects following photoirradiation. *Res. Commun. Chem. Pathol. Pharmacol.* **28**, 505–525 (1980).

146. Yushmanov, V. E., Tominaga, T. T., Borissevitch, I. E., Imasato, H. & Tabak, M. Binding of manganese and iron tetraphenylporphine sulfonates to albumin is relevant to their contrast properties. *Magn. Reson. Imaging* **14**, 255–261 (1996).

147. Rozinek, S. C., Thomas, R. J. & Brancaleon, L. Biophysical characterization of the interaction of human albumin with an anionic porphyrin. *Biochem. Biophys. Reports* **7**, 295–302 (2016).

148. Gautam, J. & Schott, H. Interaction of Anionic Compounds with Gelatin . I : Binding Studies. *J. Phar* **83**, 922–930 (1994).

149. Gautam, J. & Schott, H. Interaction of anionic compounds with gelatin. II: Effect on some physicochemical properties of gelatin. *J. Pharm. Sci.* **83**, 316–321 (1994).

150. Cheng, W. *et al.* Complementary Strategies for Developing Gd-Free High-Field T1 MRI Contrast Agents Based on MnIII Porphyrins. *J. Med. Chem.* **57**, 516–520 (2014).

151. Ricordi, C. & Strom, T. B. Clinical islet transplantation: advances and immunological challenges. *Nat. Rev. Immunol.* **4**, 259–268 (2004).

152. Orlic, D. *et al.* Bone marrow cells regenerate infarcted myocardium. *Nature* **410**, 701–705 (2001).

153. Nestle, F. O., Banchereau, J. & Hart, D. Dendritic cells: On the move from bench to bedside. *Nat. Med.* **7**, 761–765 (2001).

154. Sienkiewicz, D., Kulak, W., Okurowska-Zawada, B., Paszko-Patej, G. & Kawnik, K. Duchenne muscular dystrophy: current cell therapies. *Ther. Adv. Neurol. Disord.* **8**, 166–177 (2015).

155. Björklund, L. M. *et al.* Embryonic stem cells develop into functional dopaminergic neurons after transplantation in a Parkinson rat model. *Proc. Natl. Acad. Sci.* **99**, 2344 LP – 2349 (2002).

156. Daley, G. Q. The promise and perils of stem cell therapeutics. *Cell Stem Cell* **10**, 740–749 (2012).

157. Martinez, O., Sosabowski, J., Maher, J. & Papa, S. New Developments in Imaging Cell-Based Therapy. *J. Nucl. Med.* **60**, 730–735 (2019).

158. Tangney, M. & Francis, K. P. In vivo optical imaging in gene & cell therapy. *Curr. Gene Ther.* **12**, 2–11 (2012).

159. Tsien, R. Y. Fluorescent and Photochemical Probes of Dynamic Biochemical Signals inside Living Cells. in *Fluorescent Chemosensors for Ion and Molecule Recognition* **538**, 130-146 SE–9 (American Chemical Society, 1993).

160. Giepmans, B. N. G., Adams, S. R., Ellisman, M. H. & Tsien, R. Y. The fluorescent toolbox for assessing protein location and function. *Science* **312**, 217–224 (2006).

161. Farhadi, A., Ho, G. H., Sawyer, D. P., Bourdeau, R. W. & Shapiro, M. G. Ultrasound imaging of gene expression in mammalian cells. *Science (80-.).* **365**, 1469 LP – 1475 (2019).

162. Shapiro, M. G. *et al.* Biogenic gas nanostructures as ultrasonic molecular reporters. *Nat. Nanotechnol.* **9**, 311–316 (2014).

163. Yaghoubi, S. S. *et al.* Noninvasive detection of therapeutic cytolytic T cells with 18 F-FHBG PET in a patient with glioma. *Nat. Clin. Pract. Oncol.* **6**, 53–58 (2009).

164. Yaghoubi, S. S. & Gambhir, S. S. PET imaging of herpes simplex virus type 1 thymidine kinase (HSV1-tk) or mutant HSV1-sr39tk reporter gene expression in mice and humans using [18F]FHBG. *Nat. Protoc.* **1**, 3069–3075 (2006).

165. de Vries, I. J. M. *et al.* Magnetic resonance tracking of dendritic cells in melanoma patients for monitoring of cellular therapy. *Nat. Biotechnol.* **23**, 1407–1413 (2005).

166. Muja, N. & Bulte, J. W. M. Magnetic resonance imaging of cells in experimental disease models. *Prog. Nucl. Magn. Reson. Spectrosc.* **55**, 61–77 (2009).

167. Ahrens, E. T. & Bulte, J. W. M. Tracking immune cells in vivo using magnetic resonance imaging. *Nat. Rev. Immunol.* **13**, 755–763 (2013).

168. Ahrens, E. T. & Zhong, J. In vivo MRI Cell Tracking Using Perfluorocarbon Probes And Fluorine-19 Detection. *NMR Biomed.* **26**, 860–871 (2013).

169. Bulte, J. W. M. & Daldrup-Link, H. E. Clinical Tracking of Cell Transfer and Cell Transplantation: Trials and Tribulations. *Radiology* **289**, 604–615 (2018).

170. Chena, Q. *et al.* Morphological MRI and T2 mapping of cartilage repair tissue after mosaicplasty with tissue-engineered cartilage in a pig model. *J. Biomed. Res.* **28**, 309–319 (2014).

171. Frank, J. A. *et al.* Magnetic intracellular labeling of mammalian cells by combining (FDA-approved) superparamagnetic iron oxide MR contrast agents and commonly used transfection agents. *Acad. Radiol.* **9 Suppl 2**, S484-7 (2002).

172. Lalande, C *et al.* Magnetic resonance imaging tracking of human adipose derived stromal cells within three-dimensional scaffolds for bone tissue engineering. *Eur. Cells Mater.* **21**, 341–354 (2016).

173. Di Corato, R. *et al.* High-resolution cellular MRI: Gadolinium and iron oxide nanoparticles for in-depth dual-cell imaging of engineered tissue constructs. *ACS Nano* **7**, 7500–7512 (2013).

174. Loai, Y., Ganesh, T. & Margaret Cheng, H.-L. Concurrent Dual Contrast for Cellular Magnetic Resonance Imaging Using Gadolinium Oxide and Iron Oxide Nanoparticles. *Int. J. Mol. Imaging* **2012**, 1–10 (2012).

175. Feng, Q. *et al.* Uptake, distribution, clearance, and toxicity of iron oxide nanoparticles with

different sizes and coatings. *Sci. Rep.* **8**, 1–13 (2018).

176. Shapiro, E. M. *et al.* MRI detection of single particles for cellular imaging. *Proc. Natl. Acad. Sci. U. S. A.* **101**, 10901–10906 (2004).

177. Zhu, J., Zhou, L. & XingWu, F. Tracking neural stem cells in patients with brain trauma. *The New England journal of medicine* **355**, 2376–2378 (2006).

178. Karmarkar, P. V *et al.* MR-trackable intramyocardial injection catheter. *Magn. Reson. Med.* **51**, 1163–1172 (2004).

179. Barnett, B. P. *et al.* Magnetic resonance-guided, real-time targeted delivery and imaging of magnetocapsules immunoprotecting pancreatic islet cells. *Nat. Med.* **13**, 986–991 (2007).

180. Walczak, P. *et al.* Real-time MRI for precise and predictable intra-arterial stem cell delivery to the central nervous system. *J. Cereb. blood flow Metab. Off. J. Int. Soc. Cereb. Blood Flow Metab.* **37**, 2346–2358 (2017).

181. Janowski, M. *et al.* Cell size and velocity of injection are major determinants of the safety of intracarotid stem cell transplantation. *J. Cereb. blood flow Metab. Off. J. Int. Soc. Cereb. Blood Flow Metab.* **33**, 921–927 (2013).

182. Toso, C. *et al.* Clinical magnetic resonance imaging of pancreatic islet grafts after iron nanoparticle labeling. *Am. J. Transplant. Off. J. Am. Soc. Transplant. Am. Soc. Transpl. Surg.* **8**, 701–706 (2008).

183. Saudek, F. *et al.* Magnetic resonance imaging of pancreatic islets transplanted into the liver in humans. *Transplantation* **90**, 1602–1606 (2010).

184. Malosio, M. L. *et al.* MR imaging monitoring of iron-labeled pancreatic islets in a small series of patients: islet fate in successful, unsuccessful, and autotransplantation. *Cell Transplant.* **24**, 2285–2296 (2015).

185. Richards, J. M. J. *et al.* In vivo mononuclear cell tracking using superparamagnetic particles of iron oxide: feasibility and safety in humans. *Circ. Cardiovasc. Imaging* **5**, 509–517 (2012).

186. Jozwiak, S. *et al.* Intracerebroventricular Transplantation of Cord Blood-Derived Neural Progenitors in a Child With Severe Global Brain Ischemic Injury. *Cell Med.* **1**, 71–80 (2010).

187. Janowski, M. *et al.* Long-term MRI cell tracking after intraventricular delivery in a patient with global cerebral ischemia and prospects for magnetic navigation of stem cells within the CSF. *PLoS One* **9**, e97631–e97631 (2014).

188. Callera, F. & de Melo, C. M. T. P. Magnetic resonance tracking of magnetically labeled autologous bone marrow CD34+ cells transplanted into the spinal cord via lumbar puncture technique in patients with chronic spinal cord injury: CD34+ cells' migration into the injured site. *Stem Cells Dev.* **16**, 461–466 (2007).

189. Karussis, D. *et al.* Safety and immunological effects of mesenchymal stem cell transplantation in patients with multiple sclerosis and amyotrophic lateral sclerosis. *Arch. Neurol.* **67**, 1187–1194 (2010).

190. Vrtovec, B. *et al.* Effects of intracoronary CD34+ stem cell transplantation in nonischemic dilated cardiomyopathy patients: 5-year follow-up. *Circ. Res.* **112**, 165–173 (2013).

191. Kircher, M. F. *et al.* In vivo high resolution three-dimensional imaging of antigen-specific cytotoxic T-lymphocyte trafficking to tumors. *Cancer Res.* **63**, 6838–6846 (2003).

192. Daldrup-Link, H. E. *et al.* Comparison of iron oxide labeling properties of hematopoietic progenitor cells from umbilical cord blood and from peripheral blood for subsequent in vivo tracking in a xenotransplant mouse model XXX. *Acad. Radiol.* **12**, 502–510 (2005).

193. Moore, A. *et al.* MRI of insulitis in autoimmune diabetes. *Magn. Reson. Med.* **47**, 751–758 (2002).

194. Anderson, S. A. *et al.* Magnetic resonance imaging of labeled T-cells in a mouse model of multiple sclerosis. *Ann. Neurol.* **55**, 654–659 (2004).

195. Baumjohann, D. *et al.* In vivo magnetic resonance imaging of dendritic cell migration into the draining lymph nodes of mice. *Eur. J. Immunol.* **36**, 2544–2555 (2006).

196. Rohani, R. *et al.* In vivo cellular MRI of dendritic cell migration using micrometer-sized iron oxide (MPIO) particles. *Mol. imaging Biol.* **13**, 679–694 (2011).

197. Feng, Q. *et al.* Uptake, distribution, clearance, and toxicity of iron oxide nanoparticles with different sizes and coatings. *Sci. Rep.* **8**, 2082 (2018).

198. Wang, Y.-X. J. Superparamagnetic iron oxide based MRI contrast agents: Current status of clinical application. *Quant Imaging Med Surg* **1**, 35–44 (2011).

199. Henning, T. D. *et al.* Cell labeling with the positive MR contrast agent Gadofluorine M. *Eur. Radiol.* **17**, 1226–1234 (2007).

200. Kostura, L., Kraitchman, D. L., Mackay, A. M., Pittenger, M. F. & Bulte, J. W. M. Feridex labeling of mesenchymal stem cells inhibits chondrogenesis but not adipogenesis or osteogenesis. *NMR Biomed.* **17**, 513–517 (2004).

201. Bulte, J. W. M., Kraitchman, D. L., Mackay, A. M. & Pittenger, M. F. Chondrogenic differentiation of mesenchymal stem cells is inhibited after magnetic labeling with ferumoxides. *Blood* **104**, 3410–3413 (2004).

202. Siglienti, I., Bendszus, M., Kleinschnitz, C. & Stoll, G. Cytokine profile of iron-laden macrophages: implications for cellular magnetic resonance imaging. *J. Neuroimmunol.* **173**, 166–173 (2006).

203. Weissleder, R. *et al.* Superparamagnetic iron oxide: pharmacokinetics and toxicity. *AJR. Am. J. Roentgenol.* **152**, 167–173 (1989).

204. Metz, S. *et al.* Capacity of human monocytes to phagocytose approved iron oxide MR contrast agents in vitro. *Eur. Radiol.* **14**, 1851–1858 (2004).

205. Muller, R. N. *et al.* Relaxation by metal-containing nanosystems. *Adv. Inorg. Chem.* **57**, 239–292 (2005).

206. Bulte, J. W. M. & Kraitchman, D. L. Iron oxide MR contrast agents for molecular and cellular imaging. *NMR Biomed.* **17**, 484–499 (2004).

207. Muja, N. & Bulte, J. W. M. Magnetic resonance imaging of cells in experimental disease models. *Prog. Nucl. Magn. Reson. Spectrosc.* **55**, 61–77 (2009).

208. Srivastava, A. K. *et al.* Advances in using MRI probes and sensors for in vivo cell tracking as applied to regenerative medicine. *Dis. Model. Mech.* **8**, 323–336 (2015).

209. Tang, K. S. & Shapiro, E. M. Enhanced magnetic cell labeling efficiency using –NH2 coated MPIOs. *Magn. Reson. Med.* **65**, 1564–1569 (2011).

210. Terrovitis, J. *et al.* Magnetic resonance imaging overestimates ferumoxide-labeled stem cell survival after transplantation in the heart. *Circulation* **117**, 1555–1562 (2008).

211. Lepore, A. C., Walczak, P., Rao, M. S., Fischer, I. & Bulte, J. W. M. MR imaging of lineage-restricted neural precursors following transplantation into the adult spinal cord. *Exp. Neurol.* **201**, 49–59 (2006).

212. Baligand, C., Vauchez, K., Fiszman, M., Vilquin, J.-T. & Carlier, P. G. Discrepancies between the fate of myoblast xenograft in mouse leg muscle and NMR label persistency after loading with Gd-DTPA or SPIOs. *Gene Ther.* **16**, 734–745 (2009).

213. Amsalem, Y. *et al.* Iron-oxide labeling and outcome of transplanted mesenchymal stem cells in the infarcted myocardium. *Circulation* **116**, I38-45 (2007).

214. Berman, S. C., Galpoththawela, C., Gilad, A. A., Bulte, J. W. M. & Walczak, P. Long-term MR cell tracking of neural stem cells grafted in immunocompetent versus immunodeficient mice reveals distinct differences in contrast between live and dead cells. *Magn. Reson. Med.* **65**, 564–574 (2011).

215. Lu, M., Cohen, M. H., Rieves, D. & Pazdur, R. FDA report: Ferumoxytol for intravenous iron therapy in adult patients with chronic kidney disease. *Am. J. Hematol.* **85**, 315–319 (2010).

216. Toth, G. B. *et al.* Current and potential imaging applications of ferumoxytol for magnetic resonance imaging. *Kidney Int.* **92**, 47–66 (2017).

217. Gkagkanasiou, M., Ploussi, A., Gazouli, M. & Efstathopoulos, E. P. USPIO-Enhanced MRI Neuroimaging: A Review. *J. Neuroimaging* **26**, 161–168 (2016).

218. Nguyen, K.-L. *et al.* Multicenter Safety and Practice for Off-Label Diagnostic Use of Ferumoxytol in MRI. *Radiology* **293**, 554–564 (2019).

219. Bailie, G. R. Comparison of rates of reported adverse events associated with i.v. iron products in the United States. *Am. J. Heal. Pharm. AJHP Off. J. Am. Soc. Heal. Pharm.* **69**, 310–320 (2012).

220. U.S. Food and Drug Administration. FDA Drug Safety Communication: FDA strengthens warnings and changes prescribing instructions to decrease the risk of serious allergic reactions with anemia drug Feraheme (ferumoxytol). *U.S. Food and Drug Administration* (2015). Available at: https://www.fda.gov/drugs/drug-safety-and-availability/fda-drug-safety-communication-fda-strengthens-warnings-and-changes-prescribing-instructions-decrease. (Accessed: 30th June 2020)

221. Ahrens, E. T., Helfer, B. M., O'Hanlon, C. F. & Schirda, C. Clinical cell therapy imaging using a perfluorocarbon tracer and fluorine-19 MRI. *Magn. Reson. Med.* **72**, 1696–1701 (2014).

222. Rose, L. C. *et al.* Fluorine-19 Labeling of Stromal Vascular Fraction Cells for Clinical Imaging Applications. *Stem Cells Transl. Med.* **4**, 1472–1481 (2015).

223. Bulte, J. W. M. Hot spot MRI emerges from the background. *Nature biotechnology* **23**, 945–946 (2005).

224. Srinivas, M., Heerschap, A., Ahrens, E. T., Figdor, C. G. & de Vries, I. J. M. (19)F MRI for

quantitative in vivo cell tracking. *Trends Biotechnol.* **28**, 363–370 (2010).

225. Tirotta, I. *et al.* A Superfluorinated Molecular Probe for Highly Sensitive in Vivo19F-MRI. *J. Am. Chem. Soc.* **136**, 8524–8527 (2014).

226. Riess, J. G. Oxygen carriers ('blood substitutes')--raison d'etre, chemistry, and some physiology. *Chem. Rev.* **101**, 2797–2920 (2001).

227. Ruiz-Cabello, J., Barnett, B. P., Bottomley, P. A. & Bulte, J. W. M. Fluorine (19F) MRS and MRI in biomedicine. *NMR Biomed.* **24**, 114–129 (2011).

228. Ahrens, E. T., Flores, R., Xu, H. & Morel, P. A. In vivo imaging platform for tracking immunotherapeutic cells. *Nat. Biotechnol.* **23**, 983–987 (2005).

229. Helfer, B. M. *et al.* Functional assessment of human dendritic cells labeled for in vivo (19)F magnetic resonance imaging cell tracking. *Cytotherapy* **12**, 238–250 (2010).

230. Srinivas, M., Morel, P. A., Ernst, L. A., Laidlaw, D. H. & Ahrens, E. T. Fluorine-19 MRI for visualization and quantification of cell migration in a diabetes model. *Magn. Reson. Med.* **58**, 725–734 (2007).

231. Bonetto, F. *et al.* A novel (19)F agent for detection and quantification of human dendritic cells using magnetic resonance imaging. *Int. J. cancer* **129**, 365–373 (2011).

232. Partlow, K. C. *et al.* 19F magnetic resonance imaging for stem/progenitor cell tracking with multiple unique perfluorocarbon nanobeacons. *FASEB J. Off. Publ. Fed. Am. Soc. Exp. Biol.* **21**, 1647–1654 (2007).

233. Janjic, J. M., Srinivas, M., Kadayakkara, D. K. K. & Ahrens, E. T. Self-delivering nanoemulsions for dual fluorine-19 MRI and fluorescence detection. *J. Am. Chem. Soc.* **130**, 2832–2841 (2008).

234. Lee, H. *et al.* In vivo fluorine-19 MR imaging: Relaxation enhancement with Gd-DTPA. *J. Magn. Reson. Imaging* **4**, 609–613 (1994).

235. Dardzinski, B. J. & Sotak, C. H. Rapid tissue oxygen tension mapping using 19F inversion-recovery echo-planar imaging of perfluoro-15-crown-5-ether. *Magn. Reson. Med.* **32**, 88–97 (1994).

236. Hancu, I. *et al.* CEST and PARACEST MR contrast agents. *Acta radiol.* **51**, 910–923 (2010).

237. Chen, S. Z. *et al.* Chemical exchange saturation transfer (CEST) MR technique for in-vivo liver imaging at 3.0 tesla. *Eur. Radiol.* **26**, 1792–1800 (2016).

238. Jinyuan, Z. & Xiaohua, H. Molecular Imaging Using Endogenous Cellular Proteins. *Bo pu xue za zhi = Chinese J. Microw. radio-frequency Spectrosc.* **30**, 307–321 (2013).

239. Goffeney, N., Bulte, J. W. M., Duyn, J., Bryant, L. H. & van Zijl, P. C. M. Sensitive NMR Detection of Cationic-Polymer-Based Gene Delivery Systems Using Saturation Transfer via Proton Exchange. *J. Am. Chem. Soc.* **123**, 8628–8629 (2001).

240. Zhang, S., Winter, P., Wu, K. & Sherry, A. D. A Novel Europium(III)-Based MRI Contrast Agent. *J. Am. Chem. Soc.* **123**, 1517–1518 (2001).

241. Pumphrey, A. L. *et al.* Cardiac chemical exchange saturation transfer MR imaging tracking of cell survival or rejection in mouse models of cell therapy. *Radiology* **282**, 131–138 (2017).

242. Bleaney, B. *et al.* Origin of lanthanide nuclear magnetic resonance shifts and their uses. *J. Chem. Soc. Chem. Commun.* 791b – 793 (1972). doi:10.1039/C3972000791B

243. Bleaney, B. Nuclear magnetic resonance shifts in solution due to lanthanide ions. *J. Magn. Reson.* **8**, 91–100 (1972).

244. Ferrauto, G., Castelli, D. D., Terreno, E. & Aime, S. In vivo MRI visualization of different cell populations labeled with PARACEST agents. *Magn. Reson. Med.* **69**, 1703–1711 (2013).

245. Ferrauto, G., Di Gregorio, E., Delli Castelli, D. & Aime, S. CEST-MRI studies of cells loaded with lanthanide shift reagents. *Magn. Reson. Med.* **80**, 1626–1637 (2018).

246. Aime, S., Delli Castelli, D. & Terreno, E. Supramolecular adducts between poly-L-arginine and [TmIIIdotp]: a route to sensitivity-enhanced magnetic resonance imaging-chemical exchange saturation transfer agents. *Angew. Chem. Int. Ed. Engl.* **42**, 4527–4529 (2003).

247. Aime, S., Delli Castelli, D. & Terreno, E. Highly sensitive MRI chemical exchange saturation transfer agents using liposomes. *Angew. Chem. Int. Ed. Engl.* **44**, 5513–5515 (2005).

248. Okuhata, Y. Delivery of diagnostic agents for magnetic resonance imaging. *Adv. Drug Deliv. Rev.* **37**, 121–137 (1999).

249. Caravan, P., Ellison, J. J., McMurry, T. J. & Lauffer, R. B. Gadolinium(III) Chelates as MRI Contrast Agents: Structure, Dynamics, and Applications. *Chem. Rev.* **99**, 2293–2352 (1999).

250. Port, M. *et al.* Efficiency, thermodynamic and kinetic stability of marketed gadolinium chelates and their possible clinical consequences: a critical review. *Biometals an Int. J. role Met. ions Biol. Biochem. Med.* **21**, 469–490 (2008).

251. Geng, K. *et al.* Tracking of mesenchymal stem cells labeled with gadolinium diethylenetriamine pentaacetic acid by 7T magnetic resonance imaging in a model of cerebral ischemia. *Mol. Med. Rep.* **11**, 954–960 (2015).

252. Aime, S., Barge, A., Cabella, C., Crich, S. G. & Gianolio, E. Targeting cells with MR imaging probes based on paramagnetic Gd(III) chelates. *Curr. Pharm. Biotechnol.* **5**, 509–518 (2004).

253. Biancone, L. *et al.* Magnetic resonance imaging of gadolinium-labeled pancreatic islets for experimental transplantation. *NMR Biomed.* **20**, 40–48 (2007).

254. Haenold, R. *et al.* Magnetic resonance imaging of the mouse visual pathway for in vivo studies of degeneration and regeneration in the CNS. *Neuroimage* **59**, 363–376 (2012).

255. Simmons, J. M. *et al.* Mapping Prefrontal Circuits In Vivo with Manganese-Enhanced Magnetic Resonance Imaging in Monkeys. *J. Neurosci.* **28**, 7637 LP – 7647 (2008).

256. Guenoun, J. *et al.* Cationic Gd-DTPA liposomes for highly efficient labeling of mesenchymal stem cells and cell tracking with MRI. *Cell Transplant.* **21**, 191–205 (2012).

257. Bruckman, M. A. *et al.* Tobacco mosaic virus rods and spheres as supramolecular high-relaxivity MRI contrast agents. *J. Mater. Chem. B* **1**, 1482–1490 (2013).

258. Geninatti Crich, S. *et al.* Magnetic Resonance Visualization of Tumor Angiogenesis by Targeting Neural Cell Adhesion Molecules with the Highly Sensitive Gadolinium-Loaded Apoferritin Probe. *Cancer Res.* **66**, 9196 LP – 9201 (2006).

259. Di Corato, R. *et al.* High-Resolution Cellular MRI: Gadolinium and Iron Oxide Nanoparticles for in-Depth Dual-Cell Imaging of Engineered Tissue Constructs. *ACS Nano* **7**, 7500–7512 (2013).

260. Evanics, F., Diamente, P. R., van Veggel, F. C. J. M., Stanisz, G. J. & Prosser, R. S. Water-Soluble GdF3 and GdF3/LaF3 NanoparticlesPhysical Characterization and NMR Relaxation Properties. *Chem. Mater.* **18**, 2499–2505 (2006).

261. McDonald, R. J. *et al.* Intracranial Gadolinium Deposition after Contrast-enhanced MR Imaging. *Radiology* **275**, 772–782 (2015).

262. Kanda, T., Ishii, K., Kawaguchi, H., Kitajima, K. & Takenaka, D. High Signal Intensity in the Dentate Nucleus and Globus Pallidus on Unenhanced T1-weighted MR Images: Relationship with Increasing Cumulative Dose of a Gadolinium-based Contrast Material. *Radiology* **270**, 834–841 (2013).

263. Thomsen, H. S., Marckmann, P. & Logager, V. B. Update on Nephrogenic Systemic Fibrosis. *Magn. Reson. Imaging Clin. N. Am.* **16**, 551–560 (2008).

264. US Food and Drug Administration. FDA drug safety communication: FDA warns that gadolinium-based contrast agents (GBCAs) are retained in the body; requires new class warnings. *US Food and Drug Administration* (2018). Available at: https://www.fda.gov/drugs/drug-safety-and-availability/fda-drug-safety-communication-fda-warns-gadolinium-based-contrast-agents-gbcas-are-retained-body. (Accessed: 30th June 2020)

265. Rogosnitzky, M. & Branch, S. Gadolinium-based contrast agent toxicity: a review of known and proposed mechanisms. *Biometals an Int. J. role Met. ions Biol. Biochem. Med.* **29**, 365–376 (2016).

266. Hasebroock, K. M. & Serkova, N. J. Toxicity of MRI and CT contrast agents. *Expert Opin. Drug Metab. Toxicol.* **5**, 403–416 (2009).

267. Aime, S. & Caravan, P. Biodistribution of gadolinium-based contrast agents, including gadolinium deposition. *J. Magn. Reson. Imaging* **30**, 1259–1267 (2009).

268. Swaminathan, S. & Shah, S. V. New insights into nephrogenic systemic fibrosis. *J. Am. Soc. Nephrol.* **18**, 2636–2643 (2007).

269. Swaminathan, S. *et al.* Cardiac and vascular metal deposition with high mortality in nephrogenic systemic fibrosis. *Kidney Int.* **73**, 1413–1418 (2008).

270. Sanyal, S., Marckmann, P., Scherer, S. & Abraham, J. L. Multiorgan gadolinium (Gd) deposition and fibrosis in a patient with nephrogenic systemic fibrosis--an autopsy-based review. *Nephrol. Dial. Transplant. Off. Publ. Eur. Dial. Transpl. Assoc. - Eur. Ren. Assoc.* **26**, 3616–3626 (2011).

271. Biagi, B. A. & Enyeart, J. J. Gadolinium blocks low- and high-threshold calcium currents in pituitary cells. *Am. J. Physiol.* **259**, C515-20 (1990).

272. Morcos, S. K. Extracellular gadolinium contrast agents: differences in stability. *Eur. J. Radiol.* **66**, 175–179 (2008).

273. Canga, A. *et al.* Renal function, nephrogenic systemic fibrosis and other adverse reactions associated with gadolinium-based contrast media. *Nefrologia* **34**, 428–438 (2014).

274. U.S. Food & Drug Administration (FDA). Gadolinium-based Contrast Agents (GBCAs): Drug Safety

Communication - Retained in Body; New Class Warnings. FDA safety alert. *U.S. Food & Drug Administration (FDA)* (2017). Available at: https://www.fda.gov/drugs/drug-safety-and-availability/fda-drug-safety-communication-fda-warns-gadolinium-based-contrast-agents-gbcas-are-retained-body. (Accessed: 29th June 2020)

275. Aoki, I. *et al.* Cell labeling for magnetic resonance imaging with the T1 agent manganese chloride. *NMR Biomed.* **19**, 50–59 (2006).

276. Nofiele, J. T. & Cheng, H.-L. M. Ultrashort Echo Time for Improved Positive-Contrast Manganese-Enhanced MRI of Cancer. *PLoS One* **8**, e58617 (2013).

277. Yang, Y. *et al.* Intrastriatal manganese chloride exposure causes acute locomotor impairment as well as partial activation of substantia nigra GABAergic neurons. *Environ. Toxicol. Pharmacol.* **31**, 171–178 (2011).

278. Létourneau, M. *et al.* MnO-labeled cells: Positive contrast enhancement in MRI. *J. Phys. Chem. B* **116**, 13228–13238 (2012).

279. Guillet-Nicolas, R. *et al.* Manganese-impregnated mesoporous silica nanoparticles for signal enhancement in MRI cell labelling studies. *Nanoscale* **5**, 11499–11511 (2013).

280. Kim, T. *et al.* Mesoporous Silica-Coated Hollow Manganese Oxide Nanoparticles as Positive T1 Contrast Agents for Labeling and MRI Tracking of Adipose-Derived Mesenchymal Stem Cells. *J. Am. Chem. Soc.* **133**, 2955–2961 (2011).

281. Viglianti, B. L. *et al.* In vivo monitoring of tissue pharmacokinetics of liposome/drug using MRI: Illustration of targeted delivery. *Magn. Reson. Med.* **51**, 1153–1162 (2004).

282. Smith, T. J. *et al.* Permanganate-based synthesis of manganese oxide nanoparticles in ferritin. *Nanotechnology* **28**, 195601 (2017).

283. Zhang, J. X. *et al.* Comparative studies of the cellular uptake, subcellular localization, and cytotoxic and phototoxic antitumor properties of ruthenium(II)-porphyrin conjugates with different linkers. *Bioconjug. Chem.* **23**, 1623–1638 (2012).

284. Pan, D. *et al.* Revisiting an old friend: manganese-based MRI contrast agents. *WIREs Nanomedicine and Nanobiotechnology* **3**, 162–173 (2011).

285. Bulte, J. W. *et al.* Specific MR imaging of human lymphocytes by monoclonal antibody-guided dextran-magnetite particles. *Magn. Reson. Med.* **25**, 148–157 (1992).

286. Frank, J. A. *et al.* Clinically applicable labeling of mammalian and stem cells by combining superparamagnetic iron oxides and transfection agents. *Radiology* **228**, 480–487 (2003).

287. Arbab, A. S. *et al.* Labeling of cells with ferumoxides-protamine sulfate complexes does not inhibit function or differentiation capacity of hematopoietic or mesenchymal stem cells. *NMR Biomed.* **18**, 553–559 (2005).

288. Thu, M. S. *et al.* Self-assembling nanocomplexes by combining ferumoxytol, heparin and protamine for cell tracking by magnetic resonance imaging. *Nat. Med.* **18**, 463–467 (2012).

289. Walczak, P. *et al.* Magnetoelectroporation: improved labeling of neural stem cells and leukocytes for cellular magnetic resonance imaging using a single FDA-approved agent. *Nanomedicine* **2**, 89–94 (2006).

290. Ahrens, E. T., Feili-Hariri, M., Xu, H., Genove, G. & Morel, P. A. Receptor-mediated endocytosis of iron-oxide particles provides efficient labeling of dendritic cells for in vivo MR imaging. *Magn. Reson. Med.* **49**, 1006–1013 (2003).

291. Nejadnik, H. *et al.* The Protein Corona around Nanoparticles Facilitates Stem Cell Labeling for Clinical MR Imaging. *Radiology* **286**, 938–947 (2018).

292. Bhorade, R., Weissleder, R., Nakakoshi, T., Moore, A. & Tung, C. H. Macrocyclic chelators with paramagnetic cations are internalized into mammalian cells via a HIV-tat derived membrane translocation peptide. *Bioconjug. Chem.* **11**, 301–305 (2000).

293. Allen, M. J. & Meade, T. J. Synthesis and visualization of a membrane-permeable MRI contrast agent. *J. Biol. Inorg. Chem. JBIC a Publ. Soc. Biol. Inorg. Chem.* **8**, 746–750 (2003).

294. Olson, E. S. *et al.* Activatable cell penetrating peptides linked to nanoparticles as dual probes for in vivo fluorescence and MR imaging of proteases. *Proc. Natl. Acad. Sci. U. S. A.* **107**, 4311–4316 (2010).

295. Endres, P. J., MacRenaris, K. W., Vogt, S. & Meade, T. J. Cell-permeable MR contrast agents with increased intracellular retention. *Bioconjug. Chem.* **19**, 2049–2059 (2008).

296. Carney, C. E. *et al.* Cell labeling via membrane-anchored lipophilic MR contrast agents. *Bioconjug. Chem.* **25**, 945–954 (2014).

297. Yamane, T. *et al.* Method for enhancing cell penetration of Gd3+-based MRI contrast agents by conjugation with hydrophobic fluorescent dyes. *Bioconjug. Chem.* **22**, 2227–2236 (2011).

298. Haedicke, I. E. *et al.* An enzyme-activatable and cell-permeable MnIII- porphyrin as a highly efficient T1 MRI contrast agent for cell labeling. *Chem. Sci.* **7**, 4308–4317 (2016).

299. Walczak, P., Kedziorek, D. A., Gilad, A. A., Barnett, B. P. & Bulte, J. W. M. Applicability and limitations of MR tracking of neural stem cells with asymmetric cell division and rapid turnover: the case of the shiverer dysmyelinated mouse brain. *Magn. Reson. Med.* **58**, 261–269 (2007).

300. Cromer Berman, S. M. *et al.* Cell motility of neural stem cells is reduced after SPIO-labeling, which is mitigated after exocytosis. *Magn. Reson. Med.* **69**, 255–262 (2013).

301. Haedicke, I. E. *et al.* An enzyme-activatable and cell-permeable MnIII-porphyrin as a highly efficient: T 1 MRI contrast agent for cell labeling. *Chem. Sci.* **7**, 4308–4317 (2016).

302. Long, C. M., van Laarhoven, H. W. M., Bulte, J. W. M. & Levitsky, H. I. Magnetovaccination as a novel method to assess and quantify dendritic cell tumor antigen capture and delivery to lymph nodes. *Cancer Res.* **69**, 3180–3187 (2009).

303. Harisinghani, M. G. *et al.* Noninvasive detection of clinically occult lymph-node metastases in prostate cancer. *N. Engl. J. Med.* **348**, 2491–2499 (2003).

304. Kooi, M. E. *et al.* Accumulation of ultrasmall superparamagnetic particles of iron oxide in human atherosclerotic plaques can be detected by in vivo magnetic resonance imaging. *Circulation* **107**, 2453–2458 (2003).

305. Hubert, V. *et al.* MRI coupled with clinically-applicable iron oxide nanoparticles reveals choroid plexus involvement in a murine model of neuroinflammation. *Sci. Rep.* **9**, 1–9 (2019).

306. Ahrens, E. T., Young, W.-B., Xu, H. & Pusateri, L. K. Rapid quantification of inflammation in tissue samples using perfluorocarbon emulsion and fluorine-19 nuclear magnetic resonance. *Biotechniques* **50**, 229–234 (2011).

307. Kadayakkara, D. K., Ranganathan, S., Young, W.-B. & Ahrens, E. T. Assaying macrophage activity in a murine model of inflammatory bowel disease using fluorine-19 MRI. *Lab. Invest.* **92**, 636–645 (2012).

308. Hertlein, T. *et al.* Visualization of abscess formation in a murine thigh infection model of Staphylococcus aureus by 19F-magnetic resonance imaging (MRI). *PLoS One* **6**, e18246 (2011).

309. Hitchens, T. K. *et al.* 19F MRI detection of acute allograft rejection with in vivo perfluorocarbon labeling of immune cells. *Magn. Reson. Med.* **65**, 1144–1153 (2011).

310. Sosnovik, D. E. & Nahrendorf, M. Cells and iron oxide nanoparticles on the move: magnetic resonance imaging of monocyte homing and myocardial inflammation in patients with ST-elevation myocardial infarction. *Circulation. Cardiovascular imaging* **5**, 551–554 (2012).

311. Gaglia, J. L. *et al.* Noninvasive imaging of pancreatic islet inflammation in type 1A diabetes patients. *J. Clin. Invest.* **121**, 442–445 (2011).

312. Luciani, A. *et al.* Adipose tissue macrophages: MR tracking to monitor obesity-associated inflammation. *Radiology* **263**, 786–793 (2012).

313. Chauveau, F., Cho, T. H., Berthezène, Y., Nighoghossian, N. & Wiart, M. Imaging inflammation in stroke using magnetic resonance imaging. *Int. J. Clin. Pharmacol. Ther.* **48**, 718–728 (2010).

314. Weise, G., Basse-Luesebrink, T. C., Wessig, C., Jakob, P. M. & Stoll, G. In vivo imaging of inflammation in the peripheral nervous system by (19)F MRI. *Exp. Neurol.* **229**, 494–501 (2011).

315. Millward, J. M. *et al.* Iron oxide magnetic nanoparticles highlight early involvement of the choroid plexus in central nervous system inflammation. *ASN Neuro* **5**, e00110 (2013).

316. Millward, J. M. *et al.* Application of Europium-Doped Very Small Iron Oxide Nanoparticles to Visualize Neuroinflammation with MRI and Fluorescence Microscopy. *Neuroscience* **403**, 136–144 (2019).

317. Bernd, E. *et al.* Early Assessment of Pulmonary Inflammation by 19F MRI In Vivo. *Circ. Cardiovasc. Imaging* **3**, 202–210 (2010).

318. Flögel, U. *et al.* In vivo monitoring of inflammation after cardiac and cerebral ischemia by fluorine magnetic resonance imaging. *Circulation* **118**, 140–148 (2008).

319. Flögel, U. *et al.* Noninvasive detection of graft rejection by in vivo (19) F MRI in the early stage. *Am. J. Transplant. Off. J. Am. Soc. Transplant. Am. Soc. Transpl. Surg.* **11**, 235–244 (2011).

320. Daldrup-Link, H. E. *et al.* Detection of Stem Cell Transplant Rejection with Ferumoxytol MR Imaging: Correlation of MR Imaging Findings with Those at Intravital Microscopy. *Radiology* **284**, 495–507 (2017).

321. Bulte, J. W. M. Science to Practice: Can MR Imaging Cell Tracking of Macrophage Infiltration Be Used as a Predictive Imaging Biomarker for Transplanted Stem Cell Rejection? *Radiology* **284**, 307–309 (2017).

322. Khurana, A. *et al.* Intravenous Ferumoxytol Allows Noninvasive MR Imaging Monitoring of Macrophage Migration into Stem Cell Transplants. *Radiology* **264**, 803–811 (2012).

323. Baiu, D. C., Brazel, C. S., Bao, Y. & Otto, M. Interactions of iron oxide nanoparticles with the immune system: challenges and opportunities for their use in nano-oncology. *Curr. Pharm. Des.* **19**, 6606–6621 (2013).

324. Hamm, B. *et al.* Contrast-enhanced MR imaging of liver and spleen: first experience in humans with a new superparamagnetic iron oxide. *J. Magn. Reson. Imaging* **4**, 659–668 (1994).

325. Kershaw, M. H., Westwood, J. A. & Hwu, P. Dual-specific T cells combine proliferation and antitumor activity. *Nat. Biotechnol.* **20**, 1221–1227 (2002).

326. Bar-Shir, A. *et al.* Transforming thymidine into a magnetic resonance imaging probe for monitoring gene expression. *J. Am. Chem. Soc.* **135**, 1617–1624 (2013).

327. Alon, L. *et al.* Cardiac CEST-MRI for tracking stem cell survival and determining the role of CXCL2. *J. Cardiovasc. Magn. Reson.* **18**, P262 (2016).

328. Weissleder, R. *et al.* MR imaging and scintigraphy of gene expression through melanin induction. *Radiology* **204**, 425–429 (1997).

329. Feng, H. *et al.* TYR as a multifunctional reporter gene regulated by the Tet-on system for multimodality imaging: an in vitro study. *Sci. Rep.* **5**, 15502 (2015).

330. Louie, A. Y. *et al.* In vivo visualization of gene expression using magnetic resonance imaging. *Nat. Biotechnol.* **18**, 321–325 (2000).

331. Yu, J.-X., Kodibagkar, V. D., Hallac, R. R., Liu, L. & Mason, R. P. Dual 19F/1H MR Gene Reporter Molecules for in Vivo Detection of β-Galactosidase. *Bioconjug. Chem.* **23**, 596–603 (2012).

332. Yang, C., Tian, R., Liu, T. & Liu, G. MRI reporter genes for noninvasive molecular imaging. *Molecules* **21**, 1–16 (2016).

333. Patrick, P. S. *et al.* Development of Timd2 as a reporter gene for MRI. *Magn. Reson. Med.* **75**, 1697–1707 (2016).

334. Weissleder, R. *et al.* In vivo magnetic resonance imaging of transgene expression. *Nat. Med.* **6**, 351–355 (2000).

335. Tannous, B. A. *et al.* Metabolic biotinylation of cell surface receptors for in vivo imaging. *Nat. Methods* **3**, 391–396 (2006).

336. Moore, A., Basilion, J. P., Chiocca, E. A. & Weissleder, R. Measuring transferrin receptor gene expression by NMR imaging. *Biochim. Biophys. Acta - Mol. Cell Res.* **1402**, 239–249 (1998).

337. Richardson, D. R. & Ponka, P. The molecular mechanisms of the metabolism and transport of iron in normal and neoplastic cells. *Biochim. Biophys. Acta* **1331**, 1–40 (1997).

338. Pereira, S. M. *et al.* Evaluating the effectiveness of transferrin receptor-1 (TfR1) as a magnetic resonance reporter gene. *Contrast Media Mol. Imaging* **11**, 236–244 (2016).

339. Pereira, S. M., Moss, D., Williams, S. R., Murray, P. & Taylor, A. Overexpression of the MRI Reporter Genes Ferritin and Transferrin Receptor Affect Iron Homeostasis and Produce Limited Contrast in Mesenchymal Stem Cells. *Int. J. Mol. Sci.* **16**, 15481–15496 (2015).

340. Genove, G., DeMarco, U., Xu, H., Goins, W. F. & Ahrens, E. T. A new transgene reporter for in vivo magnetic resonance imaging. *Nat. Med.* **11**, 450–454 (2005).

341. Iordanova, B. & Ahrens, E. T. In vivo magnetic resonance imaging of ferritin-based reporter visualizes native neuroblast migration. *Neuroimage* **59**, 1004–1012 (2012).

342. He, X., Cai, J., Liu, B., Zhong, Y. & Qin, Y. Cellular magnetic resonance imaging contrast generated by the ferritin heavy chain genetic reporter under the control of a Tet-On switch. *Stem Cell Res. Ther.* **6**, 207 (2015).

343. Cai, Y. *et al.* Enhanced magnetic resonance imaging and staining of cancer cells using ferrimagnetic H-ferritin nanoparticles with increasing core size. *Int. J. Nanomedicine* **10**, 2619–2634 (2015).

344. Cohen, B. *et al.* MRI detection of transcriptional regulation of gene expression in transgenic mice. *Nat. Med.* **13**, 498–503 (2007).

345. Vande Velde, G. *et al.* Quantitative evaluation of MRI-based tracking of ferritin-labeled endogenous neural stem cell progeny in rodent brain. *Neuroimage* **62**, 367–380 (2012).

346. He, D. & Marles-Wright, J. Ferritin family proteins and their use in bionanotechnology. *N. Biotechnol.* **32**, 651–657 (2015).

347. Lee, C. W. *et al.* The Effectiveness of Ferritin as a Contrast Agent for Cell Tracking MRI in Mouse Cancer Models. *Yonsei Med. J.* **58**, 51–58 (2017).

348. Moglia, I., Santiago, M., Olivera-Nappa, Á. & Soler, M. An optimized low-cost protocol for standardized production of iron-free apoferritin nanocages with high protein recovery and suitable conformation for nanotechnological applications. *J. Inorg. Biochem.* **183**, 184–190 (2018).

349. Kim, H. S. *et al.* Noninvasive MRI and multilineage differentiation capability of ferritin-transduced human mesenchymal stem cells. *NMR Biomed.* **28**, 168–179 (2015).

350. Naumova, A. V. *et al.* Ferritin overexpression for noninvasive magnetic resonance imaging-based tracking of stem cells transplanted into the heart. *Mol. Imaging* **9**, 201–210 (2010).

351. Kim, H. S. *et al.* In vivo Tracking of Dendritic Cell using MRI Reporter Gene, Ferritin. *PLoS One* **10**, e0125291 (2015).

352. Iordanova, B. & Ahrens, E. T. In vivo magnetic resonance imaging of ferritin-based reporter visualizes native neuroblast migration. *Neuroimage* **59**, 1004–1012 (2012).

353. Ziv, K. *et al.* Ferritin as a reporter gene for MRI: chronic liver over expression of H-ferritin during dietary iron supplementation and aging. *NMR Biomed.* **23**, 523–531 (2010).

354. Kim, H. S. *et al.* In vivo magnetic resonance imaging of transgenic mice expressing human ferritin. *Mol. Imaging Biol.* **15**, 48–57 (2013).

355. Feng, Y., Liu, Q., Zhu, J., Xie, F. & Li, L. Efficiency of Ferritin as an MRI Reporter Gene in NPC Cells Is Enhanced by Iron Supplementation. *J. Biomed. Biotechnol.* **2012**, 434878 (2012).

356. Bartelle, B. B., Szulc, K. U., Suero-Abreu, G. A., Rodriguez, J. J. & Turnbull, D. H. Divalent metal transporter, DMT1: A novel MRI reporter protein. *Magn. Reson. Med.* **70**, 842–850 (2013).

357. Bjørklund, G., Dadar, M., Peana, M., Rahaman, M. S. & Aaseth, J. Interactions between iron and manganese in neurotoxicity. *Arch. Toxicol.* **94**, 725–734 (2020).

358. Liu, G., Bulte, J. W. M. & Gilad, A. A. CEST MRI reporter genes. *Methods Mol. Biol.* **711**, 271–280 (2011).

359. Gilad, A. A. *et al.* Artificial reporter gene providing MRI contrast based on proton exchange. *Nat. Biotechnol.* **25**, 217–219 (2007).

360. Robitaille, R. *et al.* Inflammatory response to peritoneal implantation of alginate-poly-L-lysine microcapsules. *Biomaterials* **26**, 4119–4127 (2005).

361. Strand, B. L. *et al.* Poly-L-lysine induces fibrosis on alginate microcapsules via the induction of cytokines. *Cell Transplant.* **10**, 263–275 (2001).

362. McMahon, M. T. *et al.* New 'multicolor' polypeptide Diamagnetic Chemical Exchange Saturation Transfer (DIACEST) contrast agents for MRI. *Magn. Reson. Med.* **60**, 803–812 (2008).

363. Liu, G. *et al.* In vivo multicolor molecular MR imaging using diamagnetic chemical exchange saturation transfer liposomes. *Magn. Reson. Med.* **67**, 1106–1113 (2012).

364. Moore, A., Josephson, L., Bhorade, R. M., Basilion, J. P. & Weissleder, R. Human Transferrin Receptor Gene as a Marker Gene for MR Imaging. *Radiology* **221**, 244–250 (2001).

365. Ahrens, E. T. & Bulte, J. W. M. Tracking immune cells in vivo using magnetic resonance imaging. *Nat. Rev. Immunol.* **13**, 755–763 (2013).

366. Vande Velde, G. *et al.* Evaluation of the specificity and sensitivity of ferritin as an MRI reporter gene in the mouse brain using lentiviral and adeno-associated viral vectors. *Gene Ther.* **18**, 594–605 (2011).

367. Naumova, A. V *et al.* Magnetic Resonance Imaging Tracking of Graft Survival in the Infarcted Heart: Iron Oxide Particles Versus Ferritin Overexpression Approach. *J. Cardiovasc. Pharmacol. Ther.* **19**, 358–367 (2014).

368. Iordanova, B., Robison, C. S. & Ahrens, E. T. Design and characterization of a chimeric ferritin with enhanced iron loading and transverse NMR relaxation rate. *JBIC J. Biol. Inorg. Chem.* **15**, 957–965 (2010).

369. Bartelle, B. B., Szulc, K. U., Suero-Abreu, G. A., Rodriguez, J. J. & Turnbull, D. H. Divalent metal transporter, DMT1: A novel MRI reporter protein. *Magn. Reson. Med.* **70**, 842–850 (2013).

370. Thomas, P. & Smart, T. G. HEK293 cell line: A vehicle for the expression of recombinant proteins. *J. Pharmacol. Toxicol. Methods* **51**, 187–200 (2005).

371. Shahryari, A. *et al.* Development and Clinical Translation of Approved Gene Therapy Products for Genetic Disorders . *Frontiers in Genetics* **10**, 868 (2019).

372. Zwaka, P. T. NIH Stem Cell Information Home Page. In Stem Cell Information. *Bethesada, MD: National Institutes of Health, U.S. Department of Health and Human Services* (2016). Available at: https://stemcells.nih.gov/info/Regenerative_Medicine/2006Chapter4.htm. (Accessed: 28th June 2020)

373. Chisholm, J., Ruff, C. & Viswanathan, S. Current state of Health Canada regulation for cellular and

gene therapy products: potential cures on the horizon. *Cytotherapy* **21**, 686–698 (2019).

374. Approved Cellular and Gene Therapy Products. *Administration, U.S. Food & Drug, Office of Tissues and Advanced Therapies* (2019). Available at: https://www.fda.gov/vaccines-blood-biologics/cellular-gene-therapy-products/approved-cellular-and-gene-therapy-products. (Accessed: 28th June 2020)

375. Szulc, D. A. *et al.* MRI method for labeling and imaging decellularized extracellular matrix scaffolds for tissue engineering. *Magn. Reson. Med.* **83**, 2138–2149 (2020).

376. Conklin, B. S., Richter, E. R., Kreutziger, K. L., Zhong, D.-S. & Chen, C. Development and evaluation of a novel decellularized vascular xenograft. *Med. Eng. Phys.* **24**, 173–183 (2002).

377. Schenke-Layland, K. *et al.* Impact of decellularization of xenogeneic tissue on extracellular matrix integrity for tissue engineering of heart valves. *J. Struct. Biol.* **143**, 201–208 (2003).

378. Farhat, W. *et al.* Porosity of porcine bladder acellular matrix: impact of ACM thickness. *J. Biomed. Mater. Res. A* **67**, 970–974 (2003).

379. Shapiro, L. *et al.* In vitro evaluation of functionalized decellularized muscle scaffold for in situ skeletal muscle regeneration. *Biomed. Mater.* **14**, 45015 (2019).

380. Shirakigawa, N. & Ijima, H. Decellularization of Liver and Organogenesis in Rats. *Methods Mol. Biol.* **1577**, 271–281 (2018).

381. Benders, K. E. M., Terpstra, M. L., Levato, R. & Malda, J. Fabrication of Decellularized Cartilage-derived Matrix Scaffolds. *J. Vis. Exp.* (2019). doi:10.3791/58656

382. Haykal, S. *et al.* The effect of decellularization of tracheal allografts on leukocyte infiltration and of recellularization on regulatory T cell recruitment. *Biomaterials* **34**, 5821–5832 (2013).

383. Uriarte, J. J., Uhl, F. E., Rolandsson Enes, S. E., Pouliot, R. A. & Weiss, D. J. Lung bioengineering: advances and challenges in lung decellularization and recellularization. *Curr. Opin. Organ Transplant.* **23**, 673–678 (2018).

384. Sarig, U. *et al.* Natural myocardial ECM patch drives cardiac progenitor based restoration even after scarring. *Acta Biomater.* **44**, 209–220 (2016).

385. Kim, B. S., Kim, H., Gao, G., Jang, J. & Cho, D.-W. Decellularized extracellular matrix: a step towards the next generation source for bioink manufacturing. *Biofabrication* **9**, 34104 (2017).

386. Szulc, D. A. & Cheng, H.-L. M. One-Step Labeling of Collagen Hydrogels with Polydopamine and Manganese Porphyrin for Non-Invasive Scaffold Tracking on Magnetic Resonance Imaging. *Macromol. Biosci.* **0**, 1800330 (2019).

387. Liang, Y. *et al.* Label-free imaging of gelatin-containing hydrogel scaffolds. *Biomaterials* **42**, 144–150 (2015).

388. Cheng, W. *et al.* Binding of a dimeric manganese porphyrin to serum albumin: towards a gadolinium-free blood-pool T 1 MRI contrast agent. *JBIC J. Biol. Inorg. Chem.* **19**, 229–235 (2014).

389. Venter, A. *et al.* A manganese porphyrin-based T1 contrast agent for cellular MR imaging of human embryonic stem cells. *Sci. Rep.* **8**, 11 (2018).

390. S. Lindsey, J., Prathapan, S., E. Johnson, T. & W. Wagner, R. Porphyrin building blocks for modular

construction of bioorganic model systems. *Tetrahedron* **50**, 8941–8968 (1994).

391. Brown, A. L. *et al.* 22 Week assessment of bladder acellular matrix as a bladder augmentation material in a porcine model. *Biomaterials* **23**, 2179–2190 (2002).

392. Freytes, D. O., Martin, J., Velankar, S. S., Lee, A. S. & Badylak, S. F. Preparation and rheological characterization of a gel form of the porcine urinary bladder matrix. *Biomaterials* **29**, 1630–1637 (2008).

393. Christman, K. L. & Young, D. A. Decellularized and delipidized extracellular matrix and methods of use. (2012).

394. Dequach, J. A., Yuan, S. H., Goldstein, L. S. B. & Christman, K. L. Decellularized porcine brain matrix for cell culture and tissue engineering scaffolds. *Tissue Eng. - Part A* **17**, 2583–2592 (2011).

395. Jang, J. *et al.* Tailoring mechanical properties of decellularized extracellular matrix bioink by vitamin B2-induced photo-crosslinking. *Acta Biomater.* **33**, 88–95 (2016).

396. Wachs, R. A. *et al.* Creation of an injectable in situ gelling native extracellular matrix for nucleus pulposus tissue engineering. *Spine J.* **17**, 435–444 (2017).

397. Daly, A. B. *et al.* Initial binding and recellularization of decellularized mouse lung scaffolds with bone marrow-derived mesenchymal stromal cells. *Tissue Eng. Part A* **18**, 1–16 (2012).

398. Price, A. P., England, K. A., Matson, A. M., Blazar, B. R. & Panoskaltsis-Mortari, A. Development of a decellularized lung bioreactor system for bioengineering the lung: the matrix reloaded. *Tissue Eng. Part A* **16**, 2581–2591 (2010).

399. Cheng, H.-L. M. & Wright, G. A. Rapid High-Resolution T1 Mapping by Variable Flip Angles: Accurate and Precise Measurements in the Presence of Radiofrequency Field Inhomogeneity. *Magn. Reson. Med.* **55**, 566–576 (2006).

400. Beaumont, M. *et al.* Accurate liver T2 measurement of iron overload: a simulations investigation and in vivo study. *J. Magn. Reson. Imaging* **30**, 313–320 (2009).

401. Simsa, R. *et al.* Systematic in vitro comparison of decellularization protocols for blood vessels. *PLoS One* **13**, 1–19 (2018).

402. Mei, J. *et al.* The angiogenesis in decellularized scaffold-mediated the renal regeneration. *Oncotarget* **7**, 27085–27093 (2016).

403. Li, N. *et al.* Efficient decellularization for bovine pericardium with extracellular matrix preservation and good biocompatibility. *Interact. Cardiovasc. Thorac. Surg.* **26**, 768–776 (2018).

404. Davis, N. F. *et al.* Construction and evaluation of urinary bladder bioreactor for urologic tissue-engineering purposes. *Urology* **78**, 954–960 (2011).

405. Haykal, S., Soleas, J. P., Salna, M., Hofer, S. O. P. & Waddell, T. K. Evaluation of the structural integrity and extracellular matrix components of tracheal allografts following cyclical decellularization techniques: comparison of three protocols. *Tissue Eng. Part C. Methods* **18**, 614–623 (2012).

406. Shojaie, S. *et al.* Acellular lung scaffolds direct differentiation of endoderm to functional airway epithelial cells: requirement of matrix-bound HS proteoglycans. *Stem cell reports* **4**, 419–430

(2015).

407. Bölükbas, D. A., De Santis, M. M., Alsafadi, H. N., Doryab, A. & Wagner, D. E. The Preparation of Decellularized Mouse Lung Matrix Scaffolds for Analysis of Lung Regenerative Cell Potential. *Methods Mol. Biol.* **1940**, 275–295 (2019).

408. Winkelman, J. The distribution of tetraphenylporphinesulfonate in the tumor-bearing rat. *Cancer Res.* **22**, 589–596 (1962).

409. Cen, L. *et al.* Labeling of Adipose-Derived Stem Cells by Oleic-Acid-Modified Magnetic Nanoparticles. *Adv. Funct. Mater.* **19**, 1158–1166 (2009).

410. Nelson, G. N. *et al.* Initial evaluation of the use of USPIO cell labeling and noninvasive MR monitoring of human tissue-engineered vascular grafts in vivo. *FASEB J.* **22**, 3888–95 (2008).

411. Lynge, M. E., van der Westen, R., Postma, A. & Städler, B. Polydopamine—a nature-inspired polymer coating for biomedical science. *Nanoscale* **3**, 4916 (2011).

412. Hong, S. *et al.* Attenuation of the in vivo toxicity of biomaterials by polydopamine surface modification. *Nanomedicine* **6**, 793–801 (2011).

413. Davis, C. D. & Greger, J. L. Longitudinal changes of manganese-dependent superoxide dismutase and other indexes of manganese and iron status in women. *Am. J. Clin. Nutr.* **55**, 747–752 (1992).

414. Agency for Toxic Substances and Disease Registry (ATSDR). Toxicological profile for Manganese. *Atlanta, GA: U.S. Department of Health and Human Services, Public Health Service.* (2012). Available at: https://www.atsdr.cdc.gov/toxprofiles/tp.asp?id=102&tid=23. (Accessed: 10th June 2020)

415. Kanda, T. *et al.* Gadolinium-based Contrast Agent Accumulates in the Brain Even in Subjects without Severe Renal Dysfunction: Evaluation of Autopsy Brain Specimens with Inductively Coupled Plasma Mass Spectroscopy. *Radiology* **276**, 228–232 (2015).

416. Department, H. S. Summarization Bioconjugation techniques. *Ebooks* (2006). doi:10.1007/s00216-009-2731-y

417. Cheng, H. L. M., Haedicke, I. E., Cheng, W., Nofiele, J. T. & Zhang, X. A. Gadolinium-free T1 contrast agents for MRI: Tunable pharmacokinetics of a new class of manganese porphyrins. *J. Magn. Reson. Imaging* **40**, 1474–1480 (2014).

418. Ding, Y. H., Floren, M. & Tan, W. Mussel-inspired polydopamine for bio-surface functionalization. *Biosurface and Biotribology* **2**, 121–136 (2016).

419. Liu, C. Y. & Huang, C. J. Functionalization of Polydopamine via the Aza-Michael Reaction for Antimicrobial Interfaces. *Langmuir* **32**, 5019–5028 (2016).

420. Lee, H., Dellatore, S. M., Miller, W. M. & Messersmith, P. B. Mussel-Inspired Surface Chemistry for Multifunctional Coatings. *Science (80-.).* **318**, 426–430 (2007).

421. Zhu, S. *et al.* Fabrication of a novel bio-inspired collagen-polydopamine hydrogel and insights into the formation mechanism for biomedical applications. *RSC Adv.* **6**, 66180–66190 (2016).

422. Liu, Z. G., Qu, S. X. & Weng, J. Application of Polydopamine in Surface Modification of Biomaterials. *Prog. Chem.* **27**, 212–219 (2015).

423. Kang, S. M. *et al.* One-step multipurpose surface functionalization by adhesive catecholamine. *Adv. Funct. Mater.* **22**, 2949–2955 (2012).

424. Bojorquez, J. Z. *et al.* What are normal relaxation times of tissues at 3 T? *Magn. Reson. Imaging* **35**, 69–80 (2017).

425. McGuigan, A. P. & Sefton, M. V. Vascularized organoid engineered by modular assembly enables blood perfusion. *Proc. Natl. Acad. Sci.* **103**, 11461–11466 (2006).

426. Khan, O. F. & Sefton, M. V. Endothelialized biomaterials for tissue engineering applications in vivo. *Trends Biotechnol.* **29**, 379–387 (2011).

427. Keller, G. Embryonic stem cell differentiation: emergence of a new era in biology and medicine. *Genes Dev* **19**, (2005).

428. Shroff, G. & Gupta, R. Human embryonic stem cells in the treatment of patients with spinal cord injury. *Ann Neurosci* **22**, (2015).

429. Stoltz, J. F. Stem Cells and Regenerative Medicine: Myth or Reality of the 21th Century. *Stem Cells Int* **2015**, (2015).

430. Cheung, J. S. Cell number quantification of USPIO-labeled stem cells by MRI: an in vitro study. *Conf Proc IEEE Eng Med Biol Soc* **1**, (2006).

431. Ma, N. *et al.* Magnetic Resonance Imaging with Superparamagnetic Iron Oxide Fails to Track the Long-term Fate of Mesenchymal Stem Cells Transplanted into Heart. *Sci. Rep.* **5**, 9058 (2015).

432. Loai, S. *et al.* Positive-contrast cellular MRI of embryonic stem cells for tissue regeneration using a highly efficient T1 MRI contrast agent. *J Magn Reson Imaging* **44**, 1456–1463 (2016).

433. Di Gregorio, E. *et al.* On the fate of MRI Gd-based contrast agents in cells. Evidence for extensive degradation of linear complexes upon endosomal internalization. *Anal. Chem.* **85**, 5627–5631 (2013).

434. Berezin, M. B. Thermochemistry of Solution of Fe(III) and Mn(III) Complexes with Natural Porphyrins. *Russ. J. Gen. Chem.* **71**, (2001).

435. Alhamami, M. *et al.* Manganese-porphyrin-enhanced MRI for the detection of cancer cells: A quantitative in vitro investigation with multiple clinical subtypes of breast cancer. *PLoS One* **13**, (2018).

436. Lindsey, J. S., Schreiman, I. C., Hsu, H. C., Kearney, P. C. & Marguerettaz, A. M. Rothemund and Adler-Longo reactions revisited: synthesis of tetraphenylporphyrins under equilibrium conditions. *J. Org. Chem.* **52**, (1987).

437. Luguya, R., Jaquinod, L., Fronczek, F. R., Vicente, M. G. H. & Smith, K. M. Synthesis and reactions of meso-(p-nitrophenyl)porphyrins. *Tetrahedron* **60**, (2004).

438. Ringot, C. *et al.* Meso-functionalized aminoporphyrins as efficient agents for photo-antibacterial surfaces. *J. Porphyr. Phthalocyanines* **14**, 925–931 (2010).

439. Zou, T. *et al.* The positive influence of fullerene derivatives bonded to manganese(III) porphyrins on water proton relaxation. *Dalt. Trans.* **44 19**, 9114–9119 (2015).

440. Zhang, Z. *et al.* Synthesis and in vitro and in vivo evaluation of manganese(III) porphyrin-dextran

as a novel MRI contrast agent. *Bioorganic Med. Chem. Lett.* **19**, 6675–6678 (2009).

441. Sheridan, S. D., Surampudi, V. & Rao, R. R. Analysis of embryoid bodies derived from human induced pluripotent stem cells as a means to assess pluripotency. *Stem Cells Int* **2012**, (2012).

442. Megnin, F., Faustino, P. J., Lyon, R. C., Lelkes, P. I. & Cohen, J. S. Studies on the mechanism of selective retention of porphyrins and metalloporphyrins by cancer cells. *Biochim Biophys Acta* **929**, (1987).

443. Strober, W. Trypan Blue Exclusion Test of Cell Viability. *Curr. Protoc. Immunol.* **111**, A3.B.1-A3.B.3 (2015).

444. Kyrylkova, K., Kyryachenko, S., Leid, M. & Kioussi, C. Detection of apoptosis by TUNEL assay. *Methods Mol Biol* **887**, (2012).

445. Anderson, S. A., Lee, K. K. & Frank, J. A. Gadolinium-fullerenol as a paramagnetic contrast agent for cellular imaging. *Invest. Radiol.* **41**, (2006).

446. Treinen, K. A., Gray, T. J. & Blazak, W. F. Developmental toxicity of mangafodipir trisodium and manganese chloride in Sprague-Dawley rats. *Teratology* **52**, (1995).

447. Sepúlveda, M. R. *et al.* Evaluation of manganese uptake and toxicity in mouse brain during continuous MnCl2 administration using osmotic pumps. *Contrast Media Mol. Imaging* **7**, 426–434 (2012).

448. Szulc, D. A., Lee, X. A., Cheng, H.-Y. M. & Cheng, H.-L. M. Bright Ferritin—a Reporter Gene Platform for On-Demand, Longitudinal Cell Tracking on MRI. *iScience* **23**, (2020).

449. Li, L. *et al.* Superparamagnetic Iron Oxide Nanoparticles as MRI contrast agents for Non-invasive Stem Cell Labeling and Tracking. *Theranostics* **3**, 595–615 (2013).

450. Lang, C. *et al.* Positron emission tomography based in-vivo imaging of early phase stem cell retention after intramyocardial delivery in the mouse model. *Eur. J. Nucl. Med. Mol. Imaging* **40**, 1730–1738 (2013).

451. Bernau, K. *et al.* In vivo tracking of human neural progenitor cells in the rat brain using bioluminescence imaging. *J. Neurosci. Methods* **228**, 67–78 (2014).

452. Koehne, G. *et al.* Serial in vivo imaging of the targeted migration of human HSV-TK-transduced antigen-specific lymphocytes. *Nat. Biotechnol.* **21**, 405–413 (2003).

453. Pan, D. *et al.* Nanomedicine strategies for molecular targets with MRI and optical imaging. *Future Med. Chem.* **2**, 471–490 (2010).

454. Cohen, B., Dafni, H., Meir, G., Harmelin, A. & Neeman, M. Ferritin as an endogenous MRI reporter for noninvasive imaging of gene expression in C6 glioma tumors. *Neoplasia* **7**, 109–117 (2005).

455. Chen, A. P., Hurd, R. E., Gu, Y., Wilson, D. M. & Cunningham, C. H. 13C MR reporter probe system using dynamic nuclear polarization. *NMR Biomed.* **24**, 514–520 (2011).

456. Patrick, P. S. *et al.* Detection of transgene expression using hyperpolarized 13C urea and diffusion-weighted magnetic resonance spectroscopy. *Magn. Reson. Med.* **73**, 1401–1406 (2015).

457. Deans, A. E. *et al.* Cellular MRI contrast via coexpression of transferrin receptor and ferritin. *Magn. Reson. Med.* **56**, 51–59 (2006).

458. Genove, G., DeMarco, U., Xu, H., Goins, W. F. & Ahrens, E. T. A new transgene reporter for in vivo magnetic resonance imaging. *Nat. Med.* **11**, 450–454 (2005).

459. Mackle, P., Charnock, J. M., Garner, C. D., Meldrum, F. C. & Mann, S. Characterization of the manganese core of reconstituted ferritin by x-ray absorption spectroscopy. *J. Am. Chem. Soc.* **115**, 8471–8472 (1993).

460. Meldrum, F. C., Douglas, T., Levi, S., Arosio, P. & Mann, S. Reconstitution of manganese oxide cores in horse spleen and recombinant ferritins. *J. Inorg. Biochem.* **58**, 59–68 (1995).

461. Meldrum, F. C., Wade, V. J., Nimmo, D. L., Heywood, B. R. & Mann, S. Synthesis of inorganic nanophase materials in supramolecular protein cages. *Nature* **349**, 684–687 (1991).

462. Lam-Yuk-Tseung, S. & Gros, P. Distinct Targeting and Recycling Properties of Two Isoforms of the Iron Transporter DMT1 (NRAMP2, Slc11A2)†. *Biochemistry* **45**, 2294–2301 (2006).

463. Lee, S. *et al.* REEP5 depletion causes sarco-endoplasmic reticulum vacuolization and cardiac functional defects. *Nat. Commun.* 1–20 (2020). doi:10.1038/s41467-019-14143-9

464. Schrand, A. M., Schlager, J. J., Dai, L. & Hussain, S. M. Preparation of cells for assessing ultrastructural localization of nanoparticles with transmission electron microscopy. *Nat. Protoc.* **5**, 744–757 (2010).

465. Cheng, H. L. & Wright, G. A. Rapid high-resolution T(1) mapping by variable flip angles: accurate and precise measurements in the presence of radiofrequency field inhomogeneity. *Magn Reson Med* **55**, (2006).

466. Sibille, J. C., Ciriolo, M., Kondo, H., Crichton, R. R. & Aisen, P. Subcellular localization of ferritin and iron taken up by rat hepatocytes. *Biochem. J.* **262**, 685–688 (1989).

467. Farrant, J. L. An electron microscopic study of ferritin. *Biochim. Biophys. Acta* **13**, 569–576 (1954).

468. Watabe, T. & Hoshino, T. Observation of individual ferritin particles by means of scanning electron microscope. *J. Electron Microsc. (Tokyo).* **25**, 31–33 (1976).

469. Kalman, F. K., Geninatti-crich, S. & Aime, S. Reduction / Dissolution of a b -MnOOH Nanophase in the Ferritin Cavity To Yield a Highly Sensitive , Biologically Compatible Magnetic Resonance Imaging Agent **. *Angew. Chemie Int. Ed.* **49**, 612–615 (2010).

470. Sana, B., Poh, C. L. & Lim, S. A manganese–ferritin nanocomposite as an ultrasensitive T2 contrast agent. *Chem. Commun.* **48**, 862–864 (2012).

471. Au, C., Benedetto, A. & Aschner, M. Manganese transport in eukaryotes: The role of DMT1. *Neurotoxicology* **29**, 569–576 (2008).

472. Gunshin, H. *et al.* Cloning and characterization of a mammalian proton-coupled metal-ion transporter. *Nature* **388**, 482–488 (1997).

473. Moos, T. & Morgan, E. H. Transferrin and transferrin receptor function in brain barrier systems. *Cell. Mol. Neurobiol.* **20**, 77–95 (2000).

474. Ehrnstorfer, I. A., Manatschal, C., Arnold, F. M., Laederach, J. & Dutzler, R. Structural and mechanistic basis of proton-coupled metal ion transport in the SLC11/NRAMP family. *Nat. Commun.* **8**, 14033 (2017).

475. Tiffen, J. C., Bailey, C. G., Ng, C., Rasko, J. E. J. & Holst, J. Luciferase expression and bioluminescence does not affect tumor cell growth in vitro or in vivo. *Mol. Cancer* **9**, 1–8 (2010).

476. Tietjen, G. T., Bracaglia, L. G., Saltzman, W. M. & Pober, J. S. Focus on Fundamentals: Achieving Effective Nanoparticle Targeting. *Trends Mol. Med.* **24**, 598–606 (2018).

477. Wennberg, A. Neurotoxic effects of selected metals. *Scand. J. Work. Environ. Health* **20**, 65–71 (1994).

478. Bernau, K. *et al.* In vivo tracking of human neural progenitor cells in the rat brain using magnetic resonance imaging is not enhanced by ferritin expression. *Cell Transplant.* **25**, 575–592 (2016).

479. Pereira, S. M., Moss, D., Williams, S. R., Murray, P. & Taylor, A. Overexpression of the MRI reporter genes ferritin and transferrin receptor affect iron homeostasis and produce limited contrast in mesenchymal stem cells. *Int. J. Mol. Sci.* **16**, 15481–15496 (2015).

480. Herynek, V., Bulte, J. W., Douglas, T. & Brooks, R. A. Dynamic relaxometry: application to iron uptake by ferritin. *J. Biol. Inorg. Chem. JBIC a Publ. Soc. Biol. Inorg. Chem.* **5**, 51–56 (2000).

481. Vymazal, J., Zak, O., Bulte, J. W., Aisen, P. & Brooks, R. A. T1 and T2 of ferritin solutions: effect of loading factor. *Magn. Reson. Med.* **36**, 61–65 (1996).

482. Hoshyar, N., Gray, S., Han, H. & Bao, G. The effect of nanoparticle size on in vivo pharmacokinetics and cellular interaction. *Nanomedicine* **11**, 673–692 (2016).

483. Theil, E. C., Liu, X. S. & Tosha, T. Gated pores in the ferritin protein nanocage. *Inorganica Chim. Acta* **361**, 868–874 (2008).

484. Wardeska, J. G., Viglione, B. & Chasteen, N. D. Metal Ion Complexes of Apoferritin. *J. Biol. Chem.* **261**, 6677–6683 (1986).

485. Ardini, M. *et al.* Study of manganese binding to the ferroxidase centre of human H-type ferritin. *J. Inorg. Biochem.* **182**, 103–112 (2018).

Appendices

Appendix A

Supplemental Information: MRI method for labeling and imaging decellularized extracellular matrix scaffolds for tissue engineering

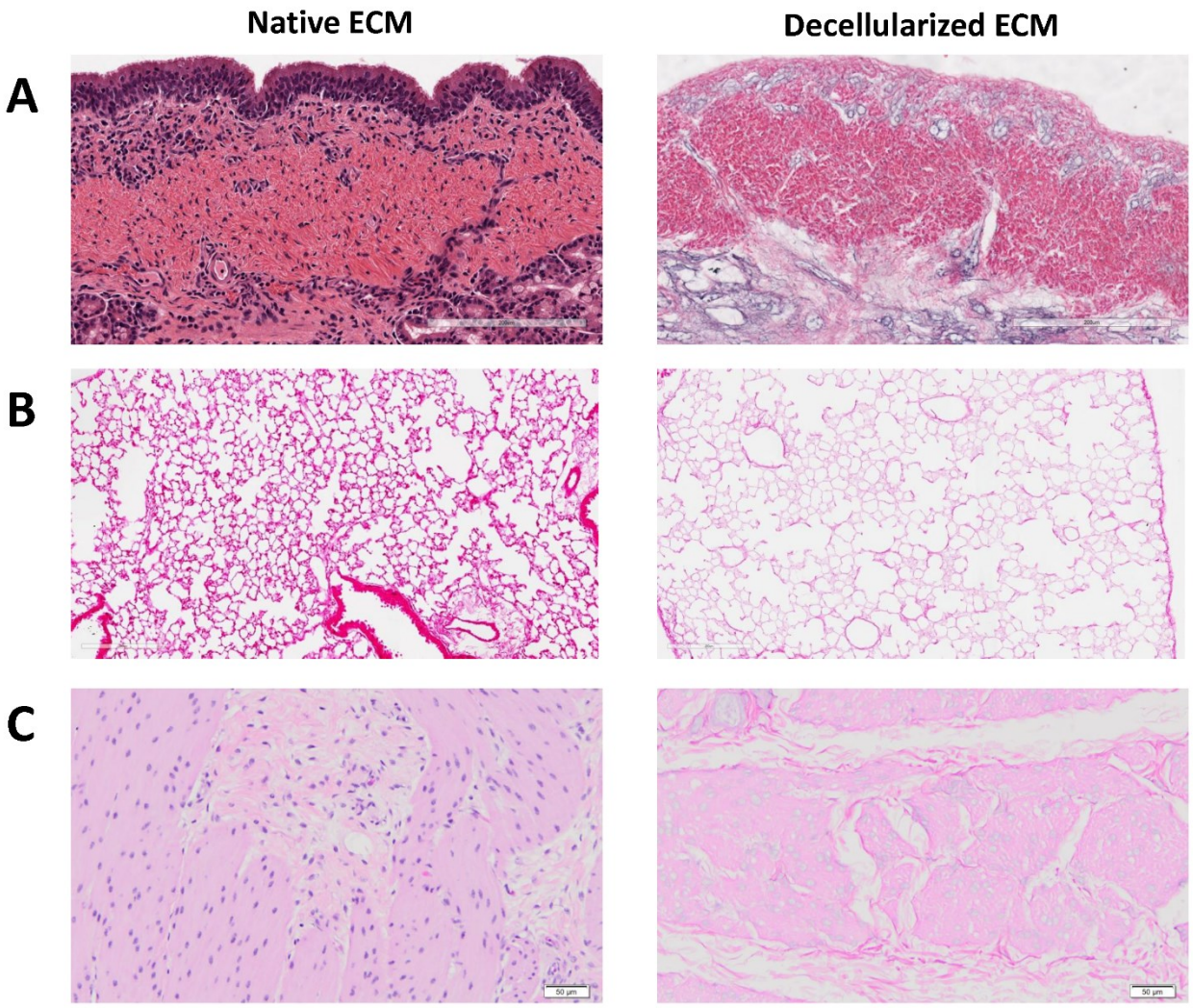

Figure A1: Histological staining of native and decellularized ECM. Hematoxylin and Eosin staining of native and decellularized tissue sections of **(A)** porcine trachea, **(B)** murine lung, and **(C)** porcine bladder demonstrates the absence of cellular/nuclear components but the retention of the ECM network of each tissue.

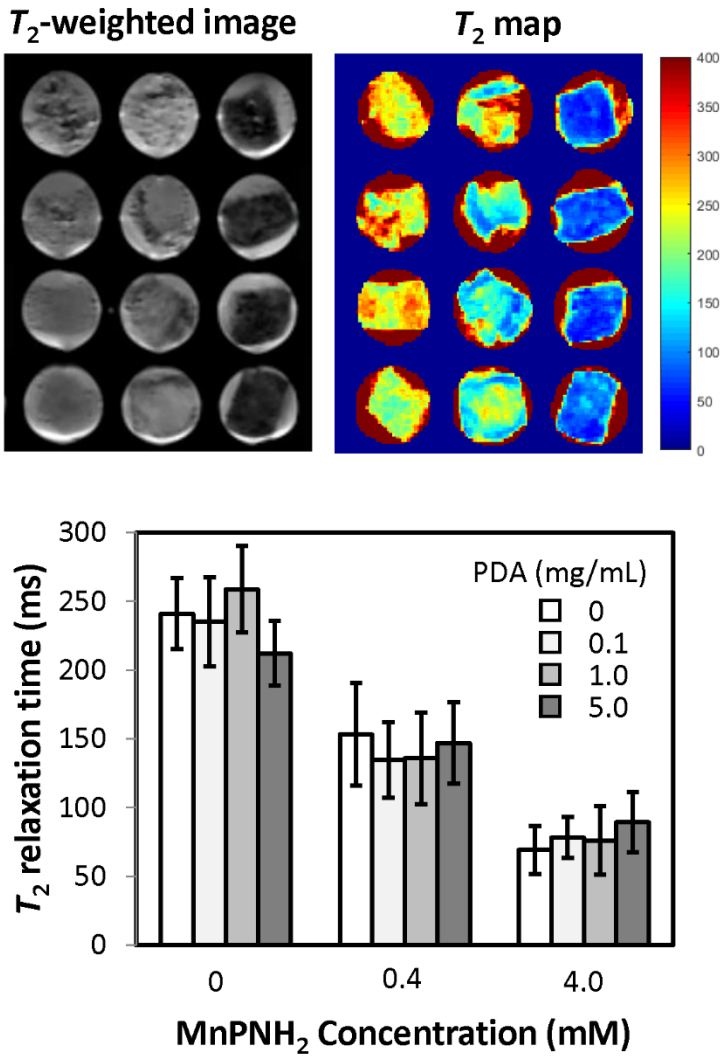

Figure A2: Optimization of labeling dECM scaffolds. Porcine bladder dECM scaffolds were labeled with varying concentrations of $MnPNH_2$ (0, 0.4, and 4.0 mM, in images from left to right within each row) and PDA (0, 0.1, 1.0, and 5.0 mg/mL, in images from top to bottom within each column). Representative T_2-weighted turbo spin-echo image (top left) and corresponding T_2 map (top right), and mean changes in T_2 (bottom center). A significant change in T_2 is observed only for different $MnPNH_2$ concentrations ($P < 0.05$) but not for PDA. Shown are mean values and standard deviations.

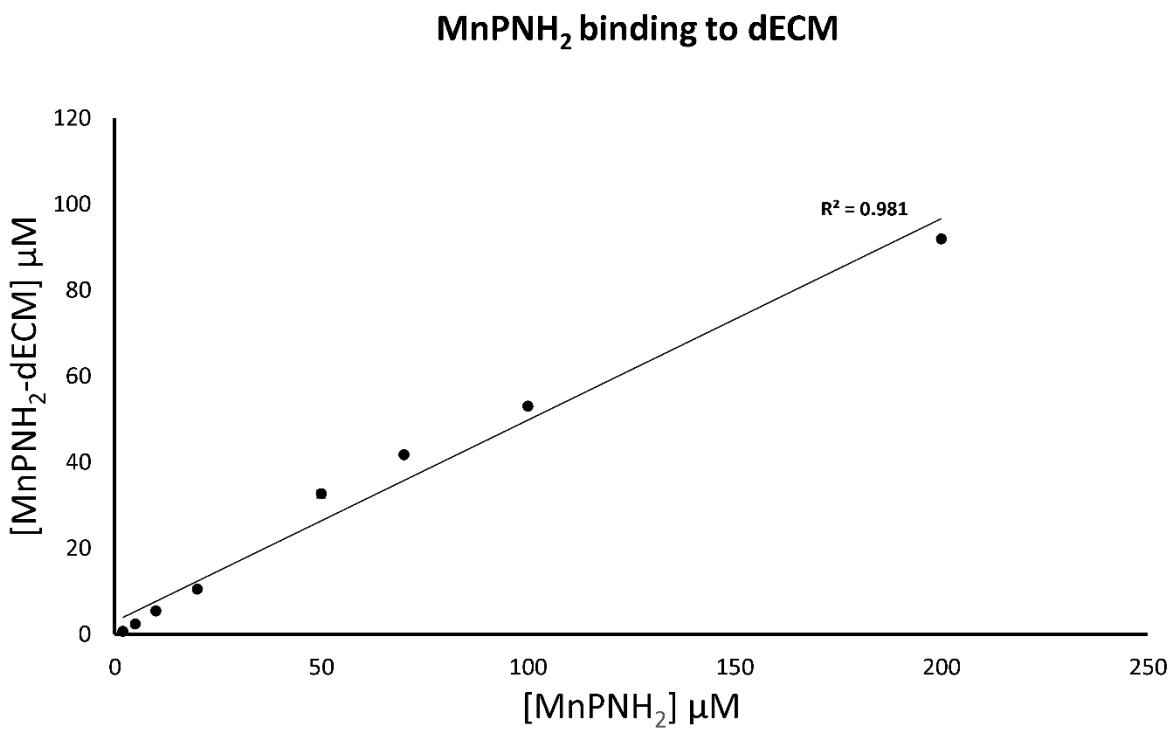

Figure A3: Binding of $MnPNH_2$ to dECM. The concentration of $MnPNH_2$ bound to dECM gel is shown over a range of $MnPNH_2$ initial labelling concentrations (0-200 µM). $MnPNH_2$ incorporation into dECM gels exhibited a linear binding efficiency of approximately 50% and no evidence of saturation up to a concentration of 200 µM.

Appendix B

Supplemental Information: One-Step Labeling of Collagen Hydrogels with Polydopamine and Manganese Porphyrin for Non-Invasive Scaffold Tracking on Magnetic Resonance Imaging

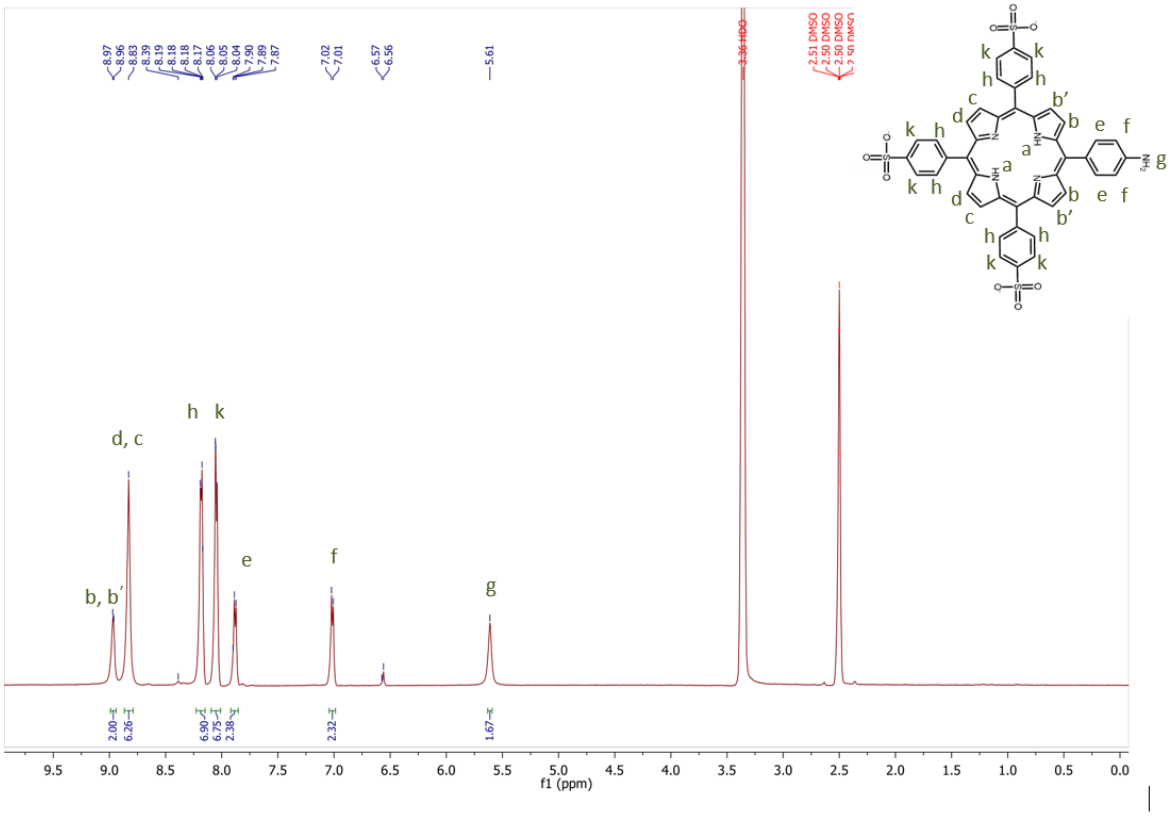

Figure B1: H^1NMR Spectrum of the Apo-PNH_2 acquired on a Bruker US 500MHz system. Chemical shifts and splitting patterns in line with literature.

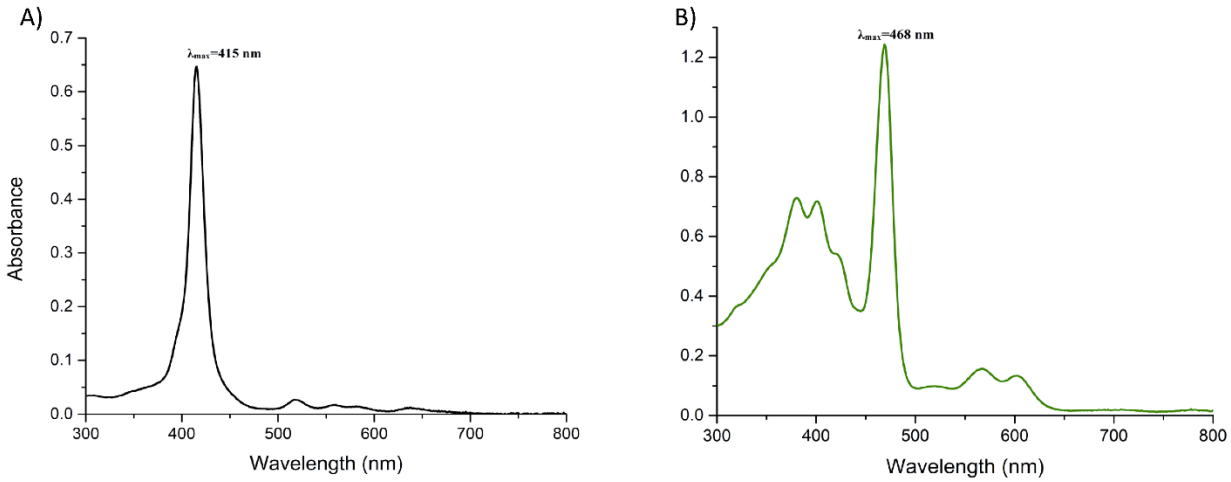

Figure B2: UV spectrum of A) Apo-PNH_2 and B) MnP-NH_2. measured in MeOH and HEPES buffer at 25°C, λ_{max}=415 nm, ε =354000 $M^{-1}cm^{-1}$ and λ_{max}=468nm, ε =93552 $M^{-1}cm^{-1}$, respectively.

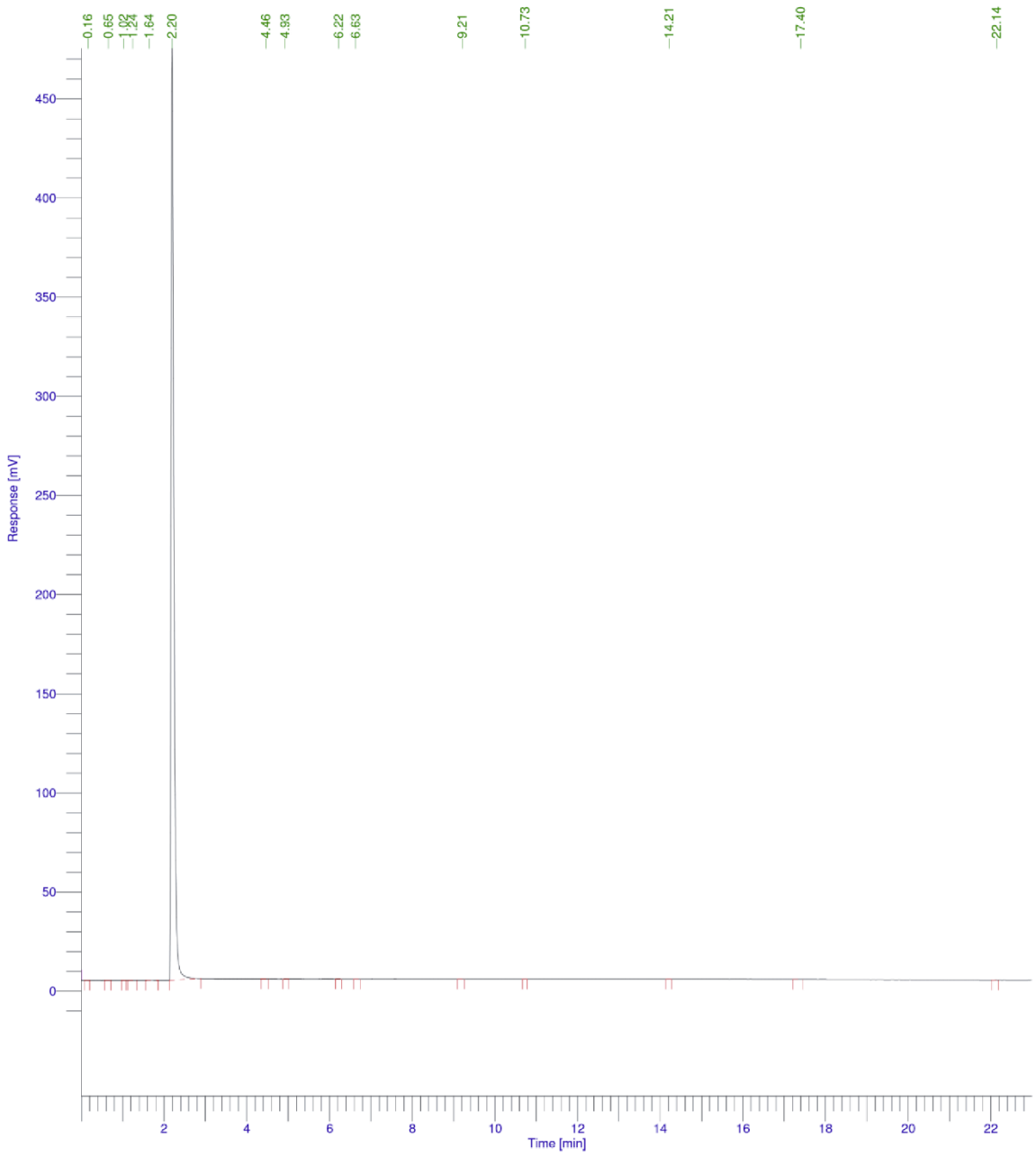

Figure B3: HPLC spectra were recorded using a PerkinElmer Series 200 system with UV/Vis detectors recording at 469 nm and using an acetonitrile and 10 mM ammonium acetate (NH_4OAc) gradient mix. Elution occurred at 2.20 minutes with 99.86% purity

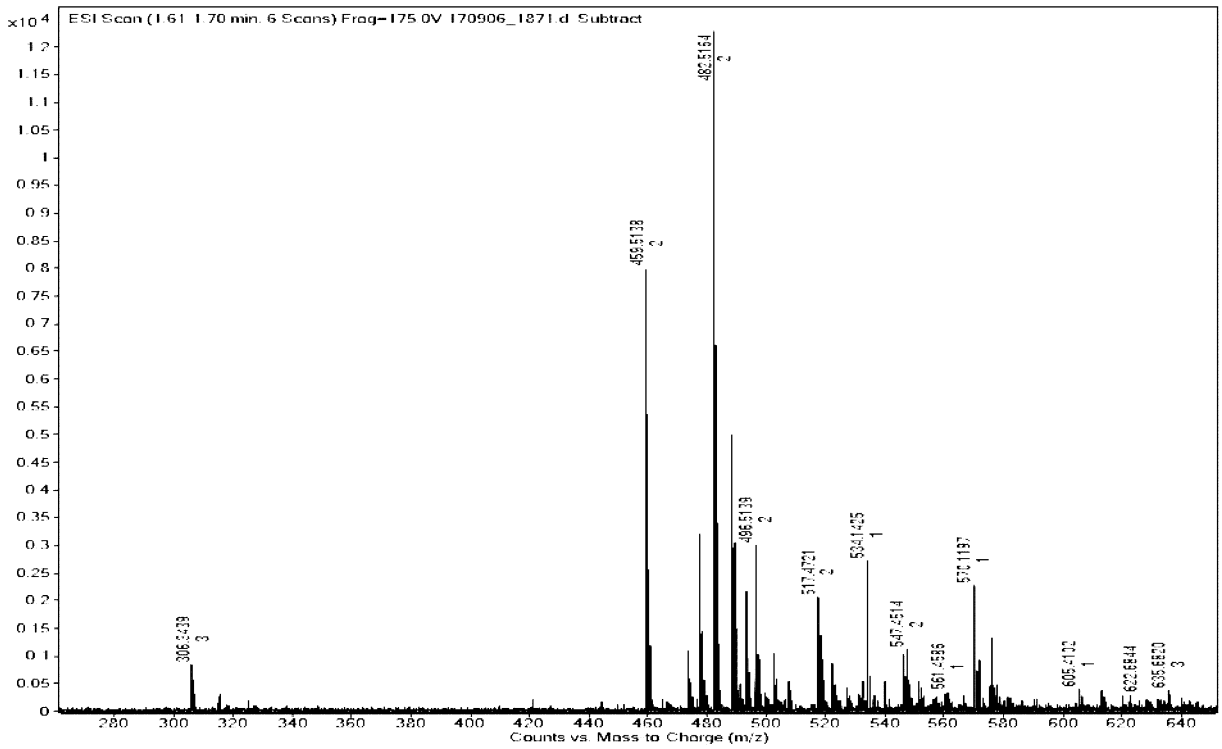

Figure B4: Mass spectroscopy was conducted on $MnPNH_2$ with an Agilent 6538 Q-TOF system in ESI MS Negative mode. ESI MS found m/z=459.5138 [M^+], calculated for $C_{44}H_{26}MnN_5O_9S_3^{-2}$, m/z=459.5142.

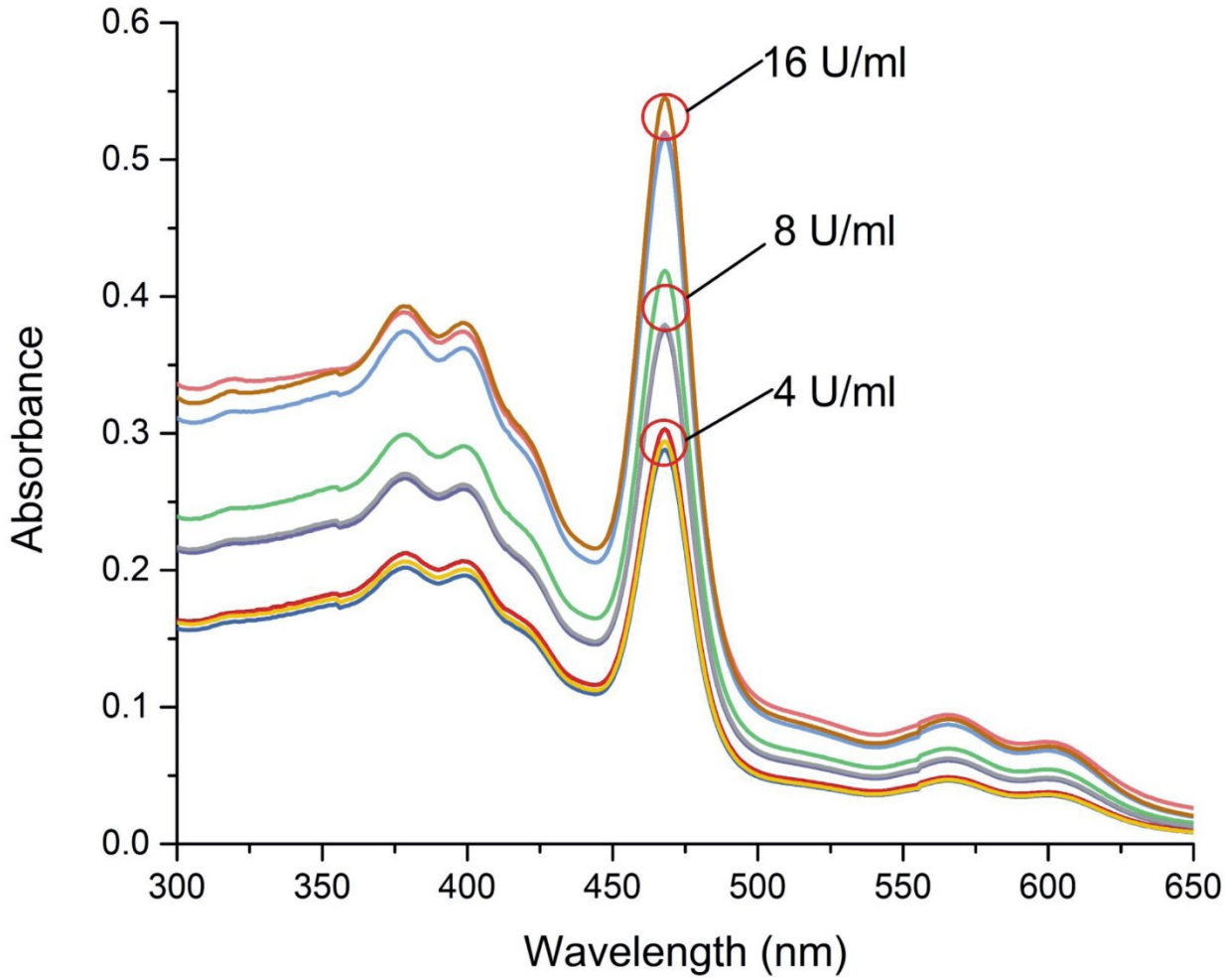

Figure B5: UV-vis analysis of labeled collagen degradation solutions.

Appendix C

Supplemental Information: Bright Ferritin – a reporter gene platform for on-demand, longitudinal cell-tracking on MRI

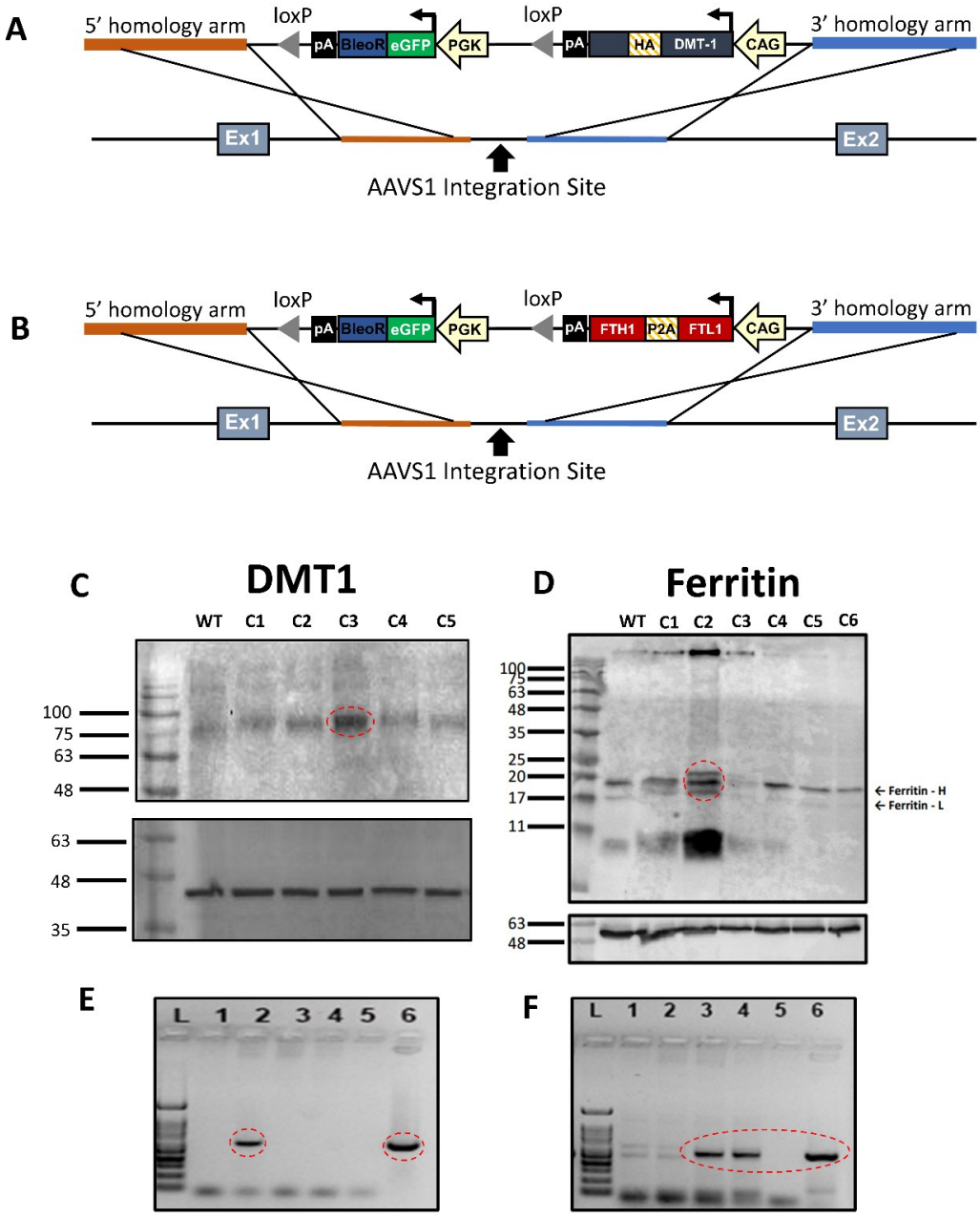

Fig. C1: Western blots and PCR of stably transfected cells. Plasmid vector diagrams for CRISPR/Cas9 gene editing for insertion of **(A)** the DMT-1 transgene and **(B)** the human ferritin transgene at the AAVS1 locus. Western blots for cells overexpressing **(C)** DMT-1 protein and **(D)** ferritin protein. Directly below are the α-tubulin blots for loading control. PCR gels demonstrated enhanced PCR product and overexpression of the **(E)** DMT-1 gene and the **(F)** ferritin gene of

transfected cells in comparison with the original DNA vector. Lanes in the PCR gels are as follows: L: ladder, 1: wild type cells, 2: DMT-1-overexpressing cells, 3: ferritin-overexpressing cells, 4: repeat ferritin-overexpressing cells, 5: water, 6: vector.

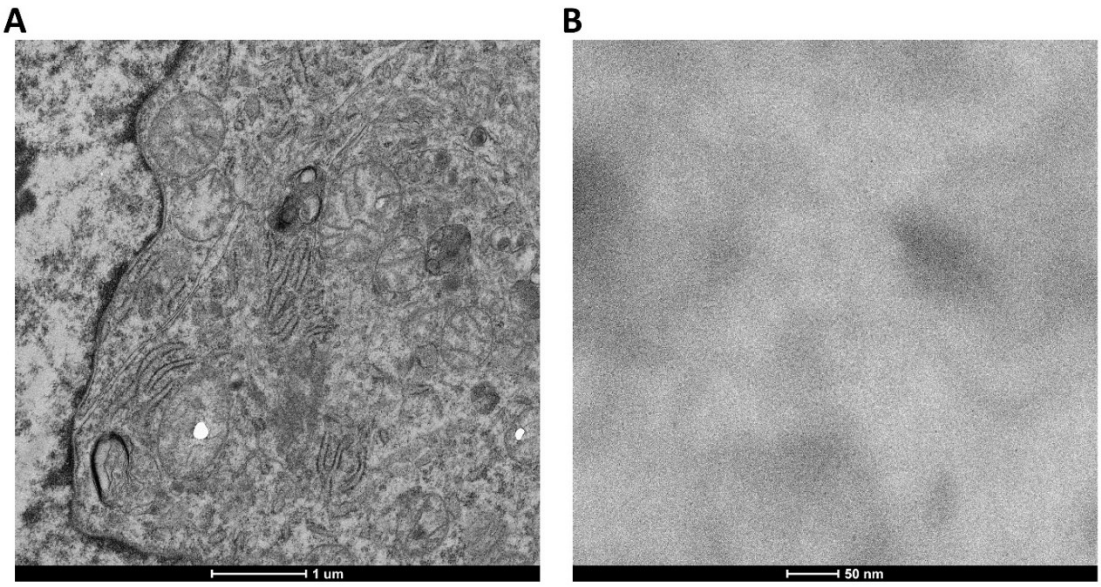

Fig. C2: Control Transmission Electron Micrographs (TEM). TEM of wild type cells **(A)** after incubation with 0.2 mM for 24 hours; no distinguishable nanoparticle aggregates are visible. TEM of purified ferritin nanoparticles **(B)** from ferritin-overexpressing cells before incubation with $MnCl_2$; electron-dense metallic particles are absent.

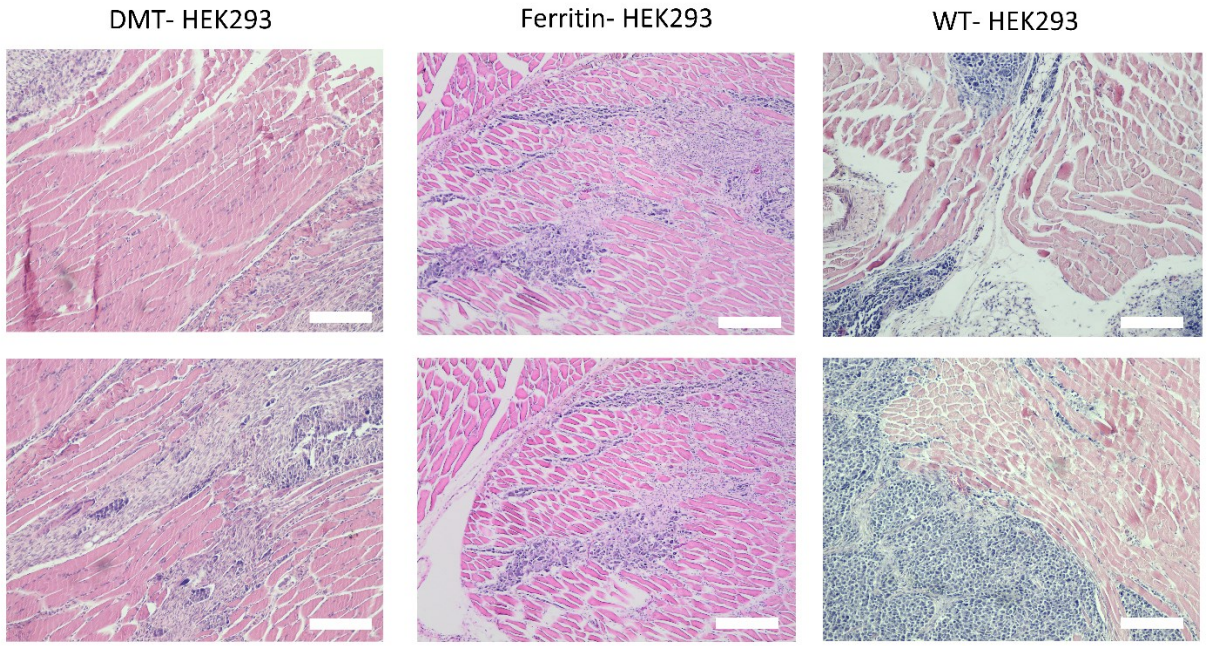

Fig. C3: Histology of cell injection sites in NOD/SCID mice on Day 7. Representative H&E staining of the inner leg muscle demonstrates the diffuse spread of injected HEK cells throughout the muscle. Scale bar = 50 um.

Appendix D

Copyright Permissions

SPRINGER NATURE LICENSE
TERMS AND CONDITIONS

Jun 25, 2020

This Agreement between Mr. Daniel Szulc ("You") and Springer Nature ("Springer Nature") consists of your license details and the terms and conditions provided by Springer Nature and Copyright Clearance Center.

License Number	4855730165029
License date	Jun 25, 2020
Licensed Content Publisher	Springer Nature
Licensed Content Publication	Nature Materials
Licensed Content Title	Tracking gene and cell fate for therapeutic gain
Licensed Content Author	Nigel G. Kooreman et al
Licensed Content Date	Jan 23, 2014
Type of Use	Thesis/Dissertation
Requestor type	academic/university or research institute
Format	electronic
Portion	figures/tables/illustrations
Number of figures/tables/illustrations	1

High-res required	no
Will you be translating?	no
Circulation/distribution	1 - 29
Author of this Springer Nature content	no
Title	The Development of Manganese-based Positive-Contrast MRI Approaches for Non-invasive Monitoring of Biomaterials and Cells in Tissue Engineering
Institution name	University of Toronto
Expected presentation date	Sep 2020
Portions	Figure 1a
Requestor Location	Mr. Daniel Szulc 661 University Ave Toronto, ON M5G1M1 Canada Attn: Mr. Daniel Szulc
Total	0.00 CAD

SPRINGER NATURE LICENSE
TERMS AND CONDITIONS

Jun 24, 2020

This Agreement between Mr. Daniel Szulc ("You") and Springer Nature ("Springer Nature") consists of your license details and the terms and conditions provided by Springer Nature and Copyright Clearance Center.

License Number	4855700475658
License date	Jun 24, 2020
Licensed Content Publisher	Springer Nature
Licensed Content Publication	Nature Reviews Immunology
Licensed Content Title	Tracking immune cells in vivo using magnetic resonance imaging
Licensed Content Author	Eric T. Ahrens et al
Licensed Content Date	Sep 10, 2013
Type of Use	Thesis/Dissertation
Requestor type	academic/university or research institute
Format	electronic
Portion	figures/tables/illustrations
Number of figures/tables/illustrations	1

High-res required	no
Will you be translating?	no
Circulation/distribution	1 - 29
Author of this Springer Nature content	no
Title	The Development of Manganese-based Positive-Contrast MRI Approaches for Non-invasive Monitoring of Biomaterials and Cells in Tissue Engineering
Institution name	University of Toronto
Expected presentation date	Sep 2020
Portions	Box 1, Figure 1, Table 1 and 2
Requestor Location	Mr. Daniel Szulc 661 University Ave Toronto, ON M5G1M1 Canada Attn: Mr. Daniel Szulc
Total	0.00 CAD

JOHN WILEY AND SONS LICENSE
TERMS AND CONDITIONS

Jun 28, 2020

This Agreement between Mr. Daniel Szulc ("You") and John Wiley and Sons ("John Wiley and Sons") consists of your license details and the terms and conditions provided by John Wiley and Sons and Copyright Clearance Center.

License Number	4857960811272
License date	Jun 28, 2020
Licensed Content Publisher	John Wiley and Sons
Licensed Content Publication	Magnetic Resonance in Medicine
Licensed Content Title	MRI method for labeling and imaging decellularized extracellular matrix scaffolds for tissue engineering
Licensed Content Author	Hai-Ling Margaret Cheng, Golnaz Karoubi, Thomas K. Waddell, et al
Licensed Content Date	Nov 14, 2019
Licensed Content Volume	83
Licensed Content Issue	6

Licensed Content Pages	12
Type of use	Dissertation/Thesis
Requestor type	Author of this Wiley article
Format	Electronic
Portion	Full article
Will you be translating?	No
Title	The Development of Manganese-based Positive-Contrast MRI Approaches for Non-invasive Monitoring of Biomaterials and Cells in Tissue Engineering
Institution name	University of Toronto
Expected presentation date	Sep 2020
Requestor Location	Mr. Daniel Szulc 661 University Ave Toronto, ON M5G1M1 Canada Attn: Mr. Daniel Szulc
Publisher Tax ID	EU826007151
Total	0.00 CAD

JOHN WILEY AND SONS LICENSE
TERMS AND CONDITIONS

Jun 28, 2020

This Agreement between Mr. Daniel Szulc ("You") and John Wiley and Sons ("John Wiley and Sons") consists of your license details and the terms and conditions provided by John Wiley and Sons and Copyright Clearance Center.

License Number	4857960684784
License date	Jun 28, 2020
Licensed Content Publisher	John Wiley and Sons
Licensed Content Publication	Macromolecular Bioscience
Licensed Content Title	One-Step Labeling of Collagen Hydrogels with Polydopamine and Manganese Porphyrin for Non-Invasive Scaffold Tracking on Magnetic Resonance Imaging
Licensed Content Author	Hai-Ling Margaret Cheng, Daniel Andrzej Szulc
Licensed Content Date	Jan 15, 2019
Licensed Content Volume	19
Licensed Content Issue	4

Licensed Content Pages	12
Type of use	Dissertation/Thesis
Requestor type	Author of this Wiley article
Format	Electronic
Portion	Full article
Will you be translating?	No
Title	The Development of Manganese-based Positive-Contrast MRI Approaches for Non-invasive Monitoring of Biomaterials and Cells in Tissue Engineering
Institution name	University of Toronto
Expected presentation date	Sep 2020
Requestor Location	Mr. Daniel Szulc 661 University Ave Toronto, ON M5G1M1 Canada Attn: Mr. Daniel Szulc
Publisher Tax ID	EU826007151
Total	0.00 CAD

SPRINGER NATURE

A manganese porphyrin-based T1 contrast agent for cellular MR imaging of human embryonic stem cells

Author: Andrei Venter et al
Publication: Scientific Reports
Publisher: Springer Nature
Date: Aug 14, 2018

ELSEVIER

Bright Ferritin—a Reporter Gene Platform for On-Demand, Longitudinal Cell Tracking on MRI

Author: Daniel A. Szulc,Xavier A. Lee,Hai-Ying Mary Cheng,Hai-Ling Margaret Cheng
Publication: iScience
Publisher: Elsevier
Date: 21 August 2020